

**Chalcogenide and metal-oxide memristive devices for
advanced neuromorphic computing**

by

Tao Guo

A thesis

presented to the University of Waterloo

in fulfillment of the

thesis requirement for the degree of

Doctor of Philosophy

in

Mechanical and Mechatronics Engineering (Nanotechnology)

Waterloo, Ontario, Canada, 2023

© Tao Guo 2023

Examining Committee Membership

The following served on the Examining Committee for this thesis. The decision of the Examining Committee is by majority vote.

External Examiner	Professor Wei D. Lu, Department of Electrical Engineering and Computer Science, University of Michigan, USA
Supervisors	Professor Norman Y. Zhou, Department of Mechanical and Mechatronics Engineering, University of Waterloo, Canada and, Professor Yimin A. Wu, Department of Mechanical and Mechatronics Engineering, University of Waterloo, Canada
Internal Member	Professor, Mustafa Yavuz, Department of Mechanical and Mechatronics Engineering, University of Waterloo, Canada
Internal-external Member	Professor Eihab Abdel-Rahman, Systems Design Engineering, University of Waterloo, Canada
Internal-external Member	Professor Lan Wei, Department of Electrical and Computer Engineering, University of Waterloo, Canada

Author's Declaration

This thesis consists of material all of which I authored or co-authored: see Statement of Contributions included in the thesis. This is a true copy of the thesis, including any required final revisions, as accepted by my examiners.

I understand that my thesis may be made electronically available to the public.

Statement of Contributions

This thesis consists of a literature review (Chapter 2) and three research data chapters written in the manuscript format (Chapters 3-5). At the time of submission, 11 papers had been published (10 first-authored papers). One manuscript (first author) has been accepted by a refereed journal. All manuscripts are modified to fit the style of the thesis. I am the primary author of all manuscripts. Dr. Norman Zhou and Yimin A. Wu are corresponding authors and have reviewed each chapter. Several co-authors on these manuscripts have been shown in this thesis. Their contributions are described below.

Chapter 3

Tao Guo, Kangqiang Pan, Yixuan Jiao, Bai Sun, Cheng Du, Joel P Mills, Zuolong Chen, Xiaoye Zhao, Lan Wei, Y Norman Zhou, Yimin A Wu. “Versatile memristor for memory and neuromorphic computing.” *Nanoscale Horizons* 7, no. 3 (2022): 299-310.

Kangqiang Pan provided support on neural circuit simulation. Yixuan Jiao, Bai Sun, and Cheng Du helped me with the electrodeposition. Joel P Mills, Zuolong Chen, and Xiaoye Zhao helped me with materials characterizations. Lan Wei provided editorial support and guidance. I conceptualized the idea, completed the device fabrication, conducted the electrical characterization, and wrote the manuscript.

Chapter 4

Tao Guo, Jiawei Ge, Yixuan Jiao, Youchao Teng, Bai Sun, Wen Huang, Hatameh Asgarimoghaddam, Kevin P Musselman, Yin Fang, Y Norman Zhou, Yimin A Wu. “Intelligent matter endows reconfigurable temperature and humidity sensations for in-sensor computing.” *Materials Horizons* (2023).

Jiawei Ge helped me with the material calculation. Yixuan Jiao, Youchao Teng, Bai Sun, Wen Huang, and Hatameh Asgarimoghaddam, helped me with the thin film fabrication. Youchao Teng helped me with SEM characterizations. Kevin P Musselman and Yin Fang provided editorial support and guidance. I conceptualized the idea, completed the device fabrication, conducted the electrical characterization, completed the pattern recognition simulation, and wrote the manuscript.

Chapter 5

Tao Guo, Baizhou Zhang, Xiyang Wang, Yi Xiao, Bai Sun, Y. Norman Zhou, and Yimin A. Wu. “Broadband optoelectronic synapse enables compact monolithic neuromorphic machine vision for information processing.” Accepted by Advanced Functional Materials (adfm.202303879).

Baizhou Zhang provided support on device fabrications. Xiyang Wang and Yi Xiao helped me with the material calculation. Bai Sun provided editorial support and guidance. I conceptualized the idea, conducted the electrical characterization, completed the pattern recognition simulation, conducted the convolutional processing, and wrote the manuscript.

Abstract

Energy-intensive artificial intelligence (AI) is prevailing and changing the world, which requires energy-efficient computing technology. However, traditional AI driven by von Neumann computing systems suffers from the penalties of high-energy consumption and time delay due to frequent data shuttling. To tackle the issue, brain-inspired neuromorphic computing that performs data processing in memory is developed, reducing energy consumption and processing time. Particularly, some advanced neuromorphic systems perceive environmental variations and internalize sensory signals for localized in-sensor computing. This methodology can further improve data processing efficiency and develop multifunctional AI products. Memristive devices are one of the promising candidates for neuromorphic systems due to their non-volatility, small size, fast speed, low-energy consumption, etc.

In this thesis, memristive devices based on chalcogenide and metal-oxide materials are fabricated for neuromorphic computing systems. Firstly, a versatile memristive device ($\text{Ag/CuInSe}_2/\text{Mo}$) is demonstrated based on filamentary switching. Non-volatile and volatile features are coexistent, which play multiple roles of non-volatile memory, selectors, artificial neurons, and artificial synapses. The conductive filaments' lifetime was controlled to present both volatile and non-volatile behaviours. Secondly, the sensing functions (temperature and humidity) are explored based on Ag conductive filaments. An intelligent matter ($\text{Ag/Cu(In, Ga)Se}_2/\text{Mo}$) endowing reconfigurable temperature and humidity sensations is developed for sensory neuromorphic systems. The device reversibly switches between two states with differentiable semiconductive and metallic features, demonstrating different responses to temperature and humidity variations. Integrated devices can be employed for intelligent electronic skin and in-sensor computing. Thirdly, the memristive-based sensing function of light was investigated. An optoelectronic synapse ($\text{ITO/ZnO/MoO}_3/\text{Mo}$) enabling multi-spectrum sensitivity for machine vision systems is developed. For the first time, this optoelectronic synapse is practical for front-end retinomorphic image sensing, convolution processing, and back-end neuromorphic computing. This thesis will benefit the development of advanced neuromorphic systems pushing forward AI technology.

Keywords: Memristive device, resistive switching, memory, neuromorphic computing, in-sensor computing

Acknowledgements

I am incredibly grateful for everything that happened during my Ph.D. journey. It is impossible to complete this research program without tremendous support from my supervisors, my friends, and my family members.

Firstly, I would like to thank my supervisors, Professor Norman Zhou and Professor Yimin Wu. They constantly guided, supported, and motivated me. The lessons they gave me regarding both research and life are great treasures for my future. I also want to thank Professor Lan Wei, Professor Kevin Musselman, Professor Zhao Pan, and Professor Yin Fang for fruitful discussions and suggestions on my research projects.

Secondly, I want to express my gratitude to my colleagues and friends. I am so lucky to meet many supportive, thoughtful, and warmhearted individuals: Yao Xu, Xiaoye Zhao, Hanwen Yang, Yixuan Jiao, Kangqiang Pan, Cheng Du, Zuolong Chen, Jiawei Ge, Joel P. Mills, Youchao Teng, Yongzan Zhou, Wei Wei, Bai Sun, Baizhou Zhang, Siyang Lu, Lei Wang, Xiyang Wang, Zhe Su, Zhilei Zhang, Jingyan Zhang, Shubham Ranjan, Bryce Joseph Kieffer, Jihui Yan, Kaiping Zhang, Ali Ghatei Kalashami, Shuo Zheng, Ningyue Mao, Rami Hakim, Yong Yan, Wen Huang. You made my study life much easier and more colorful. I wish you all the best.

Finally, I want to thank my father, mother, sister, brother-in-law, and two pretty nieces. I have received so much love from them, which makes me feel I am the luckiest person.

Today is great, tomorrow will be even better.

Dedication

To Life

Table of Contents

Examining Committee Membership.....	ii
Author’s Declaration	iii
Statement of Contributions.....	iv
Abstract	vi
Acknowledgements	vii
Dedication	viii
List of Figures	xiii
List of Tables.....	xxiv
Nomenclature	xxv
Chapter 1 . Introduction.....	1
1.1 Background	1
1.2 Objectives.....	3
1.3 Organization of the Thesis.....	3
Chapter 2 . Literature Review	6
2.1 Memristive Effects	6
2.1.1 The History of Memristive Effects.....	6
2.1.2 Memristive Characteristics and Parameters	7
2.1.3 Memristive Mechanisms	16
2.1.4 Memristive Chalcogenides and Metal Oxides.....	19
2.2 Investigation Methods for Resistive Switching.....	26
2.2.1 Transmission Electron Microscopy.....	26
2.2.2 Scanning Probe and X-ray Microscopy.....	28
2.2.3 Conduction Mechanisms Based on I-V Characteristic.....	32

2.2.4 Theoretical Model Simulations	36
2.3 Memristive Devices for Neuromorphic Computing	43
2.3.1 Neuromorphic Computing with Artificial Neural Network	43
2.3.2 Memristive-based Neuromorphic Devices	46
2.3.3 Neuromorphic Computing for Image Processing	48
Chapter 3 . Versatile Memristor for Memory and Neuromorphic Computing	52
3.1 Introduction	52
3.2 Experimental Section.....	55
3.2.1 Device Fabrication.....	55
3.2.2 Materials and Device Characterization Methods.....	57
3.2.3 Simulation Methods.....	57
3.3 Results and Discussion	59
3.3.1 Materials Characterizations	59
3.3.2 Resistive Switching Behaviors	63
3.3.3 Artificial Neurons and Synapses	69
3.3.4 Working Mechanism Investigations	74
3.4 Summary	78
Chapter 4 . Intelligent matter endows reconfigurable temperature and humidity sensations for in- sensor computing.....	79
4.1 Introduction	79
4.2 Experimental Section.....	84
4.2.1 Device Fabrication.....	84
4.2.2 Materials and Device Characterization Methods.....	84
4.2.3 Simulation Methods.....	85

4.3 Results and Discussion.....	85
4.3.1 Material Characterizations.....	85
4.3.2 Resistive Switching and Sensory Characterizations.....	86
4.3.3 Working Mechanism Investigations.....	91
4.3.4 Intelligent In-sensor Neuromorphic Computing.....	96
4.4 Summary	101
Chapter 5 . Broadband optoelectronic synapse enables compact monolithic neuromorphic machine vision for information processing.....	103
5.1 Introduction	103
5.2 Experimental Section.....	107
5.2.1 Device Fabrication.....	107
5.2.2 Material and Device Characterization Methods	108
5.2.3 Simulation Methods.....	108
5.3 Results and Discussion.....	109
5.3.1 Materials Characterizations	109
5.3.2 Retinomorphic image sensing and convolution processing.....	112
5.3.3 Neuromorphic Computing for Cognitive Tasks	125
5.3.4 Mechanism of Optoelectronic Performances	128
5.3.5 Monolithic Neuromorphic Machine Vision System.....	130
5.4 Summary	132
Chapter 6 . Conclusion and Outlook	133
6.1 Conclusions	133
6.2 Outlook.....	135
Chapter 7 . Research Contributions.....	137

7.1 Articles Published in Refereed Journals.....	137
7.2 Patent.....	138
7.3 Awards Received.....	138
Letters of Copyright permission.....	139
References	187

List of Figures

Figure 1. The computing power demand trend over 40 years. The consumption is described in petaFLOPS days. Reprinted with permission. ¹ Copyright 2022, Springer Nature.....	1
Figure 2. Four fundamental two-terminal passive circuit elements. Reprinted with permission. ⁴ Copyright 2008, Springer Nature.	7
Figure 3. (a) Diagram of a typical memristive device. (b) Integrated memristive devices in a crossbar. Reprinted with permission. ²³ Copyright 2008 Elsevier Ltd. (c) I-V curve of a unipolar switching. (d) I-V curve of a bipolar switching. Reprinted with permission. ²⁷ Copyright 2009, WILEY - VCH Verlag GmbH & Co. KGaA, Weinheim.	8
Figure 4. (a) DC switching cycle test for 100 consecutive cycles. Reprinted with permission. ³⁰ Copyright 2021, The Authors. (b) Distribution of LRS and HRS over 100 cycles, the data is extracted from the DC switching cycle test. Reprinted with permission. ³² Copyright 2022, The Authors. (c) Endurance test on the device with distinctive resistance levels by current-blind PVS. Reprinted with permission. ³¹ Copyright 2022, American Chemical Society. (d) Endurance test on the device with distinctive resistance levels by current-visible PVS. Reprinted with permission. ³³ Copyright 2013, The Authors. (e) Endurance test of potentiation/depression behaviors. Reprinted with permission. ³⁴ Copyright 2022, The Authors.....	10
Figure 5. (a) Illustration of the measurement setup for the state retention time. The inset is a typical experimental circuit. (b) State retention time under different program electronic stresses. Reprinted with permission. ³⁵ Copyright 2019, The Author(s). (c) Typical state retention time of HRS and LRS. Reprinted with permission. ³⁶ Copyright 2019, The Authors. (d) Multi-level state retention time. Reprinted with permission. ³⁷ Copyright 2022, The Authors. (e) Retention time under different temperatures. Reprinted with permission. ³⁸ Copyright 2021, The Authors.	11
Figure 6. (a) Typical DC switching cycle test for multiple cycles, 500 cycles in this specific example. Reprinted with permission. ⁶² Copyright 2022, American Chemical Society. (b) The cycle-to-cycle and device-to-device variations presented by cumulative probability plots of LRS and HRS. Reprinted with permission. ⁵³ Copyright 2012, The Authors. (c) The histogram of device SET voltages and RESET voltages of 48 devices under multi-cycle operations. Reprinted with permission. ³⁰ Copyright 2020, The Author(s). (d) Cumulative probability plots of 32 independent states. Reprinted with permission. ⁵⁴ Copyright 2020, The Author(s). (e) The variation of the potentiation/depression plasticity. Reprinted with permission. ⁵⁵ Copyright 2021, American Chemical Society. (f)	

Conductance map of the synaptic array after localized pulse programming to write the ‘UMAS’. Reprinted with permission.⁵⁶ Copyright 2019, The Author(s). 15

Figure 7. (a) Typical V-t and I-t synchronous curves corresponding to the switching process. Reprinted with permission.⁶³ Copyright 2021, The Author(s). (b) Typical setup for testing memristors. Reprinted with permission.⁶⁴ Copyright 2021, The Author(s). (c) Typical setup for testing memristors with a tandem resistor to limit the current. Reprinted with permission.⁶⁵ Copyright 2016, The Author(s). (d) Typical setup testing memristors with a pulse generator and an oscilloscope. Reprinted with permission.⁶⁶ Copyright 2012, IEEE. 16

Figure 8. (a) Illustration of set operation in anion-based devices. (b) Illustration of filamentary-type resistive switching based on anions. (c) Illustration of interface-type resistive switching based on anions. (d) Illustration of set operation in cation-based devices. (e) Illustration of filamentary-type resistive switching based on cations. (f) Illustration of resistive switching based on hybrid anions and cations..... 19

Figure 9. (a-c) TEM image of Ag₂S-based memristor at the initial state, LRS, and HRS. (d) I-V characteristic of the device. Reprinted with permission.⁹⁹ Copyright 2010 American Chemical Society. (e) The typical I-V characteristic and the corresponding electrochemical metallization process. Reprinted with permission.²⁷ Copyright 2009 WILEY-VCH Verlag GmbH & Co. KGaA, Weinheim. (f) Schematic diagram of the vertical MoTe₂-based device. (g) Atomic resolution scanning transmission electron microscopy image of the MoTe₂. Reprinted with permission.¹¹⁴ Copyright 2018 Springer Nature. (h) Schematic diagram of local 2H-T' phase transitions in Li_xMoS₂ induced by Li⁺ migration. Reprinted with permission.¹¹⁵ Copyright 2018 Springer Nature..... 21

Figure 10. (a) Equivalent circuit of boundary migration model. (b) I-V characteristic of the Pt/TiO_{2-x}/Pt device. Reprinted with permission.⁴ Copyright 2008, Springer Nature. (c) Schematic diagrams of resistive switching mechanism based on conductive channels model in the Ta₂O_{5-x}/TaO_{2-x} device. Reprinted with permission.¹⁵² Copyright 2013, Springer Nature. (d) The high-resolution transmission electron microscopy (HRTEM) image of the Ag/TiO₂:Ag/Pt device. Reprinted with permission.¹⁵³ Copyright 2017 WILEY-VCH Verlag GmbH & Co. KGaA, Weinheim. (e) I-V characteristics of a Ti/Pr_{0.7}Ca_{0.3}MnO₃(PCMO)/SrRuO₃(SRO) device in linear and semilogarithmic current scales. Insets show electronic band diagrams of the Ti/PCMO interface. Reprinted with permission.¹⁵⁵ Copyright 2004 American Institute of Physics. 24

Figure 11. (a) Schematic diagram of a typical *in-situ* TEM experimental setup, the studied device structure was Ag/SiO₂/W. Reprinted with permission.⁸⁸ Copyright 2014, Nature Publishing Group (b) *In-situ* observed metallic conductive filaments at the LRS and HRS. Reprinted with permission.⁸⁷ Copyright 2012, Nature Publishing Group. (c) The cross-section image included a channel region observed at the LRS. The studied device structure was Pt/SiO₂/Ta₂O_{5-x}/TaO_{2-x}/Pt. (d) The oxygen profiles at the channel region (shown in c) were measured under the HRS (black) and LRS (red). Reprinted with permission.¹⁵² Copyright 2013, Nature Publishing Group. (e) A typical polymorphous HfO_x region with completed conductive filaments. (f-g) FFT diffraction patterns of h-Hf₆O and m-HfO₂ region. Reprinted with permission.⁶³..... 27

Figure 12. (a) Schematic diagram of an experimental setup for a typical CAFM. Reprinted with permission.¹⁹³ Copyright 2020, WILEY - VCH Verlag GmbH & Co. KGaA, Weinheim. (b) The AFM and C-AFM images of HRS and LRS, the CAFM image was posed on the AFM image. Reprinted with permission.¹⁴⁷ Copyright 2008, AIP Publishing. (c) 3D reconstructed tomogram of a metallic conductive filament. Reprinted with permission.¹⁹⁵ Copyright 2013, IEEE. (d) Schematical diagram of STM for resistive switching investigation. (e) STM images (1 μm × 1 μm) of TaO_x film before and after scanning, corresponding SET and RESET operations. Reprinted with permission.¹⁹⁶ Copyright 2016, American Chemical Society..... 29

Figure 13. (a) Schematic diagram of the experimental setup for a typical synchrotron-based scanning transmission X-ray microscopy (STXM) measurement. (b) The X-ray transmission intensity map. Reprinted with permission.²⁰⁰ Copyright 2016, American Chemical Society. (c) The XAS and XRD spectroscopy are shown in c_1 and c_2, respectively. c_3 shows the schematic diagram of the experimental setup for the X-ray multimodal imaging. (d) The conductive channel consists of W and O elements. Reprinted with permission.²⁰¹ Copyright, 2022 Wiley - VCH GmbH..... 31

Figure 14. (a) Typical I-V curve in log-log scale. Reprinted with permission.²¹¹ Copyright 2010, AIP Publishing. (b) I-V curves tested under different temperatures. The inset shows $\ln(J)-V^{1/2}$ plots. (c) $\ln(J/T^2)-1000/T$ plots under different reading voltages. Reprinted with permission.²¹⁶ Copyright 2013, AIP Publishing. (d) The values of LRS under different temperatures. The inset shows temperature-dependent resistance for devices with varied sizes. (e) The values of HRS under different temperatures. The inset presents the plot of $\ln(I)-1/\kappa T$ to calculate the activation energy. Reprinted with permission.²¹⁸ Copyright 2008, AIP Publishing. (f) Cyclic voltammetry tests under different humidity levels. (g) Ion concentration (c_{ion}) under different humidity levels. The pH₂O means the

partial pressure of water. Reprinted with permission.²¹⁹ Copyright 2013, American Chemical Society.
..... 35

Figure 15. (a) Schematic diagram of physical models. (b) Schematic diagram of the FP simulation. (c) Schematic diagram of the MD simulation. (d) Schematic diagram of the KMC simulation. (e) Schematic diagram of the FE simulation. Reprinted with permission.⁹ Copyright 2019, The Author(s).
..... 38

Figure 16. (a) Schematic diagram of compact models. (b) The compact model that the resistance is governed by the moving of doped/undoped boundary. (c) The compact model that the resistance is governed by the modulated Schottky barriers. (d) The compact model that the resistance is governed by the modulated conductive filaments. (e) The compact model that the resistance is governed by the modulated tunneling barriers..... 41

Figure 17. (a) Schematic diagram of a biological brain relying on neurons and synapses to realize computing functions. Reprinted with permission.²⁵⁶ Copyright 2020, Springer Nature. (b) Schematic diagram of fully connected neural networks. (c) Schematic diagram of a memristive crossbar array that implements VMM operations. Reprinted with permission.²⁵⁷ Copyright 2020, Springer Nature. (d) Schematic diagram of in-sensor computing architecture. (e) Schematic diagram of fully connected neural networks that are responsible for sensory signals. S means the stimuli response to sensory information. R is the sensory responsivity presented by conductance. I is the output current. Reprinted with permission.³ Copyright 2020, Springer Nature. 44

Figure 18. (a) Illustration of gradually modulated conductance that represents synaptic weights for ANNs. (b) Illustration of gradually modulated conductance that can be modulated by sensory signals for in-sensor computing. (c) Illustration of neural spiking in artificial neuromorphic systems. (d) Illustration of a biological brain consisting of synapses and neurons for information processing..... 47

Figure 19. (a) SEM image of an integrated 12 x 12 memristive crossbar. Reprinted with permission.²⁸⁷ Copyright 2015, Nature Publishing Group. (b) Left, the photograph of a customized printed circuit board. Right, the processing element (PE) chip with a memristive array (2,048 devices) and on-chip decoder circuits. Reprinted with permission.⁵⁴ Copyright 2020, The Author(s). (c) Schematic diagram of stackable hetero-integrated chips. Reprinted with permission.²⁹³ Copyright 2022, Springer Nature.
..... 49

Figure 20. (a) Schematic diagram of an artificial neural network (ANN) photodiode array and the circuit of a single pixel. Reprinted with permission.¹⁴ Copyright 2020, The Author(s). (b) Schematic

diagram of the in-sensor computing with memristive devices sensory to humidity. (c) The modulated characteristic of artificial synapses by moisture. Reprinted with permission.²⁷⁴ Copyright, 2021 Wiley - VCH GmbH. (d) Schematic diagram of a memristive-based machine visions system enabling sensing and neuromorphic computing abilities. Reprinted with permission.³⁰¹ Copyright, 2022 Wiley - VCH GmbH..... 51

Figure 21. The fabrication process of the Ag/CISE/Mo memristor with a crossbar configuration. 55

Figure 22. (a) Cyclic voltammetry (CV) curves in an electrolytic bath for CISE deposition. The scan rate was 20 mV/s. (b) Electrodeposition current versus time during the depositing process. 57

Figure 23. Circuit design for the simulation of artificial LIF neurons. The simulation was carried out on the Cadence Virtuoso platform. SW1-3 are switches. R1-4 are resistors. M1 is a threshold switching (TS) memristor..... 59

Figure 24. Materials characterizations on the Ag/CISE/Mo device. (a) Optical micrograph of the device. (b) Cross-section SEM image of the device with a sandwich structure. (c) Surface composition EDX mapping of the deposited CISE thin film. The inset table presents the composition percentage (d) Raman spectrum of the deposited CISE. (e) The GIXRD spectrum of the CISE/Mo. (f) Wide-scan XPS spectrum of the CISE thin film. 60

Figure 25. High-resolution XPS spectra of different regions: (a) Cu 2p region; (b) In 3d region; (c) Se 3d region. The results confirm the chemical states of Cu, In, Se are +1, +3, -2, respectively¹⁵. 61

Figure 26. Impedance analysis. (a) Nyquist plot of CISE at room temperature. (b) The plot of the Modulus vs Frequency. (c) The plot of the Phase vs Frequency. (d) The equivalent circuit for fitting. 63

Figure 27. Systematic analysis on resistive switching. (a) Typical I-V curve of the device under different CCs. (b) Probability for volatile TS as a function of CC. (c) Typical I-V curve of the device under a linear scale over the sweep voltage of -1 V to 1 V. (d) Retention time under different voltage amplitudes. (e) Retention time under different temperatures. (f) The Arrhenius plot of the retention time depending on the temperature. (g) Non-volatile switching under a pulsed-voltage operation. The operation voltage pulse was $\pm 3V$ with a duration of 1s. The read voltage was 0.2 V. The duty cycle of the pulse was 50%. The box plot was based on the first 165 cycles. (h) The HRS/LRS resistance distribution over 400 switching cycles. The data was extracted from the result of the DC switching cycle test. The sweep voltage was -1 V to 1 V. (i) The distribution of the device resistance under forward and reverse biasing over 400 switching cycles. 64

Figure 28. I-V curves and RESET voltage change over different thicknesses of CISE layers. Each device operated for 50 cycles. (a) I-V curves of the device Ag/CISE@100nm/Mo. (b) I-V curves of the device Ag/CISE@300nm/Mo. (c) I-V curves of the device Ag/CISE@1200nm/Mo. (d) The cumulative probabilities of the RESET voltages for the devices with different CISE thicknesses. 65

Figure 29. (a) HRS and LRS resistance distributions over switching cycles. (b) Non-volatile memory behavior, the voltage amplitude was 3 V, the pulse duration was 1s. (c) I-V curve reproducibility of the device over 400 switching cycles. (d) The distribution of SET and RESET voltages. The σ_{SET} (and σ_{RESET}) and μ_{SET} (and μ_{RESET}) are the standard deviation and the mean value, respectively. 67

Figure 30. Device-to-device variability of HRS and LRS..... 68

Figure 31. Schematic diagram of artificial neuron system and LIF neuron simulation results. (a) Diagram of biological artificial neuron system and the LIF neuron circuit. LGP means local graded potential that reflects the dynamics of the neural membrane potential. (b) The simulation of neural spiking response under different excitation frequencies. The b-1 shows the input signals. The b-2 shows the V_C under different input signals. The b-3 shows the output signals. (c) The simulation of neural spiking response under different excitation amplitudes. The c-1 shows the input signals with different amplitudes. The c-2 shows the V_C under different input signals. The b_3 shows the output signals..... 72

Figure 32. Artificial synaptic performance. (a) Schematic diagram of a synapse. (b) Experimental result of short-term synaptic PPF behavior. (c) The potentiation and depression behaviors of the device. The pulse amplitudes for potentiation and depression operations were + 1 V and -1 V, respectively. The pulse duration was 50 ms. The read voltage was 0.1 V. 50 consecutive pulses were applied for both potentiation and depression operations. (d) Simulations of backpropagation algorithm for UCI Small image recognition (image size was 8×8 pixels)..... 73

Figure 33. (a) Typical I-V curve of the Mo/CISE/Mo device. (b) The values of LRS at different temperatures for the Ag/CISE/Mo device..... 74

Figure 34. Conduction mechanisms of the volatile TS and non-volatile MS in the Ag/CISE/Mo device. (a) Log (I) - log(V) curve, the voltage swept from 0 V \rightarrow 1 V \rightarrow 0 V. (b) Ln (|I|) - $V^{1/2}$ curve, the voltage swept from 0 V \rightarrow -1 V. (c) Ln (|I|) - $V^{1/2}$ curve, the voltage swept from -1 V \rightarrow 0 V. (d) Log (I) - log(V) curve, the voltage swept from 0 V \rightarrow 3 V \rightarrow 0 V. (e) Ln (|I|) - $V^{1/2}$, the voltage swept from 0 V \rightarrow -3 V. (f) Ln (|I|) - $V^{1/2}$, the voltage swept from -3 V \rightarrow 0 V..... 75

Figure 35. Illustration diagram of the volatile/non-volatile resistive switching. (a) Mechanism of conductive filament evolution for the volatile TS behaviors. (b) Mechanism of conductive filament evolution for the non-volatile MS behaviors..... 77

Figure 36. Conceptual illustration of intelligent matter with reconfigurable temperature and humidity sensations. (a) Schematic diagram of a biological system with synergistic temperature and humidity sensations. (b) Schematic diagram of the switchable device with temperature and humidity sensations. MCF means metallic conductive filament..... 80

Figure 37. Materials characterizations. (a) Schematic diagram of the device structure. (b) Cross-section of the device. (c) Surface topography of the deposited CIGSe switching layer. (d) Surface composition mapping (Element: Cu, In, Ga, Se) of the CIGSe film. (e) Raman spectrum of the CIGSe thin film. (f) GIXRD spectrum of CIGSe/Mo. 86

Figure 38. (a) DC switching cycle test under different compliance currents (CCs). 100 switching cycles for each test. (b) Resistance states distribution under different compliance currents (CCs). (c) The retention time of the HRS and LRS. (d) The device-to-device variation. The results are from the direct current (DC) switching cycle test. 88

Figure 39 Electronic characterizations. (a) DC switching cycle test for 60 cycles. (b) Cumulative probability of the operation voltages. CV represents the “coefficient of variation” which was defined as the standard deviation divided by the mean value. (c) The endurance of the device, which is presented by the resistance distribution under consecutive switching operations. The pulse duration was 200 ms. (d) Short-term synaptic paired-pulse facilitation (PPF) behavior. The pulse amplitude was 1V. Data points were extracted from the average values of five tests. The fitting equation was $PPF = A_1e^{-\Delta T\tau_1} + A_2e^{-\Delta T\tau_2} + y_0$. The fitting parameters of A_1 , A_2 , y_0 , τ_1 , and τ_2 were 639.4, 123.2, 22.9, 0.3 ms, and 5.4 ms respectively. (e) Conductance modulation under consecutive pulses with different amplitudes. The pulse number was 100. The pulse duration and pulse interval time were both 10 ms. (f) Potentiation and depression performance of the device. (g) Conductance changes (LRS and HRS) under different temperatures. (h) Change of LRS/HRS ratio under different temperatures. L_H Ratio means the ratio of LRS/HRS. The X-axis and Y-axis are both in linear scale. For the inset, the X-axis and Y-axis are in linear scale and natural-logarithm scale, respectively. (i) Conductance changes (LRS and HRS) under different humidity levels. 89

Figure 40. Reversibility test of conductance changes (LRS and HRS) under different humidity levels. 91

Figure 41. (a) The DC switching cycle test of the device in the log(I)-log(V) scale (positive region). (b) The DC switching cycle test of the device in the log(I)-log(V) scale (negative region). (c) The DC switching cycle test of the device in the $V^{1/2}$ -Ln(I) scale (negative region). (d) The DC switching cycle test of the Mo/CIGSe/Mo. The sweep voltage was 0 → 1 V → -1 V → 0 V..... 92

Figure 42. Working mechanism. (a) Schematic diagram of the HRS under different temperatures, Conductance increased with the increase of temperatures. The letter “T” and “G” in the picture means the temperature and conductance, respectively. The upward arrow and downward arrow mean the increase and decrease of the relevant values. (b) Schematic diagram of the LRS under different temperatures. Conductance decreased with the increase of temperature. (c) Schematic diagram of HRS under different humidity levels. Conductance barely changed as modulating the humidity. The letter “H” and “G” in the picture means the humidity and conductance, respectively. The upward arrow means the increase of the relevant values. (d) Schematic diagram of LRS under different humidity levels. Conductance increased with the increase of humidity levels. (e) Illustration of the diffusion mechanism of Ag atoms at the bare and H₂O-bonded surfaces. 94

Figure 43. Schematic diagram for the calculation of thermal transmission distribution in one direction. 97

Figure 44. (a) Theoretical simulation of the thermal transmission distribution in one direction. (b) The change of G_{Tem}/G_0 under different temperatures at the LRS model. (c) The change of G_{Tem}/G_0 under different temperatures at the HRS model. (d) The change of $Ratio_{Tem}/Ratio_0$ under different temperatures at the HRS&LRS model. $Ratio_0$ is the ratio of LRS/HRS at room temperature (288K). 98

Figure 45. In-sensor neuromorphic computing. (a) Schematic diagram of the intelligence skin with tunable thermal sensitivities. (b) 1: The thermal transmission distribution on the surface of artificial skin from a point heat source. 2-3: The output distribution on the artificial skin in the LRS model, HRS model, and HRS&LRS model, respectively. (c) Schematic diagram of ANN for in-sensory neuromorphic computing for pattern recognition. (d) Neuromorphic computing accuracy under different humidity levels..... 99

Figure 46. Electronic potentiation/depression characterizations under different humidity levels. 101

Figure 47. The concept of the artificial retina. (a) Image processing hierarchy in biological systems. (b) Schematic diagram of the biological synapse operated by electronic and photonic stimuli. (c) Schematic diagram of modulated heterojunction enabling photonic sensitivity and electronic plasticity. 104

Figure 48. (a) UV-visible absorption spectroscopy of the ITO thin film. Inset is the Tauc plot for calculating the optical band gap. (b) UV-visible absorption spectroscopy of the ZnO thin film. Inset is the Tauc plot for calculating the optical band gap. (c) UV-visible absorption spectroscopy of the MoO₃ thin film. Inset is the Tauc plot for calculating the optical band gap..... 109

Figure 49. (a-b) The surface morphology of ZnO with different magnifications. (c-d) The composition mapping of ZnO thin film. (e-f) The surface morphology of MoO₃ with different magnifications. (g-h) The composition mapping of MoO₃ thin film..... 110

Figure 50. (a-b) High-resolution XPS spectra of ZnO. (c-d) High-resolution XPS spectra of MoO₃. (e) The XRD pattern for the multilayer device. (f) The work functions of switching layer MoO₃ and ZnO measured using UPS..... 111

Figure 51. Photonic stimulations on the optoelectronic synapse. (a) The I-V curves of resistive switching under illumination with different wavelengths. 10 cycles for each test. The light density was 8 μW/cm². This power density was used in other tests if no specific instruction was given. (b) HRS and LRS under illumination with different wavelengths. Read voltage was -0.8 V. (c) Short-term synaptic PPF behavior under photonic stimulations. The light wavelength was 390 nm (ultraviolet, UV), pulse duration was 500 ms. $PPF = \alpha e - \Delta T \tau_1 + \beta e - \Delta T \tau_2 + y_0$. The fitting parameters $\alpha = 5.349$, $\beta = 18.916$, $\tau_1 = 1.803$, $\tau_2 = 0.279$, $y_0 = 100.514$. (d) EPSC responses under UV light with different power densities. The pulse frequency was 1 Hz. The duty cycle was 50%. (e) EPSC responses under the UV light with different pulse numbers. The pulse frequency was 1 Hz. The duty cycle was 50%. (f) EPSC values under photonic stimulations with different wavelength and pulse numbers. (g) Recognition results in a dark condition and illumination at 390 nm 460 nm 570 nm 620 nm for 10 pulses (pulse frequency was 1 Hz, duty cycle 50%, sample power density). (h) The decode results of the photoelectronic synapse to the American Standard Code for Information Interchange (ASCII). 113

Figure 52. (a) EPSC response of 2-pulsed photonic stimulations with different wavelengths. The pulse frequency was 1 Hz. The duty cycle was 50%. (b) EPSC response of 5-pulsed photonic stimulations with different wavelengths. The pulse frequency was 1 Hz. The duty cycle was 50%. (c) EPSC response of 10-pulsed photonic stimulations with different wavelengths. The pulse frequency was 1 Hz. The duty cycle was 50%. (d) Define the photonic pulses with different wavelengths to decode two-digit information of 00 (Red light, 620 nm), 01 (Green light, 570 nm), 10 (Blue light, 460 nm), and 11 (UV light 390 nm). One pulse with the duration of 0.5 s was used for the operation.... 114

Figure 53. (a) Schematic diagram of a flowchart for convolutional image processing. (b) Illumination of the dot product calculation in convolutional image processing. 117

Figure 54. (a) The distribution of $G_{\text{Light}}/G_{\text{Dark}}$ ratio over the applied voltage of 0.5 V to 1.1 V. The interval of measured voltages was 0.03 V. 21 points were measured over the window of voltage. (b) The probability plot of the $G_{\text{UV}}/G_{\text{Dark}}$ ratio. (c) The probability plot of the $G_{\text{Blue}}/G_{\text{Dark}}$ ratio. (d) The probability plot of the $G_{\text{Green}}/G_{\text{Dark}}$ ratio..... 119

Figure 55. Kernel design of image processing under the photonic operation. 120

Figure 56. Illustration of convolution image processing with crossbar hardware..... 121

Figure 57. Convolutional image processing. (a) Flow chart for convolutional computing based on CNNs. (b) The original image is grayscale. (c) Designed kernels for convolutional image processing using optoelectronic synapses. (d) Image processed by the kernel of “Soft”. (e) Image processed by the kernel of “Vertical”, detecting vertical edges. (f) Image processed by the kernel of “Horizontal”, detecting horizontal edges. (g) Image processed by the kernel of “Sharpen”, detecting edges. 123

Figure 58. Comparison between software-based and hardware-based convolution image processing. 124

Figure 59. (a) The comparison of the experimental pixel values and the arithmetic pixel values for the soft edge operation. (b) The comparison of the experimental pixel values and the arithmetic pixel values for the vertical edge operation. (c) The comparison of the experimental pixel values and the arithmetic pixel values for the horizontal edge operation. (d) The comparison of the experimental pixel values and the arithmetic pixel values for the sharpen edge operation. 125

Figure 60. Electronic stimulations. (a) The I-V curves of electrical resistive switching for 100 cycles. (b) The distribution of HRS and LRS over 100 operation cycles. (c) Potential performances depending on the input electronic pulse amplitudes. (d) Potential/depression performances under positive/negative electronic pulses. The pulse duration was 100 ms, and the duty cycle was 50 %. G_0 represents the initial conductance of the device. ΔG represents the change of the conductance after the electronic pulses were applied to the device. (e) The statistical mapping of device-to-device variations in a 6 x 6 array. The colour bar represents the current value (unit: A) under different resistance states (f) Schematic diagram for handwritten recognition with neural networks. (g) The results of image recognition using neuromorphic computing based on the optoelectronic synapse. 126

Figure 61. (a) The statistical analysis of ANL factor over cycle-to-cycle operations. (b) The statistical analysis of device-to-device variation. μ is expected value, σ is standard deviation, r is the ratio of HRS/LRS..... 128

Figure 62. Resistive switching mechanism. (a) The ZnO with (right) and without (left) oxygen vacancies. (b) Band structures of the ZnO. (c) Electrostatic potential curves along the z-axis, the vacuum level was normalized to 0 eV. (d) The fitting of $\ln(I)$ vs. $E^{1/2}$ for the device at HRS. (e) The fitting of $\ln(I/T^2)$ vs. $1000/T$ for the device at HRS. (f) Schematic diagram of energy band of HRS. (g) The fitting of $\ln(I)$ vs. $E^{1/2}$ for the device at LRS. (h) The fitting of $\ln(I/T^2)$ vs. $1000/T$ for the device at LRS. (i) Schematic diagram of energy band of LRS. 128

Figure 63. (a) The DOS curves of ZnO without (a) and with (b) oxygen vacancies..... 129

Figure 64. Monolithic neuromorphic machine vision system. (a) Schematic diagram of the retinomorphic sensing and processing in a human vision system. (b) Schematic diagram of the integrated optoelectronic synapse hardware for optical sensing, convolution processing, and neuromorphic computing..... 131

List of Tables

Table 1. Summary chalcogenide-based memristive devices.	22
Table 2. Summary metal-oxide-based memristive devices.	25
Table 3. The summary of the memristors with multiple functions. Vol-R means the ratio of volatile HRS/LRS. Vol-C means volatile switch cycles. N-Vol-R means the ratio of non-volatile HRS/LRS. N-Vol-C means non-volatile switch cycles. N-Ret means non-volatile retention time.....	54
Table 4. Component parameters used in the LIF neuron simulation.....	58
Table 5. The statistics summary of the HRS/LRS Ratio of the Ag/CISe/Mo device.	69
Table 6. Summary of the memristive devices-based intelligent matter for in-sensor neuromorphic computing.	81

Nomenclature

AI	Artificial intelligence
3D	Three-dimensional
ADC	Analogue-to-digital converter
AFM	Atomic force microscope
ANN	Artificial neural networks
ASCII	American Standard Code for Information Interchange
CAFM	Conductive atomic force microscopy
CC	Compliance current
CMOS	Complementary metal-oxide semiconductor
CPE	Constant-phase elements
CV	cyclic voltammetry
DC	Direct current
DFT	Density functional theory
DNN	Deep neural network
ECM	Electrochemical Metallization Memory
EDS	Energy dispersive X-ray spectroscopy
EELS	Electron energy loss spectroscopy
EIS	Electrochemical impedance spectroscopy
EPSC	Excitatory postsynaptic current
FE	Finite Element
FFT	Fast Fourier transform
FP	First principle
GIXRD	Grazing Incidence X-ray Diffraction
HH	Hodgkin-Huxley
HRS	High resistive states
IF	Integrate-and-fire
IPSC	Inhibitory postsynaptic current
ITO	Transparent conductive film
KMC	Kinetic monte carlo

LGP	Local graded potential
LIF	Leaky integrate-and-fire
LRS	Low resistive state
MCF	Metallic conductive filament
MD	Molecular dynamics
MS	Memory switching
PCB	Printed circuit board
PPF	paired-pulse facilitation
PVS	Pulsed voltage stresses
RF	Radiofrequency
SCLC	Space-charge-limited-conduction
SNN	Spiking neural network
SPICE	Simulation program with integrated circuit emphasis
SPM	Scanning probe microscopy
SRDP	Spike-rating-dependent plasticity
STM	Scanning tunneling microscopy
STXM	Transmission X-ray microscopy
TEM	Transmission electron microscopy
TS	Threshold switching
VCM	Valence change memory
VMM	Vector-matrix multiplication
XAS	X-ray absorption spectroscopy
XPS	X-ray photoelectron spectroscopy
XRD	X-ray diffraction

Chapter 1. Introduction

1.1 Background

Energy-intensive artificial intelligence (AI) which is increasingly important in our daily life imposes increased pressure on current computing and energy systems. The power consumption trend is shown in **Figure 1**.¹ The computing power consumption doubled around 24 months (about 2 years) by 2012. However, the power consumption demands doubled every 2 months in recent years. This may put excessive pressure on the power supply system soon. The root of the expensive energy budget for computers derives from the von Neumann architecture. It is used for current mainstream computers with separate memory and computing units. The frequent data shuttling between two units limits the computing speed (the ‘von Neumann bottleneck’) and increases energy consumption.² To solve this issue, brain-inspired neuromorphic computing that co-locates memory and computation has been developed. This methodology realizes massive parallelism, avoiding energy consumption for data shuttling. Particularly, the artificial neural network executing neuromorphic computing can be equipped with sensory functions. Integrating sense, memory, and computing in one single chip further shortens or eliminates the transmission between sensory nodes and memory-computing units. This can significantly improve processing efficiency, which is promising for AI systems that interact with surrounding environments.³

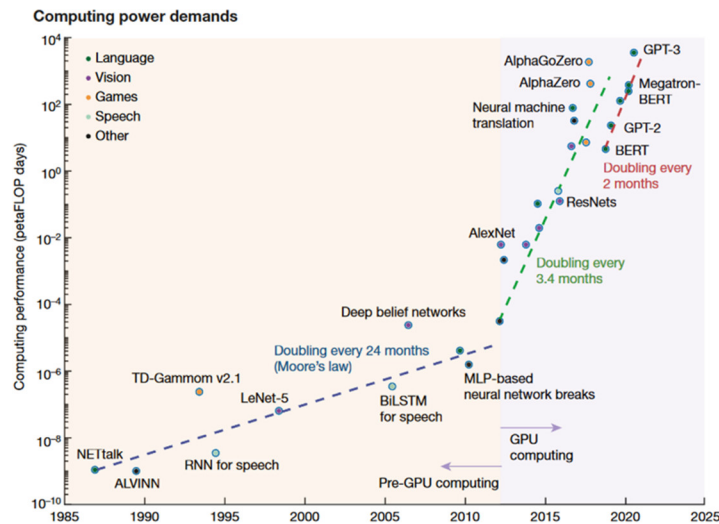


Figure 1. The computing power demand trend over 40 years. The consumption is described in petaFLOPS days. Reprinted with permission.¹ Copyright 2022, Springer Nature.

To construct advanced neuromorphic computing systems, memristive devices (or memristors) are one of the promising candidates as building blocks. Their resistance (or conductance) is programmable (resistor function), and subsequently remained for some time (memory function).⁴ The device shows commendable advantages compared to other technology, including low energy consumption (fJ)⁵, fast switching speed (ns),⁶ small size (2 nm),⁷ excellent area compaction ($4F^2$), and three-dimensional (3D) integration, etc. The device endows complex dynamic electrical responses. It can be utilized as digital memory elements, programmable weights in artificial synapses, biological neurons, and intelligent sensors.^{1,8} In memristive devices, filamentary switching and non-filamentary interfacial switching are two main types of configurations.⁹ For filamentary resistance switching, the switching mechanism is owing to the generation of single or multiple conductive filaments inside switching layers bridging the top electrode and the bottom electrode. The mobile ions are usually from the active metal of Ag, Cu, Ni, or an alloy.¹⁰ The dynamics of those ions are controllable to modulate volatile and nonvolatile properties, which can be employed to develop multifunctional devices.¹¹ Particularly, filamentary memristive devices can reversibly switch between two states with differentiable semiconductive and metallic features, which endows different sensory responses. The tailorable lifetime and sensory function of conductive filaments are attractive for advanced neuromorphic computing. For interfacial switching, the Schottky barrier height and the bulk conductance of materials can be modulated by controlling the defect distribution.¹² Metal-oxide materials are widely used due to their stable properties, straightforward process, excellent memristive properties, and compatibility with mature CMOS processes (CMOS, Complementary metal-oxide-semiconductor).¹³ Besides, metal-oxide semiconductors are usually sensitive to light. This kind of device is promising for machine vision systems that are particularly important in the AI world.¹⁴

Although progress has been made in developing neuromorphic computing systems. Some gaps regarding novel memristive devices still exist, including versatile memristive devices with multiple functions to simply neuromorphic circuits, intelligent matter with reconfigurable temperature and humidity sensations for advanced neuromorphic systems, and optoelectronic synapse for monolithic neuromorphic machine vision.

1.2 Objectives

The objective of this project is to develop advanced neuromorphic computing systems for energy-efficient AI. Filamentary memristive devices based on chalcogenide materials were developed. The controllable lifetime of conductive filaments induced both volatile and non-volatile memory for a versatile memristive device. The resistive switching performances were improved by adding Ga into the switching layer of CuInSe₂. The device reversibly switched between two states with differentiable semiconductive and metallic features, which showed different responses to temperature and humidity variations. Finally, an optoelectronic device promising for neuromorphic machine vision has been developed. The memristive devices can be utilized for sensory neuromorphic computing that is sensitive to temperature, humidity, and light. The main objectives are listed:

- (1) The development of a versatile memristor, the device of Ag/CuInSe₂/Mo was fabricated.¹⁵ The lifetime of conductive filaments was tunable by controlling electric forces, which resulted in the coexistence of volatile and non-volatile memristive effects. A versatile memristor covering the multiple roles of non-volatile memory, selectors, artificial neurons, and artificial synapses was developed.
- (2) The development of intelligent matter (Ag/Cu(In, Ga)Se₂/Mo), it showed reconfigurable temperature and humidity sensations for sensory neuromorphic computing.¹⁶ Different sensational features regarding the temperature and humidity were observed in the device under different resistance states.
- (3) Exploring the novel optoelectronic device for artificial vision systems, the device (ITO/ZnO/MoO₃/Mo) enabling multi-spectrum sensitivity can be employed for front-end retinomorphic image sensing, convolutional processing, and back-end neuromorphic computing.

1.3 Organization of the Thesis

This thesis focused on advanced neuromorphic computing based on memristive devices. Chalcogenide and metal-oxide materials were employed as switching layers to construct devices enabling memory, sensing, and computing functions.

Chapter 1 is an introduction covering the research background, objectives, and thesis organization.

Chapter 2 is the literature review. A review of memristive technology is presented, including the brief history, critical characteristics, memristive materials, and memristive mechanisms. Then, the investigating methods of resistive switching are reviewed. Imaging technology, spectroscopy technology, theoretical simulation, and compact mathematical models are discussed to investigate resistive switching mechanisms and accelerate the development of memristive systems. Finally, memristive devices for information processing, particularly based on neuromorphic computing, are summarized. The efficient artificial neural networks (ANN) implementing vector-matrix multiplication (VMM) and in-sensor computing based on memristive devices are elaborated.

Chapter 3 developed a versatile memristor (Ag/CuInSe₂/Mo). This device exhibited both volatile and non-volatile properties. It provided multiple functions covering non-volatile memory and neuromorphic computing. Particularly, the device emulated both short- and long-term synaptic plasticity, as well as neuron-like threshold switching. The leaky integrate-and-fire (LIF) neuron model and artificial synapse based on the device were studied. Such a versatile memristor enabled the functions of nonvolatile memory, selectors, artificial neurons, and artificial synapses, providing advantages regarding circuit simplification, fabrication processes, and manufacturing costs.

Chapter 4 focused on an intelligent matter (Ag/Cu(In, Ga)Se₂/Mo) that endows reconfigurable temperature and humidity sensations for sensory neuromorphic systems. The device reversibly switched between two states with differentiable semiconductive and metallic features, demonstrating different responses to temperature and humidity variations. The novel concept is that controlling materials states (with/without Ag filaments) enables reconfigurable sensory functions. More novel reconfigurable sensory intelligent matters can be potentially developed based on redox reaction materials, phase change materials, spin-transfer torque materials, and ferroelectric materials. This is promising for energy-efficient AI systems requiring temperature and humidity sensitivities.

Chapter 5 presents an optoelectronic synapse (ITO/ZnO/MoO₃/Mo) enabling multi-spectrum sensitivity. Synaptic plasticity triggered by photons can be simulated by the optoelectronic synapse, which is promising for photonic computing and information transmission. An ultra-low energy kernel generator fully controlled by photons for convolutional processing is developed. Meanwhile, the device shows memristive effects under electronic stimulations that implement brain-inspired neuromorphic computing with backpropagation algorithms. For the first time, this optoelectronic synapse is practical

for front-end retinomorphic image sensing, convolutional processing, and back-end neuromorphic computing. This work will benefit the development of advanced machine vision.

Chapter 6 gives the summary and discussion of the completed research and future works based on current progresses.

Chapter 7 lists the author's research contributions and awards.

Chapter 2. Literature Review

This chapter focuses on a literature review regarding memristive technology, including memristive effects, investigation methods, and neuromorphic computing.

2.1 Memristive Effects

2.1.1 The History of Memristive Effects

Memristive devices (often named memristors) combine the functions of resistor and memory. Resistance (or conductance) can be programmed into two or more distinguishable nonvolatile levels by applying electronic stresses.¹⁷ The fingerprint of a memristor was documented by Leon Chua and Sung Mo Kang: “A pinched-hysteresis loop under a bipolar periodic electronic signal”.¹⁸ This signature has been discovered in various electronic devices based on different materials and structures over more than a century. The first manufactured memristive device can track back to 1801.¹⁹ In the 1960s, pronounced memristive behaviors were observed with the help of advanced thin-film technology. A remarkably high electric field was achieved in metal/oxide/metal devices.^{20,21} In 1971, the memristor, considered the fourth electronic element, was theoretically reasoned from symmetry arguments.²² Apart from three known fundamental circuit elements: resistor, capacitor, and inductor, a fourth circuit element (named as memristor later) existed as shown in **Figure 2**. However, the lack of a physical model and practical device limited the application of this device although it showed valuable and interesting circuit properties. In 2008, the memristive effect was then experimentally confirmed along with a physical model by HP Laboratory.⁴ Frequently observed hysteretic I–V features in thin-film devices are now identified as memristive effects. Ever since memristive effects attracted extensive attention from both academia and industrial communities. The device has been proposed for high-performance nonvolatile memory, learning neural networks, encryption, and radio-frequency communication.¹⁷

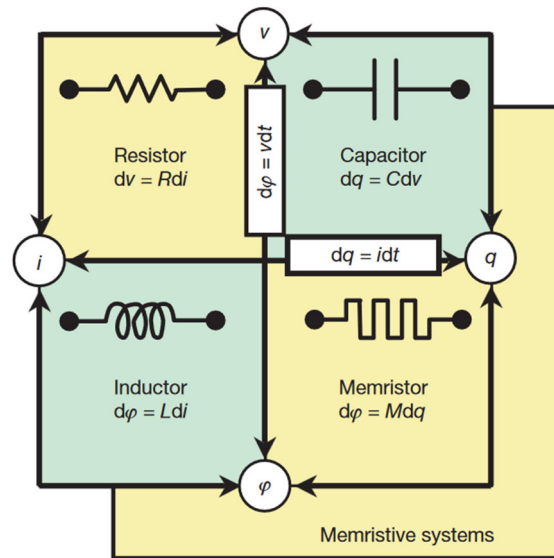


Figure 2. Four fundamental two-terminal passive circuit elements. Reprinted with permission.⁴ Copyright 2008, Springer Nature.

2.1.2 Memristive Characteristics and Parameters

Memristive devices are usually in a capacitor-like configuration consisting of a top electrode (metal or other conductive compound materials), a switching layer (semiconductor or insulator), and a bottom electrode as exhibited in **Figure 3a**.²³ The simple structure is highly scalable in the crossbar and 3D stacking integrations (**Figure 3b**). The distinguishable states can be utilized for information storage and logic operations.²⁴ Memristive devices typically have two stable resistive states, referred to as high resistive state (HRS) and low resistive state (LRS). Interestingly, some devices provide multiple resistive states that are represented by state 1, state 2, state 3, etc.²⁵ The memristive devices with multi-level resistance states show higher information storage density since one cell stores multiple bits. Whereas it is more difficult to distinguish each resistive state due to intrinsic variability, especially for large-scale integrated devices. Particularly, some memristive devices may show analog resistive switching (a special scenario of multiple states), in which the resistance (or conductance) changes gradually and linearly (or near-linearly). A series of conductance can store programable weights in ANNs for neuromorphic computing.²⁶

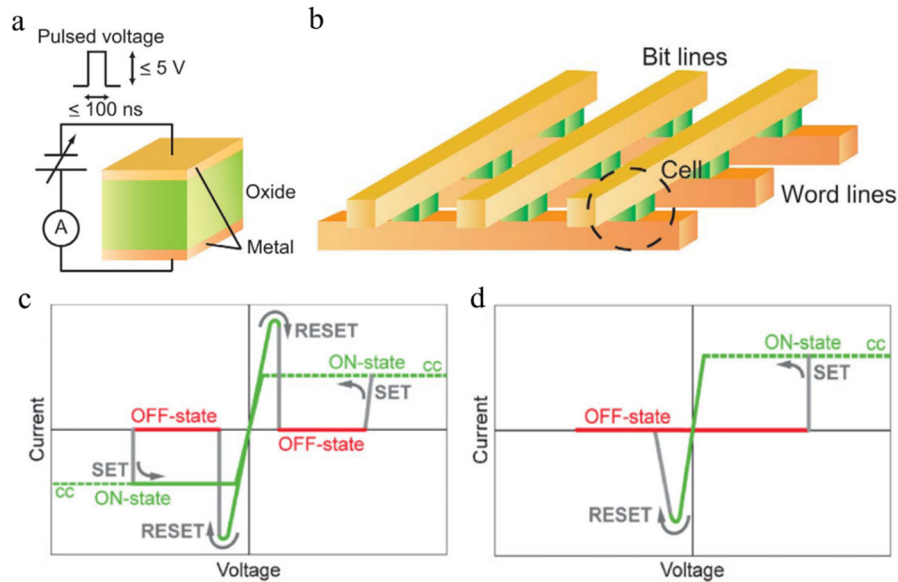


Figure 3. (a) Diagram of a typical memristive device. (b) Integrated memristive devices in a crossbar. Reprinted with permission.²³ Copyright 2008 Elsevier Ltd. (c) I-V curve of a unipolar switching. (d) I-V curve of a bipolar switching. Reprinted with permission.²⁷ Copyright 2009, WILEY-VCH Verlag GmbH & Co. KGaA, Weinheim.

It is crucial to quantitatively characterize the memristive properties. One commonly used figure is the I-V curve of current versus voltage (I-V) that presents the SET/RESET voltages (operation voltages), current values (estimating energy consumption), and HRS/LRS ratio (resistive distinguishability). To get I-V curves, a sweep voltage ($0 \rightarrow +V \rightarrow -V \rightarrow 0$) is applied to the device and current values are recorded. This test is called the direct current (DC) switching cycle test. Compliance currents (CCs) are usually imposed to constrain the current flowing through devices. This avoids unrecoverable breakdown due to striking currents.²⁸ Applied electronic stresses induce the transition from HRS to LRS, referred to as a SET process. Similarly, the voltage changes the device resistance from LRS to HRS, it is called a RESET process. Memristive effects are categorized into unipolar and bipolar resistive switching according to electrical polarity. The unipolar switching is depicted in **Figure 3c**, the SET and RESET operations are both triggered under the same electrical polarity. For the SET operation, switching devices to LRS is done by a higher voltage. The operation current is limited by CCs. The RESET operation is achieved by a small voltage without compliance currents. In comparison, the bipolar resistive switching is exhibited in **Figure 3d**. A positive voltage is employed to realize a

SET operation. A negative voltage changes the device back to the HRS, namely a RESET operation. An asymmetric structure in the capacitor-like device is usually needed to realize the bipolar mode. Notably, the two featured curves (**Figure 3c and Figure 3d**) are schematic illustrations for I-V behaviors with a specific switching direction. Experimental curves may deviate from the illustration depending on the device structure and test parameters. Notably, this I-V curve alone is not sufficient to evaluate the quality of memristive performances. Several other figures of merit, including endurance, retention time, switching speed, and variability, should be investigated as well.

Endurance: The device endurance describes the maximum operation cycles ensuring a sufficient ratio of HRS/LRS. It shows the robustness of devices. Generally, the failure is accumulated over multiple operations instead of occurring in one single cycle.²⁹ Different measurements are used to get endurance characteristics: i) DC switching multi-cycle test. ii) Current-blind pulsed voltage stresses (PVS). iii) Current-visible PVS. iv) Multi potentiation/depression cyclic test. Method i is a preliminary test to identify resistive switching. Consecutive DC switching cycles are collected as shown in **Figure 4a**.³⁰ This measurement is reliable in which one can inspect resistive switching in every cycle. Besides, the statistics of SET voltage and RESET voltages can be obtained. The distribution plots of HRS and LRS are extracted from tested curves. Using a small voltage and corresponding currents calculates resistance values, as shown in **Figure 4b**. The value of HRS/LRS (sometimes called the ON/OFF ratio) reflecting the resistance states' distinguishability can also be obtained. However, this method is very time-consuming as each cycle takes 30-60 s or even longer for low currents. Also, this method does not perform the electronic stresses in practical scenarios that use pulsed voltages for resistive switching operations. A better method is using PVS. Method ii and iii mimic the real operation scenario in integrated systems. In the inset of **Figure 4c**, a short SET pulse switches the device to the LRS, following a small pulse voltage to measure the resistance.³¹ Similarly, a short RESET pulse switches the device to the HRS, following the same small pulse voltage to measure the changed resistance. Notably, the current is not measured after every SET and RESET operation in method ii. The currents are measured after a specific number of SET and RESET PVS operations. This can shorten the overall experimental time as measuring current (especially low current) is usually time-consuming. The drawback of method ii is that it cannot monitor every switching operation effectively. Because the collected data points are spaced. Method iii also uses PVS to operate devices. The difference is that the currents are measured in every cycle of SET and RESET operations as shown in **Figure 4d**. This

method monitors every resistive switching operation mimicking practical scenarios. But this method is challenging to measure low current ($<10 \mu\text{A}$) for most equipment. The endurance test of potentiation/depression is discussed, which is vital for brain-inspired neuromorphic computing implementing VMM. Short consecutive pulses (for example 50 positive pulses) are used to mimic the synaptic potentiation operation. Each pulse follows a small pulse voltage to monitor the change of currents that can be used to calculate the conductance as shown in **Figure 4e**. Likewise, Short consecutive opposite voltage pulses (for example 50 negative pulses) are used to mimic the synaptic depression operation. Each pulse follows a small pulse voltage. One potentiation/depression operation is regarded as one cycle. Multiple cycles of the test are required to monitor the device's endurance. Notably, each method has different purposes with advantages and disadvantages. The best option is to mix them up and characterize the device from different perspectives.

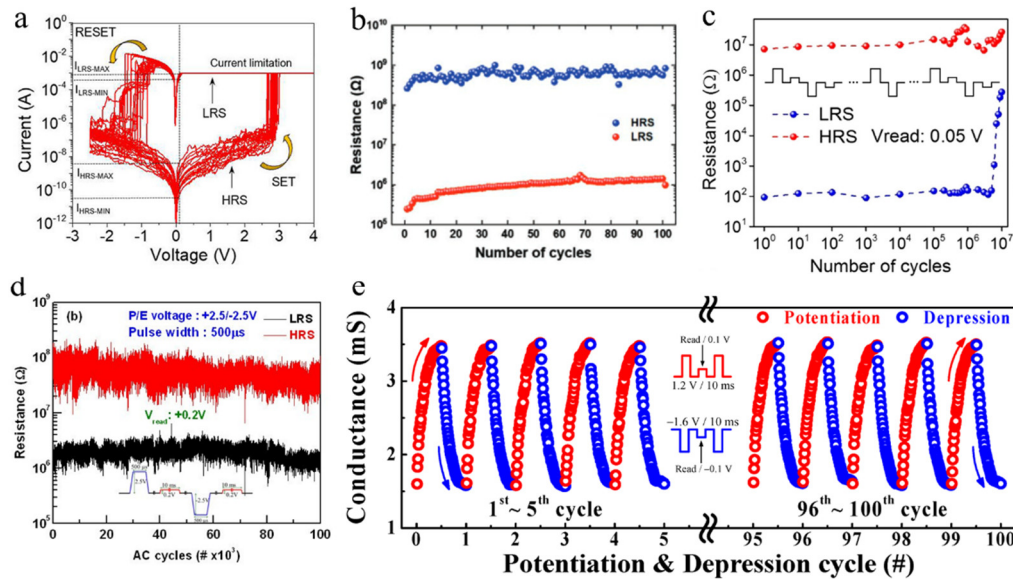


Figure 4. (a) DC switching cycle test for 100 consecutive cycles. Reprinted with permission.³⁰ Copyright 2021, The Authors. (b) Distribution of LRS and HRS over 100 cycles, the data is extracted from the DC switching cycle test. Reprinted with permission.³² Copyright 2022, The Authors. (c) Endurance test on the device with distinctive resistance levels by current-blind PVS. Reprinted with permission.³¹ Copyright 2022, American Chemical Society. (d) Endurance test on the device with distinctive resistance levels by current-visible PVS. Reprinted with permission.³³ Copyright 2013, The Authors. (e) Endurance test of potentiation/depression behaviors. Reprinted with permission.³⁴ Copyright 2022, The Authors.

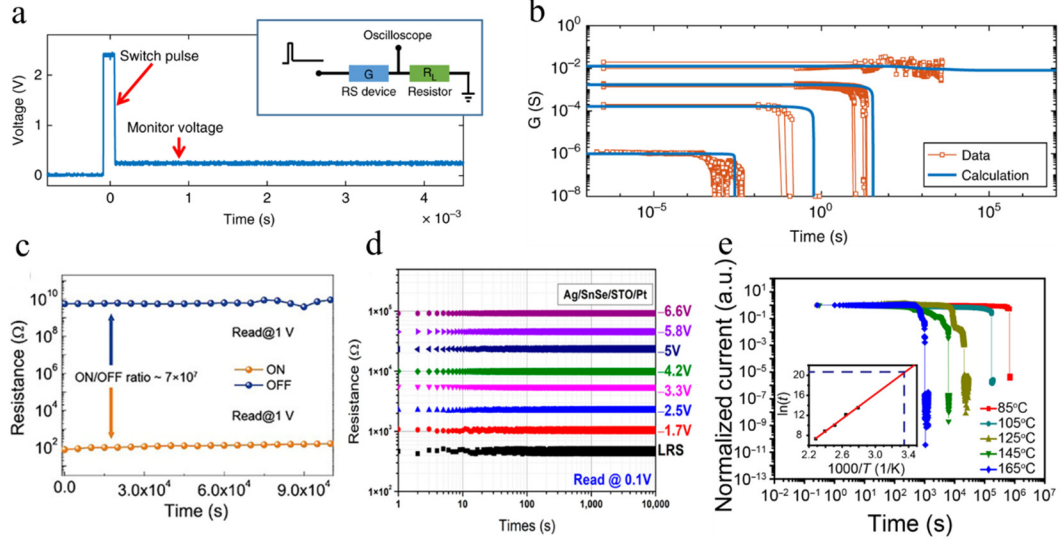


Figure 5. (a) Illustration of the measurement setup for the state retention time. The inset is a typical experimental circuit. (b) State retention time under different program electronic stresses. Reprinted with permission.³⁵ Copyright 2019, The Author(s). (c) Typical state retention time of HRS and LRS. Reprinted with permission.³⁶ Copyright 2019, The Authors. (d) Multi-level state retention time. Reprinted with permission.³⁷ Copyright 2022, The Authors. (e) Retention time under different temperatures. Reprinted with permission.³⁸ Copyright 2021, The Authors.

State retention time: Investigating state retention time is to check if the HRS and LRS are stably reserved over time after SET and RESET operations. To measure the state retention time, a small constant reading voltage (≈ 0.2 V or smaller) is applied to the device after a SET or RESET operation. The current is measured constantly to monitor the resistance (or conductance) changes over time. The reading voltage is usually orderly smaller than program voltages to avoid the resistance drifting during the test.³⁸ Thus, current-time (or resistance-time, or conductance-time) curves should be presented for the state retention time characterization.²⁹ A typical measurement setup is shown in **Figure 5a**. The memristive device (G) connects with a resistor in series. The resistor can have different values to modulate the electric forces applied on the memristive device, which modulates the changing margins of resistance and the retention time.¹¹ The auxiliary resistor can also share voltage stresses to prevent the device breakdown owing to high-current striking.³⁹ The current or the voltage on the device is measured to get conductance values. Typically, more attention is paid to the retention time of LRS. Because atomic rearrangement is generated during the SET process, which may vanish after a period.

In comparison, the HRS is the initial state of the device that is normally stabled. **Figure 5b** shows the SET conductance changes over time, the conductance and the retention time were different due to different electronic stresses of SET operations.³⁵ In this specific case, the metallic conductive filaments (MCFs) were responsible for the resistive switching. Higher electronic stress induced stronger MCFs that exhibited higher conductance and longer retention time. This programmable retention characterization shows potential applications in multifunctional devices.⁴⁰

Although the retention time of HRS is not specifically concerned, the figure of merit for both states is often presented as shown in **Figure 5c**.³⁶ The HRS/LRS (or sometimes so-called ON/OFF) feature along with retention time are elaborated, indicating distinguishable states.^{41,42} Particularly, multi-level memristive devices show promising applications for high-density memory and computing systems.⁴³ The retention time of all resistive states should be measured to demonstrate the validity as shown in **Figure 5d**.³⁷ To induce multi-level states, different electronic stresses, including various program voltages,³⁷ program currents,⁴³ and program durations (the width of program pulse),⁴⁴ are utilized. A retention time longer than 10 years is usually required for nonvolatile memory.²⁷ However, it is not doable to execute the state retention test for that long time. One strategy is to assess the retention characterization in the aggressive condition of elevated temperature instead of normal service conditions (room temperature). Atoms in memristive devices are more active under high temperatures, indicating the accelerated rearrangement speed of atoms. LRS retention time at high temperatures is shorter than the room temperature counterpart.⁴⁵ The relationship between retention time and temperature is described by the following equation:

$$\ln(t) \propto \frac{E_a}{kT} \quad \text{Eq. 1}$$

where t is retention time. E_a is the activation energy. k represents the Boltzmann constant. T represents the measurement temperature. In this method, several data points of retention time are collected at different temperatures (typically > 80 °C). An extrapolating operation to $\ln(t)$ - $1/T$ plots will be implemented based on the data points carrying failure information.⁴⁶ In **Figure 5e**, the conductance variation over time is presented, and the extrapolating fitting is shown in the inset.³⁸ The evaluated retention time was about 9×10^8 s which is much longer than the actual test time. Notably, memristive devices with short retention time (volatile resistive switching) ranging from some microseconds to a few seconds also show incredibly good prospects.¹¹ The dynamics after removing the voltage stresses

can be employed for short-term plasticity learning,⁴⁷ high-performance selectors,⁴⁸ security applications,⁴⁹ etc. For those volatile devices, the retention time is usually tested directly, for example in **Figure 5a** and **Figure 5b**.³⁵ A fast measurement speed is required to catch the transition from the LRS to HRS in the volatile resistive switching.⁵⁰

Variability: The temporal (cycle-to-cycle) variation and spatial (device-to-device) variation are the two main variabilities in memristive arrays.⁵¹ The variation characterizations of V_{SET} , V_{RESET} , HRS, and LRS are crucial parameters that need to be identified. Wherein, V_{SET} and V_{RESET} distributions indicate the reliability of programming procedures. HRS and LRS variations are vital for the accuracy of memory and computing applications. The statistical analysis of device variabilities is essential to investigate memristive devices. The cycle-to-cycle variation is determined by intrinsic properties regarding materials used, defects distributed in materials, resistive mechanisms, device structure, etc. Also, the operation strategies influence device variability. For example, the CC can protect the device from damage or breakdown, which may also benefit the device's stability since the failure is due to accumulated damage over multiple operations. As for the device-to-device variation, it is decided by the fabrication processes. The smooth surface, homogenous defects distribution, controllable thickness over a specific area, and uniform element composition in devices are important aspects of integrated devices with small spatial variations. The typical DC switching cycles are one of the important and frequently used methods to present the variations (**Figure 6a**). The SET/RESET voltages and the HRS/LRS were obtained. **Figure 6a** shows a typical multiple-cycle operation in one device, indicating the cycle-to-cycle variation. It should be noticed that the DC switching cycles of multiple devices can also be presented in the same figure to indicate the device-to-device variation, which is similar to **Figure 6a**.⁵² To quantitatively evaluate statistics variations, The cumulative probability plot and histogram are commonly employed as presented in **Figure 6b** and **Figure 6c**, respectively. The data is fitted by the Gaussian function to calculate the mean value (μ) and the standard deviation (σ). The HRS and LRS can be extracted from DC switching cycle curves (**Figure 6a**) or PVS operations. **Figure 6b** gives a typical cumulative probability plot of HRS and LRS, both cycle-to-cycle variations and device-to-device variations.⁵³ The figure indicated the resistance distribution range over two distinguished states. The SET and RESET voltages were obtained from DC switching cycle curves. **Figure 6c** shows the histogram features of operating voltages. In this specific case,³⁰ 48 devices were tested multiple cycles to collect the operation voltage variations. Cumulative probability plots and histograms are two

universal figures that depict statistical data points. Resistance and operation voltages (cycle-to-cycle and device-to-device) are presented by either cumulative probability plots or histogram figures.

Synaptic potentiation and depression are very crucial for neuromorphic computing. The output computation accuracy is significantly influenced by the operational variations coming from both temporal and spatial aspects, which should be characterized properly. Cumulative probability plots are utilized, as shown in **Figure 6d**.⁵⁴ The device-to-device variation was low and the integrated array demonstrated a high computing accuracy of over 95%, which heavily relies on a high yield of efficient devices (99.99%) and small variations.⁵⁴ The cycle-to-cycle variation is also important. In **Figure 6e**,⁵⁵ 100 consecutive potentiation/depression cycles are presented. The error bar was utilized to demonstrate the variation of each state. Another efficient way to indicate device-to-device variations is presented in **Figure 6f**,⁵⁶ conductance map of the synaptic array after localized pulse programming to write the 'UMAS' is demonstrated. This method can locate dead or stuck devices. In most papers, the cycle-to-cycle variations, including SET voltage, RESET voltage, HRS, LRS, and potentiation and depression characteristics, are usually presented using the method mentioned above. The small device-to-device variation, especially for large-scale integrated devices, is still challenging. The large integration system usually requires high-vacuum deposition equipment, lithography, clean rooms, and professional test systems. Some work focuses more on conception demonstration using novel materials (polymers,⁵⁷ biomaterials,⁵⁸ etc.) that are not compatible with lithography. Besides, some device preparation methods, such as spin coating,⁵⁹ drop casting,⁴³ electrodeposition,⁶⁰ are hard to realize very homogeneous and uniform thin films, which is especially important to device-to-device variation. Scientists should vision and estimate the probability and strategies to forward novel memristive technology to practical applications.⁶¹

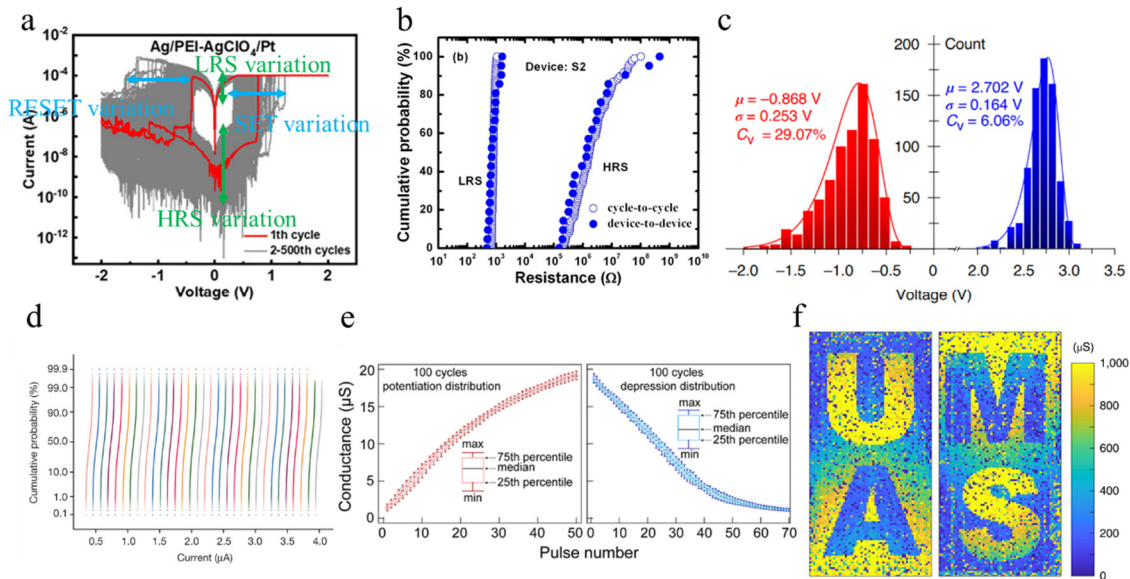


Figure 6. (a) Typical DC switching cycle test for multiple cycles, 500 cycles in this specific example. Reprinted with permission.⁶² Copyright 2022, American Chemical Society. (b) The cycle-to-cycle and device-to-device variations presented by cumulative probability plots of LRS and HRS. Reprinted with permission.⁵³ Copyright 2012, The Authors. (c) The histogram of device SET voltages and RESET voltages of 48 devices under multi-cycle operations. Reprinted with permission.³⁰ Copyright 2020, The Author(s). (d) Cumulative probability plots of 32 independent states. Reprinted with permission.⁵⁴ Copyright 2020, The Author(s). (e) The variation of the potentiation/depression plasticity. Reprinted with permission.⁵⁵ Copyright 2021, American Chemical Society. (f) Conductance map of the synaptic array after localized pulse programming to write the ‘UMAS’. Reprinted with permission.⁵⁶ Copyright 2019, The Author(s).

Switching speed: The switching speed reflects how fast a device can switch between different states. This parameter is important to computing and memory systems as it constrains the overall operating speed of whole systems. To measure the switching speed, typical V-t and I-t synchronous curves are recorded (**Figure 7a**).⁶³ The switching time is determined by extracting the current changing features, demonstrating switching speed. The simplest way is shown in **Figure 7b**.⁶⁴ The current and voltage are both recorded to get V-t and I-t synchronous curves. Usually, advanced semiconductor characterization systems equipped with pulse measure units are required, such as Keithley 4200A-SCS and Keysight B1500A semiconductor parameter analyzer. However, the SET transition is usually not self-limited. A memristive device is vulnerable under too-high currents. A series resistor can be utilized as a current

limiter as shown in **Figure 7c**.⁶⁵ Advanced semiconductor characterization systems are expensive. And extra costs are often required, including ultra-fast pulse measure units, a probe station, a microscope, and maintenance services. Another method is to use a pulse generator and an oscilloscope (**Figure 7d**).⁶⁶ A pulse source switches the device between different states. The series resistor (R_A) limits the current going through the device. The current is read out by measuring the voltage (completed by oscilloscope) on the series resistor of $50\ \Omega$ connecting with the bottom electrode. In this way, information on switching speed can be obtained.

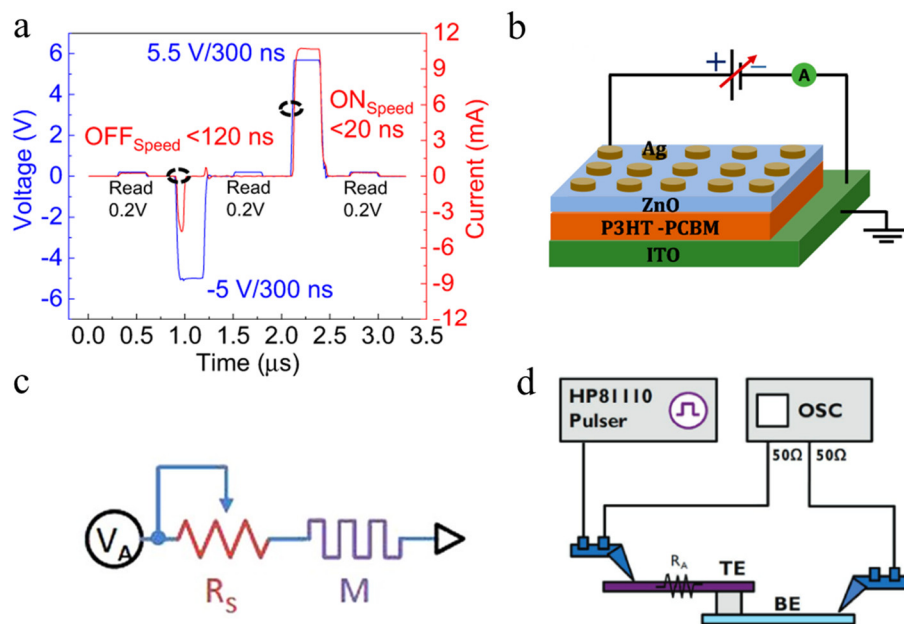


Figure 7. (a) Typical V-t and I-t synchronous curves corresponding to the switching process. Reprinted with permission.⁶³ Copyright 2021, The Author(s). (b) Typical setup for testing memristors. Reprinted with permission.⁶⁴ Copyright 2021, The Author(s). (c) Typical setup for testing memristors with a tandem resistor to limit the current. Reprinted with permission.⁶⁵ Copyright 2016, The Author(s). (d) Typical setup testing memristors with a pulse generator and an oscilloscope. Reprinted with permission.⁶⁶ Copyright 2012, IEEE.

2.1.3 Memristive Mechanisms

Distinguishable states of memristive devices are induced by external electronic stimuli. There are four fundamental mechanisms, including electrochemical redox reactions,²⁷ phase changes,⁶⁷ ferroelectric-polarization modulations,⁶⁸ and magnetic tunneling.⁶⁹ Here, electronic redox reactions are discussed

since it is the major mechanism in this work. This mechanism is owing to redox reactions and ion migrations. Mobility ions that change the resistance are anions and cations.

The anion-based resistive switching, mainly driven by oxygen ions (or equivalently oxygen vacancies), is a major part of the redox-based mechanism. It is often named as valence change memory (VCM).⁷⁰ This mechanism is found in transition-metal oxides²³ and perovskites⁷¹ consisting of oxygen ions or other mobility ions. Stable inert electrodes under electronic biases for both top and bottom electrodes are used. In particular, metal electrodes (e.g., Ta, Ti, Hf) possessing high oxygen affinity act as a reservoir layer of oxygen species.^{72,73} This benefits redox reactions/ion exchanges and the formation of oxygen vacancies that are generated under electronic activations as shown in **Figure 8a**. In general, oxygen vacancies can be induced into two forms of distribution. Firstly, the filamentary type of distribution (**Figure 8b**) is the non-uniformity of distributed oxygen vacancies (a new phase with high conductivity).⁷⁴ This kind of resistive switching shows fast switching speed and a large HRS/LRS ratio. The growth of single or multiple localized filaments is involved during the switching process. The active switching region concentrates at the filaments' tip, which means the values of LRS do not proportionally depend on the effective area of the devices.⁷⁵ Secondly, interface-type resistive switching, the oxygen vacancies are mainly distributed at the interface of the electrode/switching layer. Electronic stimuli modulate Schottky barriers as shown in **Figure 8c**. One of the electrodes uses materials with high working functions that form a prominent Schottky barrier at the interface. In comparison, another electrode has a low working function to form Ohmic contact at the other end of the interface. Accumulated oxygen vacancies change the working function of switching layers, which changes the Schottky barrier height at the interface. A high Schottky barrier shows high resistance. At LRS, the electrode/oxide interface has lower barriers and smaller resistance (high conductance). Reversing the applied voltage re-establishes the barrier and recovers the original HRS. The interface-type resistive switching is typically slow that is due to the lack of thermodynamics to accelerate ion migrations.⁹ Notably, the Schottky barrier height and bulk conductivity of switching layers both contribute to the overall resistance. Homogeneously distributed oxygen vacancies in the bulk of switching layers may also modulate the conductance of the devices.⁷⁶ In contrast to the area-independent LRS in filament-type switching, the LRS usually shows proportional relations to device areas as the active switching region is the whole interface of electrode/oxides.⁷⁷ Notably, the filaments and interface modulation may contribute to the resistive switching collectively in some cases.^{78,79}

Remarkable progress has been obtained in anion-based resistive switching regarding fundamental physics understanding and device performances. Theoretical simulation and visualizing technology have been successfully utilized for physical understanding.⁸⁰ Meanwhile, the device achieved an endurance of 10^{12} , a switching speed of <1 ns, and a small size of <10 nm.⁸¹

For cation-based resistive switching, active metal (Ag, Cu) is usually employed as a top electrode, and inert metal (Au, Pt) is used as a bottom electrode.⁸² Electrochemical oxidation induced cations (Ag^+ or Cu^{2+}) to the switching layer. The switching layer usually shows good diffusivity to cations, Such as a-Si,¹⁰ metal oxide materials (HfO_2 ,⁴⁷ Ta_2O_5 ,⁸³ etc.), chalcogenides (Ag_2Se ,⁸⁴ GeSe ,⁸⁵ etc.), and biomaterials (silk fibroin,³⁵ glucose,⁸⁶ etc.). In some cases, the switching layer is doped with Ag atoms to improve resistive switching performances.⁴⁷ The forming of conductive filaments is controlled by three processes. First, the electrochemical oxidation of the active electrode. Second, the cation migration via the active layer. Third, the reduction of cation ions.⁸¹ The conductive filaments are formed involving chemical reactions, cation drifting, and nucleation under electronic bias as shown in **Figure 8d**. Conductive filaments connect the top and bottom electrodes, demonstrating LRS (**Figure 8e**). Notably, the redox rate and ion mobilities in specific solid electrolytes determine the growth modes of filaments.^{87,88} Specifically, a low ion mobility and redox rate make filaments grow from the top active electrode to the inert bottom electrode. In comparison, the filament growth in an opposite direction (bottom electrodes to top electrodes) is expected with high ion mobility and redox rate. Before the normal operation, a forming procedure is often required in which a high voltage is applied to the device to induce initiated channels. Besides, the forming procedure changes the nano-morphology in the electrolyte. The preformed channels act as easy transport pathways for cations.⁸⁹ Interestingly, the dynamic of cations can be modulated by light,⁹⁰ temperature,⁹¹ humidity,⁹² etc. demonstrating promising prospects for in-sensor computing systems. Moreover, the resistive switching can be controlled by the dynamics of both anions and cations simultaneously as shown in **Figure 8f**.^{89,93} The anion-cation-hybrid resistive switching broadens the design of multifunctional memristive devices.

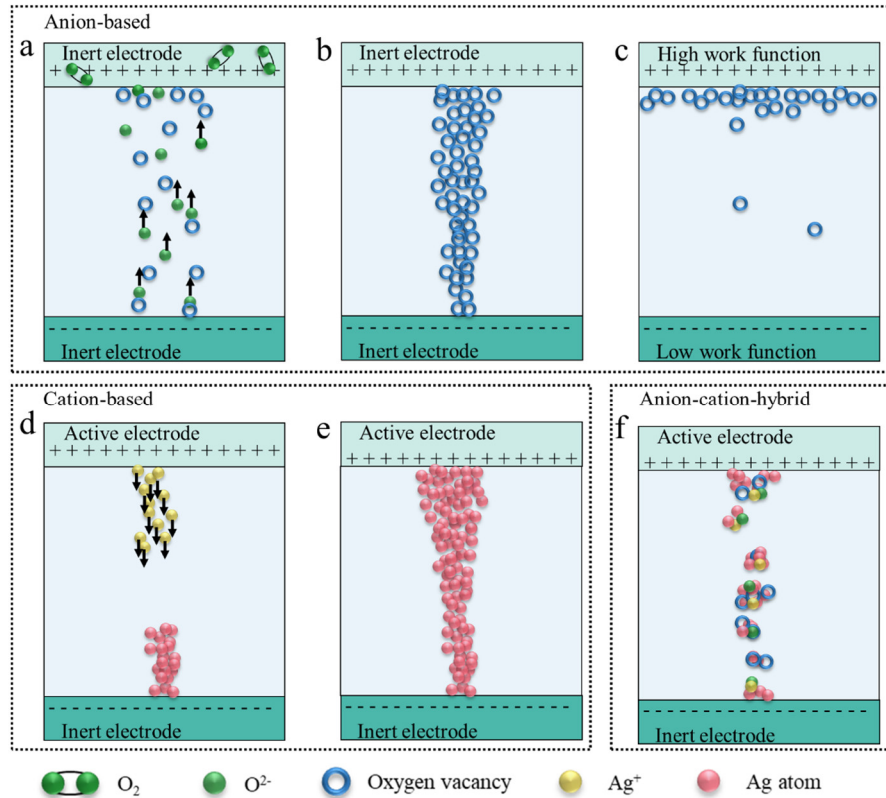


Figure 8. (a) Illustration of set operation in anion-based devices. (b) Illustration of filamentary-type resistive switching based on anions. (c) Illustration of interface-type resistive switching based on anions. (d) Illustration of set operation in cation-based devices. (e) Illustration of filamentary-type resistive switching based on cations. (f) Illustration of resistive switching based on hybrid anions and cations.

2.1.4 Memristive Chalcogenides and Metal Oxides

Typical memristive devices are in the form of electrode/switching layer/electrode two-terminal structures. The switching layer is crucial for memristive performance since it is the path for shuttling charge carriers during operation processes. Extensive investigations into memristive materials have been conducted. Chalcogenide materials,⁹⁴ metal-oxide materials,⁹⁵ carbon-based materials,⁹⁶ natural biomaterials,⁵⁸ and synthetic polymer materials⁹⁷ are the five main categories used as switching layers. Here, switching layers based on chalcogenide and metal-oxide materials are discussed in detail.

Chalcogenide Materials: Resistive switching behaviors have been observed in many chalcogenide materials. Chalcogenides are materials consisting of one or more chalcogen anions (e.g., S, Se, or Te) and at least one electropositive element.⁹⁸ Typical memristive devices based on chalcogenides are summarized in **Table 1**. Chalcogenides usually show high ion mobility that will benefit the formation/dissolution of conductive filaments. The real-time forming/rupture of a metal conductive filament was observed by a high-resolution transmission electron microscope (HRTEM) in the AgS₂ (**Figure 9a–c**).⁹⁹ The forming and rupture of conductive filaments can be controlled by electronic voltages. The high-conductivity Ag₂S argentite phase and Ag nanocrystal together generate conductive channels as shown in **Figure 9b**. **Figure 9e** shows another typical example of a chalcogenide-based device, the forming/rupture of metal conductive filaments was responsible for the resistive switching.^{27,100} The Ag conductive filament grows from the cathode (Pt) toward the anode, which is ascribed to the high ion diffusion coefficient in Ag–Ge–Se.¹⁰¹ The similar phenomenon has also been reported in Ag/As₂S₃:Ag/Au,¹⁰² Ag/GeSe:Ag/Ni,¹⁰³ and Pt:Ir/GeS:Cu/Pt:Ir.¹⁰⁴

Another important resistive switching mechanism in chalcogenide-based devices is the phase change phenomenon. Conductivity switching is associated with the phase transition relating to temperature. This is a typical phenomenon observed in chalcogenides, such as Ag₂Se,¹⁰⁵ Ge₂Sb₂Te₅,¹⁰⁶ Cu₂Se,¹⁰⁷ and Ag₂S.¹⁰⁸ Rehman et al. reported the temperature-related resistive switching behavior in the Al/Cu₂Se/Pt device.¹⁰⁷ The device showed no resistive switching behavior at room temperature. However, an obvious resistive switching behavior was obtained at 125 °C which was close to the Cu₂Se transition temperature (137 °C). The thermodynamic calculation revealed that the ordered or disordered Cu₂Se was crucial to the mobility of Cu ion, which further influenced the formation/rupture of conductive filaments. Furthermore, transition metal dichalcogenides (TMDs) can be two-dimensional (2D) materials.¹⁰⁹ They have intrinsic ultrathin geometry, inert chemical character, and tunable photoelectric properties.¹¹⁰ Sub-10 nm devices can be achieved, which is vital for high-integration density.¹¹¹ Memristive devices based on 2D materials can be either vertical or lateral configurations.¹¹² TMDs with polymorphism realize a reversible transition between semiconducting, semi-metallic, and metallic conductivities, which can be utilized for resistive switching.¹¹³ **Figure 9f** shows the schematic diagram of the MoTe₂-based vertical memristor device.¹¹⁴ This structure ensured that only vertical transport contributed to currents. The electric-field-induced phase transition was observed in **Figure 9g**. The 2H phase showed semiconducting behaviors corresponding to the HRS. Meanwhile, the T_d phase showed

metallic behaviors corresponding to the LRS. The switching time was only 10 ns with the HRS/LRS ratio of 10^6 . Moreover, the phase transition can also be induced by lithium intercalation as shown in **Figure 9h**.¹¹⁵ The localized 2H (semiconductor phase) - 1T' (metallic phase) transition was realized by controlling Li^+ migrating laterally under electric fields. The device showed excellent resistive switching behaviors. It demonstrated the electrical modulation of 2D materials with field-driven ionic processes.

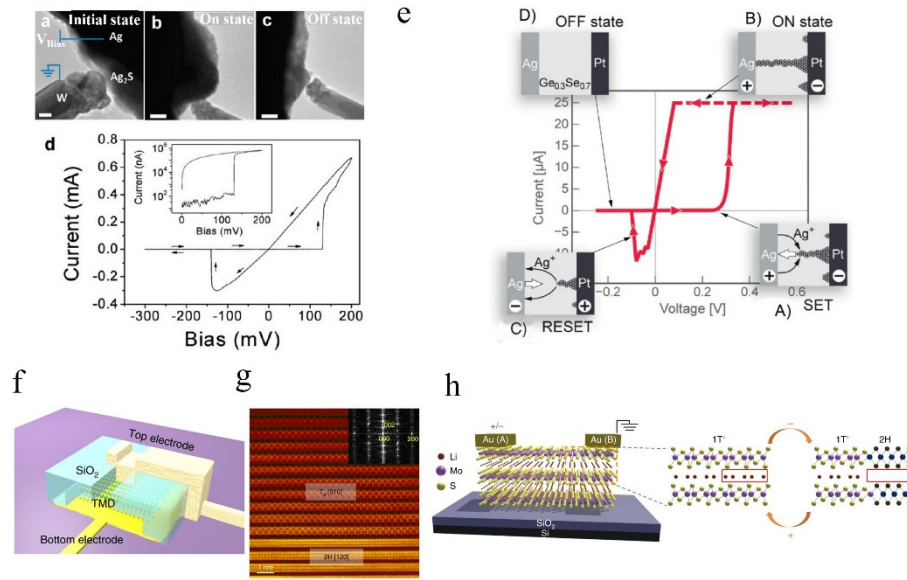


Figure 9. (a-c) TEM image of Ag_2S -based memristor at the initial state, LRS, and HRS. (d) I-V characteristic of the device. Reprinted with permission.⁹⁹ Copyright 2010 American Chemical Society. (e) The typical I-V characteristic and the corresponding electrochemical metallization process. Reprinted with permission.²⁷ Copyright 2009 WILEY-VCH Verlag GmbH & Co. KGaA, Weinheim. (f) Schematic diagram of the vertical MoTe_2 -based device. (g) Atomic resolution scanning transmission electron microscopy image of the MoTe_2 . Reprinted with permission.¹¹⁴ Copyright 2018 Springer Nature. (h) Schematic diagram of local 2H-T' phase transitions in Li_xMoS_2 induced by Li^+ migration. Reprinted with permission.¹¹⁵ Copyright 2018 Springer Nature.

Table 1. Summary chalcogenide-based memristive devices.

Device	HRS/LRS ratio	Endurance	Retention	Switch speed (s)	Ref.
Au/ZnSe/ITO	10	2×10^2	10^4 s	***	116
Ag/ZnSe-ZnS/ITO	50	1.4×10^2	10^4 s	***	117
Ag/ZnS-Ag/ZnS/ITO	$>10^2$	3×10^3	***	***	118
Cu/ZnS/graphene/Cu	10^3	10^2	3×10^3	***	119
Ag/MoSe ₂ /FTO	12	50	***	***	120
Ag/MoSe ₂ /PMMA/Cu	4×10^2	10^3	10^4 s	***	121
Ag/MoS ₂ /Au	10	10^2	10^4 s	***	122
Ni/Al ₂ O ₃ /MoTe ₂ /Ti	10^6	***	100 s	10^{-8} - 10^{-7}	114
Au/Ti/ MoTe ₂ /Au/Ti	10	10^5	10^5 s (85°C)	5×10^{-9} - 10^{-8}	123
Ag/Ag ₃₃ Ge ₂₀ Se ₄₇ /Ni	10^3	10^{11}	***	10^{-7}	124
Ag/Ag ₁₀ (As ₄₀ S ₃₀ Se ₃₀) ₉₀ /Ag	10^2	20	***	***	125
Ag/ γ -InSe/Au	10^3	50	10^5 s	***	126
Pt/Cu _x Te _{1-x} /Al ₂ O ₃ /Si	<10	10^3	10^4 s (85°C)	***	127
Pt/Cu _x Se _{1-x} /Al ₂ O ₃ /Pt	10^7	10^4	10^4 s (85°C)	***	128
Ag/Cu ₂ ZnSnSe ₄ /Mo	215	2×10^2	10^4 s	***	129
Al/Cu ₂ ZnSn(S,Se) ₄ /Mo	27.5	2×10^2	***	***	130
Ag/Sb ₂ Te ₃ /Pt	5	10^3	10^3 s	***	131
Te/Sb ₂ Te ₃ /Te	10^3	5×10^3	10^4 s	10^{-5} - 10^{-4}	132
Pt/Sb ₂ Te ₃ /GeTe (period)/TiN	10	10^4	10^4 s	6×10^{-8}	133
TiN/GeSbTe/TiN	10	70	***	***	134
TiN/Ge ₂ Sb ₂ Te ₅ /TiN	<10	10^4	10^4 s	1×10^{-5} - 8×10^{-5}	106
TiW/Ge ₂ Sb ₂ Te ₅ /TiW	10	10^4	***	5×10^{-10}	135
TiN/Ge ₂ Sb ₂ Te ₅ /Cu/SiC/Pt	10^3	10^4	10^4 s	7.8×10^{-8}	136
Pt/Ge ₂ Sb ₂ Te ₅ /Te/Pt	10^3	10^2	10^4 s (85°C)	***	137
Ag/GeSbTe/TiN	10^3	10^2	10^4 s	***	138
Pt/Ag/Ge ₂ Sb ₂ Te ₅ /Pt	10^3	10^3	8 h	***	139
Cu/N-Ge ₂ Sb ₂ Te ₅ /Pt	10^7	10^4	10^4 s	10^{-5}	140
Ag/Ge ₂ Sb ₂ Te ₅ /ZnS-SiO ₂ /W-Ti	5×10^2	10^4	10^5 s	***	141
Pt/TiGe _x Se _{1-x} /TiN	6	2×10^6	10^4 s (85°C)	4×10^{-8}	142

Chalcogenide materials can provide excellent resistive switching performances. They have been investigated in the development of data storage and computing applications. The high ion mobility of chalcogenides benefits the formation of conductive filaments and introduces a high HRS/LRS ratio. Filamentary resistive switching often suffers from severe variability due to the defect-based resistive mechanism.¹⁴³ An in-depth investigation of resistive switching based on chalcogenides is needed for further development.

Metal-Oxide Materials. Metal-oxide materials are considered one of the most important materials in both scientific and technological fields due to their excellent optical and electrical properties, materials stability, and easy formability.¹⁴⁴ The investigation on the metal-oxide memristor can track back to 1962. Hickmott reported the hysteretic current–voltage phenomenon in an Al/Al₂O₃/Al device, elaborating on the resistive switching characteristic under applied electric fields.²¹ Subsequently, many metal oxides have been employed to construct memristor devices, such as TiO₂,⁷⁴ SiO_x,¹⁴⁵ ZnO,¹⁴⁶ NiO,¹⁴⁷ HfO₂,¹⁴⁸ TaO_{5-x},⁹³ Cu₂O,¹⁴⁹ GdO_x,¹⁵⁰ SrTiO₃,⁷⁹ Pr_{0.7}Ca_{0.3}MnO₃,¹⁵¹ and so on, as summarized in **Table 2**. Dmitri B. Strukov *et al.* reported a physical model to explain resistive switching behaviors in a two-terminal Pt/TiO₂/Pt device.⁴ **Figure 10a** shows the equivalent circuit of the boundary migration model. In this system, oxygen vacancies are treated as mobile +2 charged dopants. The boundary between the insulating TiO₂ and low-resistance oxygen-deficient TiO_{2-x} layers drifts under electric fields, leading to changes in overall resistance. The I–V characteristic is shown in **Figure 10b**. An obvious hysteresis loop confirms resistive switching behaviors. Schematic diagrams of the resistive switching mechanism based on the conductive channels model in the Ta₂O_{5-x}/TaO_{2-x} device are shown in **Figure 10c**.¹⁵² The tantalum oxide clusters can generate a Ta-rich phase (TaO_{1-x} phase) under electrical stimulation due to oxygen-vacancy migration. Metal oxides are good solid electrolytes for metallic ions (Ag⁺ and Cu₂⁺) as shown in **Figure 10d** based on the Ag/TiO₂:Ag/Pt.¹⁵³ The contact resistance and interface effects should be considered in metal oxide-based devices.¹⁵⁴ Various top electrode materials with different work functions, including SrRuO₃(SRO), Ag, Pt, Au, and Ti were employed to fabricate memristor devices.¹⁵⁵ Only the Ti/Pr_{0.7}Ca_{0.3}MnO₃(PCMO)/SrRuO₃(SRO) device showed rectifying and resistive switching characteristics as shown in **Figure 10e**. Apart from the low function of the Ti electrode, high oxygen affinity induces the depletion of oxygen ions. The trapped states at the interface led to the modulation of Schottky-like barriers under different voltages, resulting in resistive switching behaviors. Furthermore, H. Y. Peng *et al.* reported that a single device can switch

between the filamentary and interfacial resistive switching modes.¹⁵⁶ Different electrodes that affect the migration of oxygen vacancies can induce different resistive switching models.

Metal-oxide resistive switching devices are very promising for commercialized products. The retention time over ten years has been reported.¹⁵⁷ Meanwhile, excellent cycle endurance of 10^{12} operation cycles has also been demonstrated.¹⁵⁸ However, little work has been involved in the devices with sensory functions. A systematic investigation is crucial for future commercial extensions.

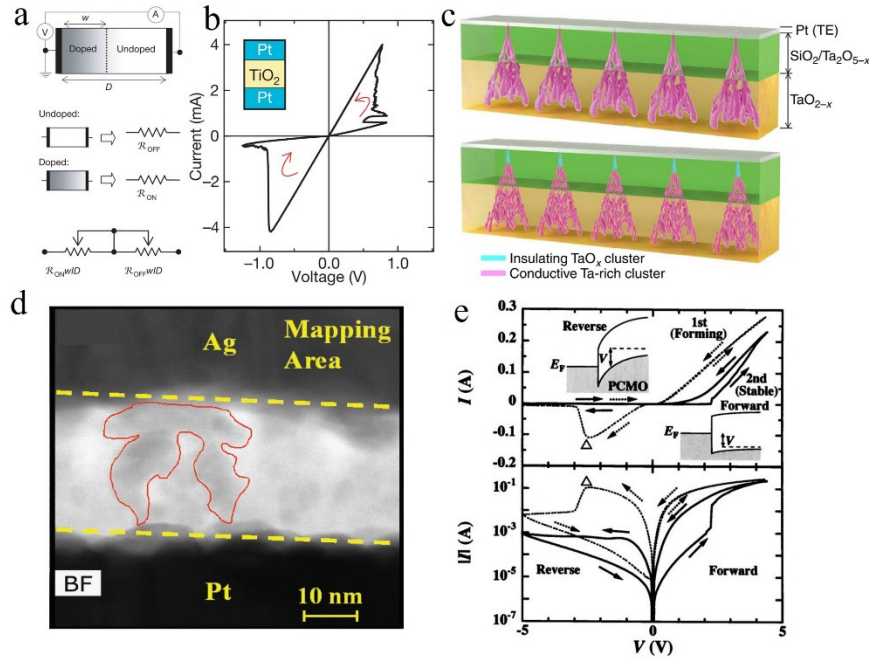


Figure 10. (a) Equivalent circuit of boundary migration model. (b) I–V characteristic of the Pt/TiO_{2-x}/Pt device. Reprinted with permission.⁴ Copyright 2008, Springer Nature. (c) Schematic diagrams of resistive switching mechanism based on conductive channels model in the Ta₂O_{5-x}/TaO_{2-x} device. Reprinted with permission.¹⁵² Copyright 2013, Springer Nature. (d) The high-resolution transmission electron microscopy (HRTEM) image of the Ag/TiO₂:Ag/Pt device. Reprinted with permission.¹⁵³ Copyright 2017 WILEY-VCH Verlag GmbH & Co. KGaA, Weinheim. (e) I–V characteristics of a Ti/Pr_{0.7}Ca_{0.3}MnO₃(PCMO)/SrRuO₃(SRO) device in linear and semilogarithmic current scales. Insets show electronic band diagrams of the Ti/PCMO interface. Reprinted with permission.¹⁵⁵ Copyright 2004 American Institute of Physics.

Table 2. Summary metal-oxide-based memristive devices.

Device	HRS/LRS ratio	Endurance	Retention (s)	Switch speed (s)	Ref.
Pt/TiO ₂ /W	10	10 ²	10 ⁵	***	159
Ti/ZrO _{2-x} /TiO ₂ /Pt	10 ²	2x10 ³	10 ⁴	***	160
Al/TiO _{1.7} /TiO ₂ /Al	20	10 ⁶	***	1x10 ⁻⁶ -5x10 ⁻⁶	161
Pt/TiO ₂ Nanorod/Ti	10 ²	10 ⁷	10 ⁵	5x10 ⁻⁸	162
Al/TiO ₂ /Al	>10	4x10 ³	10 ⁶ (85°C)	***	163
Al/a-TiO ₂ /Al	50	10 ²	10 ⁴	***	164
Au/CoO-TiO ₂ /Pt	10	10 ³	10 ⁴ (85°C)	***	165
Pt/TiO ₂ /HfO ₂ /ITO	10	5x10 ²	10 ⁴	***	166
W/HfO ₂ /TiN	10	10 ⁷	10 ⁴ (125°C)	10 ⁻⁵	167
Pt/Zn _{0.99} V _{0.01} O/Pt	10 ²	10 ⁵	3.6x10 ⁴ (85 °C)	5x10 ⁻⁷	168
Pt/ZnO:CO/ZnO:In	10 ³	10 ³	10 ⁵	***	169
Pt/Ag/ZnO:Li/Pt	10 ⁴	10 ³	10 ⁴	3x10 ⁻⁴ -3.6x10 ⁻⁴	170
Pt/ZnO:Cr/ITO	9.12 x 10 ²	10 ⁵	10 ⁵	***	171
Ag/ZnO nanosheet/Pt/	4	50	10 ⁴	***	172
Pt/Ga ₂ O ₃ /ZnO/Pt	10 ³	10 ²	10 ⁴	***	173
Ni/ZnO/n-type Si	10	10 ²	10 ⁴	***	174
ITO/HfO _x /ITO	40	10 ⁸	10 ⁵	2x10 ⁻⁸	175
Pt/HfO ₂ /ITO/TiN	10 ²	10 ⁷	10 ⁴ (125°C)	3.3x10 ⁻⁷ -3.8x10 ⁻⁷	176
Ti/HfO _x /Pt	10	2.5x10 ⁴	10 ⁴ (85°C)	2x10 ⁻⁸	177
TiN/HfO _x //GeTe/Pt	10 ³	10 ⁵	10 ⁴ (85°C)	5x10 ⁻⁷	178
Cu/HfO ₂ /Au	10 ³	10 ⁵	10 ⁴	10 ⁻⁶	179
Cu/WO _{3-x} /ITO	10 ⁵	10 ³	5 × 10 ⁵	5x10 ⁻⁴	180
Ta/TaO _x /Ru/TiN	10	10 ⁷	10 ⁴ (150°C)	10 ⁻⁵	181
Ag/TaO _x /TaO _y /Pt	10 ⁸	10 ²	***	3x10 ⁻⁸ -7.5x10 ⁻⁸	182
Ta/TaO _x /Pt	10	10 ⁸	***	10 ⁻⁶	183
Pt/NiO/Pt	10 ⁵	10 ²	10 ⁵	***	184
Ag/SrTiO ₃ :Fe/Pt	10 ⁴	2.1x10 ³	***	***	185
Au/High-entropy oxide/Pd	>15	7x10 ⁴	7.2x10 ⁴ (100°C)	2x10 ⁻⁶ -3x10 ⁻⁶	186
Ti/HfO _x /AlO _y /TiN	10	10 ⁴	10 ⁴ (85°C)	***	187

2.2 Investigation Methods for Resistive Switching

To achieve large-scale commercialization of memristive devices, problems at the device level are major challenges in addition to issues at circuit design, algorithm development, and architecture construction. A robust understanding of thermal dynamics, electron transport, and ion migration is essential to improve memristive performances regarding endurance, variability, HRS/LRS ratio, switching speed, state retention time, etc. Materials characterization techniques, physical modeling, and electronic conduction mechanisms are crucial to comprehensively explain resistive switching phenomena and further improve the device's performance.

2.2.1 Transmission Electron Microscopy

Ionic migrations are crucial in resistive switching. Therefore, visualization techniques on nano and atomic scales are required to further understand ionic dynamics, more insight into lattice variation, and conductive channel growth. Transmission electron microscopy (TEM) is a microscopic technique utilizing electron beams to realize visualizations at nano or even angstrom scales. This is an important piece of equipment to investigate the growth of metallic conductive filaments and resistive switching associated with oxygen vacancies.¹⁸⁸ Particularly, *in situ* observation goes beyond the static observation for resistive switching, which is more favorable. It monitors the real-time evolution of microstructures in devices under electric stimuli. In general, it is difficult to directly observe the *in-situ* TEM image of a real memristive device. A careful design is required to obtain a modified setup reserving the essential attributes of resistive switching in real devices. The observed region should be thin enough so that the changes in the switching layer can be visualized by electron beams. And the resistive switching should be reserved in the tested structure. **Figure 11a** shows a typical experimental setup to study the growth of Ag conductive filaments in a SiO₂ layer.⁸⁸ The electric voltage applied on a resistive switching structure of Ag/SiO₂/W. The filament growth process inside the SiO₂ was recorded. The images of conductive filaments at LRS and HRS are shown in **Figure 11b**.⁸⁷ It was clear that the bottom electrode and top electrode were connected by Ag metallic filaments, demonstrating the LRS. In comparison, after the RESET operation at the same region, the conductive filaments were dissolved and disconnected from the top and bottom electrodes, demonstrating the HRS.

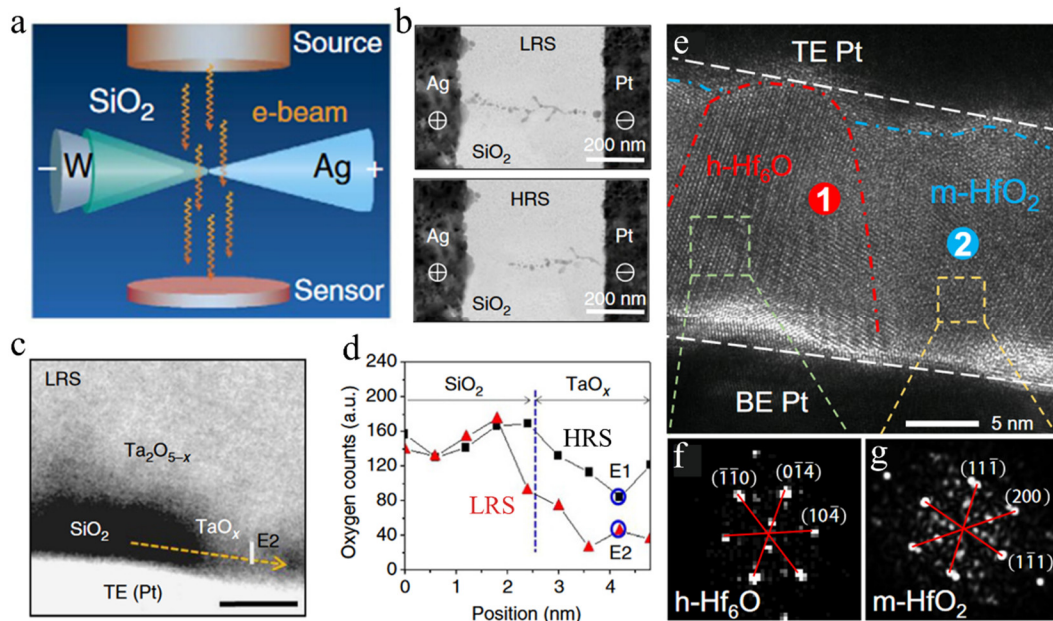


Figure 11. (a) Schematic diagram of a typical *in-situ* TEM experimental setup, the studied device structure was Ag/SiO₂/W. Reprinted with permission.⁸⁸ Copyright 2014, Nature Publishing Group (b) *In-situ* observed metallic conductive filaments at the LRS and HRS. Reprinted with permission.⁸⁷ Copyright 2012, Nature Publishing Group. (c) The cross-section image included a channel region observed at the LRS. The studied device structure was Pt/SiO₂/Ta₂O_{5-x}/TaO_x/Pt. (d) The oxygen profiles at the channel region (shown in c) were measured under the HRS (black) and LRS (red). Reprinted with permission.¹⁵² Copyright 2013, Nature Publishing Group. (e) A typical polymorphous HfO_x region with completed conductive filaments. (f-g) FFT diffraction patterns of h-Hf₆O and m-HfO₂ region. Reprinted with permission.⁶³

Particularly, the element composition analysis tool studies the composition features in the switching layer, such as energy dispersive X-ray spectroscopy (EDS) and electron energy loss spectroscopy (EELS). It is immensely helpful to get an insight understanding of resistive change mechanisms. **Figure 11c** exhibits the region of a nanoscale conductive channel obtained at the LRS.¹⁵² **Figure 11d** gives EELS lines corresponding to oxygen profiles of the conductive channel at the HRS and LRS. It confirmed that the oxygen concentration of LRS was lower than the HRS counterpart, indicating that the movement of oxygen vacancies resulted in resistive switching.¹⁵² Furthermore, electron diffraction patterns carry important crystallographic information. It is particularly useful for resistive switching investigations as crystallographic transitions often occur in memristive devices due to oxygen vacancies

migration and Joule heating effects.¹⁸⁹ **Figure 11e** shows the cross-section of a Pt/HfO₂/Pt device after a SET operation.⁶³ Distinguishable crystallization regions were observed in the high-resolution image. Fast Fourier transform (FFT) diffraction patterns of two typical regions are presented in **Figure 11e** and **f**. The diffraction spots corresponded to h-Hf₆O with high conductivity. This confirmed the crystal structure of the conductive channel which was difficult to observe by direct imaging. Ultra-high resolution and real-time investigation abilities are vital to get insights into resistive switching mechanisms. TEM, especially *in situ* TEM, is expensive. Some other auxiliary equipment (for example ion beam etching systems) is also required. Preparation usually takes a long time. Besides, the *in situ* tested sample is usually not the actual device, careful experiment design is important to mimic the operation in a real device and obtain reliable experimental results.

2.2.2 Scanning Probe and X-ray Microscopy

Scanning probe microscopy (SPM) catches the surface features, electronic properties, ferroelectric polarization, etc. on a nanoscale.¹⁹⁰ Conductive atomic force microscopy (CAFM)¹⁹¹ and scanning tunneling microscopy (STM)¹⁹² are two main SPM techniques for investigating resistive switching mechanisms. CAFM measures the morphology and conductivity of the surface independently, which is a useful tool to investigate resistive switching phenomena. For the function of morphology characterizations, it is the same as an atomic force microscope (AFM). Optical and piezoresistive systems are utilized to monitor the cantilever's deflection and reconstruct the surface morphology. The specialty of the CAFM is to characterize conductive distribution other than the solo morphology measurement in AFM. A typical setup of CAFM is shown in **Figure 12a**, a current-to-voltage preamplifier records the conductivity changes on the surface of samples.¹⁹³ It achieves a remarkably high spatial resolution of conductive variations, which is helpful to investigate resistive switching. In **Figure 12b**, a small voltage of 50 mV was applied to the CAFM tip and monitored the current values during the scanning process to obtain the conductance distribution.¹⁴⁷ Snowflake white areas indicated high conductivity areas. At the LRS, more white areas were observed, demonstrating high conductivity after a SET operation. Interestingly, the white regions usually overlapped with grain boundaries. This evidence confirmed that the forming/rupture of conductive filaments occurred at grain boundary areas.¹⁹⁴

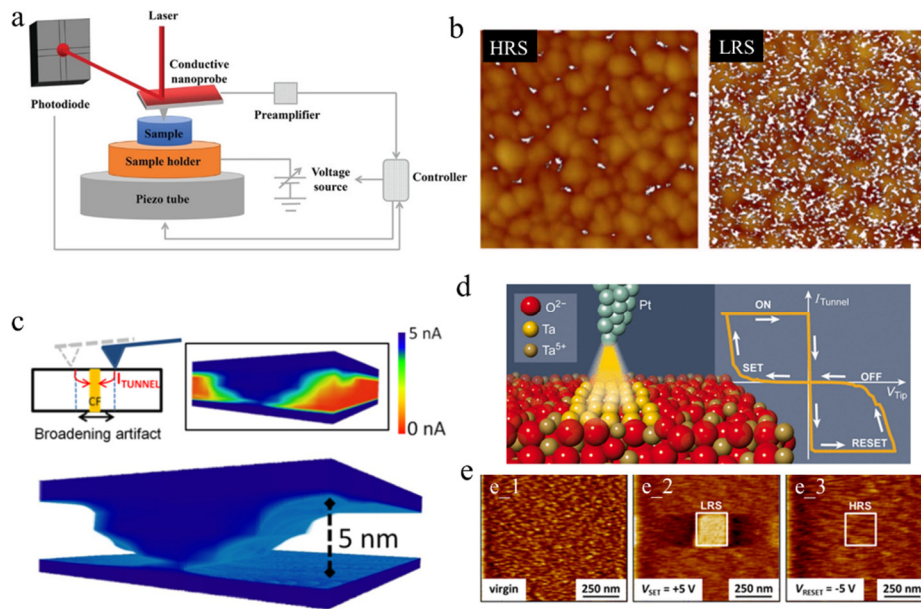


Figure 12. (a) Schematic diagram of an experimental setup for a typical CAFM. Reprinted with permission.¹⁹³ Copyright 2020, WILEY-VCH Verlag GmbH & Co. KGaA, Weinheim. (b) The AFM and C-AFM images of HRS and LRS, the CAFM image was posed on the AFM image. Reprinted with permission.¹⁴⁷ Copyright 2008, AIP Publishing. (c) 3D reconstructed tomogram of a metallic conductive filament. Reprinted with permission.¹⁹⁵ Copyright 2013, IEEE. (d) Schematical diagram of STM for resistive switching investigation. (e) STM images ($1 \mu\text{m} \times 1 \mu\text{m}$) of TaO_x film before and after scanning, corresponding SET and RESET operations. Reprinted with permission.¹⁹⁶ Copyright 2016, American Chemical Society.

The ionic-involved resistive switching often occurs in three dimensions. A technique enabling three-dimensional (3D) characterization is needed to enhance the understanding of filamentary dynamics. A possible solution is to characterize CAFM-based 3D tomography (often named SPM tomography, scalpel SPM, or 3D CAFM).¹⁹⁷ This technology visualizes conductive filaments.¹⁹⁸ In memristive devices, the conductive filaments are usually covered by top electrodes and buried in switching layers. To expose hidden filaments, a controlled tip mechanically removes materials at a sub-nm vertical removal rate. The scan operation executes during the removal process to obtain a series of 2D profiles at different depth levels of materials. The collected profile data is used to construct a 3D tomogram. In **Figure 12c**, a 3D tomogram of Cu conductive filament in a conical shape is presented. This information was very useful to investigate the forming mechanism of this filament. It was involved with drifting and interacting Cu^{2+} species with Al-vacant sites and oxygen vacancies.¹⁹⁵ Furthermore, CAFM can

achieve *in situ* resistive switching tests. The tip acts as the top electrode and directly mimics memristive operations. Besides, different working atmospheres (such as O₂ and N₂) can be used during the *in-situ* test.¹⁹⁹ This is crucial to study reactions in the switching layer during the operation process.

STM is another powerful visualization technology to investigate resistive switching mechanisms. It is built up based on quantum mechanical effects that work in a noncontact mode. Compared to CAFM using contact modes, STM provides advantages in testing soft materials and avoiding potential surface damage. Besides, the atomically sharp tip realizes higher resolutions.¹⁹⁰ Schematic diagram of a scanning STM for resistive switching investigations is shown in **Figure 12d**.¹⁹⁶ Redox reactions in oxides were realized without physical contact. **Figure 12e** shows surface characterizations measured by the STM.¹⁹⁶ SET and RESET voltages applied on selected areas induced a distinguishable conductance, indicating modulated resistance. With the assistance of XPS, the resistive switching was because of the reduction of Ta^{x+} and the generation of oxygen vacancies. The disadvantage of STM compared to CAFM is that sufficient conductivity is required, especially for the HRS. This limits the application of STM since switching layers in memristive devices are usually insulators with low conductivity. Besides, STM systems are more expensive than CAFM systems. Because a vacuum atmosphere is needed for STM tests. Some key points should be considered before using the SPM technology to study resistive switching devices. Firstly, the voltage available in commercial equipment is usually lower than 10 V. It hinders the practical usage of this technique on devices that need high operation voltages. Secondly, the current measurement margin is small, mostly within 2-4 orders of magnitude. It may encounter problems in testing the device with a large ratio of HRS/LRS. Thirdly, a current limitation cannot be applied. An undesired failure of systems may be encountered during the SET operation.

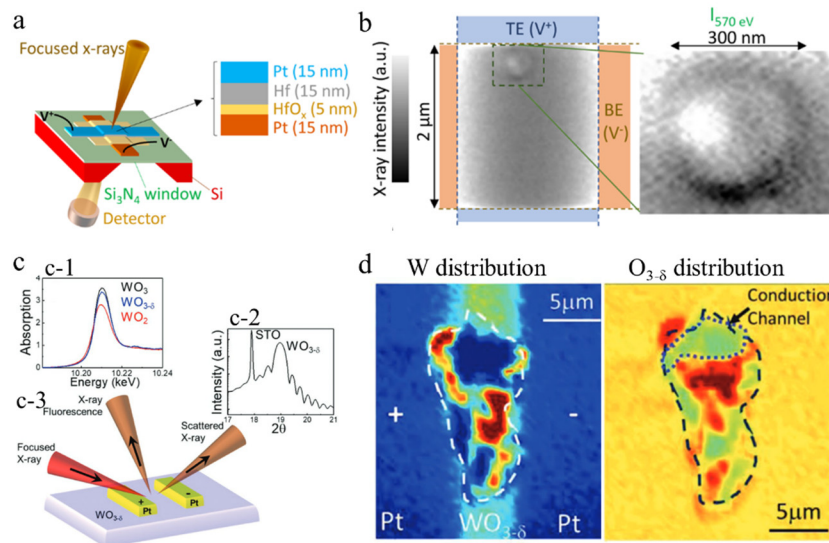


Figure 13. (a) Schematic diagram of the experimental setup for a typical synchrotron-based scanning transmission X-ray microscopy (STXM) measurement. (b) The X-ray transmission intensity map. Reprinted with permission.²⁰⁰ Copyright 2016, American Chemical Society. (c) The XAS and XRD spectroscopy are shown in c_1 and c_2, respectively. c_3 shows the schematic diagram of the experimental setup for the X-ray multimodal imaging. (d) The conductive channel consists of W and O elements. Reprinted with permission.²⁰¹ Copyright, 2022 Wiley-VCH GmbH.

X-ray microscopy plays a key role in materials characterization, especially for nondestructive measurements. X-ray shows high penetration abilities and high spatial resolutions, which makes it can “see through” tiny defects and structure variations buried inside materials.²⁰² For instance, the resistance switching is due to the variation of structures, and chemical states in switching layers. Whereas the changes are hidden behind electrodes and materials themselves. The ion beam etching in TEM systems and the scalpel process in 3D CAFM systems can expose the structure and chemical changes inside the devices. But they are destructive measurements and time-consuming. X-ray realizes non-destructive investigation of resistive switching by utilizing penetration and imaging abilities. Oxygen species are crucial for resistive switching mechanisms, particularly for metal-oxide-based memristive devices. The X-ray can realize spatial resolution at the nanoscale and the spectral resolution of meV level for O K-edge.²⁰³ **Figure 13a** shows a typical setup for X-ray transmission measurements.²⁰⁰ Focused X-ray penetrated the top electrode, switching layer, the bottom electrode, and a Si₃N₄ window. A non-uniform ring-like region was found (**Figure 13b**). The contrast variation in the image was due to changes in

oxygen concentrations over the range of 3-5%.²⁰⁰ This can be related to the generation of oxygen vacancies that led to the defect states and enhanced conductivity. Furthermore, multiple spectra can be obtained by X-ray microscopy for robust insight investigations. The device structure can be constructed in a planar geometry to get better-detecting efficiency and accuracy.²⁰⁴ X-ray multimodal imaging experimental system is shown in **Figure 13c**.²⁰¹ The spectra of X-ray absorption spectroscopy (XAS) and X-ray diffraction (XRD) were obtained simultaneously by a raster-scanned operation. It presented high accuracy and high spatial resolution of elements distributions. **Figure 13d** exhibits the distribution of W and O elements. The result confirmed that the migration of oxygen vacancies was responsible for resistive switching. Besides, the distribution feature of oxygen vacancies under different confinements of the electric field was investigated. This provided an insightful strategy to improve resistive switching stability and suppress device variations. The main drawback of X-ray microscopy investigating resistive switching is the slightly lower resolution compared to TEM and CAFM technology. Besides, the test usually requires access to advanced synchrotron radiation sources, which may be difficult for some research groups.

2.2.3 Conduction Mechanisms Based on I-V Characteristic

An in-depth study of I-V characteristics reveals the conduction mechanisms that benefit the exploration of working mechanisms.²⁰⁵ The DC switching cycle test (also referred to as the cyclic voltammetry test) is one of the essential measurements investigating resistive switching. It carries electrochemical reaction information that is crucial for redox-based resistive switching. Temperature and moisture are two crucial factors that affect electrochemical reactions, ionic migration kinetics, and electrolyte characteristics. Analyzing the electronic properties under controlled temperature and moisture variations benefits a better understanding of redox-based resistive switching behaviors. The technique is to fit experimental I-V curves with specific physical models to reveal resistive switching mechanisms. The Ohmic conduction, space-charge-limited-conduction (SCLC), and Schottky emission are discussed in detail.

The SCLC has been frequently employed to study resistive switching phenomena.²⁰⁶ Three distinguishable regions can be observed for a trap-related SCLC model: i) A Ohmic region ($I \propto V$) under small voltage values. This is governed by thermal-generated free carriers; ii) A Child's square law region ($I \propto V^2$) under large voltage values. Conduction is controlled by electrode-injected electrons;

iii) Current increases steeply region ($I \propto V^x$, $x > 2$) under high voltage values. The trap-free is achieved and shows high conductivity.²⁰⁷ The conductive channels are often formed in this stage in memristive devices.²⁰⁸ For Ohmic conduction, the current value is proportional to the applied electric field as shown in **Eq. 2**.²⁰⁹

$$I_{Ohmic} = \sigma \times V \quad \text{Eq. 2}$$

where σ represents the electrical conductivity. V is the applied voltage. I_{Ohmic} is the current governed by Ohmic conduction. Take the log of **Eq. 2**. The following equation can be obtained.

$$\log(I_{Ohmic}) = \log(\sigma) + \log(V) \quad \text{Eq. 3}$$

Based on the SCLC theory, the current under high voltage region can be described as **Eq. 4**.²¹⁰

$$I = \frac{9}{8} \varepsilon_i \mu \theta \frac{V^2}{d^3} \quad \text{Eq. 4}$$

where I is the current. V is the voltage, respectively. ε_i represents permittivity. θ represents the ratio of free and trapped charges. μ represents electron mobility. The thickness presented by d . Similarly, **Eq. 4** can be transformed to

$$\log(I) = \log\left(\frac{9}{8} \varepsilon_i \mu \theta \frac{1}{d^3}\right) + 2 \log V \quad \text{Eq. 5}$$

One frequently used method to investigate resistive switching is drawing the I-V plots in log-log scales (**Figure 14a**).²¹¹ Under low positive voltages, the slope was close to 1, indicating Ohmic conduction as described in **Eq. 3**. In comparison, a slope of 2 was obtained at a higher voltage governed by SCLC theory as described in **Eq. 5**. When further increased the voltage, the current increased sharply owing to the formation of high conductive oxygen vacancies filaments.²¹¹ Notably, a slope of 1 was obtained at the LRS under the positive voltage region in **Figure 14a**, indicating Ohmic conduction was dominated by high conductive channels.²¹² Under the negative, the slope was maintained as 1 under low voltages governed by Ohmic conduction. And a RESET operation was completed at a high negative voltage. Thus, the conduction mechanism transitions between the HRS and LRS can be depicted.

The modulated Schottky barrier height is another important resistive switching mechanism. The relevant conduction mechanism can be confirmed by fitting typical I-V curves.²¹³ The Schottky equation is shown below:²¹⁴

$$I = \frac{4\pi Sqm^*(kT)^2}{h^3} e^{-\frac{q(\phi_B - \sqrt{\frac{qE}{4\pi\epsilon}})}{kT}} \quad \text{Eq. 6}$$

where S is the device area; k is Boltzmann's constant; m^* represents the electron's effective mass. T describes the value of absolute temperature. E represents the electric field. h represents Planck's constant. ϕ_B represents the height of the junction energy barrier, and ϵ is the permittivity. **Eq. 6** can be transformed into **Eq. 7**.

$$\ln(I) = \frac{q}{kT} \left(\frac{q}{4\pi\epsilon} \right)^{\frac{1}{2}} \times E^{\frac{1}{2}} - \left(\ln \frac{h^3}{4\pi Sqm^*(kT)^2} + \frac{q\phi_B}{kT} \right) \quad \text{Eq. 7}$$

Then, the relationship between the V and the E is described by **Eq. 8**.

$$E = \frac{V}{L} \quad \text{Eq. 8}$$

where L represents the thickness. One can get **Eq. 9** from **Eq. 7** and **Eq. 8**.

$$\ln(I) = \frac{q}{kT} \left(\frac{q}{4\pi\epsilon L} \right)^{\frac{1}{2}} \times V^{\frac{1}{2}} - \left(\ln \left(\frac{h^3}{4\pi Sqm^*(kT)^2} \right) + \frac{q\phi_B}{kT} \right) \quad \text{Eq. 9}$$

The conduction mechanism governed by Schottky emission can be confirmed by plotting the relationship between $\ln(I)$ (or $\ln(J)$, J is current density) and $V^{1/2}$ (or $E^{1/2}$, E is an electric field). The $\ln(I)$ and $V^{1/2}$ are expected to have a linear relation under a fixed temperature.²¹⁵ A supplement method is to test the I-V curves under different temperatures as shown in **Figure 14b**.²¹⁶ Then, fitting the curves to get the relationship of $\ln(I)$ and $V^{1/2}$. A linear relationship can be expected under different temperatures, providing better proof for the conduction mechanism. **Eq. 7** can be transformed into **Eq. 10**.²¹⁷

$$\ln \left(\frac{I}{T^2} \right) = \ln \left(\frac{4\pi Sqm^*k^2}{h^3} \right) - \frac{q(\phi_B - \sqrt{\frac{qE}{4\pi\epsilon}})}{k} \times \frac{1}{T} \quad \text{Eq. 10}$$

Under fixed voltage, the plot of $\ln(I/T^2) - 1/T$ should show linear relation as shown in **Figure 14c**.²¹⁶ Different voltages can be used to depict the relationship between $\ln(I/T^2)$ and $1/T$. This provides more solid evidence for the electronic conduction governed by Schottky emission.

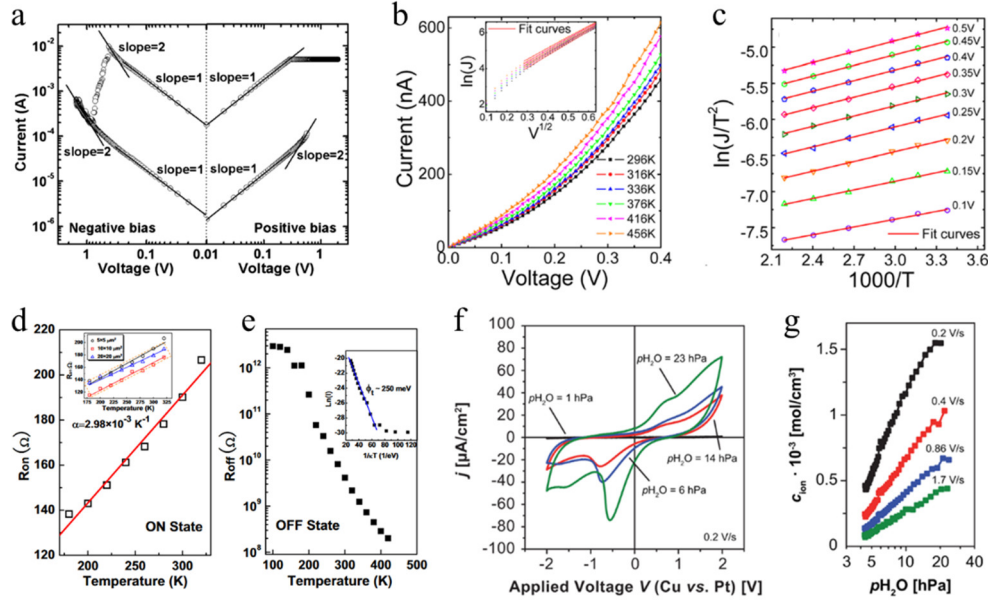


Figure 14. (a) Typical I-V curve in log-log scale. Reprinted with permission.²¹¹ Copyright 2010, AIP Publishing. (b) I-V curves tested under different temperatures. The inset shows $\ln(J)-V^{1/2}$ plots. (c) $\ln(J/T^2)-1000/T$ plots under different reading voltages. Reprinted with permission.²¹⁶ Copyright 2013, AIP Publishing. (d) The values of LRS under different temperatures. The inset shows temperature-dependent resistance for devices with varied sizes. (e) The values of HRS under different temperatures. The inset presents the plot of $\ln(I)-1/\kappa T$ to calculate the activation energy. Reprinted with permission.²¹⁸ Copyright 2008, AIP Publishing. (f) Cyclic voltammety tests under different humidity levels. (g) Ion concentration (c_{ion}) under different humidity levels. The p_{H_2O} means the partial pressure of water. Reprinted with permission.²¹⁹ Copyright 2013, American Chemical Society.

For cation-based resistive switching, a linear relationship of I-V at LRS is usually expected. The slope of I-V plots in log-log scales is close to 1 due to Ohmic conduction controlled by high-conductivity metallic filaments.^{220,221} Moreover, the resistance changes of HRS and LRS can be studied to further confirm the formation of metallic filaments based on cation migrations. The temperature-dependent metallic resistance can be described by **Eq. 11**.

$$R(T) = R_0[1 + \alpha(T - T_0)] \quad \text{Eq. 11}$$

where R_0 is the value of resistance at the temperature of T_0 . α represents the temperature coefficient of resistance. As shown in **Figure 14d**, the resistance of LRS (also referred to as ON state) increased with increased temperatures. The temperature coefficient of resistance was positive, implying a typical

electron transportation feature in metallic materials.²¹⁸ The measured α can be used to compare with metallic nanowires. The chosen nanowire should be the same materials of filaments that are suspected to form in the memristive device. This can provide extra evidence that metallic filaments are formed.^{222,223} In comparison, the HRS (also referred to as OFF) may show a different or opposite temperature coefficient of resistance. As shown in **Figure 14e**, a negative α was obtained as a semiconductor (ZrO_2) was used as the switching layer. The resistance of semiconductors decreases with the increase of temperature as more thermal-excited carriers are generated at higher temperatures.

Moisture has been considered one of the principal factors in redox-based resistive switching.²²⁴ In the cation-based redox resistive switching, the half-cell reaction ($\text{M} \rightarrow \text{M}^{x+} + x\text{e}^-$) occurs at the active electrode to generate cations.⁸² Cyclic voltammetry tests under different moisture levels can reveal a better microscopic understanding of electrochemical processes. As shown in **Figure 14f**, cyclic voltammetry tests were carried out at different moisture levels. The concentration of ions (c_{ion}) was measured as summarized in **Figure 14g**.²¹⁹ Higher $p\text{H}_2\text{O}$ (the partial pressure of water) corresponded to higher ion concentrations. The results proved two points. First, the anodic oxidation was limited by the counter charge at Pt/SiO₂ interface. Second, hydroxide ions instead of electrons acted as counter charges. This test resulted in a more comprehensive understanding of electrochemical processes in cation-based memristive devices. In the anion-based redox resistive switching, the moisture influences the redox reactions and ionic mobility. Cyclic voltammetry tests provide delicate information on redox reactions in those systems.²²⁵ This method revealed that oxygen ions/vacancies and cations both contributed to resistive switching, which was related to chemical redox and passivation.^{93,144} This information is vital for theoretical models and paves ways to further improve device performances.

Conduction mechanism investigations are macroscopic and empirical. In some cases, the fitting results may be compatible with more than one conduction mechanism.^{226,227} Researchers need to consider other investigation methods (TEM, CAFM, STM, etc.), analyze device structures, and characterize materials to evaluate the accuracy of the resistive mechanism based on I-V characteristics.

2.2.4 Theoretical Model Simulations

Theoretical model simulations and experimental measurements should be paired and complement each other to study resistive switching. Theoretical simulations are employed to optimize device performances, interpret experimental results, predict properties, and accelerate projects. Theoretical

models should link the material properties, operation processes, and device performances. Theoretical simulations of memristive devices can be catalogued into two categories based on simulation scales, including the physical and the compact models. The physical model focuses on ionic migration, chemical reaction kinetics, defect characteristics, and materials' electronic properties at a microscopic scale. It clarifies the switching mechanisms along with experimental characterizations, which provides in-depth knowledge to improve device performances.^{228,229} As for the compact model (also called the behavioral model), it emphasizes the description and reproduction of electronic properties without concerning much underlying physics. Empirical assumptions and mathematical fitting are utilized to rapidly reproduce devices' behaviors. This method is suitable for diverse types of memristive devices.²³⁰ More importantly, the compact model can be extended to Simulation Program with Integrated Circuit Emphasis (SPICE) model that can be embedded into computer-aided design tools, which can be used for circuit simulations and system-level design. Notably, the combination of the physical model and compact model is preferred to depict memristive properties more accurately.²³¹

Physical models provide a deeper knowledge of resistive switching mechanisms regarding defects (generation, diffusion, and recombination), electron transportation, and inherent stochasticity as shown in **Figure 15a**. Experimental information about the properties of materials should be input into physical models to calibrate the models and improve simulation accuracy, including the crystal structure, band structure, work function, thermal conductivity, etc. Several simulation methods have been frequently used, such as First Principle (FP, also named *ab initio*), Molecular dynamics (MD), Kinetic Monte Carlo (KMC), and Finite Element (FE). FP calculations are good at simulating the conduction properties and the transition energy in memristive operations.²³² As shown in **Figure 15b**, a supercell was constructed to calculate the activation barrier of defect formation energy and the defect energy level, which benefits the device design with better reliability and uniformity.²³³ Furthermore, the diffusion of oxygen vacancies and defects charging/discharging can also be investigated by FP simulations.^{234,235} The drawbacks of FP simulations are the difficulties of modeling complex structures, such as amorphous, polycrystalline, and multi-layered structures.

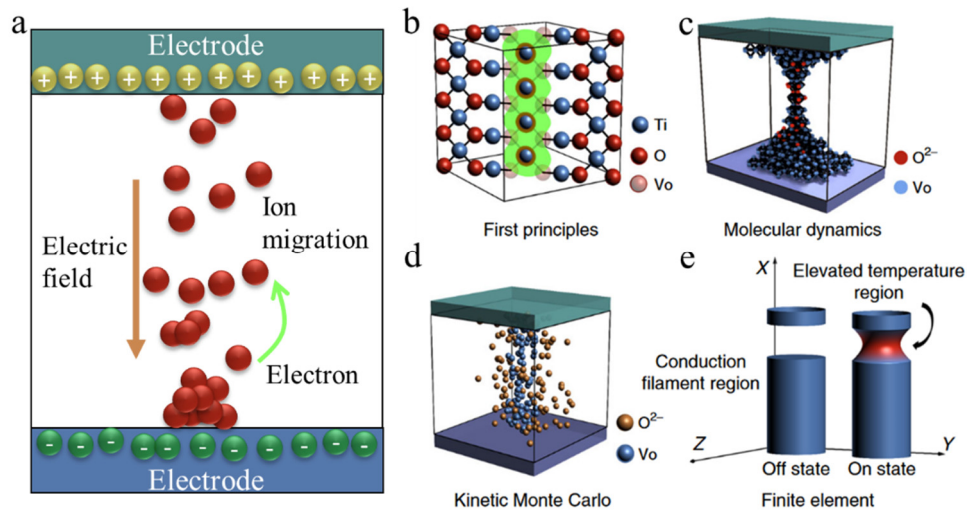


Figure 15. (a) Schematic diagram of physical models. (b) Schematic diagram of the FP simulation. (c) Schematic diagram of the MD simulation. (d) Schematic diagram of the KMC simulation. (e) Schematic diagram of the FE simulation. Reprinted with permission.⁹ Copyright 2019, The Author(s).

Dynamic simulations are popular to investigate ionic migrations and relevant stochastic features, typical simulation techniques are MD²³⁶ and KMC simulations.²³⁷ MD (**Figure 15c**) can catch dynamical phenomena of atoms (oxygen vacancies,²³⁸ Ag atoms³⁵) constructing filaments and atom chains that are responsible for resistive switching behaviors. In comparison, KMC (**Figure 15d**) is considered an event-driven and stochastic simulation technique. This method covers a big margin of time scale ranging from nanoseconds to years. The evolution of conductive channels and structure can be described by KMC.^{237,239} As shown in **Figure 15e**, FE employs mathematical models to quantify and understand resistive switching performances. It is usually a simplified model without concerning all variables in real devices.²⁴⁰ FE simulations are usually used with dynamic simulation techniques to describe ionic distribution accurately.²⁴¹ The disadvantages of KMC and FE simulations are too many assumptions and simplified parameters, which may influence the simulation accuracy. Notably, the combination of multiple theories can build up physical models more accurately.²⁴² The physical models should not be isolated from experimental results. The setup of parameters in simulation software must be based on experimental measurements as much as possible. A mutual corroboration between simulations and experiments should be achieved before proposing a model to explain the resistive switching performances.

Compact models are particularly important to circuit analysis and system-level design. A qualified compact model for memristive devices goes beyond basic electronic performances in CMOS transistors. The variability and endurance degradation features should also be considered. Firstly, analytical equations based on simplified physical images are developed. Then, index parameters are introduced to simulate degradation and stochastic characteristics.²⁴³ Finally, mathematical fitting with experimental results is carried out to identify the validity of the model and extract critical parameters of the model. The mathematical definition of memristive devices is shown below.⁴

$$V = R(w) \times I \quad \text{Eq. 12}$$

A differential form is shown below:

$$\frac{dw}{dt} = I \quad \text{Eq. 13}$$

where V means voltage. I means current. R is the generalized resistance depending on internal states. w represents the variable state. It was later generalized to nonlinear dynamical systems.²⁴⁴

$$V = R(w, I) \times I \quad \text{Eq. 14}$$

$$\frac{dW}{dt} = f(w, I) \quad \text{Eq. 15}$$

where w represents a series of state variables. R and f in general elaborate functions of time. The resistance changes (state variables of w) in memristive systems are derived from modulated doped regions, Schottky barriers, conductive filaments, and tunneling barriers (**Figure 16a**).²⁴⁵ The two models of modulated doped regions, and modulated Schottky barriers are usually used in anion-based resistive switching. The modulated conductive filaments and modulated tunneling barriers are usually used in filamentary-type resistive switching controlled by either anion-based switching or cation-based switching. The physical models can be described by electronic elements and corresponding equations, which is the foundation of compact models. **Figure 16b** shows the schematic diagram of a compact model that the resistance is governed by the moving of doped/undoped boundary proposed by HP Labs.⁴ The applied voltage generated oxygen vacancies and drove them moving, resulting in two separated doped (low resistance) and undoped regions (high resistance) due to the drifting of the boundary. The process of modulated resistance is described as follow:⁴

$$V(t) = (R_{ON} \frac{w_{DL}(t)}{D} + R_{OFF}(1 - \frac{w_{DL}(t)}{D}))I(t) \quad \text{Eq. 16}$$

$$\frac{dw(t)}{dt} = \mu_V \frac{R_{ON}}{D} I(t) \quad \text{Eq. 17}$$

where R_{ON} (the whole switching layer is doped) and R_{OFF} (the whole switching layer is undoped) are the lowest and highest resistance of the device, respectively. w in this model is the length of the doped region (**Figure 16b**). μ_V is the average ion mobility. Bipolar switching was demonstrated in the model. More importantly, the model was verified by experimental results on a TiO_x -based device.

The modulated Schottky barrier is another important resistive switching mechanism. Two main models, barrier height^{246,247} and barrier area²⁴⁸ have been reported (**Figure 16c**). The applied voltage adjusts the distributed oxygen vacancies located at the interface, which modulates the resistance of the Schottky junctions. The Schottky barrier can be adjusted by applying electronic stimuli.²⁴⁹

$$I_{Schottky} = AA^*T^2 e^{\left(\frac{-e\Phi_B}{k_B T}\right)} (e^{\frac{eV}{k_B T}} - 1) \quad \text{Eq. 18}$$

where A^* means the Richardson constant. Φ_B represents the barrier height. k_B represents Boltzmann's constant. T is temperature.

The barrier lowering is described by the following equation:²⁴⁹

$$\Phi_B = \Phi_{Bn0} - \sqrt[4]{\frac{e^3 N(\Phi_{Bn0} - \Phi_n - V)}{8\pi^2 \epsilon_S^3 \epsilon_{\Phi_B}}} \quad \text{Eq. 19}$$

where Φ_B means lowered Schottky barrier height. Φ_{Bn0} means the original Schottky barrier height. N means the concentration of oxygen vacancies. $\epsilon_S \epsilon_{\Phi_B}$ represents the effective dielectric constant of the emission process. The modulated Schottky barrier height is responsible for resistive switching. Another model is due to the modulated area of the Schottky junction. The resistance of the device is consisting of two parts, including the Schottky junction and the conductive area governed by Ohmic contact or tunneling effects.^{248,250} As described by equations:²⁴⁸

$$I = (1 - w_{BA})\alpha[1 - e^{-\beta V}] + w_{BA}\gamma \sinh(\delta V) \quad \text{Eq. 20}$$

$$\frac{dw_{BA}}{dt} = \lambda(e^{\eta_1 V} - e^{\eta_2 V}) \quad \text{Eq. 21}$$

where w_{BA} is the state variable. $\alpha, \beta, \gamma, \delta, \eta_1$, and η_2 are all positive-valued parameters determined by material characteristics. The first term in **Eq. 20** is the Schottky term. The second term in **Eq. 20** is the tunneling term. **Eq. 21** describes the change rate of w_{BA} under applied voltages.

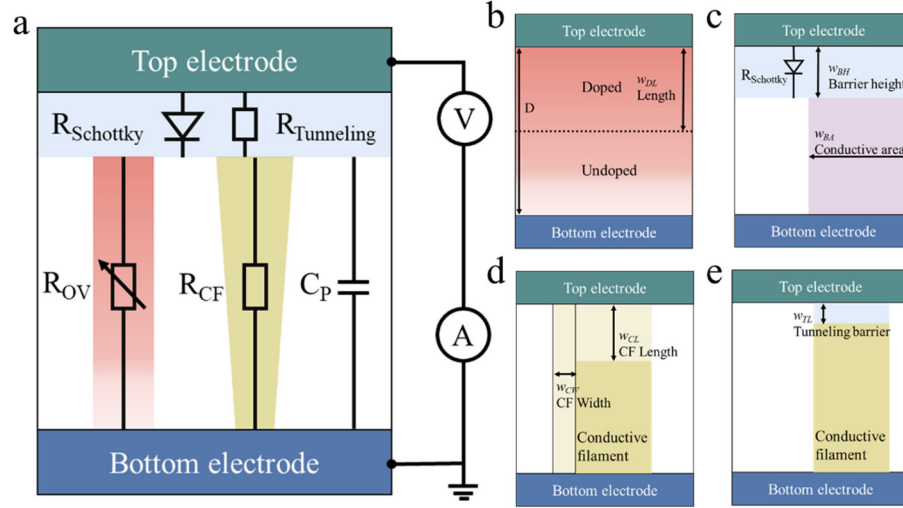


Figure 16. (a) Schematic diagram of compact models. (b) The compact model that the resistance is governed by the moving of doped/undoped boundary. (c) The compact model that the resistance is governed by the modulated Schottky barriers. (d) The compact model that the resistance is governed by the modulated conductive filaments. (e) The compact model that the resistance is governed by the modulated tunneling barriers.

Resistive switching behaviors controlled by conductive filaments have also been demonstrated by compact models. The state variants were due to morphological changes, including the thickness and length of filaments as shown in **Figure 16d**. Conductive filaments usually dominate the overall conductivity of devices. In real devices, multiple conductive filaments may exist in the devices. To simplify the model, one single cylinder-shaped filament with modulated thickness and length is projected. For the controllable filament thickness. The current following through conductive filaments is shown below:²⁵¹

$$I_{CF} = E\pi\sigma_{CF}r_{CF}^2 \quad \text{Eq. 22}$$

where E is the electric field. σ_{CF} is the conductivity of the conductive filament. r_{CF} is the diameter of the conductive filament. The evolution of conductivity filaments follows the equation shown below:²⁵¹

$$r_{CFmax_{i-1}} = (r_{CFmax_i} - r_{work})e^{-\frac{\Delta t}{\tau_{Form}}} + r_{work} \quad \text{Eq. 23}$$

$$r_{CF_{i+1}} = \left(r_{CF_i} - r_{CF_{max_i}} \frac{\tau_{eq}}{\tau_{Red}} \right) e^{\frac{-\Delta t}{\tau_{eq}}} + r_{CF_{max_i}} \frac{\tau_{eq}}{\tau_{Red}} \quad \text{Eq. 24}$$

$$\tau_{eq} = \frac{\tau_{Red}\tau_{OX}}{\tau_{Red} + \tau_{OX}} \quad \text{Eq. 25}$$

where $r_{CF_{max}}$ means the maximum diameter of the conductive filament. r_{Work} means the diameter of the effective device area. τ_{Form} is the nominal forming rate. τ_{Red} and τ_{OX} are the electrochemical reduction rate and the oxidation rate, respectively. Solving the above differential equations step-by-step will give the evolution process of the conductive filaments that dominates the overall resistance of devices. Furthermore, changes in the conductive length (or the gap between the filaments and electrode) have also been used to create a compact model. The modulated gap can be described by the following equation:²⁵²

$$\frac{dg}{dt} = -\frac{1}{2} e^{-\frac{E_a}{kT_{CF}}} \left(\frac{\alpha_1 a^2 f}{L-g-l_0} - 2af \sinh\left(\frac{qaE}{2kT_{CF}}\right) \right) \quad \text{Eq. 26}$$

where g means the distance between the top of conductive filaments to the electrode. f represents the escape-attempt frequency, the effective hopping distance described as a . E_a is the activation energy of V_O . α_1 is a fitting parameter. E is the electronic field. The first term corresponds to the diffusion flux. The second term corresponds to the drift flux. In some filamentary models, the modulated tunneling barriers dominate the resistance of the devices, as shown in **Figure 16e**. The device was SET to LRS before the bridging occurs by conductive filaments. Electrons tunnel through the very tunneling barrier and exhibit high conductivity.²⁵³ The tunneling barrier governing conduction can be described by the following equations.²⁵⁴

$$I_{Tunneling} = \frac{3\sqrt{2m_{eff}\Delta W_0}}{2x} \left(\frac{e}{h}\right)^2 \times e^{-\frac{4\pi x}{h}\sqrt{2m_{eff}\Delta W_0}} AV \quad \text{Eq. 27}$$

where m_{eff} is the effective electron tunneling mass, ΔW_0 represents the tunnel barrier height. Planck's constant is described as h . V is the tunneling voltage. A is the area of the filament/insulator interface. x is the tunneling gap. Besides, the tunneling gap can be modulated by electronic forces as shown in **Eq. 28**, which changes the device resistance.²⁵⁵

$$\frac{dx}{dt} = f_{fb} \sinh\left(\frac{I}{I_{fb}}\right) \times e^{\left(-e\left(\frac{x-a_{fb}}{x_c} - \frac{l}{b}\right) - \frac{x}{x_c}\right)} \quad \text{Eq. 28}$$

where fitting parameters are $f_{fb}, f_{rb}, i_{fb}, i_{rb}, a_{fb}, a_{rb}, x_c,$ and b . In compact models, many assumptions and simplifications may be applied.

Although compact models may give a decent accuracy for circuit simulations and design, it is recommended to consider device structures, experiment characterizations, and physical simulations before building compact models. This will give a more accountable and accurate compact model, benefiting the development of hardware systems.

2.3 Memristive Devices for Neuromorphic Computing

2.3.1 Neuromorphic Computing with Artificial Neural Network

The development of neuroscience triggered the idea of constructing electronic hardware to mimic biological brain systems. Human brains rely on synapses and neurons for recognition and decision-making tasks, which feature less energy consumption compared to conventional von Neumann computing systems (**Figure 17a**).^{256,257} Neuromorphic computing systems inspired by human brains process information in memory units, combining memory and computing (also referred to as in-memory computing).²⁵⁸ This configuration does not need frequent data shuttling between memory and computing units as von Neumann architecture does, which benefits computing speed and energy efficiency.²⁵⁹ Deep learning has been explored for brain-inspired neuromorphic computing.^{260,261} ANN hardware implementing deep learning is gaining more and more popularity. Neural networks have input layers, hidden layers, and output layers consisting of artificial neurons and artificial synapses. Neurons receive, process, and transmit information. Artificial synapses connect neurons with different plasticity (weights). The illustration of a neural network is shown in **Figure 17b**. The memristive device can be used to build up ANN hardware implementing deep learning algorithms performing sophisticated computations. VMM is the main computing task in deep learning, which, however, is very resource-expensive in traditional COMS systems.²⁶² The schematic diagram of a memristive crossbar array is depicted in **Figure 17c**. Synaptic weights are stored in the form of memristive conductance. The current at each point follows Ohm's law under specific input voltages. Besides, the current flowing through each column governed by Kirchhoff's current law is the summation of currents from every cross point. This can efficiently execute VMM operations. The computing results are measured at once no matter

how big the matrix size, demonstrating huge parallelism. The data does not need to be moved between units. This technique can realize exceedingly high energy-efficient and fast computing speed.

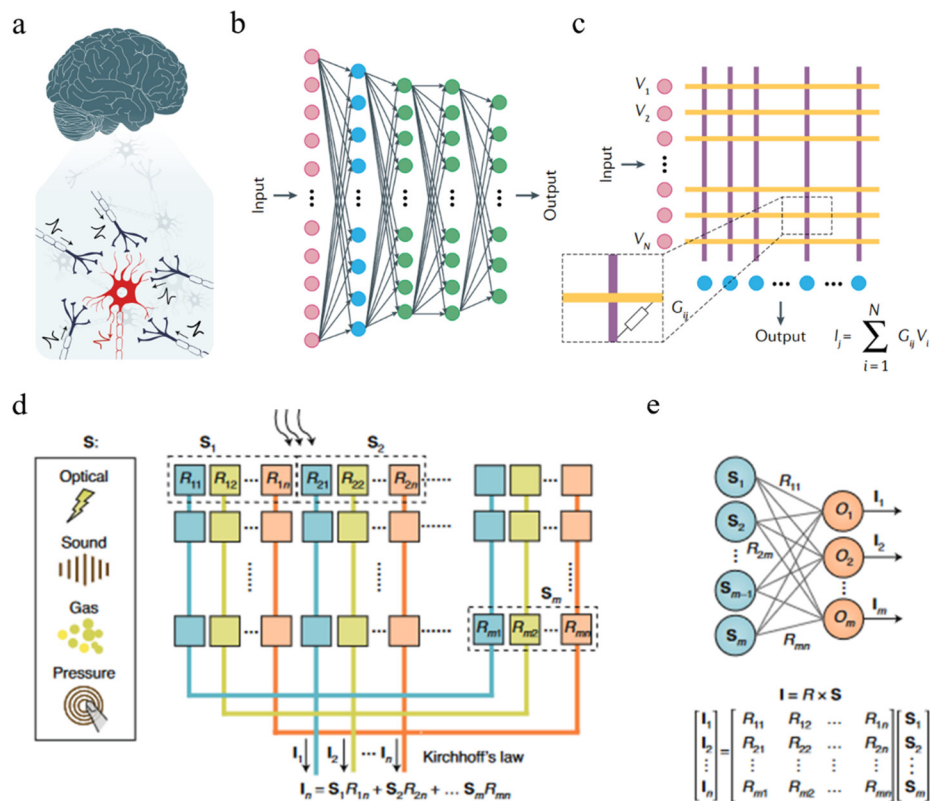


Figure 17. (a) Schematic diagram of a biological brain relying on neurons and synapses to realize computing functions. Reprinted with permission.²⁵⁶ Copyright 2020, Springer Nature. (b) Schematic diagram of fully connected neural networks. (c) Schematic diagram of a memristive crossbar array that implements VMM operations. Reprinted with permission.²⁵⁷ Copyright 2020, Springer Nature. (d) Schematic diagram of in-sensor computing architecture. (e) Schematic diagram of fully connected neural networks that are responsible for sensory signals. **S** means the stimuli response to sensory information. **R** is the sensory responsivity presented by conductance. **I** is the output current. Reprinted with permission.³ Copyright 2020, Springer Nature.

Another very important extension of neuromorphic computing based on ANNs is in-sensor neuromorphic computing architectures.²⁶³ A substantial content of AI is to interact with surrounding environments and make the machine more like human beings.²⁶⁴ Human perceives environmental variation through hearing, vision, smell, taste, and touch that are correlated with acoustic sensors,

photodetectors (or light sensors), odor sensors (or gas sensors), and chemical sensors in machine respectively. Sensory signals need to be processed by computing processors for cognitive tasks, such as pattern recognition, decision-making, chemical identification, etc. In conventional architectures, sensory units, memory units, and computing units are separated from each other, resulting in high-energy consumption due to frequent data transmission. Besides, sensing information is usually in the analogue form that is required to be transformed into the digital form for processing in digital COMS von Neumann systems, which generates a lot of redundant data and poses more pressure to memory and computing units. Analogue-to-digital converters (ADC) are necessary for transforming analogue data into digital data. This is very energy expensive and takes up large areas of computing chips. To overcome the problem, an advanced neuromorphic computing system called in-sensor computing is proposed to execute data-centric approaches.²⁶⁵ Reconfigurable sensor arrays enable sensing and computing abilities simultaneously. They can be employed to construct in-sensor neuromorphic systems implementing deep learning algorithms, as shown in **Figure 17c**. The outputs are determined by the sensory input and electronic programming operations. The illumination of sensory neural networks and corresponding matrix calculation is shown in **Figure 17d**.²⁶⁶ The output results of the vector can be described by the following equation.

$$\mathbf{I} = \begin{bmatrix} I_1 \\ I_2 \\ I_3 \\ \vdots \\ I_n \end{bmatrix} = \mathbf{R} \times \mathbf{S} = \begin{bmatrix} R_{11} & R_{12} & R_{13} & \cdots & R_{1m} \\ R_{21} & R_{22} & R_{23} & \cdots & R_{2m} \\ R_{31} & R_{32} & R_{33} & \cdots & R_{3m} \\ \vdots & \vdots & \vdots & \ddots & \vdots \\ R_{n1} & R_{n2} & R_{n3} & \cdots & R_{nm} \end{bmatrix} \begin{bmatrix} S_1 \\ S_2 \\ S_3 \\ \vdots \\ S_m \end{bmatrix} \quad \text{Eq. 29}$$

where the sensory element is described by the vector $\mathbf{S} = [S_1 \ S_2 \ S_3 \ \dots \ S_m]^T$. The responsivity of the array is presented by the matrix \mathbf{R} . The synaptic and neural characteristics in the integrated systems are sensitive to external stimuli, combining the sensory and computing processes.²⁶⁷ The computing results are measured directly governed by Kirchhoff's law, as shown below:

$$I_n = \sum_{m=1}^m I_{mn} = \sum_{m=1}^m R_{mn} S_m \quad \text{Eq. 30}$$

The responsivity of sensors is adjustable by external modulation, leading to the change of synaptic plasticity and neural spiking characteristics during the learning process. Thus, sensing and computing are combined in a single system. The in-sensor computing systems can simplify the hardware

configurations and poses low latency and high-energy efficiency. The technique shows promising prospects for autonomous vehicles, machine vision, speech recognition, and robotics.

2.3.2 Memristive-based Neuromorphic Devices

Memristive devices show promising prospects for neuromorphic systems. The modulated resistance in memristive devices usually relies on moving ions that are similar to neurotransmitter dynamics in biological neurons and synapses.²⁶⁸ The long-term potentiation and depression shown in **Figure 18a**, which is crucial for memory and learning. The conductance corresponding to synaptic weights can be modulated gradually over a certain margin, which is crucial for the training process of deep learning algorithms.²⁶⁹ The conductance modulation in neuromorphic computing systems can be described by the following equations.²⁷⁰

$$G_p = B \left(1 - e^{-\frac{P}{A_p}} \right) + G_{min} \quad \text{Eq. 31}$$

$$G_d = -B \left(1 - e^{-\frac{P-P_{max}}{A_d}} \right) + G_{max} \quad \text{Eq. 32}$$

$$B = \frac{G_{max} - G_{min}}{1 - e^{-\frac{P_{max}}{A_{p,d}}}} \quad \text{Eq. 33}$$

where G_p and G_d are the conductance, respectively. G_{max} and G_{min} are the maximum and minimum conductance, respectively. P_{max} represents the maximum number of electronic pulses. A_p and A_d are the linearities of potentiation and depression respectively. The linearity of conductance, the ratio of G_{max}/G_{min} , and the state number are crucial factors influencing computing accuracy. Moreover, excitatory/inhibitory postsynaptic currents (EPSC/ IPSC), spike-rating-dependent plasticity (SRDP), and paired-pulse facilitation (PPF) are also important synaptic properties, which can support other brain-inspired neuromorphic systems, such as Spiking neural networks (SNNs),²⁷¹ reservoir computing²⁷², Hopfield neural networks,²⁷³ etc.

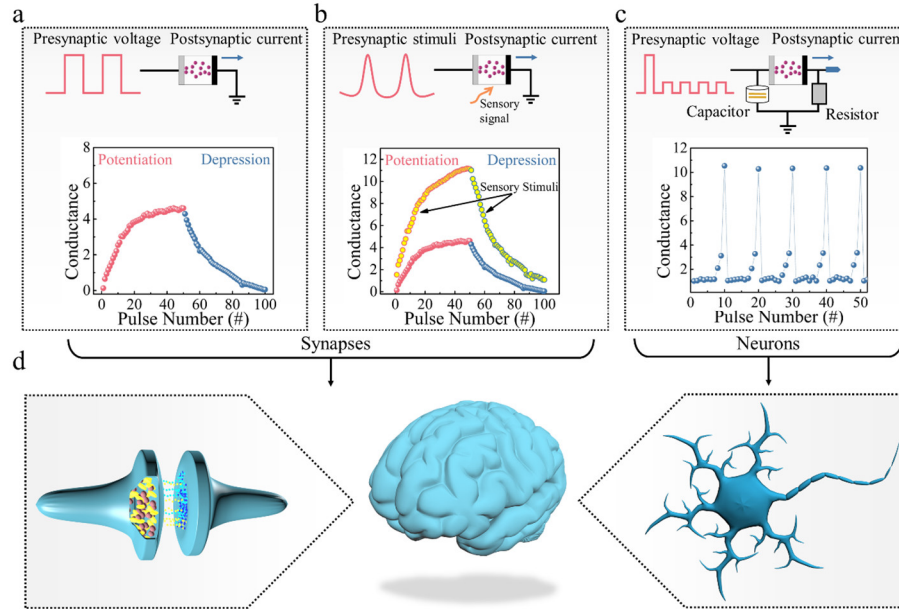


Figure 18. (a) Illustration of gradually modulated conductance that represents synaptic weights for ANNs. (b) Illustration of gradually modulated conductance that can be modulated by sensory signals for in-sensor computing. (c) Illustration of neural spiking in artificial neuromorphic systems. (d) Illustration of a biological brain consisting of synapses and neurons for information processing.

For in-sensor neuromorphic computing systems, artificial synapses show sensing and computing capabilities. One typical example is that the external stimuli change the characteristics of potentiation/depression as shown in **Figure 18b**. The modulated ratio of G_{max}/G_{min} and nonlinearity change the output results.^{274,275} In particular, mini circuits enabling sensory and synaptic abilities have been developed for in-sensor neuromorphic computing.²⁷⁶ For example, the triboelectric nanogenerator, the photodetector, and the thermoelectric module act as the mechanical, photonic, and heat receptors, respectively. Stimulated signals from sensory units are transmitted to the gate of synaptic transistors or neural circuits to realize high-level data processing.^{277,278} However, the data is required to be transmitted among different units in circuits, indicating computing energy and delay penalty. Additionally, peripheral components perplex the system and increase manufacturing costs.^{14,279,280}

Neurons integrate signals from previous neurons via synapses and generate spiking. In hardware-based neuromorphic computing systems, artificial neurons enabling neural activations are also essential for computing processes, which can be developed based on memristive devices. The currents measured

from the memristive crossbar based on VMM principles are collected by neural units. Neural activation functions can be carried out in CMOS-based arithmetic units separately, utilizing sigmoid or rectified linear unit (ReLU) functions.²⁸¹ For fully-hardware controlled neuromorphic computing systems, artificial neurons are required. Several neural models have been developed, including the Hodgkin-Huxley (HH) model,²⁸² the integrate-and-fire (IF),²⁸³ and the leaky integrate-and-fire (LIF) model.²⁸⁴ Among them, the LIF model has been widely investigated due to its simplicity, reliability, and capturing biological dynamics. The LIF neuron hardware is a combination of a “leaky” resistor term and a capacitor as shown in **Figure 18c**. The LIF neuron model can be described by the following equation:²⁸⁵

$$C \frac{dV_c(t)}{dt} = I(t) - \frac{V_c(t)}{R+R_m} \quad \text{Eq. 34}$$

where C is the capacitance. $V_c(t)$ is the voltage across the capacitor. $I(t)$ is the current input from artificial synapses. R is a series resistor. R_m is the resistance of a memristive device. Some memristive devices have parasitic capacitance possessing integrating abilities, which further simplifies the circuits.^{50,250} **Figure 18d** illustrates the biological brain consisting of synapses and neurons which are the two main building blocks for neuromorphic computing systems. More insights and understanding of neuroscience should help explore new algorithms for brain-inspired systems. Furthermore, optimized artificial synapses and artificial neurons with better performances and novel properties can also accelerate the advances of neuromorphic systems.

2.3.3 Neuromorphic Computing for Image Processing

Image processing technology is prevailing, demonstrating great demand for medical diagnosis, autonomous vehicles, human-robot interaction, smart homes, etc.²⁸⁶ However, image processing, especially for cognitive tasks, is very resource and energy expensive. Neuromorphic computing with parallel processing provides significant computing efficiency compared to conventional von Neumann counterparts. Remarkable progress has been made to process images with memristive-based neuromorphic computing.²⁵⁶ The first hardware array-level neuromorphic network was reported by Dmitri Strukov *et al.*²⁸⁷ A 12 x 12 crossbar array (Pt/Al₂O₃/TiO_{2-x}/Pt) is shown in **Figure 19a**. The integrated mini array physically performed VMM operations. This is a critical cornerstone for analog hardware with complex neuromorphic networks. Then, several expanded experimental demonstrations have been reported for neuromorphic computing.^{288–290} Convolutional neural network (CNNs) is a very

powerful architecture and shows elite abilities for image processing.²⁹¹ A fully hardware-implemented CNN was developed by He Qian *et al*, as shown in **Figure 19b**.⁵⁴ The array size consisted of 2048 devices with a high yield of 99.99%. The systems performed MNIST image recognition, reaching a high recognition accuracy of 96%. Notably, the crossbar array has the potential for high-density 3D integration that is more area efficient and benefits larger integration scales. Besides, photodetectors and processors are essential components for machine vision systems. Building a neuromorphic vision chip in a 3D vertical structure is energy-efficient and promising for edge computing applications.²⁹² As shown in **Figure 19c**, a Lego-like chip consisting of multiple neuromorphic sensors and computing processors is demonstrated.²⁹³ Different components are connected by chip-to-chip optical communication. More importantly, the hetero-integrated design has replaceable chips and ANNs for neuromorphic computing, demonstrating unparalleled adaptability.

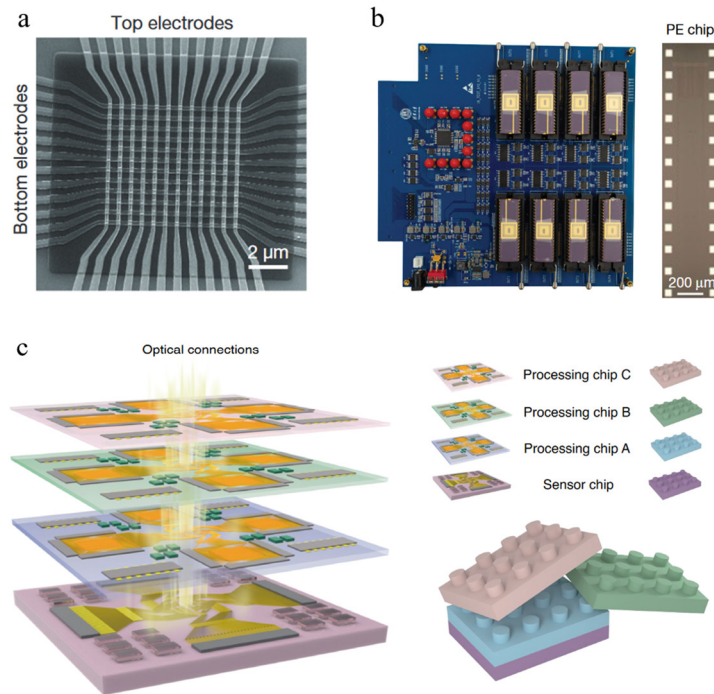


Figure 19. (a) SEM image of an integrated 12 x 12 memristive crossbar. Reprinted with permission.²⁸⁷ Copyright 2015, Nature Publishing Group. (b) Left, the photograph of a customized printed circuit board. Right, the processing element (PE) chip with a memristive array (2,048 devices) and on-chip decoder circuits. Reprinted with permission.⁵⁴ Copyright 2020, The Author(s). (c) Schematic diagram of stackable hetero-integrated chips. Reprinted with permission.²⁹³ Copyright 2022, Springer Nature.

Advanced neuromorphic computing with sensory abilities for image processing has been explored.^{294,295} Modern image sensors can efficiently capture visual signals from surrounding environments. However, a lot of redundant data is generated, and analogue-to-digital conversion is required, resulting in operation latency and high energy consumption. Besides, as the number of pixels increases, the limitation of bandwidth hinders the shuttling of data and real-time processing. A neural network photodiode array was developed to realize parallel in-sensor computing, as shown in **Figure 20a**.¹⁴ The photodiode acted as sensors and artificial synapses simultaneously, which utilized voltage-modulated photovoltaic effects. The photocurrent intensity represents synaptic weights, the integrated array can realize the VMM operations for computation tasks. This is a pioneer strategy that can be extended to other physical inputs, such as tactile,²⁹⁶ auditory,²⁹⁷ and olfactory sensing.²⁹⁶ Another type of in-sensor computing for image processing is to capture the variants from environments and identify their influence. For example, human perception accuracy is affected by humidity levels. Thus, it is desirable to explore an intelligent device that is sensitive to humidity. So, it can mimic the adaptive behavior of human eyes in different environments. As shown in **Figure 20b** and **c**, the characteristics of artificial synapses constructing ANNs were adjusted by moisture.²⁷⁴ And the pattern recognition accuracy was modulated at different humidity levels. This technique reduced the circuitry complexity of traditional neuromorphic visual systems. It contributed to the promotion of developing artificial intelligence at a device level. Temperature is another key factor for AI systems. So far, intelligent sensory devices (also referred to as intelligence matter) enabling temperature and humidity sensations simultaneously for in-sensor neuromorphic computing have not been reported yet. Hence, designing and constructing two-terminal in-sensor computing devices with intelligent temperature and humidity sensations are attractive for advanced AI applications. Machine visions usually need front-end image processing (image sensing, image preprocessing) and back-end computational processing (cognitive pattern recognition, motion tracking, decision-making, etc.). The limitation of acquired progresses merely worked at one aspect of front-end image sensing or back-end computing.²⁹⁸⁻³⁰⁰ Developing a monolithic neuromorphic machine vision system that mimics the biological retinomorph vision poses enormous potential to avoid bulky architectures, decrease fabrication costs, and improve energy efficiency. **Figure 20d** presents a monolithic machine vision system enabling sensing and neuromorphic computing abilities.³⁰¹ A ferroelectric-semiconductor-transistor was employed due to broadband photo-response and linearly programmable plasticity. The technique demonstrated the

feasibility of sensing and computing. Notably, image preprocessing, such as contrast enhancement, feature extraction, and image compression, is a crucial step for image processing. While a monolithic visual system based on one device with front-end retinomorphic image sensing, convolution processing, and back-end neuromorphic computing, has not been reported. The technology poses very promising prospects for advanced neuromorphic machine visions.

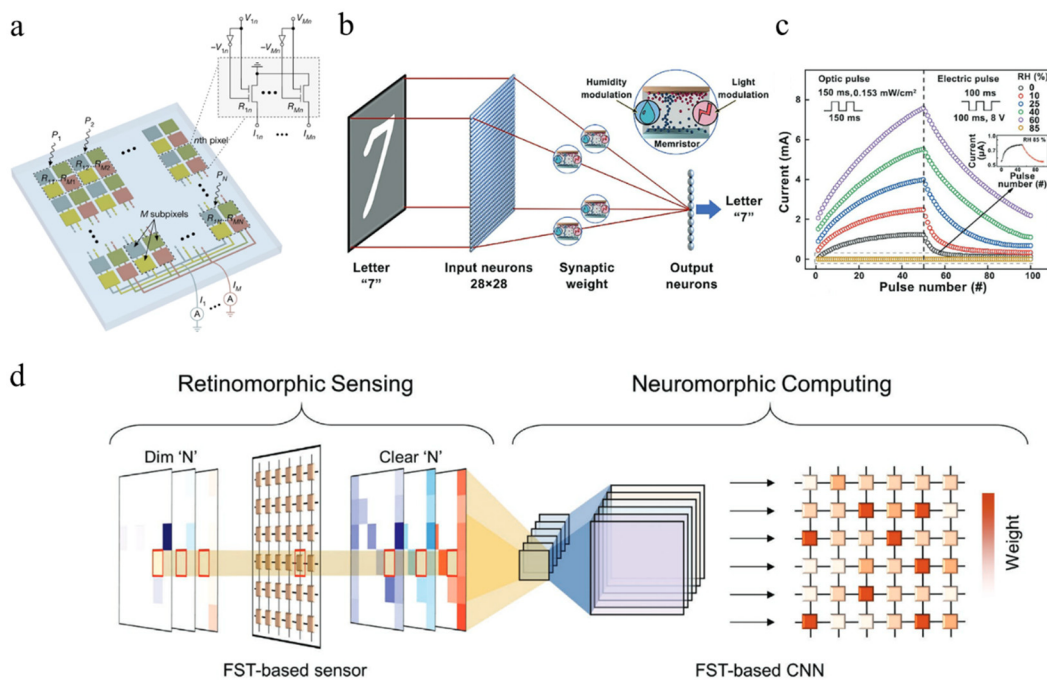


Figure 20. (a) Schematic diagram of an artificial neural network (ANN) photodiode array and the circuit of a single pixel. Reprinted with permission.¹⁴ Copyright 2020, The Author(s). (b) Schematic diagram of the in-sensor computing with memristive devices sensory to humidity. (c) The modulated characteristic of artificial synapses by moisture. Reprinted with permission.²⁷⁴ Copyright, 2021 Wiley-VCH GmbH. (d) Schematic diagram of a memristive-based machine vision system enabling sensing and neuromorphic computing abilities. Reprinted with permission.³⁰¹ Copyright, 2022 Wiley-VCH GmbH.

Chapter 3. Versatile Memristor for Memory and Neuromorphic Computing

The memristor is a promising candidate to implement high-density memory and neuromorphic computing. Based on the characteristic retention time, memristors are classified into volatile and non-volatile types. However, a single memristor provides a specific function based on electronic performances, which poses roadblocks for further developing novel circuits. Versatile memristors exhibiting both volatile and non-volatile properties can provide multiple functions covering non-volatile memory and neuromorphic computing. In this work, a versatile memristor with volatile/non-volatile bifunctional properties was developed. Non-volatile functionality with a storage window of 4.0×10^5 was obtained. Meanwhile, the device can provide threshold volatile functionalities with a storage window of 7.0×10^4 and a rectification ratio of 4.0×10^4 . The leaky integrate-and-fire (LIF) neuron model and artificial synapse based on the device have been studied. This versatile memristor enables non-volatile memory, selectors, artificial neurons, and artificial synapses, which will provide advantages regarding circuit simplification, fabrication processes, and manufacturing costs.

3.1 Introduction

Modern computers need higher-density memory and more effective computation for integration into numerous areas of societal importance, including healthcare, education, and the economy. The memristor has been investigated to develop memory and computation systems due to its fast operation speed, low energy consumption, and small feature size.³⁰² A memory density of up to 4.5 terabits per square inch was reported with a single-layer configuration, which is comparable to that of multilevel 3D-NAND flash memory.⁷ The memristor is also considered an excellent emulator of biological synapses and neurons that are fundamental elements for brain-inspired neuromorphic computing.³⁰³ The novel memory and computation systems can revolutionize the current computer capacity.^{304,305}

Versatile memristors enabling multiple functions simultaneously are attractive for memory and computing systems. So far, few previous reports have addressed versatile memristors. A single type of memristor taking multiple roles in circuits can provide many advantages in terms of circuit simplification, lowering energy consumption, and lowering manufacturing costs.^{274,306} Memristors are classified into non-volatile memory switching (MS) and volatile threshold switching (TS) based on the retention time.³⁵ In the non-volatile MS, both LRS and HRS can be maintained for a long time after

removing the bias until a SET voltage or a RESET voltage is applied to modulate resistance states. In comparison, the volatile TS cannot maintain the LRS after the voltage is removed.^{11,90} The non-volatile MS shows promising prospects in developing high-density memory and in-memory computing.³⁰⁷ On the other hand, the volatile TS can be employed for synapse emulators, selectors, hardware security, and artificial neurons.^{11,308} Interestingly, Min Ji Yu et al. demonstrated memristive devices based on a Ag/Ag-GeTe/Ag structure, which can provide multi-functions of memory, selectors, and artificial synapses.³⁰⁹ However, the concentration of Te needs to be adjusted for different electronic functions. Volatile/non-volatile bifunctional memristors may endow chips with both data storage and computing abilities, indicating great prospects in novel circuits. For advanced data storage, a single system with volatile/non-volatile bifunctional memristors can provide both volatile and non-volatile performance, enabling multifunctional data processing strategies. Furthermore, bifunctional memristors can mimic both functions of artificial synapses and neurons for neuromorphic computing. The reported volatile/non-volatile bifunctional memristors with one or two functions have been studied, as shown in **Table 3**.³¹⁰⁻³²⁷ However, versatile memristors covering multiple functions, such as non-volatile memory, selectors, artificial neurons, and artificial synapses have not been investigated. It is difficult to guarantee large storage windows (both volatile and non-volatile models), excellent endurance, and multiple functions simultaneously. More efforts regarding materials selection, device structure design, fabrication process, and physical models are needed to develop versatile memristors for multi-function circuits.

To obtain volatile/non-volatile bifunctional memristors, the dynamics of Ag and Cu in the dielectric layer (switching layer) are crucial.³²⁸ Particularly, the switching layer significantly influences the diffusion of Ag or Cu ions, which is vital for both short- and long-term resistive switching properties.³²⁹ CuInSe₂ (CISE) has been extensively investigated in thin-film solar cells due to its excellent electronic and optical properties. Previous experimental results reported that Ag ions show good diffusivity in CISE layers.^{330,331} Besides, the injected Ag atoms can be stably reserved instead of reacting with the CISE host material, which is also crucial for reversible resistive switching behaviors. Therefore, we hypothesize that the dynamics of Ag ions in the CISE can be explored to develop CISE-based versatile memristors.

Table 3. The summary of the memristors with multiple functions. Vol-R means the ratio of volatile HRS/LRS. Vol-C means volatile switch cycles. N-Vol-R means the ratio of non-volatile HRS/LRS. N-Vol-C means non-volatile switch cycles. N-Ret means non-volatile retention time.

Device structure	Vol-R	Vol-C	N-Vol-R	N-Vol-C	N-Ret	Applications	Ref.
Ag/CuInSe ₂ /Mo	7×10 ⁴	400	4×10 ⁵	160	10 ⁴ s	Synapse, neuron, selector, memory	this work
Cu/TaO _x /δ-Cu/Pt	10 ²	***	10 ⁵	***	10 ⁶ s	Memory	310
Au/Ti/h-BN/Cu	***	50	10 ⁵	50	120 s	Synapse, memory	311
Ag/HfO ₂ /Pt	10 ⁵	300	10 ⁵	300	2×10 ⁴ s	Synapse, memory	312
Cu/ZrO ₂ /TiO ₂ /Ti	***	***	10 ²	100	10 ⁴ s	Selector, memory	313
Ag/IGZn/MnO/Pt	10 ³	200	10 ⁶	200	5×10 ⁴ s	Selector, memory	314
Cu/ZrO ₂ /Pt	10 ²	100	10	100	10 ⁴ s	Selector, memory	315
Cu/ZnO ₂ /ZnO/ITO	10	100	40	100	10 ⁴ s	Memory	316
Cu/SiO _x /p ⁺ Si	45	50	10 ³	50	10 ⁵ s	Synapse, memory	317
Ag/AlZS/TiO ₂ /Pt	10 ⁵	200	10 ⁵	120	10 ⁴ s	Synapse, memory	318
Au/Ti/TiO ₂ /Hf/Au	10 ⁵	***	10 ²	30	2×10 ³ s	Selector, memory	319
Ag/CoFe ₂ O ₄ /Pt	10 ²	100	10 ³	500	10 ³ s	Selector, memory	320
Ag/MXene/SiO ₂ /Pt	***	100	10 ³	100	10 ⁴ s	Synapse, memory	321
Cu/AlN/TiN	***	***	10	100	10 ⁴ s	Synapse, memory	322
Al/MnO ₂ /steel	***	***	***	500	10 ⁴ s	Synapse, memory	323
Pt/Co ₃ O ₄ /Pt	***	***	***	75	10 ³ s	Synapse, memory	324
Al/Ti ₃ C ₂ /Pt	***	***	6×10 ³	1000	10 ⁴ s	Synapse, memory	325
Ag/CNT/TiO ₂ /FTO	***	***	100	500	10 ⁴ s	Synapse, memory	326
Pt/NCO/Pt	***	***	***	100	10 ⁴ s	Synapse, memory	327

Here, a versatile memristor (Ag/CuInSe₂/Mo) array was demonstrated. Non-volatile functionalities with a storage window of 4.0×10^5 and a retention time of 10,000s were obtained, which can be used for non-volatile memory. Meanwhile, the device can provide diode-like volatile functionalities with a storage window of 7.0×10^4 and a rectification ratio of 4.0×10^4 . This feature enables the device to be potentially utilized as selectors integrated with non-volatile memristors to alleviate sneak currents. The device can be operated for 400 switching cycles, ensuring a mean HRS/LRS ratio of over 10^4 . The LIF neuron model due to its neuron-like threshold switching and artificial synaptic properties were investigated, demonstrating the applications of neuromorphic computing. The versatile memristor can play multiple roles in non-volatile memory, selectors, artificial neurons, and artificial synapses. The results will benefit the development of advanced data storage and neuromorphic computing systems.

3.2 Experimental Section

3.2.1 Device Fabrication

The proposed devices were fabricated by magnetron sputtering and electrodeposition methods. The fabrication flow chart is shown in **Figure 21**. The glass was used as substrate. Note, substrates with similar characteristics are all practicable for the fabrication process, including the silicon wafer covered by SiO₂ oxide film and some flexible substrates. The bottom Mo electrode was deposited by DC sputtering (ATC ORION SERIES SPUTTERING SYSTEMS). The patterned Mo electrode was obtained with the help of a shadow mask. Then, the electrodeposition was used to deposit the CISE thin film as a switching layer. For the solution preparation, 2.5 mM CuCl₂·2H₂O, 240 mM LiCl, 2.4 mM InCl₃, and 4.5 mM H₂SeO₃ were dissolved in deionized water. Chemicals were purchased from Sigma-Aldrich. The electrolytic bath was buffered with a pHydrion buffer (pH 3.00). HCl drops were used to tune the solution pH to 2 - 3. After the deposition of the CISE switching layer, Ag strip electrodes were deposited by DC sputtering with the help of a shadow mask to form a crossbar configuration.

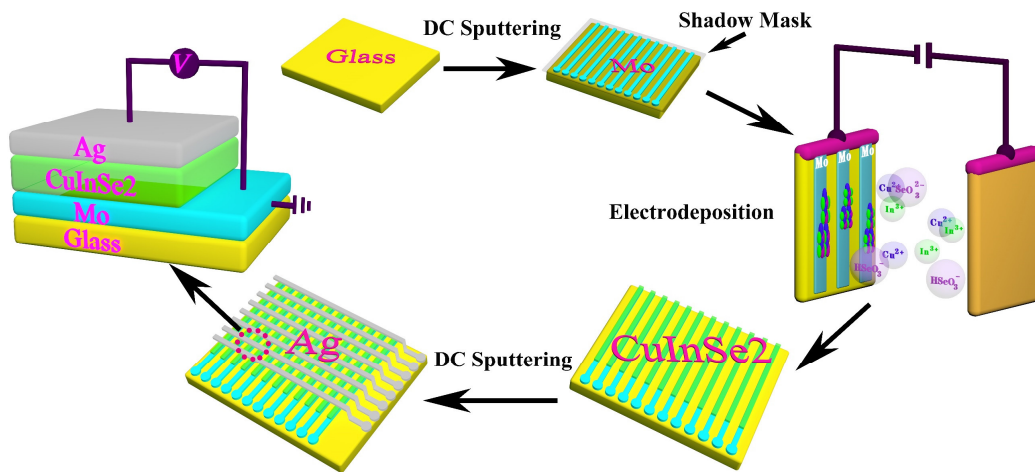


Figure 21. The fabrication process of the Ag/CISE/Mo memristor with a crossbar configuration.

Electrodeposition was carried out using an electrochemical workstation (CHI Model 660E Series Electrochemical Analyzer/Workstation) with a conventional 3-electrode setup. During the depositing process, a constant cathodic potential was applied to the working electrode. The deposition of compound CISE thin films is related to the individual chemical reactions.³³² Selenide compounds can

directly occur due to large formation energies (ΔG : e.g., -386 kJ/mol for In_2Se_3 , -10^4 kJ/mol for Cu_2Se). It is hard to directly electrodeposit In metal from a single-bath solution. However, it is easy to co-deposit compounds, such as Cu_2Se , In_2Se_3 , and CuInSe_2 .³³³

The cyclic voltammetry (CV) test over the range of 0 V to -1 V was done to study the chemical reactions in the bath. CV curves in the electrolytic bath are shown in **Figure 22a**. For the first cycle, the small peak at approximately -0.1 V was attributed to the reaction of Se. Then, strong peaks corresponding to the generation of Cu, CISE, and H_2 showed up. From the second cycle to the tenth cycle, the intensity of reduction peaks was decreased, especially for the reduction of Cu and H_2 . This phenomenon is because the deposited film covering the work electrodes increased the resistance.³³⁴ Under the same potential, higher resistance corresponds to smaller current intensities. The hydrogen evolution was suppressed after the first cycle, which benefits the adhesiveness of the deposited thin film on substrates.³³⁵ The CISE film was formed after the negative potential of -0.66 V (vs. Ag/AgCl). Therefore, the potential was set at -0.66 V for the CISE deposition.

A typical current-time (I-t) curve is shown in **Figure 22b**. At the very beginning of the deposition, the absolute value of current sharply decreased from about 6 mA to 0.7 mA within 50 s. This phenomenon is due to the forming of CISE on the surface of the Mo electrode, which significantly increased the overall resistance.³³⁶ Notably, the current remained almost constant after the first 50 s. The small current variance indicates stable electrochemical reactions and film growth. During the electrodeposition, two phases contribute to the interface where film growth occurs.³³⁷ One phase is the solution carrying ions toward the working electrode. Another phase is the boundary of the substrate covering the conductive coating that carries electrons. When the potential of the working electrode shifts from the equilibrium values to negative potentials. The reduction reactions of ions conveyed by the solution occur if a suitable potential is provided.³³⁸ This working mechanism determines that only the areas covered by Mo electrodes can grow CISE film, enabling the direct construction of switching layers on specific patterns.³³⁹ The deposition rate was approximately 23 nm/min. CISE film only grew on the patterned bottom electrode. Decreasing manufacturing costs and materials consumption are crucial for practical large-scale production. The electrodeposition endows remarkable advantages in terms of costs, deposition rates, morphology control, film uniformity, and template-based structure fabrication.³³⁷ Moreover, this method enables high utilization efficiency of materials because all reacted

elements are utilized to form films. This technique paves the way to construct integration arrays with high materials utilization efficiency and low manufacturing costs.

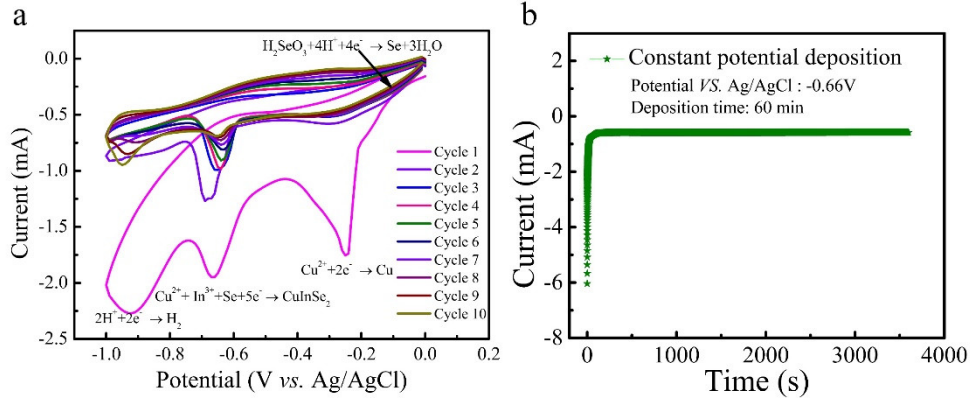


Figure 22. (a) Cyclic voltammetry (CV) curves in an electrolytic bath for CISE deposition. The scan rate was 20 mV/s. (b) Electrodeposition current versus time during the depositing process.

3.2.2 Materials and Device Characterization Methods

The optical micrograph was taken by an Oxford BX51M optical microscope and measurements were carried out by the ImageJ software. The morphology of CISE films was examined by Scanning Electron Microscopy (SEM, UltraPlus FESEMs) at the acceleration voltage of 10 kV. The composition of the thin film was measured by Energy Disperse Spectroscopy (EDS, UltraPlus FESEMs). To analyze the crystal structure of deposited films, Raman spectrum analysis was carried out by a Renishaw micro-Raman spectrometer with a laser wavelength of 633nm (red, He-Ne). Grazing Incidence Xray Diffraction (GIXRD) on the CISE thin film was carried out using the PANalytical X'Pert PRO system (CuK α irradiation, $\lambda = 1.5406 \text{ \AA}$). The surface valence states of the CISE thin film were measured by X-ray photoelectron spectroscopy (XPS, Thermo-VG Scientific ESCALab 250). The electrical characterization of the prepared devices was performed with a 4200A-SCS Parameter Analyzer equipped with the probe station of MPI TS150. The test diagram can be found in **Figure 21**.

3.2.3 Simulation Methods

Simulation method for LIF neurons: The circuit was designed to demonstrate the functionalities of the LIF neurons based on the Ag/CISE/Mo device. The theoretical model of the Ag/CISE/Mo device was developed in Verilog-A based on experimental data under the volatile model. The key parameters

were extracted from experimental data, including HRS, LRS, V_{SET} , and V_{RESET} . The model can capture the resistive switching and volatile features of the actual device. The volatile memristor model was used in the LIF neuron circuit built up in the Cadence Virtuoso platform. The neuron circuit design is shown in **Figure 23**. Three artificial synapses were integrated into the circuit. A capacitor, a resistor, and an Ag/CISe/Mo memristor were used to mimic the function of neurons. The specifications of components employed in the circuit are listed in **Table 4**.

Table 4. Component parameters used in the LIF neuron simulation.

Component parameter	Frequency Simulation	Amplitude simulation
V_{IN1}	Amplitude = 1 V Period = 400 μ s (2.5 KHz) Pulse width = 3 μ s Delay = 0.3 ms	Amplitude = 0.8 V Period = 100 μ s (10 KHz) Pulse width = 3 μ s Delay = 0.3 ms
V_{IN2}	Amplitude = 1V Period = 200 μ s (5 KHz) Pulse width = 3 μ s Delay = 6.7 ms	Amplitude = 1V Period = 100 μ s (10 KHz) Pulse width = 3 μ s Delay = 3.3 ms
V_{IN3}	Amplitude = 1 V Period = 100 μ s (10 KHz) Pulse width = 3 μ s Delay = 13.1 ms	Amplitude = 1.2 V Period = 100 μ s (10 KHz) Pulse width = 3 μ s Delay = 6.3 ms
$R1, R2, R3$	140 M Ω	150 M Ω
MI	LRS resistance = 2 M Ω with $V_{SET} = 0.8V$ HRS resistance = 300 G Ω Transition time from LRS to HRS, 400 μ s Transition time from HRS to LRS, 10 μ s	
$SW1, SW2, SW3$	Ideal switches that are closed only if the corresponding V_{IN} is not at 0 V. They are used for simulating a current injection.	

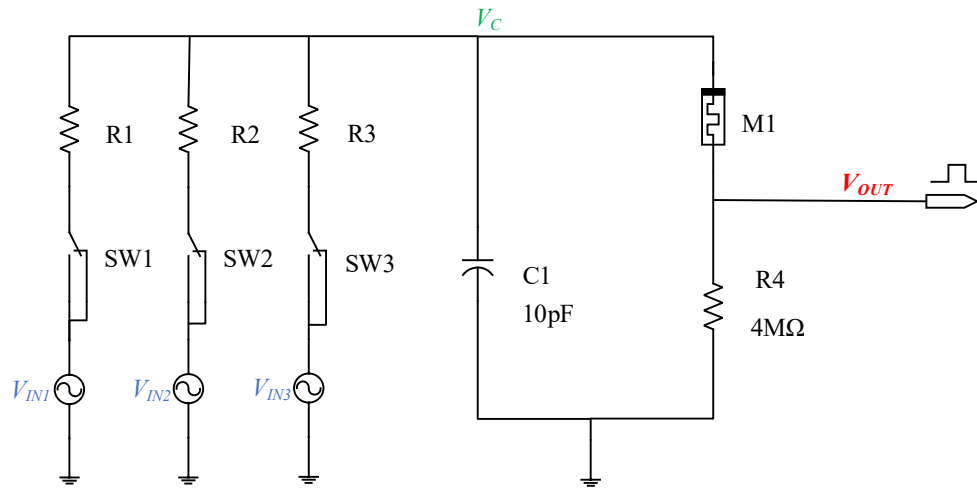


Figure 23. Circuit design for the simulation of artificial LIF neurons. The simulation was carried out on the Cadence Virtuoso platform. SW1-3 are switches. R1-4 are resistors. M1 is a threshold switching (TS) memristor.

Pattern recognition simulation: The recognition simulation was carried out on the CrossSim platform written with Python.^{340,341} The numerical weights in the network were mapped onto the tested device conductance states. The nonlinearity and asymmetry of potentiation/depression curves were considered. The cycle-to-cycle variability was considered Gaussian noise during the simulation process. The conductance (weight) updating was based on the average value of conductance change (under a single pulse) with different initial conductance (G_0). A neural network with the size of $64 \times 40 \times 10$ was constructed to implement a backpropagation algorithm. The UCI small images were used as data set for training and testing processes.³⁴² The neural network was trained for 30 epochs to get saturated accuracy.

3.3 Results and Discussion

3.3.1 Materials Characterizations

Figure 24a presents the optical micrograph of the device. The left image in **Figure 24a** shows the patterned Mo bottom electrode with a width of approximately $50 \mu\text{m}$. The Mo electrode covered with the CISE film is shown in the right image in **Figure 24a**. Only the areas covered with the Mo layer grew CISE, demonstrating a high materials utilization efficiency. The cross-section scanning electron microscopy (SEM) image is exhibited in **Figure 24b**. The thickness of the CISE thin film was

approximately 400 nm. The good adhesiveness exhibited in the image benefits electrical performance. To investigate the composition of the deposited CISE film, energy-dispersive X-ray spectroscopy (EDX) mapping is shown in **Figure 24c**. The composition deviated slightly from the stoichiometric ratio (Cu : In : Se = 1 : 1 : 2).³⁴³ Atomic percentages of Cu and In are lower than the stoichiometric ratio (25%), meanwhile, a slightly high content of Se was obtained.

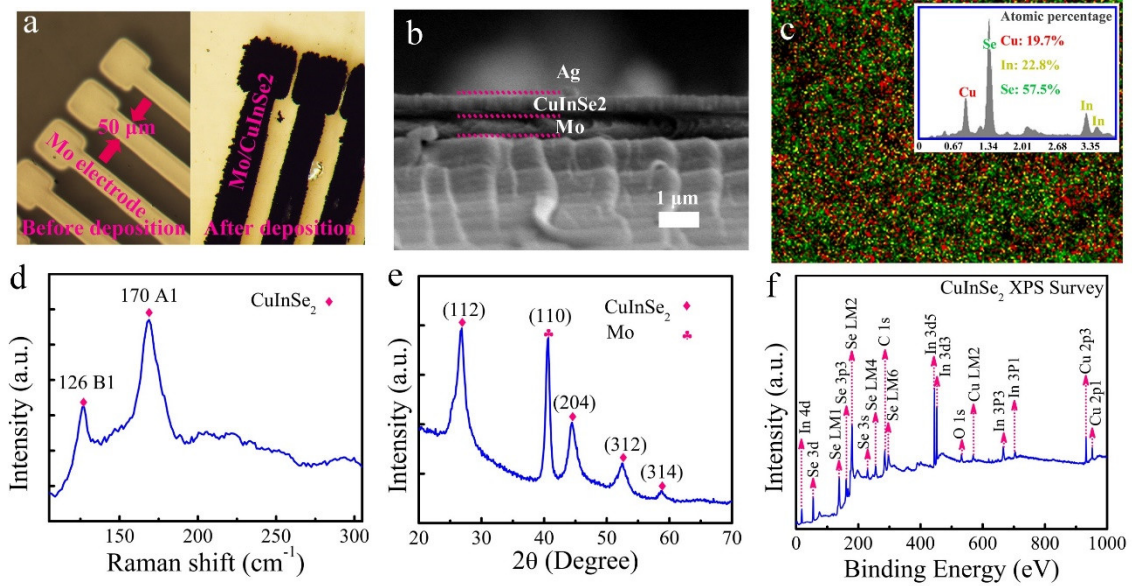


Figure 24. Materials characterizations on the Ag/CISE/Mo device. (a) Optical micrograph of the device. (b) Cross-section SEM image of the device with a sandwich structure. (c) Surface composition EDX mapping of the deposited CISE thin film. The inset table presents the composition percentage (d) Raman spectrum of the deposited CISE. (e) The GIXRD spectrum of the CISE/Mo. (f) Wide-scan XPS spectrum of the CISE thin film.

The Raman spectrum, GIXRD, and XPS were employed to investigate the crystalline structure and surface chemical states of the CISE. The Raman spectrum is shown in **Figure 24d**. The A1 vibration mode at 170 cm^{-1} and B1 vibration mode at 126 cm^{-1} were observed, corresponding to the tetragonal CISE structure.³⁴⁴ The GIXRD spectrum is shown in **Figure 24e**. The characteristic peaks of tetragonal CISE at 26.6° , 44.1° , 52.4° , and 59.7° corresponding to the (112), (204), (312), and (314) planes respectively (JCPDS file: 03-065-4869) were found.³⁴⁵ The GIXRD confirmed the crystalline structure of CISE, which was consistent with the Raman Spectrum result. Meanwhile, a strong peak at 40.5° was observed. This peak is assigned to the (110) plane of the Mo electrode (JCPDS file: 01-089-5156). The

surface chemical states of CISE were analyzed by XPS. The wide-scan XPS spectrum of the CISE thin film is exhibited in **Figure 24f**. The characteristic peaks of Cu 2p, In 3d, and Se 3d can be observed. High-resolution XPS spectra of the three main elements are shown in **Figure 25**. The Cu 2p peaks were located at 932.16 eV ($2p_{3/2}$) and 952.09 eV ($2p_{1/2}$) with a splitting orbital of 19.9 eV. This result confirmed the oxidation state of Cu was +1.³⁴⁶ Meanwhile, the peak positions of In were 444.75 eV ($3d_{5/2}$) and 452.3 eV ($3d_{3/2}$), indicating the oxidation state of In⁺³. The Se 3d peak at 54.71 eV ($3d_{5/2}$) and 55.53 eV ($3d_{3/2}$) demonstrated that the valance state of Se was -2.³⁴⁶ Additionally, two impurity peaks at 284.69 eV and 531.6 eV indicated the contamination of carbon and oxygen due to the sample exposure to the atmosphere.³⁴⁶

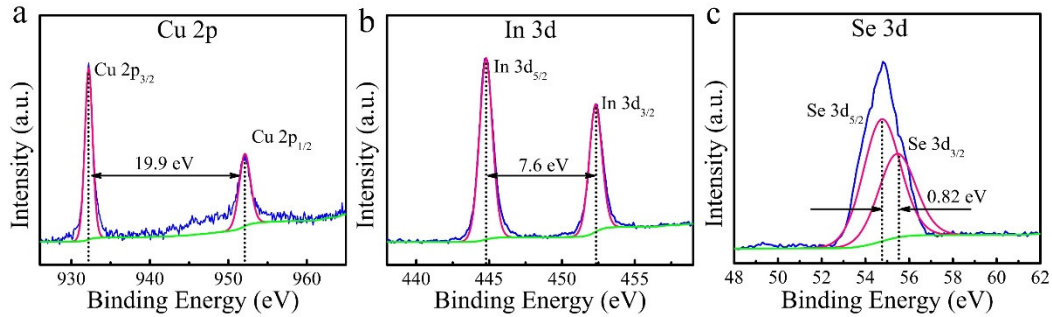


Figure 25. High-resolution XPS spectra of different regions: (a) Cu 2p region; (b) In 3d region; (c) Se 3d region. The results confirm the chemical states of Cu, In, Se are +1, +3, -2, respectively¹⁵.

Moreover, the permittivity ϵ of the CISE film was measured based on electrochemical impedance spectroscopy (EIS).³⁴⁷ To avoid the influence of Ag atoms, the EIS of the CISE was measured based on the Mo/CISE/Mo device. The Nyquist plot and Bode plot are shown in **Figure 26**. According to the Nyquist plot (**Figure 26a**), two separated semicircles were observed, corresponding to the bulk capacitor and the grain boundary capacitor.³⁴⁸ The Bode plots and fitting curves of modulus ($|Z|$) vs. frequency (f) and phase vs. frequency (f) are shown in **Figure 26b** and **Figure 26c** respectively. The equivalent circuit for fitting is shown in **Figure 26d**. R_s is the series resistor that corresponds to the series resistance on electrodes. The constant-phase elements (CPE) are described in **Eq. 35**:³⁴⁷

$$Z_{CPE} = \frac{1}{Q(j\omega)^n} \quad \text{Eq. 35}$$

Where Z_{CPE} is the impedance of the CPE. Q is a constant. j represents the imaginary number. ω represents the angular frequency ($\omega = 2\pi f$, f is the frequency). n represents a constant relating to the

angle of a capacitive line's rotation on complex plane plots. The fitting process was executed on the ZView2 software. The solid lines shown in **Figure 26** are fitting curves that matched well with experimental results. According to the fitting results, the capacitance can be calculated by the following **Eq. 36**.³⁴⁹

$$C = (R^{1-n}Q)^{\frac{1}{n}} \quad \text{Eq. 36}$$

where C is capacitance, R is the resistance value of parallel resistance. n and Q are fitting parameters. The assignment of the two semicircles was according to the magnitude of the capacitance.³⁴⁸ Based on the “brickwork” model, the capacitance value derived from bulk (grain) falls in the order of 10^{-10} F. Meanwhile, the capacitance value derived from the grain boundary ranges from 10^{-9} F to 10^{-6} F. In this work, the C_1 (based on $R_1//CPE_1$) was 6.0×10^{-11} F which corresponded to the bulk (grain) capacitor. The C_2 (based on $R_2//CPE_2$) was 2.3×10^{-9} F which corresponded to the grain boundary capacitor. The permittivity is calculated with **Eq. 37**.³⁵⁰

$$\varepsilon = \frac{4\pi KdC}{S} \quad \text{Eq. 37}$$

Where ε is permittivity. K is electrostatic constant. d is the thickness. S is the area. The permittivity ε of 7.9 was calculated. The permittivity value slightly deviated from the reported value of 13.6 ± 0.8 due to the different status of the material, including composition, crystalline status, fabrication process, etc.³⁵¹ The materials characterization results confirm that the single CISE phase has been formed by the single-bath electrodeposition at room temperature. The electrodeposition can construct CISE-based memristor arrays, which shows remarkable advantages. The electrodeposition process is much cheaper than vacuum-based processes. In addition, electrodeposition is based on oxidation/reduction processes on the electrodes driven by electrical potentials. The film selectively grows on areas where charge exchange occurs. This method enables high utilization efficiency of materials because all reacted elements are utilized to form films.

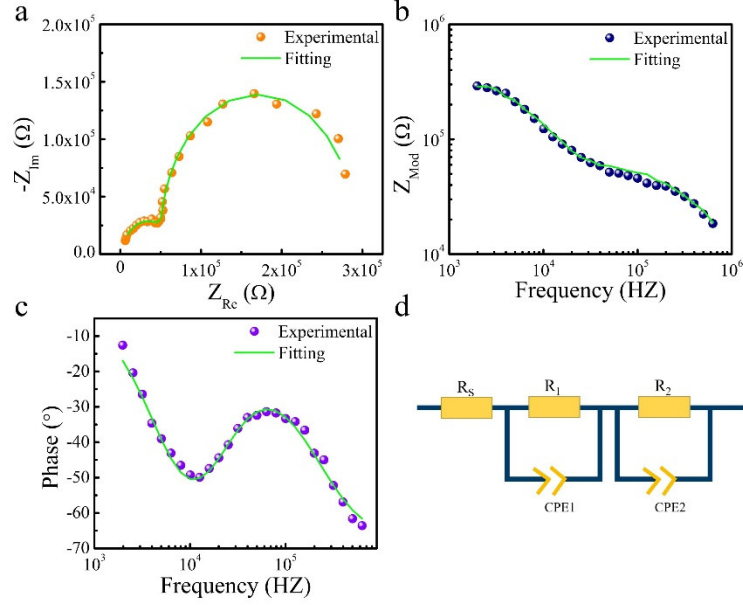


Figure 26. Impedance analysis. (a) Nyquist plot of CISe at room temperature. (b) The plot of the Modulus vs Frequency. (c) The plot of the Phase vs Frequency. (d) The equivalent circuit for fitting.

3.3.2 Resistive Switching Behaviors

A systematic analysis of resistive switching behaviors was implemented. The DC switching cycle test under different CCs is shown in **Figure 27a**. The voltage swept from -3 V to 3V. The pristine device showed high resistance. When the voltage swept from 0 V to 3 V, the current abruptly increased with a voltage of approximately 0.9 V. The device switched from the original HRS to LRS, corresponding to a SET process. As the voltage swept from 3 V to 0 V, the I-V curves under different CCs showed different characterizations. For the $CC \leq 10^{-4}$ A, the device switched back to the HRS spontaneously when the applied voltage stress was close to zero, demonstrating a signature feature of volatile TS performance.³⁵ In comparison, the device switched back to the HRS under the negative region when higher CCs were applied. The result means that the LRS can be maintained after the voltage was removed and a negative voltage was required to RESET the device, indicating a non-volatile MS performance.³⁵ Additionally, the RESET voltage shifted from positive to negative with the increase of CCs, demonstrating the transition from the volatile TS to the non-volatile MS.³⁵² **Figure 27b** exhibits the probability for volatile TS as a function of CCs. The device can be switched between volatile TS and non-volatile MS modes by controlling the CCs.

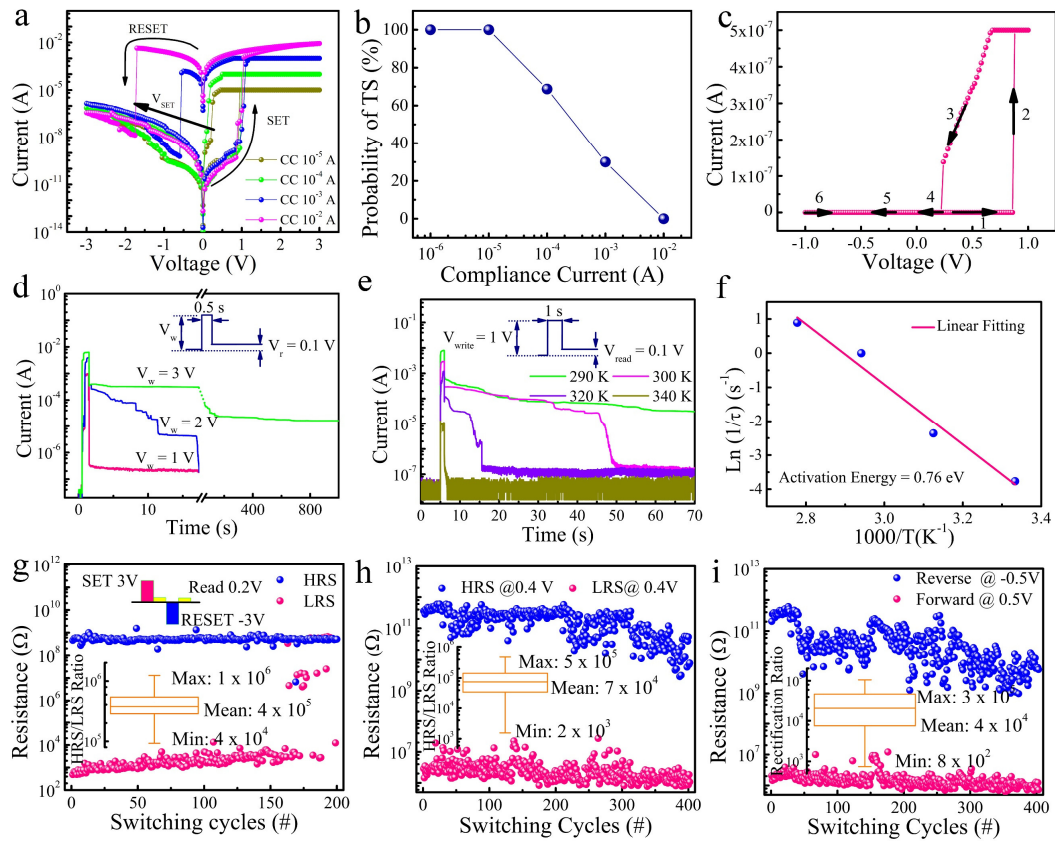


Figure 27. Systematic analysis on resistive switching. (a) Typical I-V curve of the device under different CCs. (b) Probability for volatile TS as a function of CC. (c) Typical I-V curve of the device under a linear scale over the sweep voltage of -1 V to 1 V. (d) Retention time under different voltage amplitudes. (e) Retention time under different temperatures. (f) The Arrhenius plot of the retention time depending on the temperature. (g) Non-volatile switching under a pulsed-voltage operation. The operation voltage pulse was ± 3 V with a duration of 1 s. The read voltage was 0.2 V. The duty cycle of the pulse was 50%. The box plot was based on the first 165 cycles. (h) The HRS/LRS resistance distribution over 400 switching cycles. The data was extracted from the result of the DC switching cycle test. The sweep voltage was -1 V to 1 V. (i) The distribution of the device resistance under forward and reverse biasing over 400 switching cycles.

Moreover, I-V curves and RESET voltage changes over the different thicknesses of CISE layers are shown in **Figure 28**. Under the same voltage stress, devices evolved from non-volatile to volatile characteristics when increasing the thickness of CISE, which was attributed to the different accumulations features of Ag atoms. Thicker and stronger conductive filaments were easier to form in

thinner switching layers, resulting in the RESET voltage shifting to negative regions. The non-volatile MS characteristics demonstrate the application for non-volatile memory. In the non-volatile mode, the HRS/LRS resistance distributions over 70 operation cycles (DC switching cycle test, the voltage swept from -3 V to 3 V) are shown in **Figure 29a**. An HRS/LRS ratio of 9×10^6 (Mean value) was obtained. Notably, the device can provide diode-like volatile properties (**Figure 27c**). When the voltage swept from 0 V to 1 V, the current abruptly increased under the voltages of approximately 0.9 V. The device switched from HRS to LRS, corresponding to a SET process. As the voltage swept from 1 V to 0 V, the LRS transformed to HRS under the voltages of approximately 0.2 V spontaneously, corresponding to a RESET process. This diode-like feature can be used as a selector that co-integrates with non-volatile memory devices to suppress sneak currents in crossbar arrays.³⁵³ Besides, the volatile properties indicate promising prospects as artificial neurons.

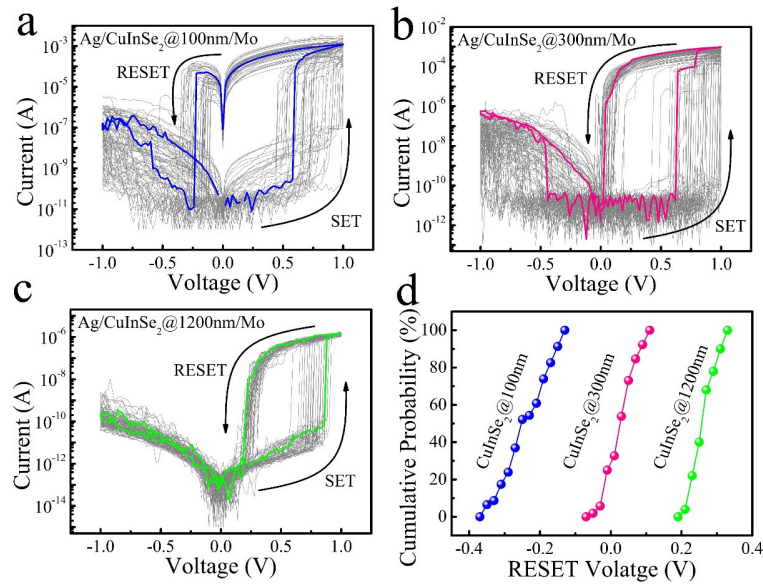


Figure 28. I-V curves and RESET voltage change over different thicknesses of CISe layers. Each device operated for 50 cycles. (a) I-V curves of the device Ag/CuInSe₂@100nm/Mo. (b) I-V curves of the device Ag/CuInSe₂@300nm/Mo. (c) I-V curves of the device Ag/CuInSe₂@1200nm/Mo. (d) The cumulative probabilities of the RESET voltages for the devices with different CISe thicknesses.

The retention time of the Ag/CuInSe/Mo device under different voltages and temperatures has been studied. To measure the retention time, a short pulse was used to switch the device to the LRS. Then, a small read voltage of 0.1 V was applied to monitor the resistance evolution. The influence of pulse

voltage amplitudes on the retention time was studied, as shown in **Figure 27d**. When using the operation-pulse voltage of 1.0 V, the device went back to the HRS closely following the end of the pulse. In comparison, when the voltage was 2.0 V, the retention time extended to approximately 17 s. More interestingly, the retention time was significantly extended when the pulse voltage amplitude was 3.0 V. As shown in **Figure 29b**, the LRS can be maintained for over 10,000 s when a pulse voltage of 3.0 V with a pulse duration of 1 s was applied, demonstrating non-volatile switching characteristics.³⁵⁴ This was because the higher voltage and longer pulse duration induced thicker and stronger conductive filaments due to more Ag atoms being pumped into the switching layer.³⁵⁵ Those stable Ag conductive filaments had a long lifetime and led to a long retention time. **Figure 27e** shows the retention time under different temperatures. The retention time decreased with the increase of temperatures. This is due to the increased mobility of Ag atoms at higher temperatures.³⁵⁶ Hence, the conductive filaments are easier to rupture and lead to the resistance states transition, which is consistent with previously reported results.⁴⁷ The Arrhenius plot of the relaxation time vs temperature is shown in **Figure 27f**. The Arrhenius equation is used to analyze the relationship between rate constants and temperature. Here, it is used to investigate the minimum energy of molecules reaction, which is related to the interaction of Ag atoms and host materials.³⁵⁷ The Arrhenius equation is shown below:

$$k = Ae^{-\frac{E_a}{k_B T}} \quad \text{Eq. 38}$$

where k is the rate constant that equals $1/\tau$; τ is the retention time of LRS. A represents the pre-exponential factor, k_B represents the Boltzmann constant. E_a represents the activation energy. T represents the temperature. Taking a natural logarithm on the previous **Eq. 38** gives **Eq. 39**:

$$\ln k = \ln A - \frac{E_a}{k_B} \left(\frac{1}{T}\right) \quad \text{Eq. 39}$$

Eq. 39 was used to calculate the activation energy in the material system.³⁵⁸ The fitting result matched well with experimental results (**Figure 27f**). The activation energy was 0.76 eV which was higher than those in $\text{SiO}_x\text{N}_y:\text{Ag}$ (0.27 eV) and Ag/Silk (0.52 eV).⁴⁷ The activation energy is related to the energy barrier of Ag diffusion, which may benefit the stability of the device. The above results demonstrated that the device can be modulated between the volatile and non-volatile switching models.

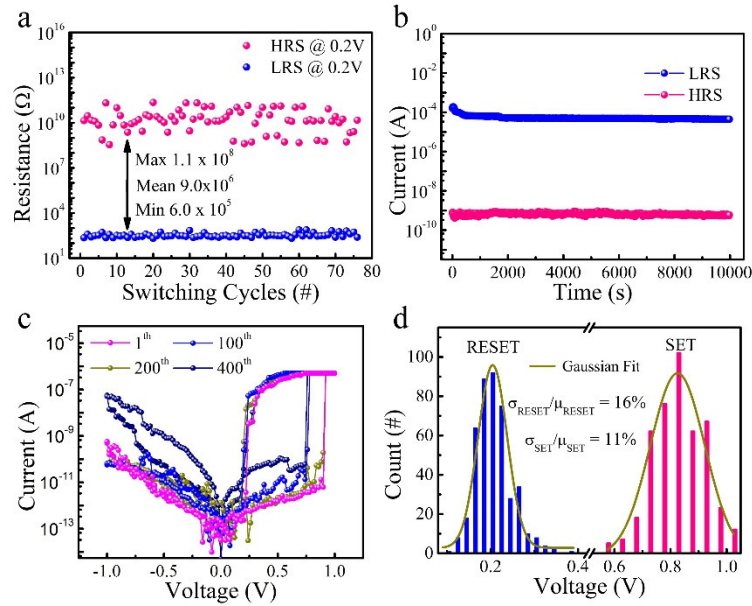


Figure 29. (a) HRS and LRS resistance distributions over switching cycles. (b) Non-volatile memory behavior, the voltage amplitude was 3 V, the pulse duration was 1s. (c) I-V curve reproducibility of the device over 400 switching cycles. (d) The distribution of SET and RESET voltages. The σ_{SET} (and σ_{RESET}) and μ_{SET} (and μ_{RESET}) are the standard deviation and the mean value, respectively.

The endurance and stability of the device were investigated on both non-volatile and volatile switching models. For the non-volatile MS model, to mimic the voltage stresses applied on memory devices in practical applications, the resistance distribution under pulsed-voltage operation was carried out, as shown in **Figure 27g**. The device was operated normally for around 165 cycles, giving an HRS/LRS ratio of 4×10^5 (The mean value over 165 cycles). Then, abnormal resistive switching behaviours showed up, including invalid SET/RESET operation (the storage window was ≈ 0) and a small HRS/LRS ratio (approximately 100). The device degradation was due to heat damage over the switch operation. As can be seen in **Figure 27g**, the device was stuck in HRS after a few hundred cycles, which resulted in resistive switching failure. The CISE decomposes at a temperature higher than 600 K, indicating relatively low stability.³⁵⁹ During the pulsed operation process, the generated heat will be accumulated. The heat may damage the structure of the CISE film, which hindered the diffusion of Ag atoms, and the device cannot switch to LRS. Ma et al. reported that repeated switching operations can cause phase segregation in the switching layer, resulting in resistive switching failure by stuck-in-

HRS, which is similar to our devices.³⁶⁰ There is still room to improve the endurance of the device for practical application. Future work is necessary to improve the device endurance for practical applications, such as the electronic packaging process (prevent the damage of humidity and oxygen), optimization of the switching layer (such as thickness, roughness, crystal phase, et al), heat management of the device, and adjusting the device structure. For the volatile TS model, **Figure 29c** exhibits the DC switching cycle test for 400 operation cycles. The sweep voltage was from -1 V to 1 V. The distribution of LRS and HRS is shown in **Figure 27h**, the read voltage was 0.4 V. The overall HRS/LRS ratio was 7×10^4 (Mean value over 400 cycles). No obvious degradation was observed for the first 250 cycles. When further operating the device, the device degenerated gradually, but it still can hold the HRS/LRS ratio of 1.5×10^4 (The mean value of the last 20 cycles). **Figure 29d** shows the distribution of SET and RESET voltages. The results were fitted with the Gaussian equation **Eq. 40**.

$$y = y_0 + Ae^{-\frac{(x-\mu)^2}{2\sigma^2}} \quad \text{Eq. 40}$$

where A is a constant, σ is the standard deviation and μ represents the mean value. The σ_{SET}/μ_{SET} and $\sigma_{RESET}/\mu_{RESET}$ were 11 % and 16 %. **Figure 27i** shows the forward and reverse resistance at ± 0.5 V over 400 operation cycles, the results elaborated on the stability of the volatile TS regarding the rectification characteristic. The rectification ratio was as high as 4.0×10^4 . The selector with a high rectification ratio can efficiently alleviate sneak currents in crossbar memristors.

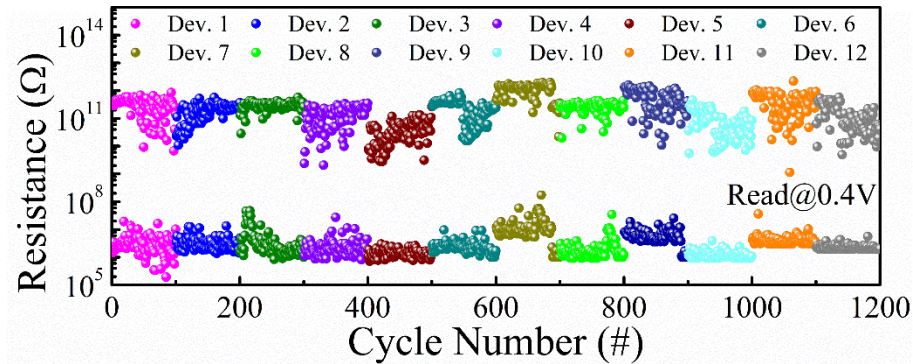


Figure 30. Device-to-device variability of HRS and LRS.

Table 5. The statistics summary of the HRS/LRS Ratio of the Ag/CISe/Mo device.

Device Number	HRS/LRS Ratio Mean value	HRS/LRS Ratio Maximum value	HRS/LRS Ratio Minimum value	HRS/LRS Ratio Higher than 10^4 (%)
Device 1	1.7×10^5	1.7×10^6	2.5×10^3	95 %
Device 2	8.0×10^4	2.1×10^5	2.2×10^3	95 %
Device 3	1.3×10^5	4.8×10^5	5.0×10^3	96 %
Device 4	8.7×10^4	3.4×10^5	1.6×10^3	93 %
Device 5	3.4×10^4	1.6×10^5	1.5×10^3	76 %
Device 6	1.6×10^5	2.7×10^5	7.4×10^3	97 %
Device 7	1.3×10^5	2.7×10^5	7.1×10^3	98 %
Device 8	1.7×10^5	4.0×10^5	7.0×10^3	98 %
Device 9	1.2×10^5	4.2×10^5	2.5×10^3	93 %
Device 10	8.1×10^4	4.9×10^5	4.3×10^3	90 %
Device 11	1.3×10^5	6.2×10^5	3.8×10^2	94 %
Device 12	7.1×10^4	2.7×10^5	2.5×10^3	89 %

A crossbar of 4×5 was fabricated. 12 of 20 devices can be operated over 100 cycles (DC switching cycle test, -1 V to 1 V). The yield was 60%. The LRS and HRS revolution over switching cycles is shown in **Figure 30**. The statistics analysis summary of the HRS/LRS ratio is shown in **Table 5**. The mean ratio of HRS/LRS varied between 3.4×10^4 and 1.7×10^5 . Indeed, the device yield in this paper is lower than wafer-scale integrated memristor arrays (a high yield of 98%).³⁰ Future work is needed to optimize the fabrication processes and device structures to realize practical applications.

3.3.3 Artificial Neurons and Synapses

Human brain activities rely on neural networks consisting of $\sim 10^{15}$ synapses and $\sim 10^{11}$ neurons. The working principle of neural networks and the equivalent hardware circuit are shown in **Figure 31a**. To mimic biological systems with artificial neural networks, the artificial neuron and artificial synapse are two main components. Artificial neurons generate spiking signals. Artificial synapses are connectors linking different neurons. The connection strength between neurons is determined by synapse weights (presented by the conductance of memristors).² To realize neural functions by artificial devices, several neural models have been developed, including the Hodgkin–Huxley (HH) model, the integrate-and-fire

(IF), and the integrate-and-fire (LIF) model.² Among them, the LIF model has been widely investigated due to its simplicity, reliability, and capturing biological dynamics. The LIF neuron hardware is a combination of a “leaky” resistor term and a capacitor as shown in the schematic diagram of **Figure 31a**. The LIF neuron model is described by **Eq. 41**.²⁸⁵

$$C \frac{dV_c(t)}{dt} = I(t) - \frac{V_c(t)}{R+R_m} \quad \text{Eq. 41}$$

where C is the capacitance of the capacitor. The capacitor receives charges from synaptic inputs.³⁶¹ $V_c(t)$ is the voltage across the capacitor reflecting the dynamic change of membrane potential. $I(t)$ is the current input from artificial synapses. R is the series resistor. R_m is the resistance of the volatile TS memristor. The $R+R_m$ is the “leaky” term. In a neural network, neurons receive inputs from other neurons with various amplitudes and frequencies through synapses. The received charges are stored and accumulated in the capacitor. The accumulation of charges in the capacitor will increase the voltage attributed to the memristor (M1). The SET process on the memristor occurs once the voltage applied on the memristor (M1) is higher than the SET voltage (V_{SET}). The voltage across the resistor R4 increases drastically due to the resistance reduction of the memristor (M1). Thus, a spiking action will be generated and sent out.²⁸⁵ Notably, the memristor used in the artificial neuron system should endow volatile properties so that it can go back to the initial state spontaneously after the spiking action.¹¹ The neural circuit design is shown in **Figure 23**. By default, the volatile memristor (M1) was at HRS. The received inputs were stored and accumulated in the capacitor, resulting in the increased potential (V_C) stored on the capacitor. V_C can be calculated by **Eq. 42**.

$$V_C = \frac{1}{C} \int I dt \quad \text{Eq. 42}$$

where I represent input currents. C is the capacitance of the capacitor C1. Meanwhile, the charge stored in the capacitor slowly leaks through a conductive path consisting of M1 and R4. The leakage RC time constant (τ), was determined by C1, M1, and R4, according to **Eq. 43**.

$$\tau = C \times (R_{M1} + R_4) \quad \text{Eq. 43}$$

where R_{M1} is the resistance of the memristor (M1). V_{OUT} can be calculated from V_C using **Eq. 44**.

$$V_{OUT} = V_C \times \frac{R_4}{R_{M1} + R_4} \quad \text{Eq. 44}$$

V_{OUT} is the voltage on the R4. The voltage on the memristor (M1) can be obtained with **Eq. 45**.

$$V_{memristor} = V_C - V_{OUT} \quad \text{Eq. 45}$$

Where $V_{memristor}$ is the voltage applied on the memristor (M1). R4 has a resistance of 4 M Ω that was much smaller than that of M1 at HRS. $V_{out} \approx 0V$ when M1 was at HRS according to **Eq. 43**. As increased electrons were stored in the capacitor, V_C and $V_{memristor}$ increased gradually provided that the charging speed was faster than the leaky speed. When the $V_{memristor}$ was high enough, the memristor (M1) switched from HRS to LRS, which induced the abrupt increase of the V_{OUT} . As memristor (M1) entered LRS and a non-zero V_{OUT} was generated. C1 was rapidly discharged, and the V_C decreased to 0 V. The V_C dropped below the RESET voltage of 0.2 V. The memristor (M1) resumed HRS due to the volatile property. As a result, V_{OUT} returns to 0 V as C1 starts to accumulate charges from input signals again. Notice that during the period when M1 stays in LRS, any incoming signals stored in C1 are rapidly discharged. This feature can mimic the refractory period in biosystems. The neuron responses under different input frequencies (with a fixed input voltage of 1 V) are shown in **Figure 31b**. Under a low frequency of 2.5 kHz, only 1 firing event happened with $V_{OUT} \approx 0.55$ V. In comparison, the spiking frequency increased when the input frequency increased to 5 kHz. This was because the accumulation of charges in the C1 capacitor was faster so that the memristor (M1) can be switched to LRS more frequently. Meanwhile, as the input signal frequency further increased to 10 kHz, the frequency of output spike signals increased correspondingly, demonstrating input-controlled spiking behaviors. On the other hand, the influence of input amplitudes (with a fixed frequency of 10 kHz) on neuron spiking performance has also been studied, as shown in **Figure 31c**. Neuron spiking was not generated under the input voltage of 0.8 V, because the charge accumulation was insufficient. Hence, the voltage on M1 was not high enough to transform M1 into LRS and generate an output spike. In comparison, stable neuron spiking signals were obtained when the input voltage amplitude was 1 and 1.2 V. This neuron spiking under different frequencies and amplitudes can mimic the actions in biological neuron systems to implement neuromorphic computing.³⁶²

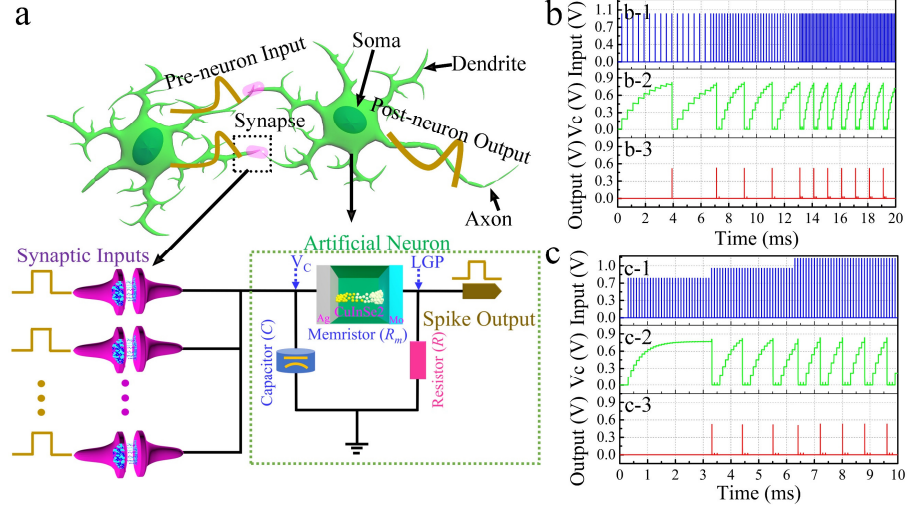


Figure 31. Schematic diagram of artificial neuron system and LIF neuron simulation results. (a) Diagram of biological artificial neuron system and the LIF neuron circuit. LGP means local graded potential that reflects the dynamics of the neural membrane potential. (b) The simulation of neural spiking response under different excitation frequencies. The b-1 shows the input signals. The b-2 shows the V_C under different input signals. The b-3 shows the output signals. (c) The simulation of neural spiking response under different excitation amplitudes. The c-1 shows the input signals with different amplitudes. The c-2 shows the V_C under different input signals. The b_3 shows the output signals.

Synapses are crucial in biosystems, which have been investigated in the Ag/CISe/Mo device. The schematic diagram of a biological synapse is shown in **Figure 32a**. Biological synapses connect neurons by controlling the absorption and extrusion of neurotransmitters (K^+ , Na^+ , Ca^+), inducing plasticity reactions. Synaptic plasticity is the change of synaptic strength under external stimuli over time. This phenomenon is the foundation of memory and learning activities in human brains. In artificial neural networks, synaptic plasticity can be mimicked by the memristor with adjustable conductance.⁴⁷ When two spikes occur in rapid succession, synaptic strength changes by the second spike are enhanced. Because the interval time is too short for carriers to go back to their initial equilibrium states, namely paired-pulse facilitation (PPF). The plasticity of PPF is described by **Eq. 46**.³⁶³

$$PPF = \frac{(G_2 - G_1)}{G_1} \times 100\% \quad \text{Eq. 46}$$

where G_1 and G_2 are the conductance of the device after the first pulse and the second pulse, respectively. The PPF was successfully simulated as shown in **Figure 32b**. The interval time between two pulses

was denoted as ΔT . The voltage amplitude was 1.0 V. Conductive (synaptic weight) changes depending on ΔT were obtained. The second pulse induced a larger conductance increase. Besides, the conductance returned to its original state gradually after the pulsed excitation. When the ΔT increased from 20 ms to 600 ms, the conductance change decreased accordingly. A shorter interval between two stimuli can reinforce the memory effects, demonstrating agreement with biological synapses. This follows an exponential relationship described by Eq. 47.³⁶⁴

$$\Delta G = c_1 e^{-\frac{\Delta T}{\tau_1}} + c_2 e^{-\frac{\Delta T}{\tau_2}} + y_0 \quad \text{Eq. 47}$$

Where c_1 , c_2 , and y_0 are constants treated as fitting parameters. τ_1 and τ_2 are the fast and slow decaying terms, respectively. The fitting result is shown in Figure 32b (the pink line). The fast (τ_1) and slow (τ_2) decaying terms were 2.4 ms and 54.8 ms, respectively.

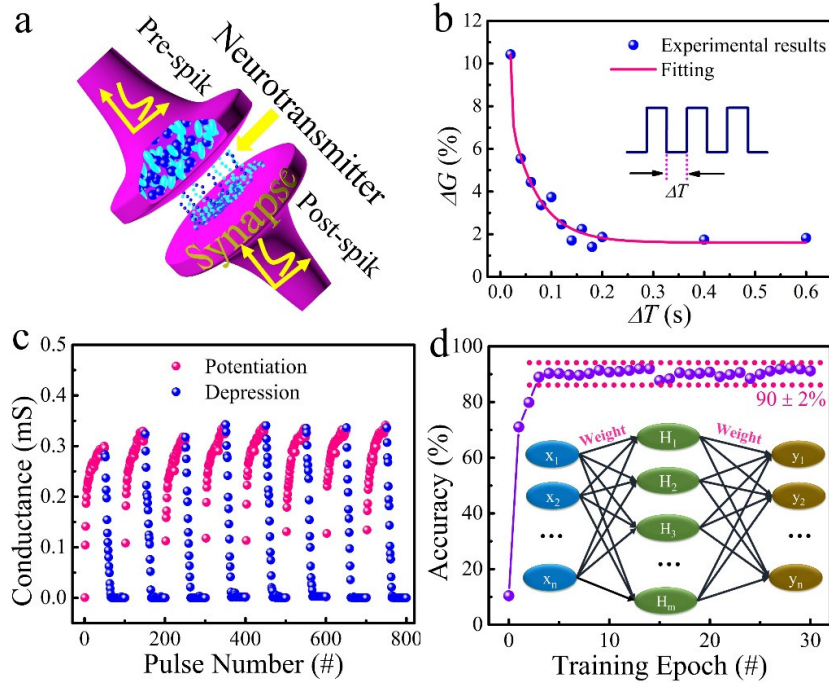


Figure 32. Artificial synaptic performance. (a) Schematic diagram of a synapse. (b) Experimental result of short-term synaptic PPF behavior. (c) The potentiation and depression behaviors of the device. The pulse amplitudes for potentiation and depression operations were +1 V and -1 V, respectively. The pulse duration was 50 ms. The read voltage was 0.1 V. 50 consecutive pulses were applied for both potentiation and depression operations. (d) Simulations of backpropagation algorithm for UCI Small image recognition (image size was 8×8 pixels).

Long-term potentiation and depression behaviors under pulsed-voltage programming schemes were obtained as shown in **Figure 32c**. The conductance increased as the positive-pulse voltage was used, corresponding to the potentiation process. In comparison, the conductance decreased under negative pulses, indicating the depression process. To demonstrate the feasibility of the Ag/CISe/Mo artificial synapse for neuromorphic computing, the backpropagation algorithm for pattern recognition was simulated based on a three-layer ANN. An 8 x 8 version of UCI Small images was employed as the training and test dataset.³⁴² The recognition accuracy reached over 90 % after four training epochs as shown in **Figure 32d**. The pattern recognition accuracy was $90 \pm 2\%$ over 30 training epochs. The small accuracy fluctuation was due to the algorithm.³⁴⁰ The simulation results claim the potential and practicability of the artificial synapse for neuromorphic computing. Based on the above results, the versatile memristor can provide the functions of non-volatile memory, selectors, artificial neurons, and artificial synapses.

3.3.4 Working Mechanism Investigations

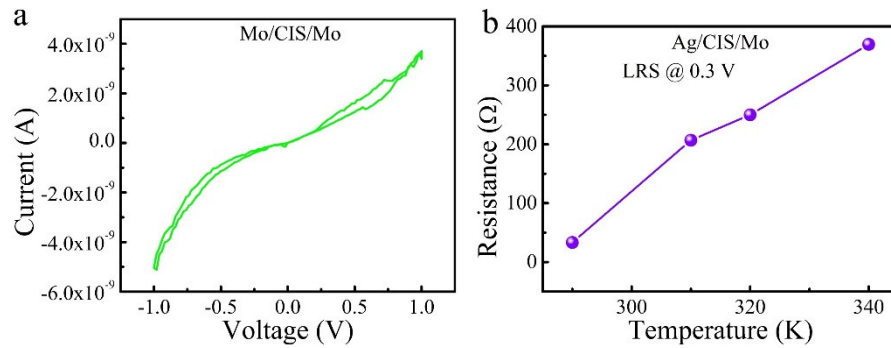


Figure 33. (a) Typical I-V curve of the Mo/CISe/Mo device. (b) The values of LRS at different temperatures for the Ag/CISe/Mo device.

The resistive mechanism has been investigated systematically. To confirm that Ag dynamics dominated the resistive switching, the devices with different top electrodes and operation temperatures were studied. The electrical performance of the device with inert electrodes is shown in **Figure 33a**. No resistive switching was observed in the Mo/CISe/Mo device, confirming that Ag is essential for resistive switching. Furthermore, the LRS values of the Ag/CISe/Mo device under different temperatures were measured, as shown in **Figure 33b**. The resistance of LRS increased with the

increase of temperature, which is the signature feature of metallic conducting, claiming that the metallic conductive filaments governed the LRS.⁸⁷

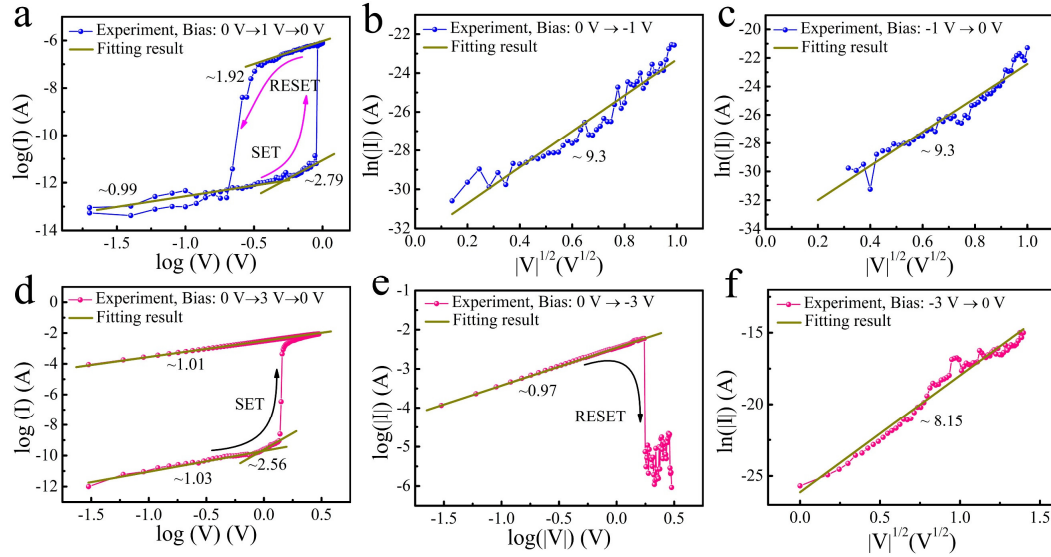


Figure 34. Conduction mechanisms of the volatile TS and non-volatile MS in the Ag/CISe/Mo device. (a) Log (I) - log(V) curve, the voltage swept from 0 V \rightarrow 1 V \rightarrow 0 V. (b) Ln (|I|) - $V^{1/2}$ curve, the voltage swept from 0 V \rightarrow -1 V. (c) Ln (|I|) - $V^{1/2}$ curve, the voltage swept from -1 V \rightarrow 0 V. (d) Log (I) - log(V) curve, the voltage swept from 0 V \rightarrow 3 V \rightarrow 0 V. (e) Ln (|I|) - $V^{1/2}$, the voltage swept from 0 V \rightarrow -3 V. (f) Ln (|I|) - $V^{1/2}$, the voltage swept from -3 V \rightarrow 0 V.

Moreover, the electrical mechanism of the versatile memristor was investigated. Ohmic conduction and interface-dominated conduction were observed in memristor devices.³⁶⁵ The switching layer of CISe was a p-type semiconductor.³⁴⁵ A Schottky barrier was formed at the interface of metal electrodes and the switching layer. **Figure 34** summarizes the fitting results to elaborate conduction mechanisms in the Ag/CISe/Mo device with the volatile and non-volatile performance. **Figure 34a** shows the typical log (I) - log(V) curve under positive bias (0 V \rightarrow 1 V \rightarrow 0 V). When applying the voltage from 0 V to 1 V, the slope was 0.99, close to 1, at the low voltage region (0 V to approximately 0.6 V). The current increased proportionally with the increase of voltage, indicating Ohmic conduction. Afterward, the slope increased to 2.79 at a voltage range of approximately 0.6 V to 0.9 V. The concentration of injected electrons exceeded the equilibrium concentration, indicating the SCLC effects.³¹⁴ Further increasing the voltage led to an abrupt current increase. This was due to the formation of Ag conductive

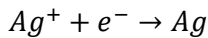
filaments.³⁶⁶ After the device was switched to LRS, the slope was about 1.92 instead of 1.0. It did not follow Ohmic conduction due to the dynamic diffusion of Ag conductive filaments. When the voltage decreased to a certain value (approximately 0.2 V), the current decreased abruptly, demonstrating the rupture of Ag conductive filaments. When reversing the applied voltage, the device remained at the HRS. The $\ln(|I|) - V^{1/2}$ curves of the device at the negative region are shown in **Figure 34b** and c. A linear fit was obtained, indicating the conduction mechanism was governed by Schottky emission.²¹⁴

For the non-volatile MS performance in the device, the $\log(I) - \log(V)$ curve under positive bias (0 V \rightarrow 3 V \rightarrow 0 V) is shown in **Figure 34d**. The slope over the low voltage region (0 V-0.7 V) was 1.03, indicating Ohmic conduction. Then, a slope of 2.56 showed up over the high voltage region (0.7 V to 1.0 V), indicating the SCLC conduction model. Further increasing the voltage, a sharp current increase was observed due to the formation of Ag conductive filaments. For the LRS, the slope was 1.01 following the Ohmic conduction mechanism. The abrupt change was not found when the voltage swept from 3 V to 0 V. When reversing the voltage to the negative region, the slope was 0.97 in the low voltage region (0 V to approximately -1.7 V), which indicates the Ag conductive filament was stable and the device was still at LRS, as shown in **Figure 34e**. When the absolute value of voltage exceeded 1.7 V, the current decreased suddenly. The conductive filament ruptured, and the device RESET to HRS. **Figure 34f** shows the $\ln(|I|) - V^{1/2}$ curve as the voltage sweeps from -3 V to 0 V. The linear behaviour demonstrated that the conduction mechanism was governed by Schottky emission.

To elaborate on the conductivity evolution of the Ag/CISe/Mo device under different voltages, schematic diagrams of the resistive switching mechanism are shown in **Figure 35**. Based on the above discussion, the dynamics of Ag conductive filaments were responsible for the resistance switching. Additionally, the volatile and non-volatile behaviors were due to the different stability of conductive filaments, which were determined by voltage stress.³⁵⁵ For volatile resistive switching, as shown in **Figure 35a**, Ag atoms from the top electrode were oxidized into Ag^+ under positive voltages (Figure 35a1). This is described by **Eq. 48**.⁸⁷



The ionized Ag^+ penetrated the CISe film and migrated to the Mo electrode under the electrical field, as shown in **Figure 35a2**. Then the Ag^+ ions were reduced into Ag atoms shown in **Eq. 49**:¹⁸⁸



Eq. 49

Conductive filaments connecting the top and bottom electrodes will form when sufficient Ag atoms were accumulated in the switching layer as shown in **Figure 35a3**. The resistance of the device decreased suddenly owing to the high-conductive Ag filaments. However, the conductive filament was slim and unstable, resulting in filament rupture due to the minimization of filament surface energy when the applied bias was small,³⁵ as shown in **Figure 35a4**. When a reversed voltage was applied to the device, it remained at HRS since the inert Mo electrode cannot induce conductive filaments (**Figure 35a5 and a6**). Thus, the device showed volatile TS characterizations.

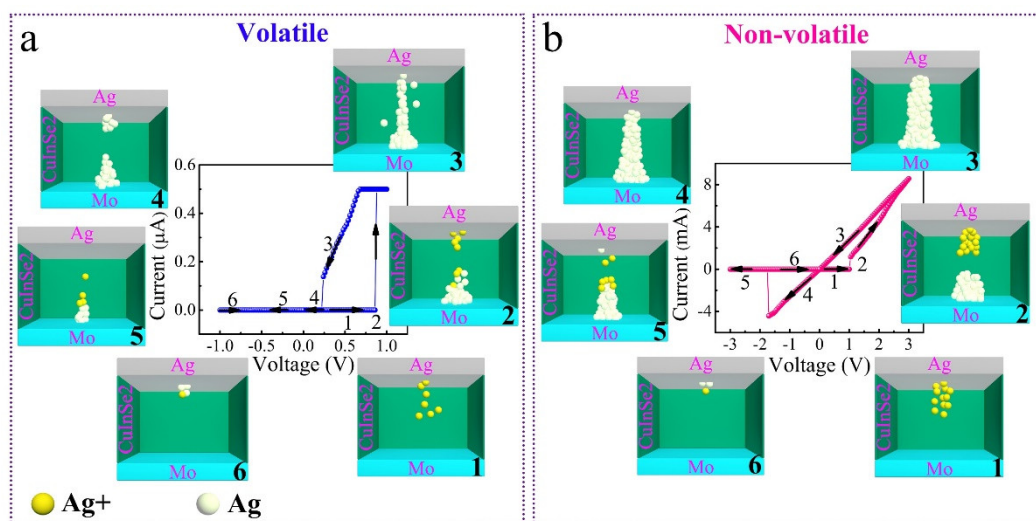


Figure 35. Illustration diagram of the volatile/non-volatile resistive switching. (a) Mechanism of conductive filament evolution for the volatile TS behaviors. (b) Mechanism of conductive filament evolution for the non-volatile MS behaviors.

With a higher operational voltage, more Ag atoms were oxidized into ions and then reduced into atoms, as shown in **Figure 35b1** and **b2**. Hence, the conductive filament was thicker and stronger, as shown in **Figure 35b3** and **b4**. The stable filaments did not break until the reversed voltage reached a certain value. Ag atoms were oxidized into Ag^+ under negative voltages, inducing the dissolution of conductive filaments and the transition from LRS to HRS (**Figure 35b5**). As the negative voltage was further applied, the residual Ag atoms in the switching layer were further dissolved and the device recovered to the initial condition (**Figure 35b6**). Thus, the device showed non-volatile MS behaviors.

The versatile memristor with the adjustable retention time enables multi-functions for memory and computation.

3.4 Summary

In summary, a versatile memristor (Ag/CISe/Mo) array covering multiple functions was developed. Non-volatile functionalities with a storage window of 4.0×10^5 and a retention time of 10,000s were obtained, indicating the application of non-volatile memory. Besides, the Ag/CISe/Mo device showed diode-like volatile functionalities with a storage window of 7.0×10^4 and a rectification ratio of 4×10^4 . The high rectification ratio can be used as selectors to suppress sneaky currents in memristor arrays. The device was operated stably over 400 cycles, ensuring a mean HRS/LRS ratio of over 10^4 . The LIF neuron model based on the device has been studied, demonstrating potential as artificial neurons. Furthermore, the short-term synaptic PPF and long-term potentiation/depression performances were obtained in the same device. The image recognition simulation with an accuracy of $90 \pm 2\%$ was achieved, indicating the practicability of the artificial synapse for neuromorphic computing. A versatile memristor taking the multiple roles of non-volatile memory, selectors, artificial synapses, and artificial neurons will provide many advantages regarding circuit simplification, fabrication processes, and manufacturing costs. The devices with different top electrodes, operation temperatures, switching layer thicknesses, and conduction mechanisms were investigated to reveal the resistive switching mechanism. It has been confirmed that the volatile/non-volatile bifunctional resistive switching was attributed to the dynamics of Ag atoms. Moreover, this work presented a novel bottom-up approach to fabricate crossbar arrays, where the CISe was grown locally by electrodeposition to form a patterned switching layer. This method can potentially decrease manufacturing costs and achieve high utilization efficiency of materials. The results will promote the development of advanced data storage and neuromorphic computing systems.

Chapter 4. Intelligent matter endows reconfigurable temperature and humidity sensations for in-sensor computing

In the previous chapter, a versatile memristive device was developed by controlling the lifetime of conductive filaments. Here, the sensing function (temperature and humidity) will be explored based on the filamentary memristive device.

Data-centric tactics with in-sensor neuromorphic computing go beyond the conventional computing-centric tactic that is suffering from processing latency and excessive energy consumption. The multifunctional intelligent matter with dynamic smart responses to environmental variations paves the way to implement in-sensor neuromorphic computing with high energy efficiency. However, intelligent matter with humidity and temperature sensitivity has not been reported. In this work, a design is proposed based on a single memristive device to achieve reconfigurable temperature and humidity sensations. Opposite temperature sensations at the LRS and HRS were observed for sensory processing. Integrated devices mimicking intelligent electronic skin (e-skin) can work in three modes to adapt to different scenarios. Additionally, the device acts as a humidity-sensory artificial synapse that can implement high-level cognitive in-sensor neuromorphic computing. Intelligent matter with reconfigurable temperature and humidity sensations is promising for energy-efficient AI systems.

4.1 Introduction

Intelligent technology is fundamentally revolutionizing our daily life by updating the paradigm of computing systems inspired by energy-efficient human brains.⁸ Intelligence embracing learning and adapting abilities is mostly observed in biological organisms.³⁶⁷ The intensive proliferation of AI constantly advances modern technology limits, making machines behave more like intelligent creatures. However, two main technical barriers to more powerful intelligent machines are yet to be solved, namely, (i) a large amount of redundant and unstructured raw data from sensory nodes; and (ii) energy-inefficient and time-consuming data processing.³ To overcome the challenges, one strategy is shifting from a computing-centric tactic to a data-centric tactic by co-integrating various functional components into a single device for in-sensor computing, whereby the sensory data will be processed locally without data shuttling.²⁶³ To construct novel intelligent systems, intelligent matter enabling dynamic smart responses to the environment would inspire an entirely novel concept of AI.⁸ The

intelligent matter comprehending environmental variations enables reconfigurable sensation and memory abilities to external stimuli (mechanical stress, chemical molecules, light, temperatures, humidity, etc.). The reconfigurable functionalities go far beyond the capability of static matter (conventional sensors)³⁶⁸ and benefit intelligent systems interacting with environments.³⁶⁹ Intelligent matter is the basic building block for advanced in-sensor neuromorphic computing and AI technology.⁸

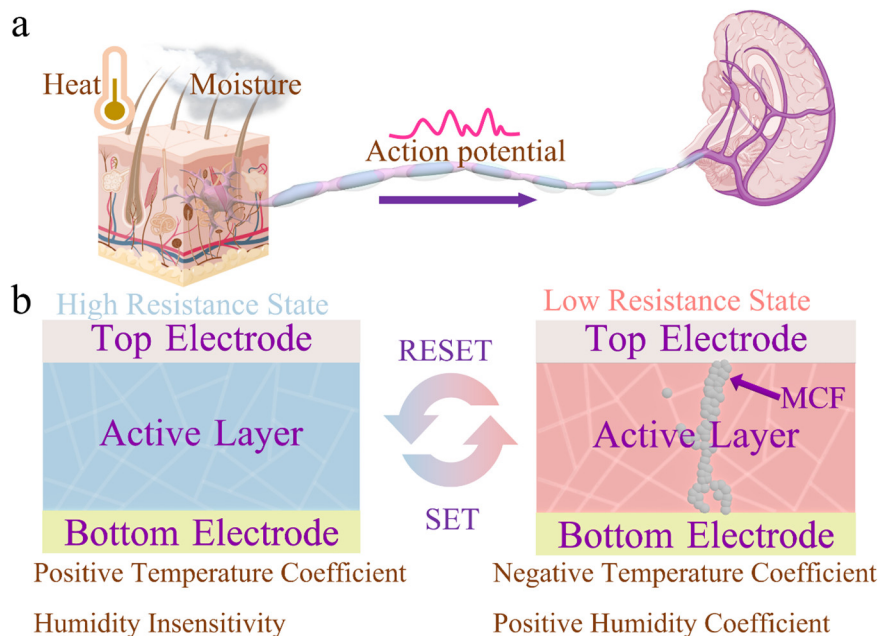


Figure 36. Conceptual illustration of intelligent matter with reconfigurable temperature and humidity sensations. (a) Schematic diagram of a biological system with synergistic temperature and humidity sensations. (b) Schematic diagram of the switchable device with temperature and humidity sensations. MCF means metallic conductive filament.

Developing intelligent matter with novel sensory functions and easy-integrability structures is important for in-sensor neuromorphic computing. Sensory signals consist of mechanical contacts (tactile, press, strain), photonic stimulations (spanning from the ultraviolet region to the near-infrared region), temperature changes, humidity variations, and chemical molecules.³⁶⁹ Thereinto, temperature and humidity are two main pieces of sensory information that are crucial for biological individuals. As shown in **Figure 36a**, the stimulation from the changes in temperature and humidity generates the excitation spikes that will be transmitted to the central processing unit of the brain. Then, the brain will

send orders to muscles and take actions to avoid damage or search for a safe spot, which is crucial for biological survival. In brain-inspired in-sensor neuromorphic computing systems, matter-level components equip sensory functions and capabilities of biological organs (synapses and neurons, etc.), which can implement high-level physiological learning and cognitive abilities.

Table 6. Summary of the memristive devices-based intelligent matter for in-sensor neuromorphic computing.

Sensing type	Intelligent sensational matter	Application	Ref.
Tactile	Ferroelectric-gated synapse	Realtime decisions and	279
Ultraviolet light	Reconfigurable phototransistor	Neuromorphic vision	370
Ultraviolet light	Ferroelectric photosensor	Real-time machine vision	280
Ultraviolet light	Light-mediated memristor	Real-time collision detection	90
Ultraviolet light	Photo-induced phase transition	Neuromorphic vision	371
Ultraviolet light	Reconfigurable photodiode	Ultrafast machine vision	14
Visible light	Li ⁺ -mediated phototransistor	Sensing-memory for retina perception	372
Visible light	Phototransistors	Scotopic and photopic adaptation	373
Chemical, Alcohol	Covalent organic framework	Gas identification system	374
Humidity	Porous zwitterionic sensor	Locating water sources	275
Temperature	Floating gate synaptic transistor	Temperature-facilitated learning	375
Multi-modal: Tactile, green light	Stretchable nanowire transistor	Gesture recognition	376
Multi-modal: Ultraviolet, humidity	MXene-ZnO memristor	Sensory neuromorphic vision	274
Multi-modal: Temperature, humidity	Filamentary memristor	Sensory neuromorphic vision	This work

Intelligent matter based on a single device with different sensory functionalities has been reported for in-sensor neuromorphic computing, as summarized in **Table 6**.^{14,90,274,275,279,280,370–376} One strategy for constructing intelligent matters is to develop three-terminal artificial synapses. External stimuli (such as tactile or light) imposed on the gate terminal induce ionic insertion or ferroelectric polarization modulation. The device presents sensory synaptic performances that can be utilized for in-sensor neuromorphic computing.^{279,372} Another strategy is to design two-terminal devices enabling sensory

reconfiguration and memorizing ability to changing environments. Notably, two-terminal devices show better integrability compared to their three-terminal counterparts. However, only a few works have reported the two-terminal intelligent matter.^{90,274} Furthermore, intelligent matter enabling temperature and humidity sensations simultaneously for in-sensor computing has not been reported yet. Hence, designing and constructing two-terminal in-sensor computing devices with intelligent temperature and humidity sensations are attractive for advanced AI applications.

A memristive device was employed to design an intelligent matter with reconfigurable temperature and humidity sensations. The memristive device presents programmable and non-volatile resistance.⁴ It can reversibly switch between different resistance (or conductance) states determined by the history of electrons following through it. Non-volatile internal states can be obtained by applying voltage or current excitations. Several mechanisms, such as phase change, ferroelectric polarization modulation, electrochemical redox reactions, and magnetic tunnelling have been reported to explain resistive switching phenomena.³⁷⁷ Variation occurs inside a memristive device during the resistive switching process. Therefore, different temperature and humidity sensations can be expected when the memristive device is at different states. Another specialty of this design is that the state switching is reversible, which means the intelligent computing exhibits reconfigurable sensory capabilities. A counterintuitive philosophy is utilized in this design. A memristive device is expected to be sensitive instead of resilient (in traditional ideology) to environmental changes.³⁷⁸ Besides, memristive devices have a simple capacitor-like sandwich structure that is beneficial to high integration density.³⁷⁹ With the rapid development of microsystems and nanosystems, such as microelectromechanical systems (MEMS),³⁸⁰ lab-on-a-chip,³⁸¹ biology at a single cell level,³⁸² microfluidic systems,³⁸³ and microscale biological reactors.³⁸⁴ On-chip temperature sensors and microscale humidity gradient monitors are crucial. Demand has risen for microscale or even nanoscale temperature and humidity sensors. Particularly, the device reported in this work can be used as a sensory artificial synapse that can implement neuromorphic computing. State-of-the-art deep neural networks (DNNs) contain millions of weights or more, which must be mapped to on-chip synaptic memories. Therefore, high-density integration of synaptic devices is required.

The filamentary resistive switching due to electrochemical redox reactions is one of the main working mechanisms. The pristine device is at a high resistant state (HRS) as shown in **Figure 36b**. The

temperature and humidity sensations are determined by the properties of the switching layer (generally insulators or semiconductors). After the SET process, the metallic conductive filament (MCF) bridging the top and bottom electrodes is generated inside the switching layer. The device is at a low resistance state (LRS). The electronic property at the LRS is dominated by the metallic filament, which shows different temperature and humidity sensations compared to its HRS counterparts. More specifically, the semiconductor switching layer presents a positive temperature coefficient of conductance, indicating that the conductance of the HRS increases with increased temperature. In comparison, the metal shows a negative temperature coefficient of conductance, which means the conductance of the LRS decreases with increased temperature.³⁸⁵ Besides, the humidity level affects electrochemical redox reactions during the SET process, which will change the conductivity of the metallic filament. The conductance at LRS thus is sensitive to humidity.²¹⁹ The sensory performance is programable as it is reversible between the HRS and LRS. Those reconfigurable sensory properties can be utilized for in-sensory neuromorphic computing.

In this work, a novel intelligent matter based on a memristive device with reconfigurable temperature and humidity sensations was developed. The device structure was Ag/ Cu (In, Ga) Se₂ (CIGSe)/Mo, as shown in **Figure 37a**. The Ag acts as an active electrode that shows active chemical reactivity and can be induced into the CIGSe. Ag species exhibit good diffusivity in the CIGSe, which is crucial for the formation of conductive channels.^{15,331} The device showed reliable resistive switching behaviors, with an HRS/LRS ratio of 1700, an endurance of over 5000 cycles, and artificial synapse functions. The device showed different responses to the temperature and humidity sensations when the device was at different states. The in-sensor low-level data processing (temperature patterns detection, enhancement, and reconfiguration) and in-sensor high-level data processing (humidity-sensitive neuromorphic computing) were demonstrated. The intelligent matter showed a positive temperature coefficient of conductance at the HRS, while it exhibited a negative temperature coefficient of conductance at the LRS. The system with integrated intelligent matter can work in the LRS mode, HRS mode, and HRS&LRS mode due to different temperature sensations. This can be potentially used for advanced-intelligence artificial skins for different working scenarios. Furthermore, high-level data processing under different humidity was demonstrated by implementing a neuromorphic computing simulation. The in-sensor computing can be extended to decision making, language processing, real-time predictive analytics, etc. The intelligent matter enabling reconfigurable temperature and humidity sensations

accelerates the neoteric technology toward advanced e-skin, neurorobotics, cyborg, and human-machine interaction in the post-Moore era.

4.2 Experimental Section

4.2.1 Device Fabrication

The Ag/CIGSe/Mo and Mo/CIGSe/Mo devices were fabricated by magnetron sputtering and electrochemical deposition. The Mo/CIGSe/Mo device was used as a comparative trial to investigate resistive switching mechanisms. The Mo layer was deposited by direct current sputtering (ATC ORION SERIES SPUTTERING SYSTEMS) as the bottom electrode. A shadow mask was used to obtain a patterned Mo electrode. Then, the CIGSe switching layer was formed via the electrodeposition process. To prepare the reaction bath, 2.5 mM $\text{CuCl}_2 \cdot 2\text{H}_2\text{O}$, 2.4 mM InCl_3 , 6 mM GaCl_3 , 240 mM LiCl , 4.5 mM H_2SeO_3 were dissolved in DI water. All chemicals used in this experiment were purchased from Sigma-Aldrich. Besides, pHydrion (pH 3.00) was employed as the buffer. HCl drops were added to adjust the electrolyte pH to 2 - 3. The electrodeposition process was carried out with an electrochemical workstation (CHI Model 660E Series Electrochemical Analyzer/Workstation). A conventional 3-electrode setup was used. The CIGSe film was obtained by applying a constant potential (-0.63 V in this work) to the working electrode. Relative smooth and density CIGSe can be obtained on the patterned Mo electrode. Then, the Ag (or Mo) strip electrode was deposited on the top of the CIGSe to form a capacitor-like sandwich structure.

4.2.2 Materials and Device Characterization Methods

The optical micrograph of the device was taken by an optical microscope (Oxford BX51M). The surface morphology of the CIGSe film and the cross-section of the device was characterized by SEM (UltraPlus FESEMs). The composition information was measured by EDS (UltraPlus FESEMs). The GIXRD was carried out to characterize the crystalline structure of CIGSe (PANalytical X'Pert PRO system, $\text{CuK}\alpha$ irradiation, $\lambda = 1.5406 \text{ \AA}$). The Raman spectrum was measured by the Renishaw micro-Raman spectrometer (laser wavelength of 633nm, red He-Ne). The electrical measurement of the fabricated devices was performed on a Keithley 2985A source meter.

4.2.3 Simulation Methods

Theoretical material simulation: Density functional theory calculations were performed on the platform of CP2K software. The Gaussian Plane method was based on double- ζ MOLOPT basis sets (DZVP-MOLOPT-SR-GTH) and Goedecker-Teter-Hutter (GTH) pseudopotentials. The convergence criterion was 1×10^{-6} and the cut-off energy was set as 450 Ry. Periodic models with vacuum space were chosen to describe the interaction between CIGSe and Ag clusters. Firstly, the creation of the CIGSe model with vacuum space was optimized. And then, the Ag cluster was absorbed on the CIGSe model for ab initio molecular dynamics calculations (AIMD) in the ensemble-canonical ensemble (NVT). The time step was set as 1 fs for 2000 steps under the temperature of 303K. Similarly, the O-functional group generated due to the existence of H₂O molecules was used to bind on the surface of CIGSe model (labeled as CIGSe-O), and further were applied by AIMD calculations under the same parameters. Metadynamics calculations of free energy were carried out to investigate the reaction mechanism, the temperature was set at 303 K. Based on two collective variables: the distance of Ag atom on XZ plane (CV1) and YZ plane (CV2). These simulations allow Ag atom to relax in Z direction with the minimum activation energy.

4.3 Results and Discussion

4.3.1 Material Characterizations

Materials characterizations for the device are shown in **Figure 37**. The device has a capacitor-like sandwich structure that can be integrated into a high-density crossbar structure as presented in **Figure 37a**. A cross-sectional SEM image of a device is shown in **Figure 37b**. The thickness of the CIGSe was approximately 230 nm. A dense and crack-free feature in the CIGSe can be observed. **Figure 37c** presents the surface morphology of the CIGSe film. The crystalline grain grew into flower-like grain particles. Surface composition mapping illustrated that the four elements (Cu, In, Ga, Se) were distributed uniformly (**Figure 37d**). No obvious composition segregation was observed in the deposited film. The atomic percentages of Cu, In, Ga, and Se were 27.1 %, 14.39 %, 7.71 %, and 50.89 % respectively. To clarify the crystalline structure of the materials, the Raman and GIXRD spectra were measured. **Figure 37e** shows the Raman spectrum of the CIGSe, in which the characteristic peak corresponding to the A1 mode can be found.³⁸⁶ The GIXRD pattern is shown in **Figure 37f**. The

characteristic peaks corresponding to (112), (220), and (312) crystal planes of a tetragonal structure (JCPDS 00-035-1102) were observed.³⁸⁷ Notably, the peak at approximately 40.5° corresponded to the (110) crystal plane of the Mo bottom electrode (JCPDS file: 01-089-5156).¹⁵ The Raman spectrum and GIXRD pattern confirmed that the CIGSe with a chalcopyrite structure was formed by the electrochemical deposition process.

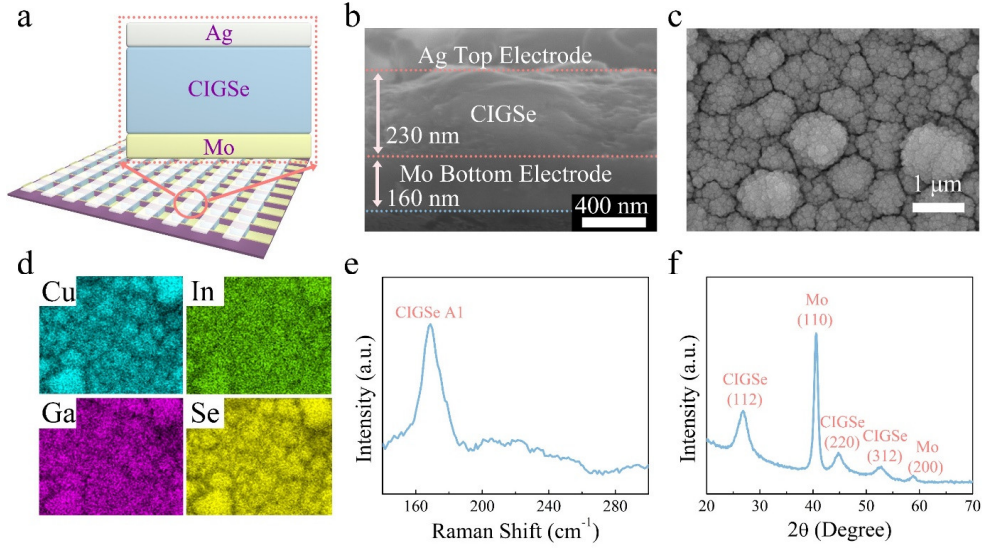


Figure 37. Materials characterizations. (a) Schematic diagram of the device structure. (b) Cross-section of the device. (c) Surface topography of the deposited CIGSe switching layer. (d) Surface composition mapping (Element: Cu, In, Ga, Se) of the CIGSe film. (e) Raman spectrum of the CIGSe thin film. (f) GIXRD spectrum of CIGSe/Mo.

4.3.2 Resistive Switching and Sensory Characterizations

The electronic characterizations of the device have been investigated systematically as shown in **Figure 39**. The DC switching cycle test is shown in **Figure 39a**. The sweep voltage was $0 \rightarrow 2 \text{ V} \rightarrow -2 \text{ V} \rightarrow 0 \text{ V}$. The pristine device exhibited the HRS, as the voltage swept from 0 to 2 V, the current increased sharply at the voltage of $0.18 \text{ V} \sim 0.32 \text{ V}$. The device switched to the LRS, corresponding to a SET process.^{27,388} When the applied voltage swept from 0 to -2 V, the device returned to the HRS at the negative voltage of around $-1.05 \text{ V} \sim -0.54 \text{ V}$. The switching process was reversible and dependable. To investigate the operational stability, the cumulative probability of the operating voltage is shown in

Figure 39b. The coefficient of variations (CVs) of the SET and RESET voltages were 0.12 and 0.20, respectively. Moreover, DC switching cycle tests under different CCs were carried out as shown in **Figure 38a**. The CCs influence the LRS; smaller CC corresponds to a lower value of current (larger resistance). Resistance-state distributions are shown in **Figure 38b**. The device demonstrated a multistate feature, indicating the potential of ultrahigh multistate memory and tunable states for neuromorphic computing.³⁸⁹ The endurance of the device is shown in **Figure 39c**. The device can be operated reliably over 5000 cycles with a large memory window of 1700 (mean value of HRS/LRS ratio). The retention time in both states was measured as shown in **Figure 38c**. The switched states can be maintained for approximately 4500s, indicating a non-volatile feature.¹¹⁵ Additionally, the device-to-device variation is shown in **Figure 38d**, indicating good process reliability. The above results demonstrate that the device shows reliable resistive switching properties, good endurance, and a large memory window.

The device also presented synaptic functionalities, which are crucial for in-sensor neuromorphic computing. In biological neurological systems, synapses connect neurons, ensuring neurotransmitters can travel among neurons to transmit messages from neurons to neurons or from neurons to muscles. Synaptic plasticity (excitatory/inhibitory) represents the connection strength between neurons, which is fundamental for information transmission and processing.³⁰⁴ In artificial synapse systems based on electronic devices, the plasticity can be represented by modulated conductance. The paired-pulse facilitation (PPF) behavior is short-term plasticity. The synaptic strength change is enhanced by the second stimulation when two rapid-consecutive stimulations are imposed. It is due to the interval time between the two excitations being too short for carriers to return to initial equilibrium states. **Figure 39d** shows the PPF behavior of the device.³⁴⁰ It can be found that the PPF index decreased as the interval time increased, indicating that a shorter interval time of stimuli reinforces the memory effects. The pink line in **Figure 39d** is the fitting result. An exponential relationship was confirmed, which is consistent with the feature in biological systems. The potentiation responses under consecutive voltage pulses with different amplitudes are shown in **Figure 39e**. A monotonic increase in the pulse number was observed. It means that more pulses induced stronger potentiation effects. Additionally, the ratio of G_{100}/G_1 (G_1 and G_{100} are the conductance after the first and 100th pulse respectively) increased with the increase of pulse voltage amplitudes. The G_{100}/G_1 ratio of 3.7 was obtained when the voltage amplitude of 1 V was used. In comparison, the G_{100}/G_1 ratio increased to 16.2 when the voltage

amplitude increased to 2 V. In a biological system, one of the essential synaptic functions is stimulation-strength-dependent responses. Higher stimulation resulted in higher potentiation effects. This feature can help biological identities to identify stronger stimulations and sometimes protect them from hazardous external stimulation.³⁹⁰ The experimental results were consistent with the feature in biological systems, in which stronger stimulations induce higher neural excitations.^{391,392} Furthermore, the potentiation/depression performance was observed in the device as shown in **Figure 39f**. When consecutive positive pulses were applied to the device, the conductance increased monotonously, corresponding to a potentiation process. In contrast, the conductance of the device decreased monotonously as negative pulses were applied, corresponding to a depression process. The performance is crucial for brain-inspired neuromorphic computing in artificial neural networks (ANNs) that can process data locally.³⁷⁹

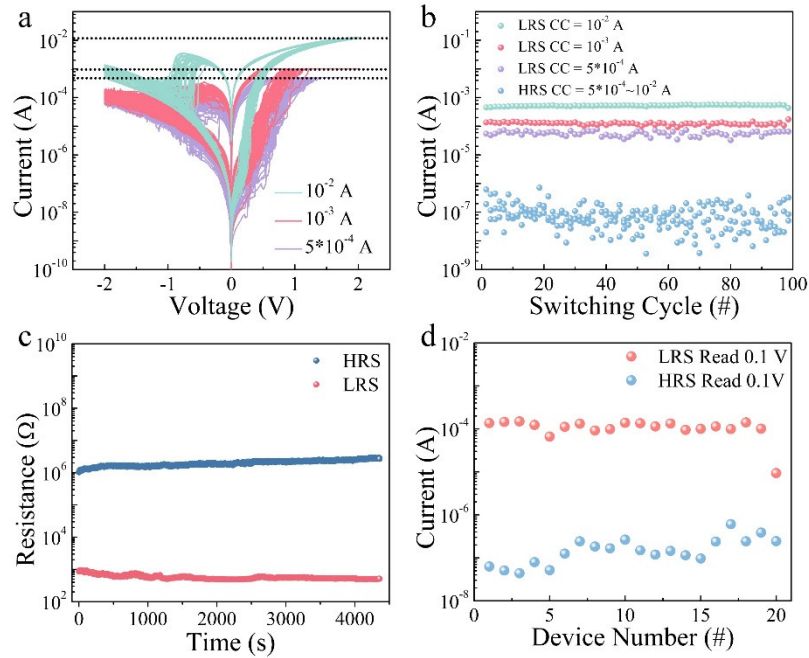


Figure 38. (a) DC switching cycle test under different compliance currents (CCs). 100 switching cycles for each test. (b) Resistance states distribution under different compliance currents (CCs). (c) The retention time of the HRS and LRS. (d) The device-to-device variation. The results are from the direct current (DC) switching cycle test.

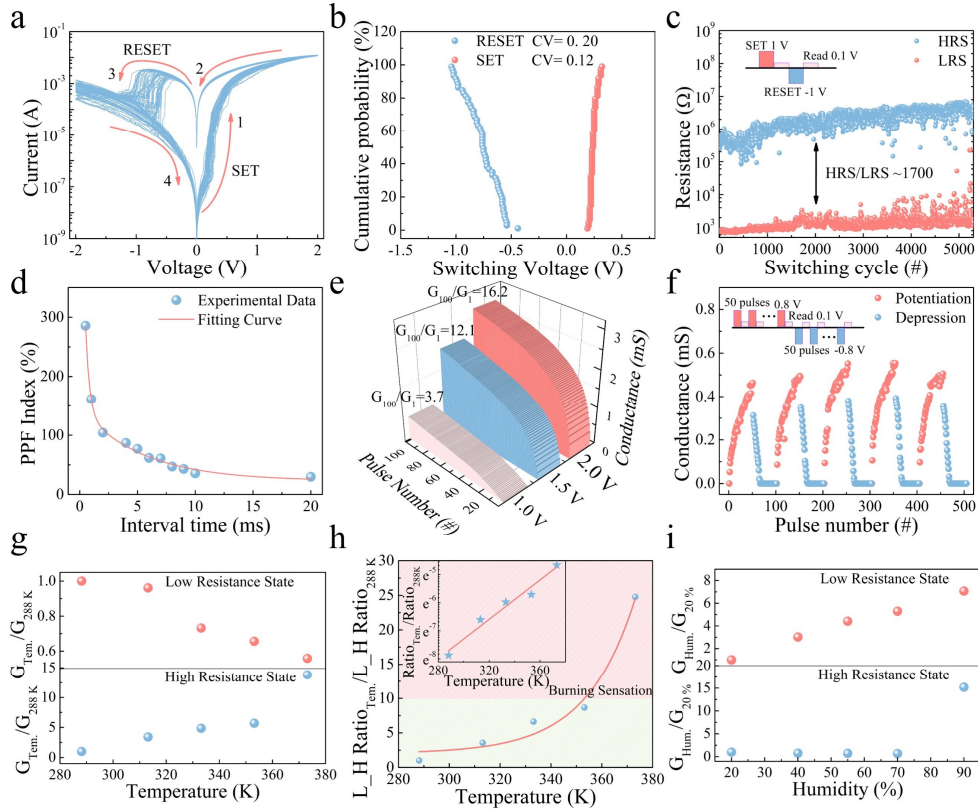


Figure 39 Electronic characterizations. (a) DC switching cycle test for 60 cycles. (b) Cumulative probability of the operation voltages. CV represents the “coefficient of variation” which was defined as the standard deviation divided by the mean value. (c) The endurance of the device, which is presented by the resistance distribution under consecutive switching operations. The pulse duration was 200 ms. (d) Short-term synaptic paired-pulse facilitation (PPF) behavior. The pulse amplitude was 1V. Data points were extracted from the average values of five tests. The fitting equation was $PPF = A_1 e^{-\frac{\Delta T}{\tau_1}} + A_2 e^{-\frac{\Delta T}{\tau_2}} + y_0$. The fitting parameters of A_1 , A_2 , y_0 , τ_1 , and τ_2 were 639.4, 123.2, 22.9, 0.3 ms, and 5.4 ms respectively. (e) Conductance modulation under consecutive pulses with different amplitudes. The pulse number was 100. The pulse duration and pulse interval time were both 10 ms. (f) Potentiation and depression performance of the device. (g) Conductance changes (LRS and HRS) under different temperatures. (h) Change of LRS/HRS ratio under different temperatures. L_H Ratio means the ratio of LRS/HRS. The X-axis and Y-axis are both in linear scale. For the inset, the X-axis and Y-axis are in linear scale and natural-logarithm scale, respectively. (i) Conductance changes (LRS and HRS) under different humidity levels.

The temperature and humidity sensory responses under different states of the intelligent matter were studied. As shown in **Figure 39g**, the temperature sensations at the LRS and HRS were measured. When the device was at LRS, the conductance value decreased (resistance increased) with the increase of temperature, indicating a negative temperature coefficient of conductance. On the contrary, when the device was at HRS, the conductance increased (resistance decreased) with an increased temperature. It demonstrated a positive temperature coefficient of conductance. Because the device can reversibly switch between the LRS and HRS, the temperature sensation was reconfigurable and programmable by the voltage. Additionally, the ratio of LRS/HRS increased monotonically with increased temperature, as shown in **Figure 39h**. The LRS/HRS ratio changed slowly with the temperature increase when the temperature was lower than around 350 °C. In comparison, the ratio increased exponentially when the temperature was further increased (>350 °C). As shown in the inset of **Figure 39h**, data points followed a linear feature in the linear and natural-logarithm scales. This exponential temperature sensation is analogous to that in biological systems, which can be considered a protection scheme to improve the survival rate.³⁹³ When the temperature of the surrounding environment surpasses a certain threshold point, the stimulation signal from sensory systems would be enhanced exponentially to alert the host that evasive action is required to escape from the current situation. Besides, the temperature can also potentially modulate short-term memory behaviors, which might be useful for temperature sensing.³⁹⁴ Furthermore, the conductance changes of LRS and HRS under different humidity levels are presented in **Figure 39i**. The water molecules were penetrating the switching layer from the lateral sides.^{219,395} The results were measured from low relative humidity (RH) to high RH. The HRS was insensitive to the humidity as the conductance was kept almost constant until the humidity level was too high. The conductance increased to a larger value at the humidity of 90%. In contrast, the conductance of the LRS increased constantly as the humidity increased, indicating a humidity-sensing functionality. To further confirm the reversibility of humidity sensation, the reversibility test of conductance changes is shown in **Figure 40**. The result confirmed that the effects of humidity on conductivity were reversible. It indicates that the device can be switched between humidity-sensitive and humidity-non-sensitive modes by switching the device between the HRS and LRS. The systematic electronic characterizations demonstrated that intelligent matter provided adjustable temperature and humidity sensations.

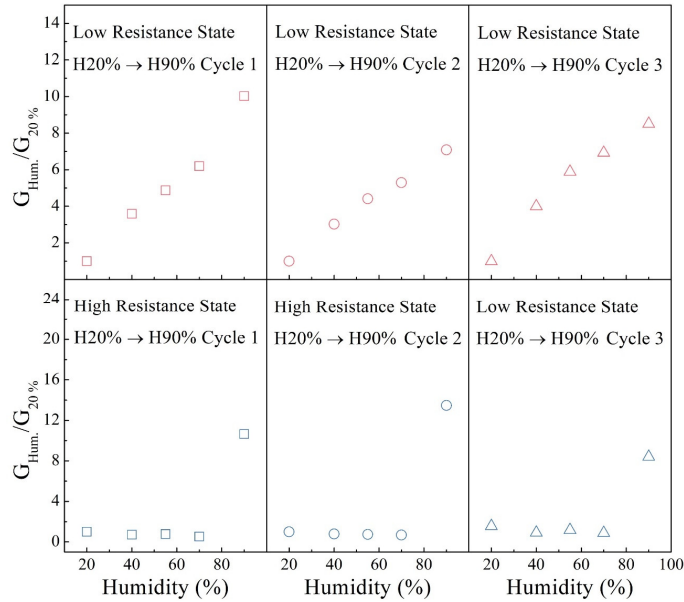


Figure 40. Reversibility test of conductance changes (LRS and HRS) under different humidity levels.

4.3.3 Working Mechanism Investigations

The working principle of the reconfigurable sensations has been investigated via experimental measurements and theoretical simulations. The typical $\log(I)$ - $\log(V)$ curve of the device over the positive voltage region is shown in **Figure 41a**. When the applied voltage was at the low-value region ($\text{Log}(|V|)$: $-2 \rightarrow -0.9$), the slope was around 1.13 which was nearly 1.0. The current increased proportionally to the applied voltage, which indicated the conduction mechanism was governed by Ohm's law. When further increasing the voltage, the current increased abruptly (resistance decreased abruptly). The device was SET to the LRS from the HRS due to the formation of the silver filaments.¹⁰ When the positive voltage was applied on the top Ag electrode, Ag atoms are oxidized into Ag^+ . The generated Ag^+ moved to the counter electrode side and was reduced into the Ag atom. High-conductivity Ag channels bridging the top and bottom electrodes were formed once enough Ag atoms were accumulated in the CIGSe switching layer, and the device showed the LRS. As shown in **Figure 41a**, the slope of the $\log(I)$ - $\log(V)$ curve was 1.09, close to 1.00, when the device was at LRS ($\text{Log}(|V|)$: $-2 \rightarrow 0.3$ V), indicating that Ohm's law governs the conduction mechanism, which is consistent with the filamentary model.¹⁰ When the voltage was reversed (negative voltage was applied), the inserted Ag atoms were reduced into Ag^+ , and the conductivity filaments were resolved. The device was RESET

to the HRS. **Figure 41b** exhibits the log (I)-log(V) curve over the negative voltage region. When the applied voltage was at the low-value region (Log(|V|): -2 → -0.2 V), the slope was around 1.01 which was close to 1.00, indicating Ohmic conduction that was the same as that of LRS over the positive region. It means the formed conductive filaments were stable under low negative voltages. When the negative voltage was high (Log(|V|) > 0.4), the current decreased suddenly, which indicated the conductive filaments ruptured and the device returned to HRS. When the device was at HRS under negative bias, the electrical conduction curve was fitted with the Schottky emission mechanism as shown in **Figure 41c**. To further confirm the transition between HRS and LRS was because of the Ag conductive filaments, a device of Mo/CIGSe/Mo with an inert top electrode was fabricated. The DC switching cycle test is shown in **Figure 41d**. No resistive switching phenomenon was observed, which confirmed that Ag atoms were essential for the resistance change. The resistive switching was derived from the formation/rupture of silver conductive filaments.

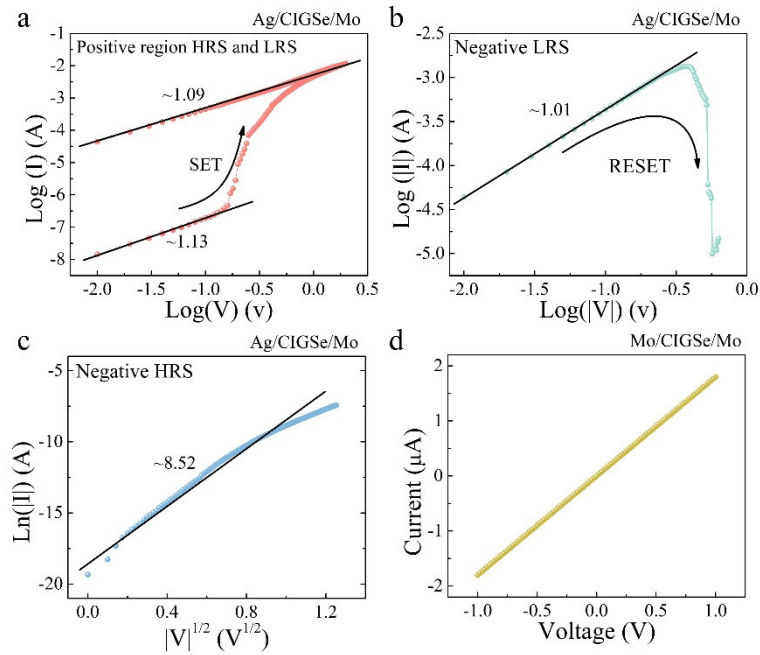


Figure 41. (a) The DC switching cycle test of the device in the log (I)-log(V) scale (positive region). (b) The DC switching cycle test of the device in the log (I)-log(V) scale (negative region). (c) The DC switching cycle test of the device in the $V^{1/2}$ -Ln(I) scale (negative region). (d) The DC switching cycle test of the Mo/CIGSe/Mo. The sweep voltage was $0 \rightarrow 1 \text{ V} \rightarrow -1 \text{ V} \rightarrow 0 \text{ V}$.

The principle of the opposite temperature sensations at the HRS and LRS was elaborated. As mentioned above, the foundation of resistive switching was the formation and rupture of the silver conductive channels, which implied that the electron conduction can be shifted between semiconductive and metallic states. At the HRS, the conductance was determined by the switching layer of CIGSe which is a p-type semiconductor.³⁹⁶ Ideally, at 0 K, semiconductors cannot conduct electrons or their conductivity is zero because all charge carriers are frozen in the valence band and below the Fermi level.³⁸⁵ With the increase of temperature, electrons in the valence band absorb thermal energy and jump to the conduction band, generating electron-hole pairs that act as charge carriers, as shown in **Figure 42a** (right). Electrical current will flow when voltage is applied due to the existence of charge carriers. Additionally, a higher temperature means that more thermal energy creates more electron-hole pairs and a higher density of charge carriers.³⁸⁵ Therefore, the conductance increased with the increased temperature when the device was at the HRS, indicating a semiconductive feature. In comparison, metal conducts electricity because many electrons in the metal can move freely.³⁹⁷ The main resistance for electrons' directional migration is from the thermal vibration of metallic atoms that scatter moving electrons. Thus, the conductivity of metals decreases with the increase of temperature, as higher temperature corresponds to stronger atomic vibrations. As shown in **Figure 42b**, the metallic filaments were formed at LRS. The conductance was dominated by the high-conductivity metallic filaments that exhibit metallic features. Therefore, the overall conductivity of the device decreased as the temperature increased. The intelligent matter enables opposite temperature sensations derived from semiconductive (HRS) and metallic (LRS) modes.

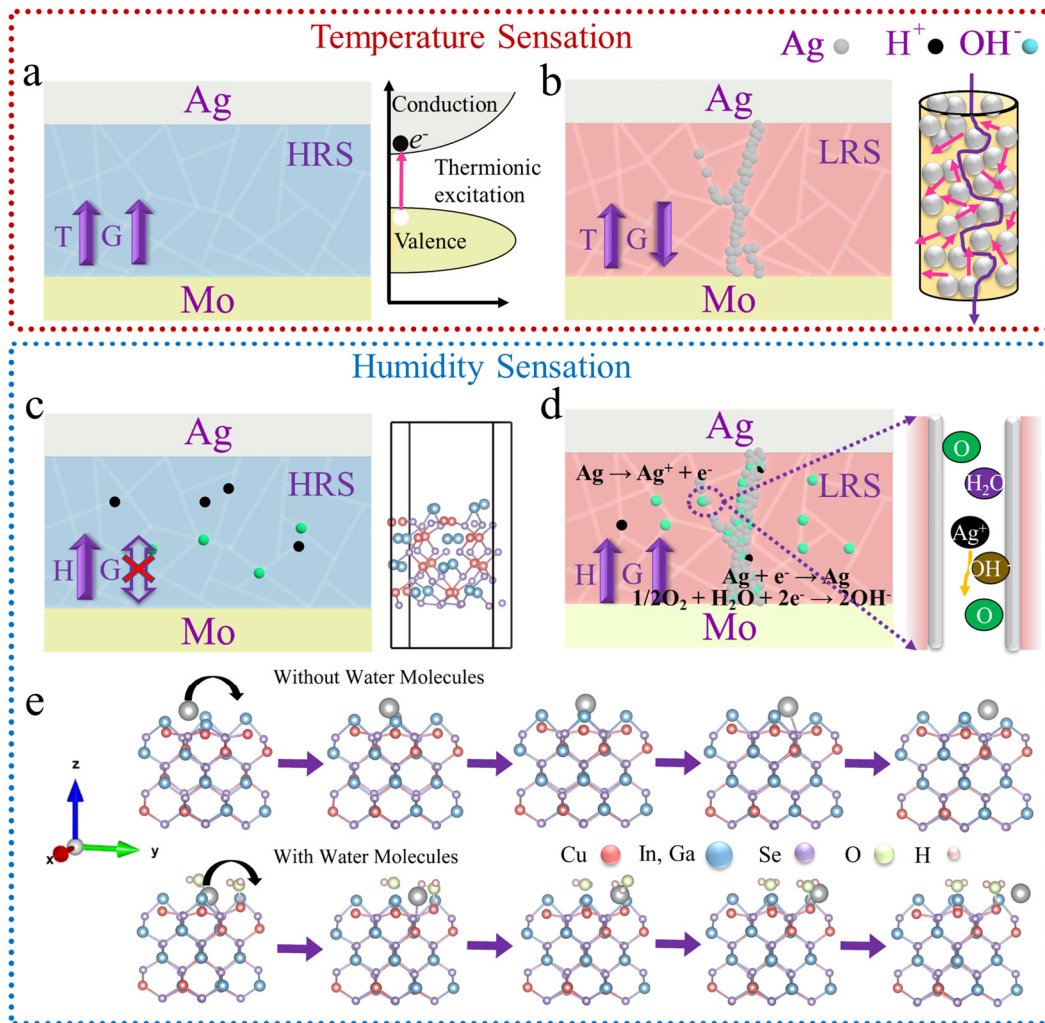
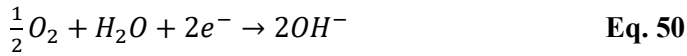


Figure 42. Working mechanism. (a) Schematic diagram of the HRS under different temperatures, Conductance increased with the increase of temperatures. The letter “T” and “G” in the picture means the temperature and conductance, respectively. The upward arrow and downward arrow mean the increase and decrease of the relevant values. (b) Schematic diagram of the LRS under different temperatures. Conductance decreased with the increase of temperature. (c) Schematic diagram of HRS under different humidity levels. Conductance barely changed as modulating the humidity. The letter “H” and “G” in the picture means the humidity and conductance, respectively. The upward arrow means the increase of the relevant values. (d) Schematic diagram of LRS under different humidity levels. Conductance increased with the increase of humidity levels. (e) Illustration of the diffusion mechanism of Ag atoms at the bare and H₂O-bonded surfaces.

As for the humidity sensory property, the device at different states showed different humidity sensitivities. The memristive device (based on the electrochemical metallization mechanism) operated under different humidity levels can be regarded as an electrochemical cell that is divided into two half-cells.³⁹⁵ Both half-cell electrochemical reactions, including the anodic oxidation and cathodic reduction, occurred separately during the resistive switching process. When the positive voltage was applied, anodic oxidation took place at the Ag/CIGSe interface, which induced the Ag ions into the switching layer. The oxidation reaction of anodic oxidation to generate oxygen was also plausible.³⁹⁸ But the oxidability of Ag was higher than the hydroxyl counterpart, which means the oxidation of Ag dominated the anodic oxidation reaction. The cathodic reduction at the counter electrode (bottom electrode) was described below:²¹⁹



When the device was at the HRS, the electronic properties were dominated by the switching layer of CIGSe. The main functional group that can be bounded to the CIGSe crystal structure with the existence of H₂O molecules was -O because oxygen molecules can be generated due to hydrolysis reaction under extra voltages.^{224,398} The -O functional group posed a robust interaction with the CIGSe crystal, indicating it can be bonded to the CIGSe surface. The work function (φ) was calculated by the following equation:

$$\varphi = E_{vac} - E_F \quad \text{Eq. 51}$$

where E_{vac} and E_F represent the vacuum level and Fermi level, respectively. The φ values of CIGSe and CIGSe-O were 5.40, and 5.15eV, respectively. A small variation of work function was observed before and after the bonding of the O- group. This means the CIGSe can show stable electronic features even with the existence of CIGSe-O (**Figure 42c**).³⁹⁹ However, when the humidity was too high, the conductance jumped to a high value compared to the pristine value (**Figure 39i**). The reason was that more hydroxyl ions and protons were generated and accumulated, which improves the conductivity of the switching layer.²⁷⁴ In comparison, the LRS showed humidity-sensitive features as shown in **Figure 42d**. The electronic properties of the LRS were dominated by the Ag conductive filaments. A higher humidity level facilitated the oxidation rate of Ag atoms since the total cell reaction was limited by the counter-electrode reaction.³⁹⁵ A higher humidity level provided more residual water species and

improved the reaction kinetics of the electrochemical cell, leading to a higher injection rate of Ag ions. Additionally, the water species (mainly $\text{-H}_2\text{O}$ and -O) absorbed on the surface of grain boundaries lowered the barrier of Ag ions migration, which was confirmed by the atomistic simulation.²²⁴ **Figure 42e** illustrates the diffusion mechanism of Ag atoms at the bare and O- bonded CIGSe crystalline surfaces. A higher humidity level was likely to cause more absorbed water molecules, which promoted the forming of thicker Ag metallic filaments corresponding to higher conductivity. The improved oxidation rate and migration of Ag ions in the presence of moisture both benefited the formation of thicker conductive filaments and higher conductivity (**Figure 42d**). Thus, a comprehensive explanation is provided to explain the intelligent temperature and humidity sensations.

4.3.4 Intelligent In-sensor Neuromorphic Computing

Intelligent low-level sensory and high-level cognitive in-sensor neuromorphic computing applications based on intelligent matter are demonstrated to clarify its promising prospects (**Figure 45**).³ The schematic diagram of the intelligent skin with tunable thermal sensitivities is shown in **Figure 45a**. When a point-source heat, such as a lighted candle, approaches the skin, the thermal energy is transmitted to the skin surface via thermal radiation. Thermal energy is received by thermal receptors and stimulated receptors then transmit relevant signals to the brain for further processing. The received thermal energy is distributed as a gradient on the surface. Because the radiation energy decays as it travels forward, further points receive less thermal energy. More specifically, the received heat decreases from the central point (the closest point to the thermal source) to the far point. A simplified model was built to mathematically demonstrate the thermal transmission distribution on a surface, as shown in **Figure 43**. The thermal source is assumed as a point. A constant amount of energy is spread out in an expanding sphere as it is transmitted away from the source. The thermal intensity at a certain point is described by **Eq. 52**.

$$S_F = \frac{P}{4\pi r^2} \quad \text{Eq. 52}$$

where S_F is the thermal radiation intensity at a specific point F. P is the total energy released per second. r is the distance between the light source and the specific point (the length of SF in **Figure 43**). The thermal radiation intensity at point F is described by **Eq. 53**:

$$S_F = \frac{d_0^2}{x^2 + d_0^2} S_C \quad \text{Eq. 53}$$

where S_C is the thermal radiation intensity at the central point C. The normalized thermal radiation intensity is shown in **Figure 44a**. The thermal energy density decreased quickly as the points got away from the central point. Mathematical manipulation can extend the thermal energy distribution from a one-dimensional space to a two-dimensional plane, which describes the thermal distribution more accurately and visually, as shown in **Figure 45b_1**.

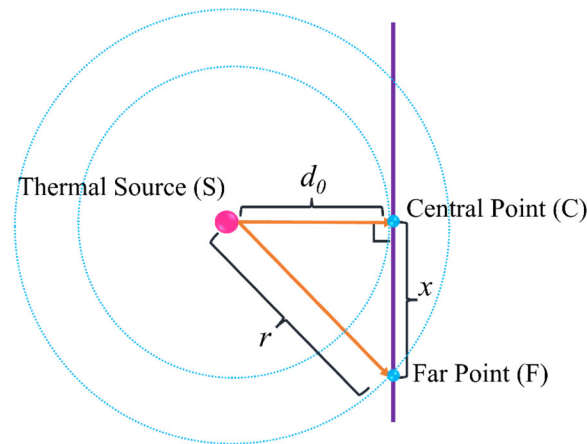


Figure 43. Schematic diagram for the calculation of thermal transmission distribution in one direction.

Additionally, the heat received by a specific point is proportional to the thermal energy density. The temperature increase due to the absorbed heat is described by :⁴⁰⁰

$$Q = mc\Delta T \quad \text{Eq. 54}$$

where Q is heating transfer, m is substance mass, and c is specific heat capacity. To simplify the model, the temperature at the central point (C) was assumed as 100 °C (393 K). The temperature of other points proportionally decreases, as determined by the received heat. Integrated intelligent thermal sensors act as thermal receptors mimicking the human skin. The reconfigurable temperature sensation enables different sensation responses under different operational modes to adapt to different environments. The HRS mode means that the temperature-sensory signals were conductance (or current) changes from the device at the HRS. Likewise for the LRS mode. Meanwhile, the HRS&LRS mode means the temperature-sensory signals of the LRS/HRS ratio change due to temperature variations. As shown in **Figure 45b_2**, the thermal array worked in the LRS mode which showed a negative coefficient of

conductance. The output decreased at the points closer to the central point. Besides, the output intensity decreased gradually as it was closed to the central point, which was consistent with the sensation response of the linear characteristic in the LRS mode **Figure 44a**. In comparison, the output signals increased at the points closer to the central point under the HRS and HRS&LRS modes. It can be observed that nonlinear features showed up in the two modes, which is due to the exponential relationship between the conductance and the temperature **Figure 44c** and **Figure 44d**. Furthermore, the sensitivity between the HRS and HRS&LRS modes was different. The output at the central point under the HRS mode (around 1.4) was smaller than that for the LRS&HRS mode (around 2.4) in **Figure 45b_3** and **Figure 45b_4**. The tunable and controllable thermal sensations may provide a promising strategy for advanced intelligence artificial skins for different working scenarios.

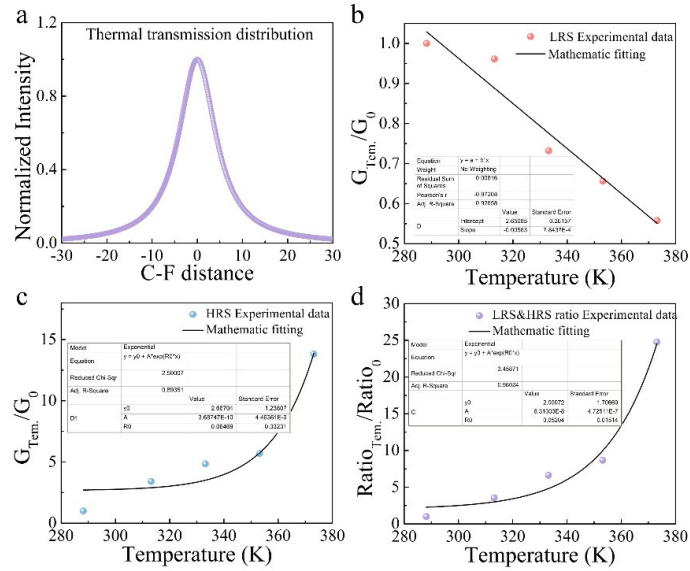


Figure 44. (a) Theoretical simulation of the thermal transmission distribution in one direction. (b) The change of $G_{Tem.}/G_0$ under different temperatures at the LRS model. (c) The change of $G_{Tem.}/G_0$ under different temperatures at the HRS model. (d) The change of Ratio $_{Tem.}/$ Ratio $_0$ under different temperatures at the HRS&LRS model. Ratio $_0$ is the ratio of LRS/HRS at room temperature (288K).

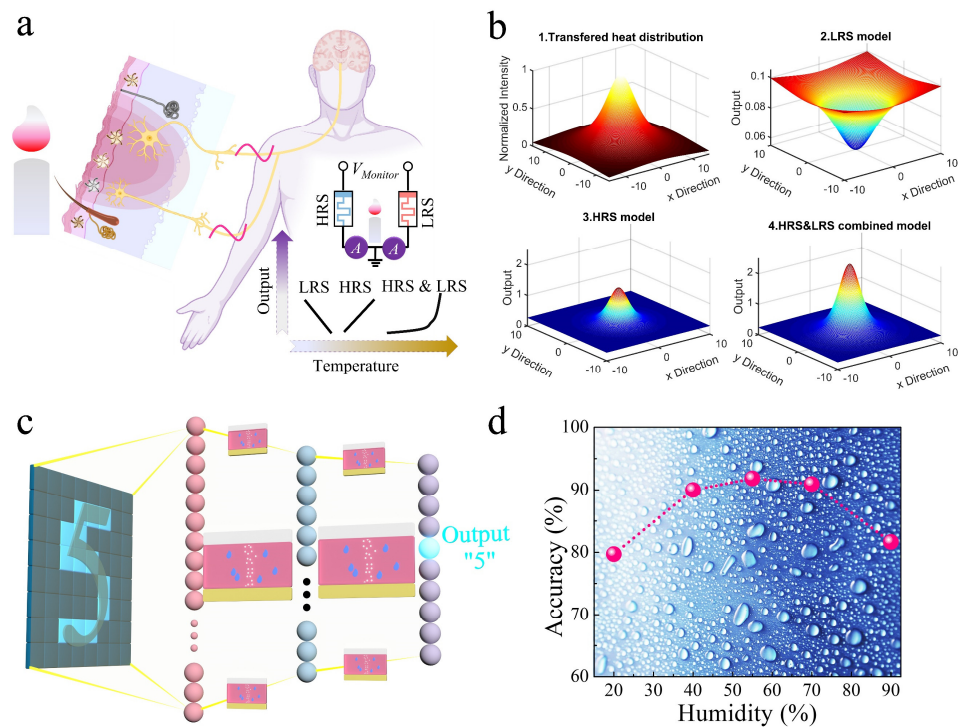


Figure 45. In-sensor neuromorphic computing. (a) Schematic diagram of the intelligence skin with tunable thermal sensitivities. (b) 1: The thermal transmission distribution on the surface of artificial skin from a point heat source. 2-3: The output distribution on the artificial skin in the LRS model, HRS model, and HRS&LRS model, respectively. (c) Schematic diagram of ANN for in-sensory neuromorphic computing for pattern recognition. (d) Neuromorphic computing accuracy under different humidity levels.

The high-level cognitive in-sensor computing based on intelligent matter under different humidity levels has been investigated. As shown in **Figure 46**, the intelligent sensor exhibits different conductance modulation features under different humidity levels, acting as a sensory artificial synapse enabling synaptic potentiation and depression. The intelligent matter with synaptic functions (or named sensory artificial synapse) is fundamental for constructing artificial neural networks (ANNs) for brain-inspired neuromorphic computing.³⁷⁹ The artificial synapse in ANNs stores intermediate synaptic weights as conductance, in which the matrix manipulation is implemented in the crossbar based on Kirchhoff's current law and Ohm's law. This methodology borrowed from the human brain can achieve massive parallelism computation by detecting electronic signals directly. Sensory artificial synapses can complete state-of-the-art in-sensor neuromorphic computing. Sensory synapses can sense the

changes in humidity, which means the humidity affects computing results. Human perception accuracy is affected by humidity levels.²⁷⁴ Thus, it is desirable to explore an intelligent device that is sensitive to humidity. So, it can be cooperative with light- and proton-dependent signal processing systems for mimicking the adaption behavior of human eyes under different environments.²⁷⁴ This work is part of the investigation for developing bionic robots, which makes the artificial machine more like human beings. For example, humidity or other external environmental factors induce deteriorative eyesight, which will trigger extra caution regarding outdoor activities by cooperating with other auxiliary systems. **Figure 45c** demonstrates a schematic diagram of the ANN used for in-sensor neuromorphic computing. The in-sensor neuromorphic computing was carried out based on the backpropagation algorithm for pattern recognition. The ANN is fully connected with the input layer of 64 neurons, the hidden layer of 36 neurons, and the output layer of 10 neurons. **Figure 45d** shows the pattern recognition accuracy under different humidity levels. It can be observed that the accuracy increased and peaked at the humidity level of 55 % and then decreased with further increased humidity. The variants of humidity levels changed the features of potentiation and depression in the memristive device, especially the nonlinearity of conductance modulations.⁴⁰¹ Lower nonlinearity can give a higher computing accuracy.³⁷⁹ The nonlinearity of the device was calculated to be 0.637 (RH 20%), 0.454 (RH 40%), 0.314 (RH 55%), 0.473(RH 70%), and 0.665(RH 90%).⁴⁰² The small nonlinearity for 55% RH gave a higher recognition accuracy.²⁷⁴ The results demonstrated that in-sensory neuromorphic computing was achieved by the intelligent matter acting in the role of sensory synapses in different humidity conditions. Notably, the pattern recognition simulation shown here was for conceptual elaboration based on the novel sensory synapse. Intelligent matter can potentially be used for advanced neuromorphic computing systems enabling multimodal sensory functions. The current intelligent device still suffers from the difficulty of decoupling the entangled temperature and humidity changes. The device can be individually used for either temperature or humidity sensing, demonstrating broader applications compared to the device with single sensing functions. More work is needed to investigate polynomial functions to track multiple variants at the same time, which can effectively deconvolute (or differentiate) the changes in temperature and humidity.

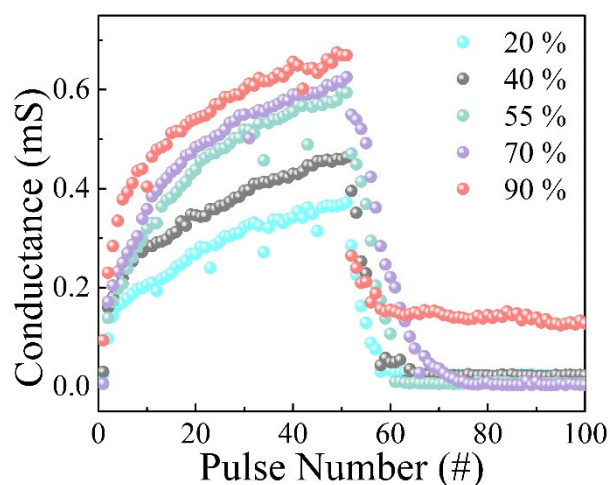


Figure 46. Electronic potentiation/depression characterizations under different humidity levels.

4.4 Summary

In summary, an intelligent matter enabling reconfigurable temperature and humidity sensations has been demonstrated for in-sensor neuromorphic computing. The delicate design was based on a memristive device with resistive switching capabilities to achieve reconfigurable sensory properties in a single device. Active Ag was employed as the top electrode to initiate filamentary resistive switching. CIGSe was used as the switching layer and showed good Ag mobility and semiconductive properties. External voltage triggered the formation/rupture of Ag MCF, which dominated the resistive switching. The device (Ag/CIGSe/Mo) can achieve an HRS/LRS ratio of 1700 and an endurance of 5000 cycles, indicating reliable resistive switching behaviors. Additionally, synaptic functions were realized, including PPF, and synaptic potentiation/depression behaviors. The existence and nonexistence of conductive filaments determined the metallic and semiconductive properties under different temperatures. Thus, opposite temperature coefficients of conductance were obtained at the LRS and HRS. Intelligent low-level sensory data processing was demonstrated. The intelligent matter with temperature sensations can work in the LRS mode, HRS mode, and HRS&LRS mode. Each mode has different sensation features and sensitivities. The reconfigurable sensation characteristics are promising for intelligent artificial skins for different working scenarios. Besides, water molecules influence the growth of conductive filaments, which affects the size of high-conductivity filaments and further modulates the value of LRS. The device acted as sensory artificial synapses that can be utilized for

high-level cognitive in-sensor computing. The humidity modulates the weight modulation (weight update margin and nonlinearity) of potentiation and depression characteristics, which affects the neuromorphic computing accuracy. An ANN was constructed to implement the backpropagation algorithm for pattern recognition. Different recognition accuracies were obtained under different humidity levels, demonstrating in-sensory computing capabilities. The intelligent sensor with reconfigurable temperature and humidity sensations benefits the development of innovative computational and sensory technology toward advanced e-skin, neurorobotics, cyborg, and human-machine interaction.

Chapter 5. Broadband optoelectronic synapse enables compact monolithic neuromorphic machine vision for information processing

The temperature and humidity sensing functions were investigated in the previous chapter. This chapter will extend the sensing function to light sensing and image processing with memristive devices, which is crucial for machine vision systems.

Traditional machine vision is suffering from redundant sensing data, bulky structures, and high energy consumption. Biological-inspired neuromorphic systems are promising for compact and energy-efficient machine vision. Multifunctional optoelectronics enabling multi-spectrum sensitivity for broadband image sensing, feature extraction, and neuromorphic computing are vital for machine visions. Here, we design an optoelectronic synapse that enables image sensing, convolutional processing, and computing. Multiple synaptic plasticity triggered by photons can implement photonic computing and information transmission. Convolutional processing is realized by ultra-low energy kernel generators fully controlled by photons. Meanwhile, the device shows the ability of conductance modulations under electronic stimulations that implement neuromorphic computing. For the first time, this two-terminal broadband optoelectronic synapse enables front-end retinomorphic image sensing, convolutional processing, and back-end neuromorphic computing. The integrated photonic information encryption, convolutional image pre-processing, and neuromorphic computing capabilities are promising for compact monolithic neuromorphic machine vision systems.

5.1 Introduction

The Von Neumann bottleneck and the difficulty of further shrinking device size triggered the rising of post-Moore techniques. Propelling computing technology beyond the scaling limits requires a comprehensive reconsideration of chip technologies ranging from fundamental physics, to material science, device design, electronic circuits, and architectures.⁴⁰³ In conventional machine vision systems, an integrated photoreceptive array, an analog-to-digital converter system, a memory unit, and a processing unit are needed to complete sensing and cognitive tasks. The physical separation of those units causes sensing data redundancy, data access delay, frequent data shuttling, and high energy consumption.²⁶³ Particularly, multiple components make the traditional machine vision system bulky with high fabrication costs. Innovative technology like biology-inspired neuromorphic systems may

provide solutions to these challenges. Neuromorphic machine vision enabling sensing and processing on-site can significantly improve processing efficiency by avoiding frequent data shuttling.⁴⁰⁴ Developing optoelectronics devices for neuromorphic machine vision systems with broadband sensing and fast data processing abilities are crucial, which have the potential to revolutionize the fields of real-time video analysis, autonomous vehicles, medical diagnosis, etc.⁸

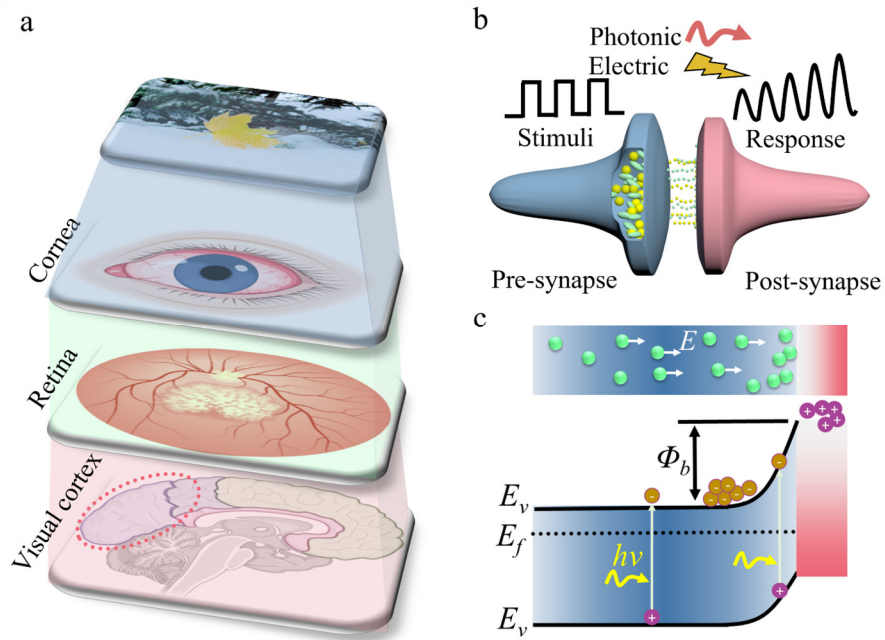


Figure 47. The concept of the artificial retina. (a) Image processing hierarchy in biological systems. (b) Schematic diagram of the biological synapse operated by electronic and photonic stimuli. (c) Schematic diagram of modulated heterojunction enabling photonic sensitivity and electronic plasticity.

Neuromorphic machine visions with compact configurations are promising for energy-efficient sensing and computing systems.^{3,388} The simplified image processing hierarchy in human eyes is illustrated (**Figure 47a**).⁴⁰⁵ The light goes through the cornea and is projected on the innermost layer of the eyeball structure called the retina. High-density photoreceptive cells on the membrane of the retina can detect the photons and respond by generating neural spikes. The image pre-processing in the retina is vital for high-level object recognition, location, tracing, and so on.⁴⁰⁶ Particularly, the color of the object carries important information, which requires color-sensitive photoreceptors to detect light rays with different wavelengths.³⁰¹ After being preprocessed appropriately (filtered, reflected, and

refracted), the received image is transformed into the visual cortex of the brain via optic nerves, where the image is processed into vision information.⁴⁰⁵ To realize neuromorphic vision systems, although challenging, it is essential to develop artificial optoelectronic synapses that can complete multi-spectrum sensing and computational tasks.

An optoelectronic synapse that is sensitive to both broadband photonic and electronic stimulations is essential for image sensing,⁴⁰⁷ pre-processing,⁴⁰⁸ transmitting signals,⁴⁰⁹ and neuromorphic computing.¹⁴ Whereas, a single broadband optoelectronic synapse device undertaking the above multiple tasks for compact monolithic neuromorphic vision systems is yet to come. Memristive-based optical devices can sense photonic signals and show memory functions. They are promising to develop compact machine vision systems with both image sensing and neuromorphic computing.⁴¹⁰ Table 1 summarizes memristive-based optoelectronic synapses for neuromorphic machine vision. Two-terminal metal-oxide devices enable high-density crossbar and 3D integration. This is crucial for neuromorphic systems that require high-density artificial synapses and neurons integrated into a single chip.²⁵⁷ Besides, image sensing, especially broadband sensing, is vital for high-precision image recognition as images from the surrounding world are a mixture of multiple colors with different light wavelengths. Some light-sensitive materials, such as 2D materials,⁴¹¹ perovskite materials,⁴¹² phase change materials,⁴¹³ are employed to construct optoelectronic synapses. A gate voltage is needed to modulate the defects distribution,⁴¹⁴ ferroelectric orientations,⁴¹⁵ or crystal structure⁴¹³ to achieve broadband sensing, which will sacrifice the integration density compared to two-terminal counterparts. Furthermore, image preprocessing is executed before the actual cognitive recognition and other tasks.⁴¹⁶ The key feature of the image needs to be extracted to improve the processing accuracy and efficiency. Convolution image processing is an essential step for CNNs that is considered one of the most powerful deep learning algorithms.⁴¹¹ However, light-controlled kernel generators that can read out filtered images directly have not been demonstrated, which can avoid parasitic currents, decrease energy consumption, and increase processing speed by avoiding data shuttling. The sensed and preprocessed image is the input of the artificial neural networks that complete the neuromorphic computing for cognitive tasks. Artificial neural networks implementing vector-matrix multiplication (VMM) have achieved some pioneering progresses.⁵⁴ Gradually modulated conductance is required to program the synaptic weight in artificial neural networks. So far, to our best knowledge, the broadband two-terminal optoelectronic synapse that can realize front-end retinomorphic image sensing, convolution processing,

and back-end neuromorphic computing, has not been reported. The technology poses very promising prospects for advanced neuromorphic machine vision.

Table 1. Summary of memristive-based optoelectronic synapse for neuromorphic machine vision.

Materials	Two terminals	Image sensing	Broadband sensing	Image preprocess	Neuromorphic computing	Ref.
ZnO/MoO ₃	✓	✓	✓	✓	✓	This work
MXene-ZnO	✓	✓	✗	✓	✓	274
MoO _x	✓	✓	✗	✓	✗	417
NiO/TiO ₂	✓	✓	✗	✗	✗	418
Ag-TiO ₂	✓	✗	✗	✓	✓	419
Pb(Zr _{0.2} Ti _{0.8})O ₃	✓	✓	✗	✗	✓	280
FAPbI ₃	✓	✓	✗	✗	✓	412
PdSe ₂ /MoTe ₂	✗	✓	✓	✓	✗	411
ZnO/In ₂ O ₃	✗	✓	✓	✗	✓	414
α-In ₂ Se ₃	✗	✓	✓	✗	✓	420
MoS ₂ /BaTiO ₃	✗	✓	✓	✗	✓	421
AlGaIn/GaN	✗	✓	✓	✗	✓	422
WS ₂ /PbZr _{0.2} Ti _{0.8} O ₃	✗	✓	✓	✗	✗	415
MoS ₂	✗	✓	✗	✓	✗	407
WSe ₂	✗	✓	✗	✗	✓	14
WS ₂	✗	✓	✗	✗	✓	423
VO ₂	✗	✓	✗	✗	✓	413

To develop a broadband compact optoelectronic synapse with multiple functions (**Figure 47b**), we designed a two-terminal device to mimic an optoelectronic synapse that is sensitive to photonic and electronic stimulations. The fabrication process was compatible with current available COMS techniques. The switching layer was ZnO/MoO₃ whose conductance was tunable under photonic and electronic stimulations. The ZnO showed particularly good broadband photo-detective and non-volatile resistive switching properties.^{172,424,425} The MoO₃ acted as a hole transport layer that will facilitate the photocurrent generation under light illuminations.⁴²⁶ Meanwhile, the Schottky-like contact was formed between ITO/ZnO (ITO, indium tin oxide) (**Figure 47c**). The oxygen vacancies in the ZnO can be moved under the applied electrode field.⁴²⁷ This changed the barrier height at the interface of ITO/ZnO and the resistance of bulk ZnO, which realized reversible resistive switching to mimic synaptic

plasticity. Besides, ITO as the top electrode was transparent which was essential for photonic-tunable devices. It also benefited the resistive switching stability as it can act as the oxygen ion reservoir.¹⁷⁶

In the fabricated broadband optoelectronic synapse, synaptic plasticity triggered by photons, including the EPSC, SADP, PPF, and SNDP was demonstrated. It was promising for image sensing, photonic computing, and information transmission. The energy consumption for the photonic operation was around 37 pJ, demonstrating low energy consumption. The broadband optoelectronic synapse exhibited different sensitivity to different wavelengths, demonstrating the function of broadband image-sensing. Particularly, the current gains were constant over a certain voltage window under different light illumination, which was employed to develop an ultra-low energy kernel generator fully controlled by photons for convolution processing. This can realize the pre-processing of feature extraction. Meanwhile, the device showed reliable resistive switching under electronic stimulations. The 6 x 6 device array was fabricated with small variations of 0.7 % (HRS) and 3.4 % (LRS). The potentiation/depression was obtained to implement neuromorphic computing. The image recognition accuracy was higher than 90 %, which confirmed the practicable application for cognitive tasks. The resistive switching mechanism was investigated. The modulated barrier height at the ITO/ZnO interface and the change of ZnO conductivity were responsible for the tunable conductance. This was due to the electronic-controlled oxygen vacancy migration. The device has a capacitor-like two-terminal structure. This benefits a high integration density. For the first time, this broadband optoelectronic synapse can be utilized for front-end retinomorphic image sensing, convolutional processing, and back-end neuromorphic computing for cognitive tasks. This technology is promising for compact monolithic neuromorphic machine vision systems enabling photonic information encryption, convolutional image processing, and neuromorphic computing.

5.2 Experimental Section

5.2.1 Device Fabrication

The wafer covered with SiO₂ oxide (280 nm) was used as the substrate. The device structure was ITO (Indium tin oxide)/ZnO/MoO₃/SiO₂/Si (from the top to the bottom). The substrate was ultrasonically cleaned in water, ethanol, and acetone sequentially. The electrode and switching layer materials were deposited by magnetic sputtering with a background pressure of 5x10⁻⁷ Torr. The target

was Mo metal, which was used as a bottom electrode by DC magnetic sputtering. 100 W was the sputtering power. 5 mTorr was the deposition pressure. The working gas was pure Ar. The MoO₃ layer was deposited via reactive sputtering. 100 W was the sputtering power. 5 mTorr was the deposition pressure. The working gas was pure Ar/O₂ (3/1). For the ZnO, radiofrequency (RF) magnetic sputtering was used. The target was ZnO. 200 W was the sputtering power. 5 mTorr was the deposition pressure. The working gas was Ar/O₂ (24/1). A piece of shadow mask was utilized to fabricate the 100 μm device. The ITO was deposited by RF magnetic sputtering. The target was ITO. 100 W was the deposition power. 5 mTorr was the deposition pressure. The working gas was Ar/O₂ (20/0.3). The deposition temperature was set to 200 °C (substrate temperature).

5.2.2 Material and Device Characterization Methods

Scanning Electron Microscopy (SEM, Hitachi SU5000 FESEM) images were measured. The accelerating voltage was 15.0 kV. The materials composition mapping was measured by EDX (Hitachi SU5000 FESEM). GIXRD (PANalytical X'Pert PRO system) was used to study the crystal structures of materials. The UV-vis absorption spectroscopies of materials were obtained by Shimadzu UV-2600i to investigate optical properties. XPS (Thermo-VG Scientific ESCALab 250) was employed to study the surface characteristics of materials. Besides, ultraviolet photoelectron spectroscopy (UPS, Thermo-VG Scientific ESCALab 250) was utilized to measure the work function (Φ) of material surfaces. The electronic properties of the devices were measured by a Keysight B2985A equipped with the probe station of MPI TS150. The light illuminations with different wavelengths and powers were provided by LEDs driven by a waveform generator (Agilent 33220A).

5.2.3 Simulation Methods

Materials simulations: Density functional theory (DFT) simulations were employed to study electronic properties. The Vienna ab initio simulation package (VASP) was utilized. The core electrons and nucleus were described by the projector augmented wave (PAW) method. The Heyd-Scuseria-Ernzerhof (HSE) hybrid function was utilized to describe electron exchange and correlation. In all calculations, the cut-off energy of 400 eV was used for the plane-wave basis restriction. K-points were sampled as 2×2×4 for the Brillouin-zone integration under the Monkhorst-Pack scheme. Forces applied on atoms were < 0.02 eV/Å in fully relaxed structures. The self-consistency accuracy (10⁻⁵ eV) was

obtained for electronic loops. To obtain the density of states (DOS) and band structure, the model of $2 \times 2 \times 1$ supercell was utilized. To calculate the work function of materials, 4-atomic-layer-thick slabs were used. A gap of ~ 20 Å between the surface and vacuum was inserted to prevent spurious interactions induced by periodic boundary conditions.

Neuromorphic computing and convolution image processing: Neuromorphic computing for pattern recognition was carried out on the CrossSim platform. The code for the color recognition convolutional image processing was developed with MATLAB. In the convolutional image processing, 3×3 simple kernels with the functions of soft, vertical edge detection, horizontal edge detection, and edge sharpening were applied to 2D input images. The image was taken with a phone camera. The “Padding” was applied to produce the output that is the same size as the input counterpart (pad edges with extra “fake” of value 0). The stride of 1 was used during the convolution process.

5.3 Results and Discussion

5.3.1 Materials Characterizations

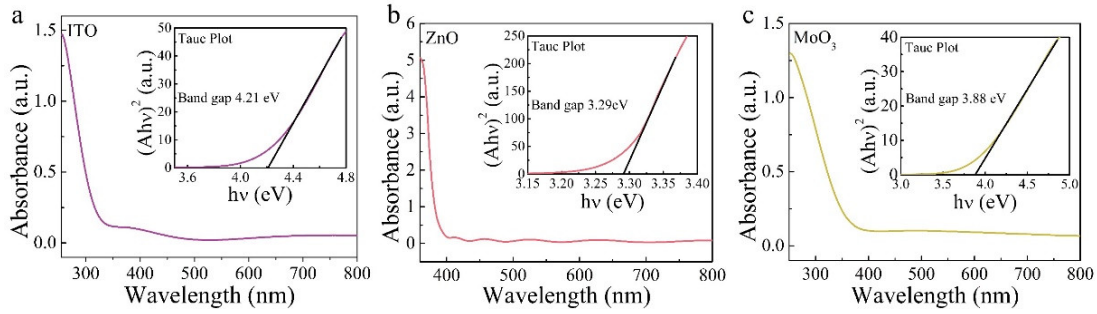


Figure 48. (a) UV-visible absorption spectroscopy of the ITO thin film. Inset is the Tauc plot for calculating the optical band gap. (b) UV-visible absorption spectroscopy of the ZnO thin film. Inset is the Tauc plot for calculating the optical band gap. (c) UV-visible absorption spectroscopy of the MoO₃ thin film. Inset is the Tauc plot for calculating the optical band gap.

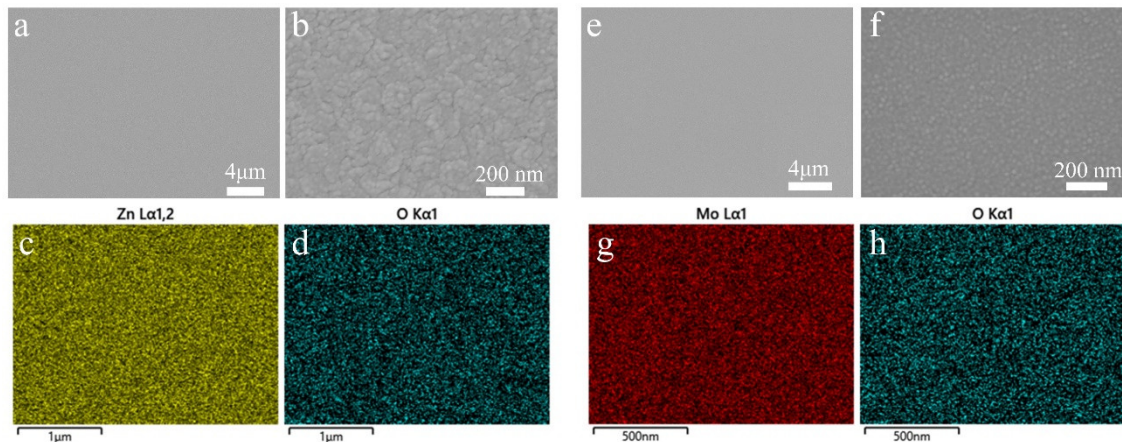


Figure 49. (a-b) The surface morphology of ZnO with different magnifications. (c-d) The composition mapping of ZnO thin film. (e-f) The surface morphology of MoO₃ with different magnifications. (g-h) The composition mapping of MoO₃ thin film.

The structure of the optoelectronic synapse was ITO/ZnO/MoO₃/Mo/Si (from top to bottom). A transparent conductive film (ITO) was utilized as the top electrode so that the light can go through the top electrode and interact with the switching layer to realize photonic-controlled synaptic behaviors. The ITO showed good conductivity with a sheet resistance of 5 Ω/sq. The optical absorption spectroscopy of the ITO thin film (**Figure 48a**) showed a sharp decrease in the wavelength range of 260-330 nm followed by a plateau region. The optical band gap was calculated based on the absorption spectrum described by the Tauc plot (the inset of **Figure 48a**).⁴²⁸ The band gap of ITO in this device was 4.21 eV. The transmittance spectroscopy of the ITO thin film shows that the transmittance to light with the wavelength higher than 390 nm surpassed 80 %. The high transmittance allowed more photons with a wide range of wavelengths to go through the top electrode, which benefited the photonic modulation of the device. The Tauc plots of optical absorption spectroscopies of ZnO (**Figure 48b**) and MoO₃ thin films (**Figure 48c**) determined the band gaps of 3.29 eV (ZnO) and 3.88 eV (MoO₃). This confirmed the strong absorption feature over the ultraviolet region. This can explain the reason the device was sensitive to ultraviolet light (390 nm). Particularly, the device also showed responses to light illumination with wavelengths of 460 nm and 570 nm. Because some defects (oxygen vacancies) in the switching layer induced impurity energy levels inside the forbidden band of ZnO and MoO₃.²⁰⁰ These defect energy levels can absorb photons with higher wavelengths and change the carrier density of the switching layer, demonstrating multi-spectrum sensitivity.⁴²⁹

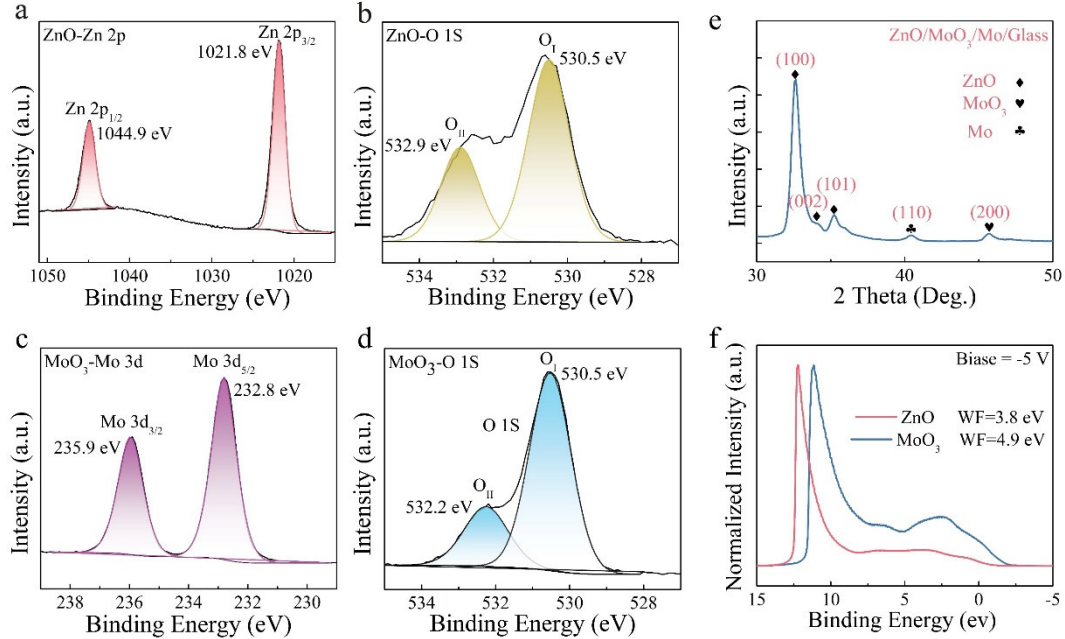


Figure 50. (a-b) High-resolution XPS spectra of ZnO. (c-d) High-resolution XPS spectra of MoO₃. (e) The XRD pattern for the multilayer device. (f) The work functions of switching layer MoO₃ and ZnO measured using UPS.

The film of ZnO was smooth and crack-free (**Figure 49a** and **b**). The composition distribution was homogeneous (**Figure 49c** and **d**). The surface of MoO₃ (**Figure 49e** and **f**) was dense and crack-free. The round shape and uniform grain with a size of around 10 nm were observed (**Figure 49f**). The Mo and O elements were distributed homogeneously in the composition mapping of the MoO₃ thin film (**Figure 49g** and **h**). Homogeneity films for constructing integrated array with small device-to-device variations is important.⁵¹ The thickness of MoO₃ and ZnO were around 20 nm and 200 nm respectively, which were employed as the switching layer. The multi-layers showed good adhesiveness. To further study the chemical states of the material surface, XPS was employed. In the high-resolution XPS spectra of ZnO, two characteristic peaks of binding energy at 1044.9 eV and 1021.8 eV were observed, corresponding to Zn 2p_{3/2} and Zn 2p_{1/2} respectively (**Figure 50a**). The split of these spin-orbital components was approximately 23.1 eV, which confirmed the +2 oxidation state of Zn atoms.⁴³⁰ In the O 1s spectrum (**Figure 50b**), two peaks at 530.5 eV and 532.9 eV corresponded to the O²⁻ in the Zn-O bonding and absorbed oxygen.⁴³⁰ The high-resolution scan of the Mo 3d core level spectra exhibited two characteristic peaks at 232.8 eV (Mo 3d_{5/2}) and 235.9 eV (3d_{3/2}) in the XPS spectra of MoO₃

(**Figure 50c**). The split of these spin-orbital components was around 3.1 eV. The results fitted the Mo^{6+} state.⁴¹⁷ Two O 1s peaks were assigned to the bonded (530.5eV) and absorbed (532.2 eV) oxygen (**Figure 50d**). Besides, GIXRD was utilized to further investigate the crystalline structure of the thin film as shown in **Figure 50e**. The intensive peak at 32.6° was attributed to the (100) plane of wurtzite-structured ZnO.⁴³¹ Weak peaks at 34.1° and 35.2° assigned to ZnO were also observed. The characteristic peaks at 40.5° and 45.7° corresponding to Mo (110) and MoO_3 (200) can be found.^{129,432} The results confirmed that only characteristic peaks of desired materials were detected, and no impurity phase was observed. Besides, the work functions of switching layers were measured (**Figure 50f**) to investigate the band gap alignment in the device. The above characterizations showed that high-quality materials regarding surface morphology, composition distribution, and crystal purity were fabricated. This is vital for high-performance optoelectronic devices.

5.3.2 Retinomorphic image sensing and convolution processing.

Optoelectronic synapse with multi-spectrum sensitivity has been investigated. The I–V curves were shown under different illuminations (**Figure 51a**). A typical hysteresis loop was observed, demonstrating memristive effects.¹⁷ The pristine device was at a HRS. It was switched to a LRS when positive voltages were applied. The device was switched back to HRS when negative voltages were applied (**Figure 51a**). The device exhibited an analog resistive switching. The resistance changed gradually instead of abruptly changes, which is crucial to mimic synaptic plasticity for neuromorphic computing.⁴³³ Besides, the resistive switching was asymmetric due to the asymmetric structure of the device. This feature benefits the alleviation of sneak currents in integrated crossbar arrays. Notably, the device was sensitive to multiple spectra maintaining resistive switching capabilities. The current under both HRS and LRS increased by different margins when the UV light (390 nm), blue light (460 nm), and green light (570 nm) were shined on the device. The changes in the HRS and LRS under different photonic stimuli are shown (**Figure 51b**). The error bar describes the cycle-to-cycle variation. The resistance of both HRS and LRS was decreased under light illumination compared to their dark counterparts. This reflects in the current increase under illumination (UV, green, blue) versus dark state (**Figure 51b**). Notably, UV (390 nm) induced more significant changes in device resistance compared to the blue light (460 nm), and green light (570 nm) counterparts. The device was insensitive to red light (620 nm). Because the photon of red light did not have enough energy to generate carriers.

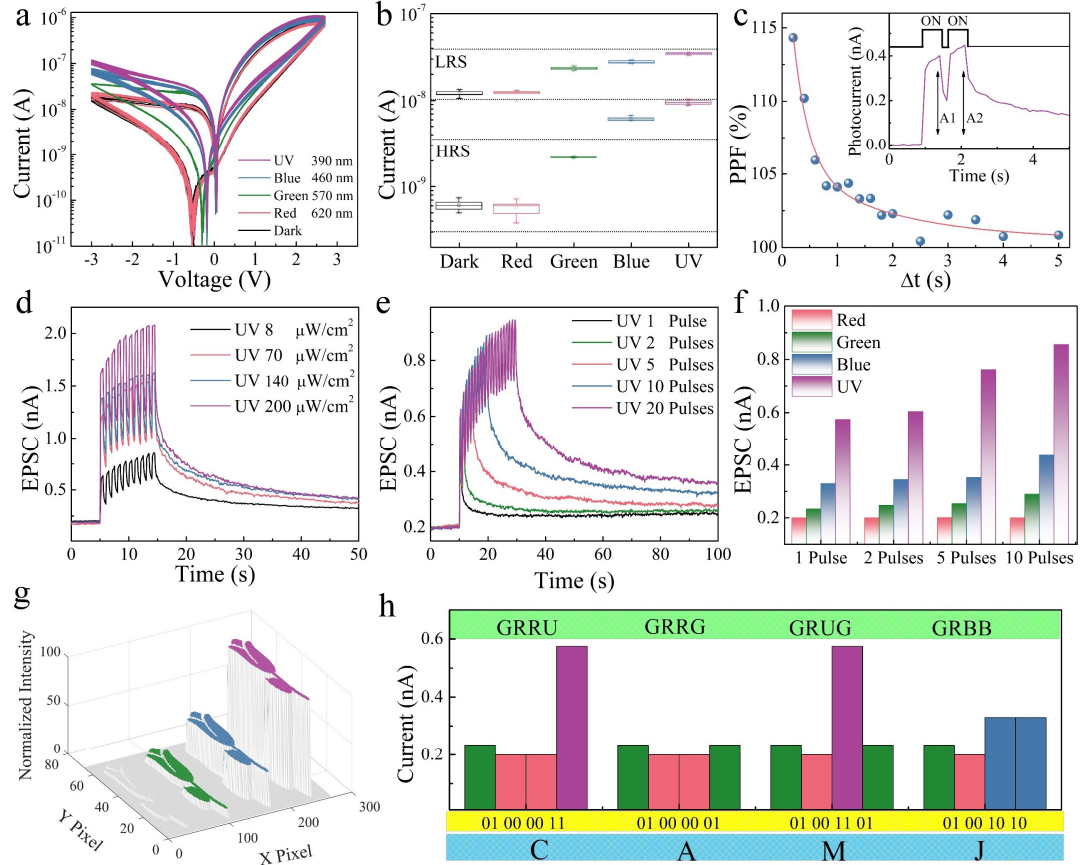


Figure 51. Photonic stimulations on the optoelectronic synapse. (a) The I-V curves of resistive switching under illumination with different wavelengths. 10 cycles for each test. The light density was $8 \mu\text{W}/\text{cm}^2$. This power density was used in other tests if no specific instruction was given. (b) HRS and LRS under illumination with different wavelengths. Read voltage was -0.8 V . (c) Short-term synaptic PPF behavior under photonic stimulations. The light wavelength was 390 nm (ultraviolet, UV), pulse duration was 500 ms . $PPF = \alpha e^{\frac{-\Delta T}{\tau_1}} + \beta e^{\frac{-\Delta T}{\tau_2}} + y_0$. The fitting parameters $\alpha = 5.349$, $\beta = 18.916$, $\tau_1 = 1.803$, $\tau_2 = 0.279$, $y_0 = 100.514$. (d) EPSC responses under UV light with different power densities. The pulse frequency was 1 Hz . The duty cycle was 50% . (e) EPSC responses under the UV light with different pulse numbers. The pulse frequency was 1 Hz . The duty cycle was 50% . (f) EPSC values under photonic stimulations with different wavelength and pulse numbers. (g) Recognition results in a dark condition and illumination at 390 nm 460 nm 570 nm 620 nm for 10 pulses (pulse frequency was 1 Hz , duty cycle 50% , sample power density). (h) The decode results of the photoelectronic synapse to the American Standard Code for Information Interchange (ASCII).

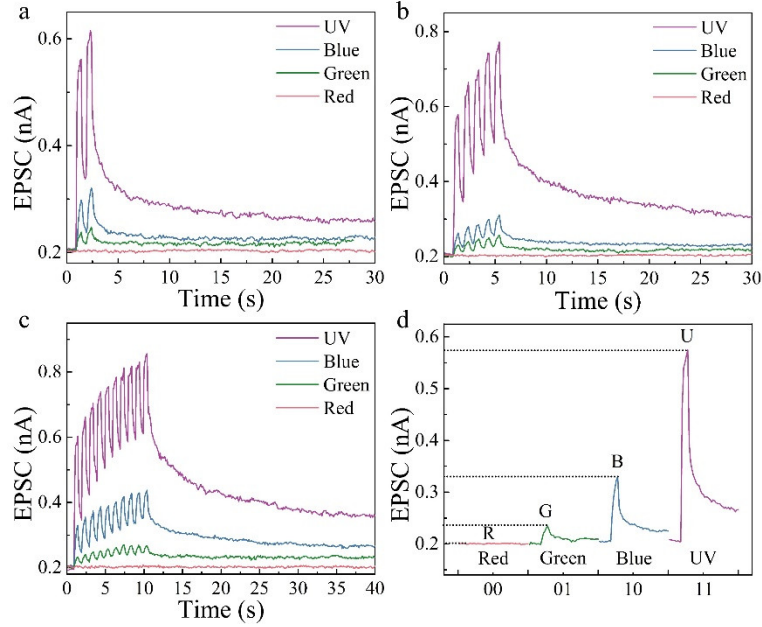


Figure 52. (a) EPSC response of 2-pulsed photonic stimulations with different wavelengths. The pulse frequency was 1 Hz. The duty cycle was 50%. (b) EPSC response of 5-pulsed photonic stimulations with different wavelengths. The pulse frequency was 1 Hz. The duty cycle was 50%. (c) EPSC response of 10-pulsed photonic stimulations with different wavelengths. The pulse frequency was 1 Hz. The duty cycle was 50%. (d) Define the photonic pulses with different wavelengths to decode two-digit information of 00 (Red light, 620 nm), 01 (Green light, 570 nm), 10 (Blue light, 460 nm), and 11 (UV light 390 nm). One pulse with the duration of 0.5 s was used for the operation.

Moreover, the synaptic plasticity of the device under different light illuminations has been studied. In biological systems, the transmission of neurotransmitters via synapses requires a certain delay time to relax after excitation. The net synaptic strength can be observed because of residual neurotransmitter ions in the last excitation. This is the characterization of PPF.⁴³⁴ The PPF feature was investigated in the device operated by UV photons.³⁴⁰ It can be found that the plasticity strength decreased exponentially with the increase of interval time between two consecutive pulses (**Figure 51c**). The inset presents the typical photocurrent characteristics under two photonic stimulations. The experimental results fitted well with the theoretical equation, demonstrating that the device can mimic the biological short-term PPF by photonic operations.⁴³⁵ Besides, the SADP was obtained. 10 pulses with different power densities were applied to the device (**Figure 51d**). The EPSC represented by currents following

through the device increased with the increase of the power density. This mimicked the biological function that stronger stimulations trigger higher amplitudes of responses. The EPSC changes under different pulse numbers were also presented (**Figure 51e**). Higher EPSC responses after more pulses were observed. This feature was like the SNDP in biological systems, in which multiple and repeated stimulations can induce stronger responses from biological individuals.⁴³⁶ Notably, the device was sensitive to multiple spectra. The EPSC response curves under different photonic wavelengths and pulse numbers are presented (**Figure 52**). Summarized EPSC values (**Figure 51f**) showed that the device was insensitive to red light (620 nm). In comparison, obvious responses were observed when the photonic wavelength was shorter than 570 nm. The UV light induced the strongest responses as the EPSC reached 0.8 A. The green light (570 nm) triggered the weakest responses compared to UV (390 nm) and blue (460 nm) light counterparts. Moreover, more pulses induced stronger EPSC responses, which was consistent with the UV operations (**Figure 51e**). Our optoelectronic synapse is sensitive to broadband spectrums, which provides a chance to develop versatile advanced artificial vision systems.

The broadband multi-spectra sensitivity of our optoelectronic synapse endows the device with the capability of colour recognition, image sensing, cognitive tasks, and optical communications. The optoelectronic synapse can recognize the colour of the rose pattern when a light goes through a mask (**Figure 51g**). The normalized output signals were 8, 35, and 100 for the green light, blue light, and UV light, respectively. The distinguishable output signals were practicable for colour recognition, which is crucial for artificial vision systems for high recognition accuracy, and object tracking. Information communication is another vital aspect in the AI world. The different responses of our optoelectronic synapse to different light wavelengths can be utilized for optical communications, which can realize data transmission that demonstrate better transmission speed and energy efficiency compared to electrical system counterparts. Specifically, the photonic wavelengths of 620 nm (Red), 460 nm (Green), 570 nm (Blue), 390 nm (UV) represent “00”, “01”, “10”, and “11” respectively (**Figure 52d**). The digital information in the form of binary code (“0” and “1”) can be demodulated, stored, and transmitted by photonic signals. The EPSC responses of Red, Green, Blue, and UV photons were around 0.20 nA (R), 0.23 nA (G), 0.33 nA (B), and 0.58 nA (U) respectively as presented in **Figure 52d**. One pulse of light stimulation with the duration of 0.5 s was used. Based on the ASCII, four photonic pluses can be demodulated into four letters “CAMJ” (GRRU represented 01000011, GRRG represented 01000001, GRUG represented 01001101, GRBB represented 01001010). Particularly, the

energy consumption was low, the average electronic energy consumption for one letter was approximately 150 pJ. The low energy consumption makes the optoelectronic synapse appealing for energy-efficient systems.

CNN is powerful and popular for image recognition.⁴³⁷ It consists of convolution layers, pooling layers, and fully connected classification layers (**Figure 57a**). Convolutional layers are used to pre-process images to extract high-level features, which benefits dealing with complex images and achieving higher recognition accuracy. The pooling layers are employed to reduce the spatial size of inputs. This action speeds up processing procedures. The fully connected layer performs deep learning algorithms to complete image recognition tasks, which can be implemented by memristive-based hardware for neuromorphic computing.⁵⁴ Therein, kernel operations occurring in convolution layers are vital for CNNs. The kernel can be a 2D matrix that “slides” over the input image pixel by pixel to complete the convolution operation. Different convolution kernels can achieve the functions of soft (blurring edge), edge detection (vertical edge highlight and horizontal edge highlight), sharpening edge, and more. Based on the optoelectronic synapse with multi-spectra sensitivity, a photonic kernel generator was developed to realize high-speed and low-energy convolutional processing. The flowchart of convolution image processing with the photonic kernel generator is illustrated in **Figure 53a**. The grayscale image can be considered as a matrix, in which each value presents the intensity of a specific pixel. The pixels can be normalized into voltages that are applied to the optoelectronic synapse array. The current can be directly obtained according to the equation $I=V \cdot G$, where I is current, V is voltage, and G is conductance. More detailed operations are here. First, the pixel values of grayscale (0-255), for example, a 3x3 sub-image, were extracted. Secondly, the pixel values were normalized into voltage values. To shrink the processed data volume, the pixel values (0-255) were quantized into 21 points corresponding to 21 voltage values (0.5-1.1 V) uniformly. The voltage interval was 0.03 V which was the same as the value in the measurement setup. Thirdly, the currents carrying convolution computing results were measured based on the multiply-and-accumulate (MAC) operation.⁴³⁸ A software-based post-processing involving a database was required to transform the current signal into pixel value and reconstruct the image. To build up the database, the relationship among the pixel, voltage, and current needs to be identified. Any measured currents can track back the specific pixel to reconstruct the filtered image.

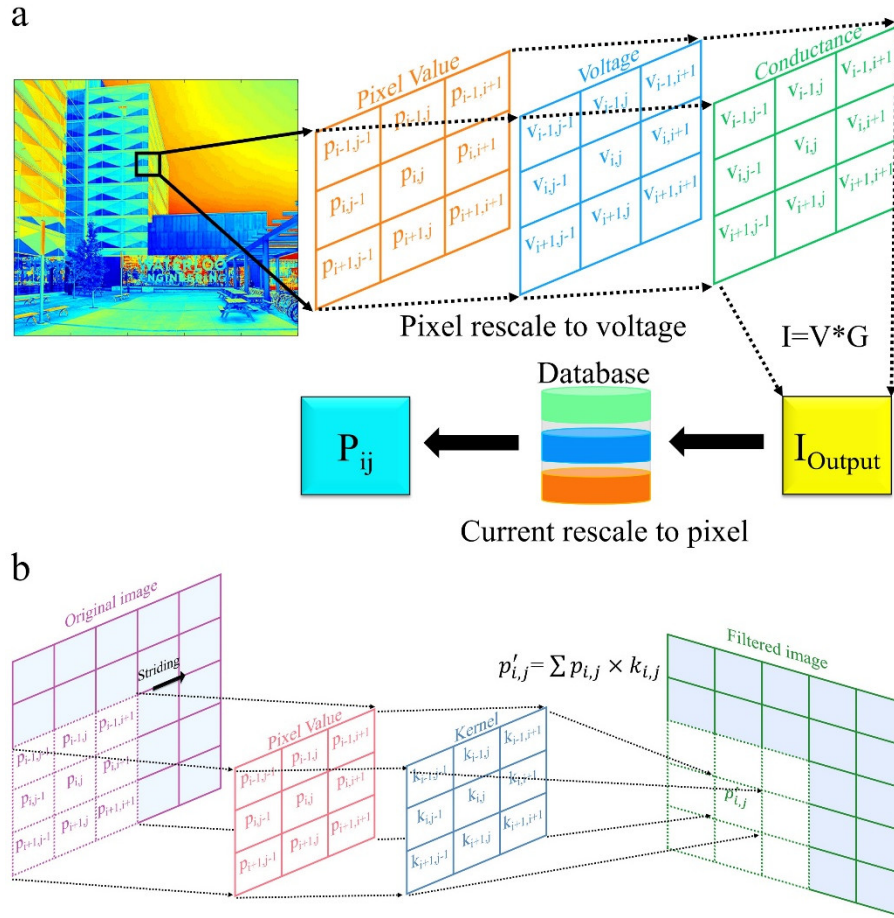


Figure 53. (a) Schematic diagram of a flowchart for convolutional image processing. (b) Illustration of the dot product calculation in convolutional image processing.

For a specific position (P_{ij}) in the image, the neighbouring 8 pixels were extracted to form a 3×3 input sub-image. A dot product between the input pixels and the kernel was calculated to get P'_{ij} as shown in **Figure 53b**. A striding action was required so that the kernel swept over the entire processed image. Over multiple iterations, a series of dot product results are obtained to reconstruct a pixel map (a convolved image or a filtered image). In a conventional system with separated memory and computing units, this is resource-expensive regarding energy consumption and processing time. Based on our optoelectronic synapse device sensitive to multiple spectra, a photonic kernel generator is developed. In GoogLeNet, 68% of energy is consumed by moving the feature maps.⁴³⁹

Based on our optoelectronic synapse device sensitive to multiple spectra, a photonic kernel generator is developed. The key to kernel operation based on the photonic generator is that the optoelectronic synapse is sensitive to multiple spectra so that the conductance can be modulated by lasers to complete convolution calculations. Furthermore, a better degree of freedom is expected since different photonic illumination can induce different conductance modulation amplitudes. This can complete complex and advanced convolution operations. The energy consumption for hardware-based image processing is much smaller than the traditional software counterpart.⁴⁴⁰ In this proposed configuration, the processed images are read out directly without frequent data transmission in traditional software-based systems, indicating more energy-efficient features.⁴⁴¹ The lasers with different light wavelengths were employed to change the conductance of the optoelectronic synapse. Because the optoelectronic synapse exhibited different sensitivity to the photons with different wavelengths. Different conductance modulation was induced corresponding to $1.9 G^D$, $2.4 G^D$, and $3.6 G^D$ by the illumination of green light, blue light, and UV light respectively, where G^D means the conductance under a dark condition. Particularly, as shown in **Figure 54a**, the conductance enlargement by different lights was stable with a small variation over a range of voltages. The distributions of conductance change ratios for all three lights were measured (**Figure 54b** to **Figure 54d**). The $G_{\text{Green}}/G_{\text{Dark}}$ ratio, $G_{\text{Blue}}/G_{\text{Dark}}$ ratio, and $G_{\text{UV}}/G_{\text{Dark}}$ ratio were 1.9, 2.4, and 3.6 respectively governed by Gaussian normal distribution. The Gaussian normal function was employed to describe the variance observed in the experimental measurements. The Gaussian Function is described as the following equation.

$$y = y_0 + \frac{A}{w\sqrt{\pi/2}} e^{-2\frac{(x-x_c)^2}{w^2}} \quad \text{Eq. 55}$$

where y_0 and A are constant, w is the standard deviation, x_c is the expected value. y_0 , A , w , and x_c were considered as variances during the fitting procedure. This function can effectively describe random variation in experimental systems. The fitted parameters can be used to simulate and predict the system characteristics in specific applications.

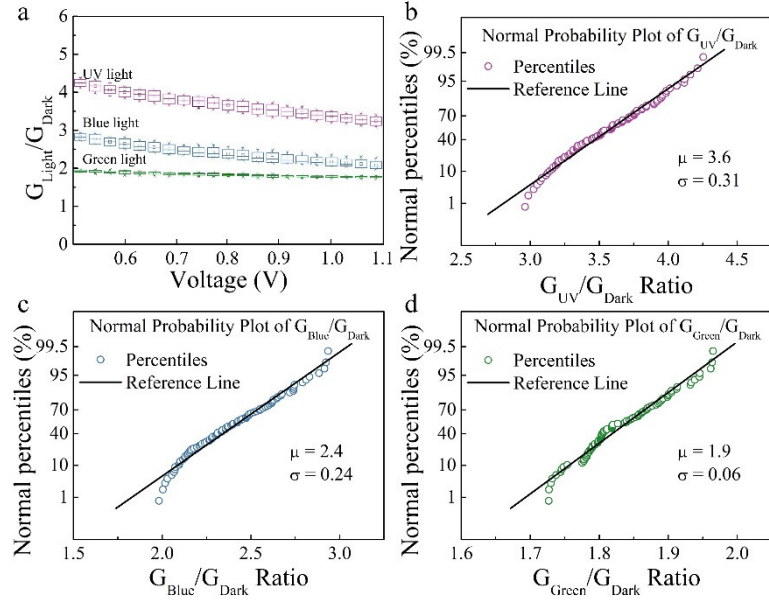


Figure 54. (a) The distribution of $G_{\text{Light}}/G_{\text{Dark}}$ ratio over the applied voltage of 0.5 V to 1.1 V. The interval of measured voltages was 0.03 V. 21 points were measured over the window of voltage. (b) The probability plot of the $G_{\text{UV}}/G_{\text{Dark}}$ ratio. (c) The probability plot of the $G_{\text{Blue}}/G_{\text{Dark}}$ ratio. (d) The probability plot of the $G_{\text{Green}}/G_{\text{Dark}}$ ratio.

According to the responsivity of the optoelectronic to lights with different wavelengths, the conductance gain (the ratio of $G_{\text{Light}}/G_{\text{Dark}}$) was constant over the voltage window of 0.5-1.1 V. Notably, the conductance gains were different when the device was shined with different lasers with different light wavelengths. This provided a chance to design more complicated kernels for various functions. For the proof-of-concept, the original image in grayscale is shown in **Figure 57b**. Four kernels were designed based on the optoelectronic synapse, as shown in **Figure 55**, corresponding to the kernel design shown in **Figure 57c**. The kernel values can be presented by the conductance-based operation. The operations of soft edge, vertical edge, horizontal edge, and sharpen edge were integrated into a crossbar. Currents carrying convolutional information can be measured directly. These current values can be used to reconstruct the convolved image based on the database as mentioned above.

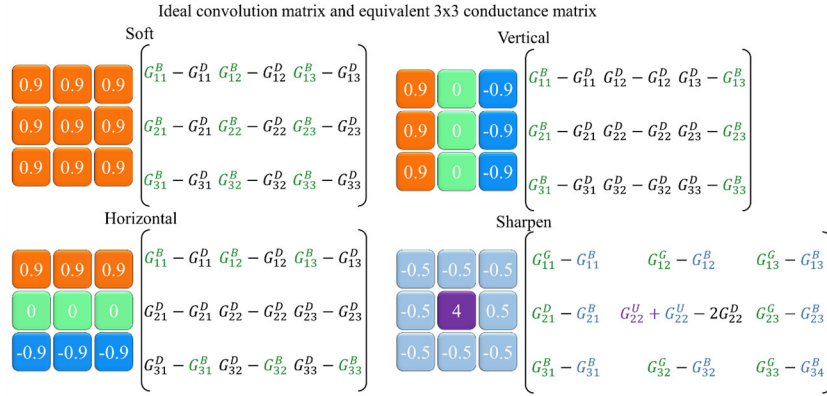


Figure 55. Kernel design of image processing under the photonic operation.

The conceptual circuit design is shown in **Figure 56**. The upper part demonstrates the procedure steps in convolutional image processing. The original image was transformed into a grayscale. Then the grayscale values were normalized into a voltage mapping representing the image. The pixel values were quantized into 21 values normalized into the voltage ranging from 0.5 V to 1.1 V. The interval voltage was 0.03 V which was the same as the measurement parameter. The bottom part of the diagram is the circuit design for hardware convolutional operations. Four kernel operation strategies were demonstrated. The current values difference among devices under different photonic stimulations were measured to obtain kernel operation results directly. This is more energy-efficient and has a shorter time delay since the data was not shuttled between different units (for example, memory and processing units in conventional configurations). Devices on cross points with green, blue, and purple spots are exposed to green, blue, and UV lasers, respectively. The devices without colourful spots are devices under dark conditions (no laser shines on them). For the dot product results, the current flowing through devices under dark conditions (without light illumination) can be described by the following equation:

$$I^D = V \times G^D \quad \text{Eq. 56}$$

where I means current, V means applied voltage, G^D means the conductance of the device under dark conditions (without light illumination). Similarly, the current flow through the device under illumination can be described by the following equations.

$$I^U = V \times G^U \quad \text{Eq. 57}$$

$$I^B = V \times G^B \quad \text{Eq. 58}$$

$$I^G = V \times G^G$$

Eq. 59

where I^U , I^B , and I^G are currents flowing through the device under the shining of UV light, blue light, and green light, respectively. G^U , G^B , and G^G are the conductance of the device under the shining of UV light, blue light, and green light, respectively. The modulated conductance by light can achieve arithmetical functions that can be used for convolution calculating.

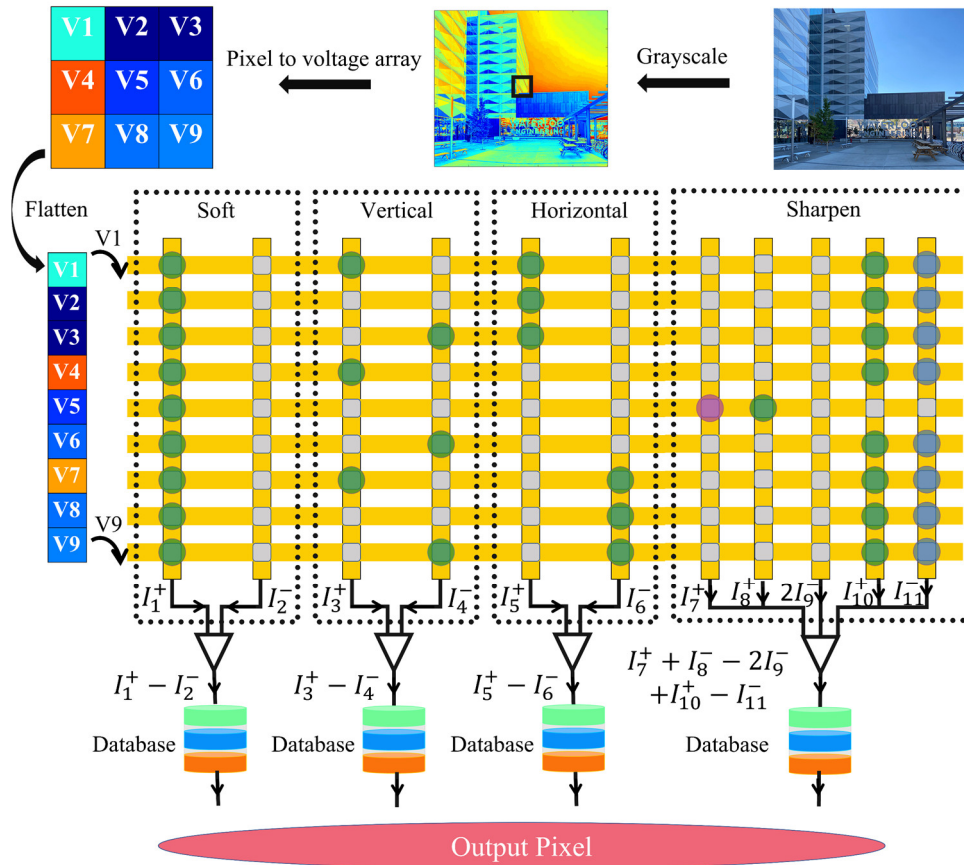


Figure 56. Illustration of convolution image processing with crossbar hardware.

Particularly, the conductance change margin can be identified over a range of applied voltage (Figure 54a to Figure 54d). A positive index, for example, 0.9, was generated by G^G (device conductance under green light illumination) minus G^D (device conductance under dark conditions). In comparison, A negative index, for example, -0.9, was generated by G^D minus G^B . Similar rules were applied to generate indices of -0.5 and 4, which utilized different light wavelengths to induce different magnitudes of

conductance changes. **Figure 56** (bottom part) shows the kernel design for image processing and the corresponding modulated device conductance by lasers. For the arithmetical methodology, the dot product result was obtained based on the following equation, in which the 3x3 matrix was flattened:

$$p'_{i,j} = p_{i-1,j-1} \times k_{i-1,j-1} + p_{i-1,j} \times k_{i-1,j} + p_{i-1,j+1} \times k_{i-1,j+1} + p_{i,j-1} \times k_{i,j-1} + p_{i,j} \times k_{i,j} + p_{i,j+1} \times k_{i,j+1} + p_{i+1,j-1} \times k_{i+1,j-1} + p_{i+1,j} \times k_{i+1,j} + p_{i+1,j+1} \times k_{i+1,j+1} \quad \text{Eq. 60}$$

Take horizontal edge operation as an example to demonstrate how the photonic kernel generator works (kernel shown in **Figure 55**), the above equation can be shown in the flowing version:

$$p'_{i,j} = p_{i-1,j-1} \times 0.9 + p_{i-1,j} \times 0.9 + p_{i-1,j+1} \times 0.9 + p_{i,j-1} \times 0 + p_{i,j} \times 0 + p_{i,j+1} \times 0 - p_{i+1,j-1} \times 0.9 - p_{i+1,j} \times 0.9 - p_{i+1,j+1} \times 0.9 \quad \text{Eq. 61}$$

In the actual operation circuit, pixel values were presented by voltage values. Notably, the relationship between pixel-voltage-current was identified to build up the database. The measured current can track back the specific pixel to reconstruct the filtered image. The result of the flowing equation needs to be solved:

$$I_{i,j} = V_{i-1,j-1} \times G_{i-1,j-1}^D \times 0.9 + V_{i-1,j} \times G_{i-1,j}^D \times 0.9 + V_{i-1,j+1} \times G_{i-1,j+1}^D \times 0.9 + V_{i,j-1} \times G_{i,j-1}^D \times 0 + V_{i,j} \times G_{i,j}^D \times 0 + V_{i,j+1} \times G_{i,j+1}^D \times 0 - V_{i+1,j-1} \times G_{i+1,j-1}^D \times 0.9 - V_{i+1,j} \times G_{i+1,j}^D \times 0.9 - V_{i+1,j+1} \times G_{i+1,j+1}^D \times 0.9 \quad \text{Eq. 62}$$

As it is known that $G_{\text{Green}}/G_{\text{Dark}} = 1.9$, which means the conductance (or current) increased to 1.9 times compared to the original value when the green laser shines on the device. Therefore, the equation can be transformed into the following equation:

$$I_{i,j} = V_{i-1,j-1} \times (G_{i-1,j-1}^G - G_{i-1,j-1}^D) + V_{i-1,j} \times (G_{i-1,j}^G - G_{i-1,j}^D) + V_{i-1,j+1} \times (G_{i-1,j+1}^G - G_{i-1,j+1}^D) + V_{i,j-1} \times (G_{i,j-1}^D - G_{i,j-1}^D) + V_{i,j} \times (G_{i,j}^D - G_{i,j}^D) + V_{i,j+1} \times (G_{i,j+1}^D - G_{i,j+1}^D) + V_{i+1,j-1} \times (G_{i+1,j-1}^D - G_{i+1,j-1}^G) + V_{i+1,j} \times (G_{i+1,j}^D - G_{i+1,j}^G) + V_{i+1,j+1} \times (G_{i+1,j+1}^D - G_{i+1,j+1}^G) \quad \text{Eq. 63}$$

Thus, the convolution results can be measured based on the circuit shown in **Figure 56**. A similar principle is valid for the soft edge, vertical edge, and sharpen edge convolution operations. Particularly, the green laser was employed for the soft edge, vertical edge, and vertical edge. For the edge sharpening operation, green, blue, and UV were involved.

$$-0.5G^D = G^G - G^B \quad \text{Eq. 64}$$

$$4G^D = G^U - G^D + G^B - G^D \quad \text{Eq. 65}$$

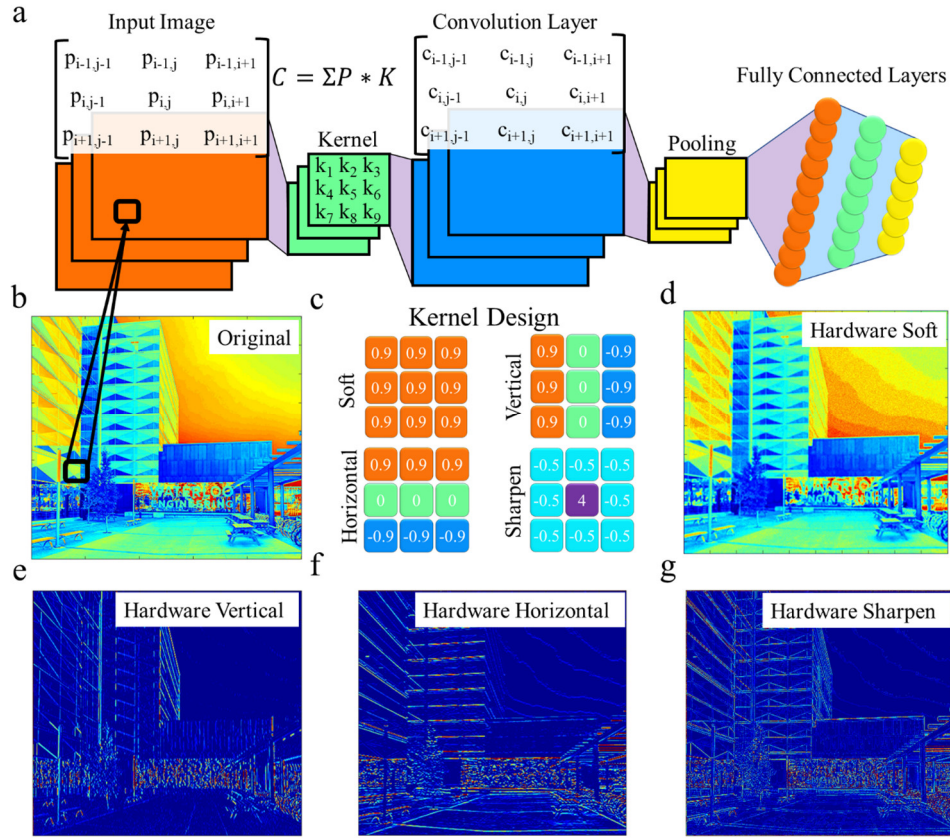


Figure 57. Convolutional image processing. (a) Flow chart for convolutional computing based on CNNs. (b) The original image is grayscale. (c) Designed kernels for convolutional image processing using optoelectronic synapses. (d) Image processed by the kernel of “Soft”. (e) Image processed by the kernel of “Vertical”, detecting vertical edges. (f) Image processed by the kernel of “Horizontal”, detecting horizontal edges. (g) Image processed by the kernel of “Sharpen”, detecting edges.

To demonstrate the realistic operation scenario, the variation of the light-modulated conductance was applied to the processed images. After the soft edge processing, the blurred image (**Figure 57d**) was obtained because of the average operation on each pixel. Blurring is important in image processing, which realizes smooth transitions between adjacent pixels instead of sharp changes.⁴⁴² This is especially necessary for shrinking images, in which sharp details will be sacrificed. The smoothing process

distributes the pixel transition over more adjacent pixels to preserve edges in smaller images. Particularly, edge detection is vital for image processing to extract crucial information and object tracking for autonomous vehicles.⁴⁴³ The Prewitt kernel edge detectors of both vertical and horizontal filters were utilized for image processing.⁴⁴² The vertical edge detection using our optoelectronic synapses is shown in **Figure 57e**. The vertical edges in the image became sharper. Meanwhile, the horizontal edges were more prominent after the horizontal edge detection (**Figure 57f**). Besides, the image edge sharpening was achieved (**Figure 57g**), and the intensity of edges was increased obviously.

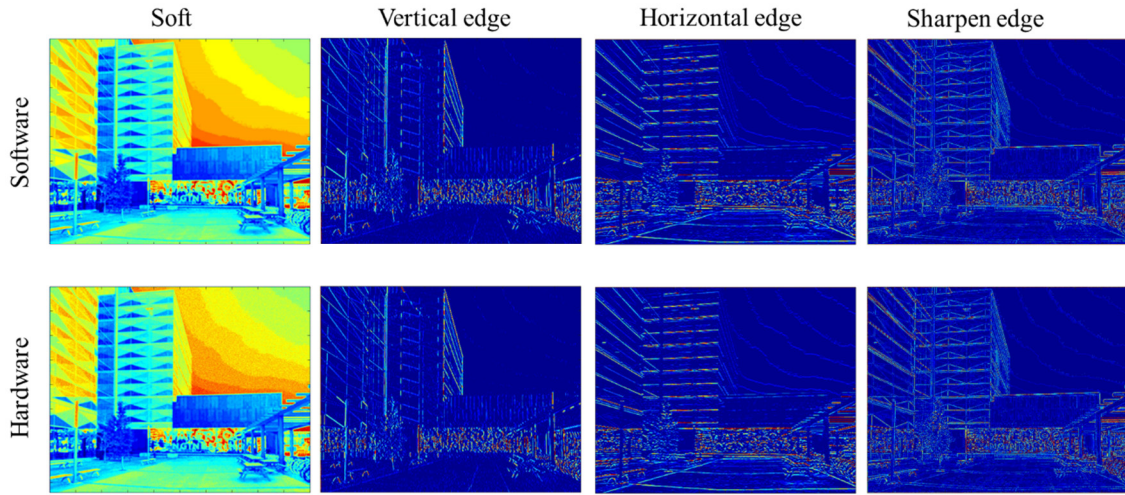


Figure 58. Comparison between software-based and hardware-based convolution image processing.

Furthermore, to demonstrate the reliability of the photonic kernel generator using the optoelectronic synapses hardware, traditional software-based convolution image processing was carried out to compare with the hardware-based results as shown in **Figure 58**. In the arithmetical processing, the kernel values were ideally equal to designed values with a device-variation-free condition. A negligible difference was observed, indicating a tolerable device variance for convolutional image processing. Besides, the relationship between the experimental pixel values by hardware and the arithmetic pixel values of the processed image by software is shown in **Figure 59**. The slope was close to 1, which means a high coincidence between hardware and software-based processing results. The results demonstrate that the optoelectronic synapse is reliable for developing a photonic kernel generator for convolutional processing.

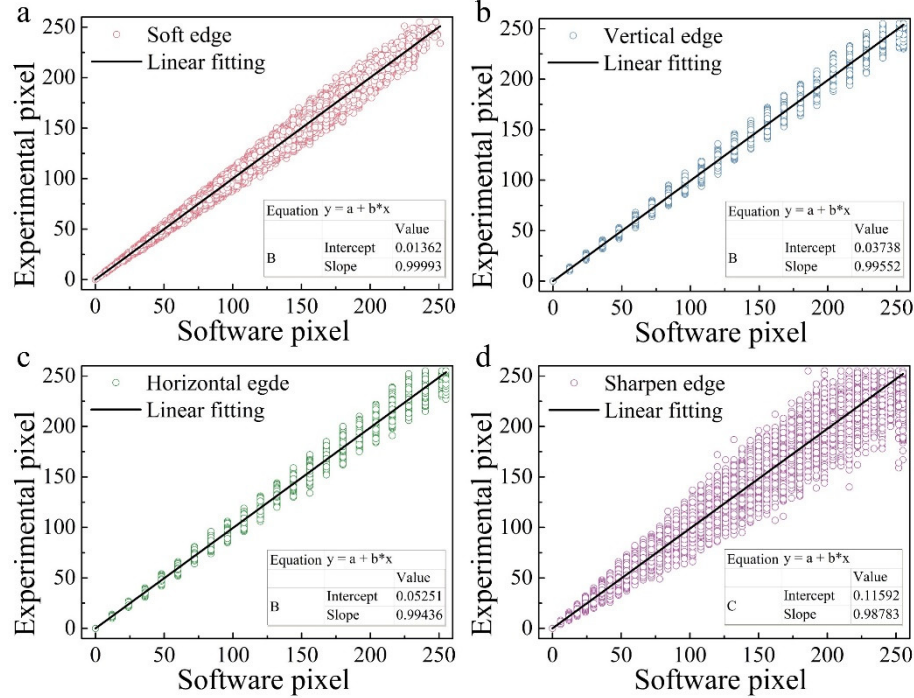


Figure 59. (a) The comparison of the experimental pixel values and the arithmetic pixel values for the soft edge operation. (b) The comparison of the experimental pixel values and the arithmetic pixel values for the vertical edge operation. (c) The comparison of the experimental pixel values and the arithmetic pixel values for the horizontal edge operation. (d) The comparison of the experimental pixel values and the arithmetic pixel values for the sharpen edge operation.

5.3.3 Neuromorphic Computing for Cognitive Tasks

The device also showed reliable synaptic performance under electronic operations. The typical memristive resistive switching was measured. In **Figure 60a**, no degradation was observed over 100 cycles. The HRS and LRS distribution over multiple operations is shown in **Figure 60b**. A small variation was observed, indicating good robustness. To mimic biological synaptic behaviors, 50 consecutive voltage pulses with various amplitudes were used (**Figure 60c**). Stronger plasticity was found when higher voltages were utilized, which mimicked SADP in biological individuals. When the stimulation was weak, for example, 0.2 V, the conductance change margin was very narrow ($\sim 2\%$). Instead, the $\Delta G/G_0$ was over 25 % when the higher voltage of 0.8 V was utilized.

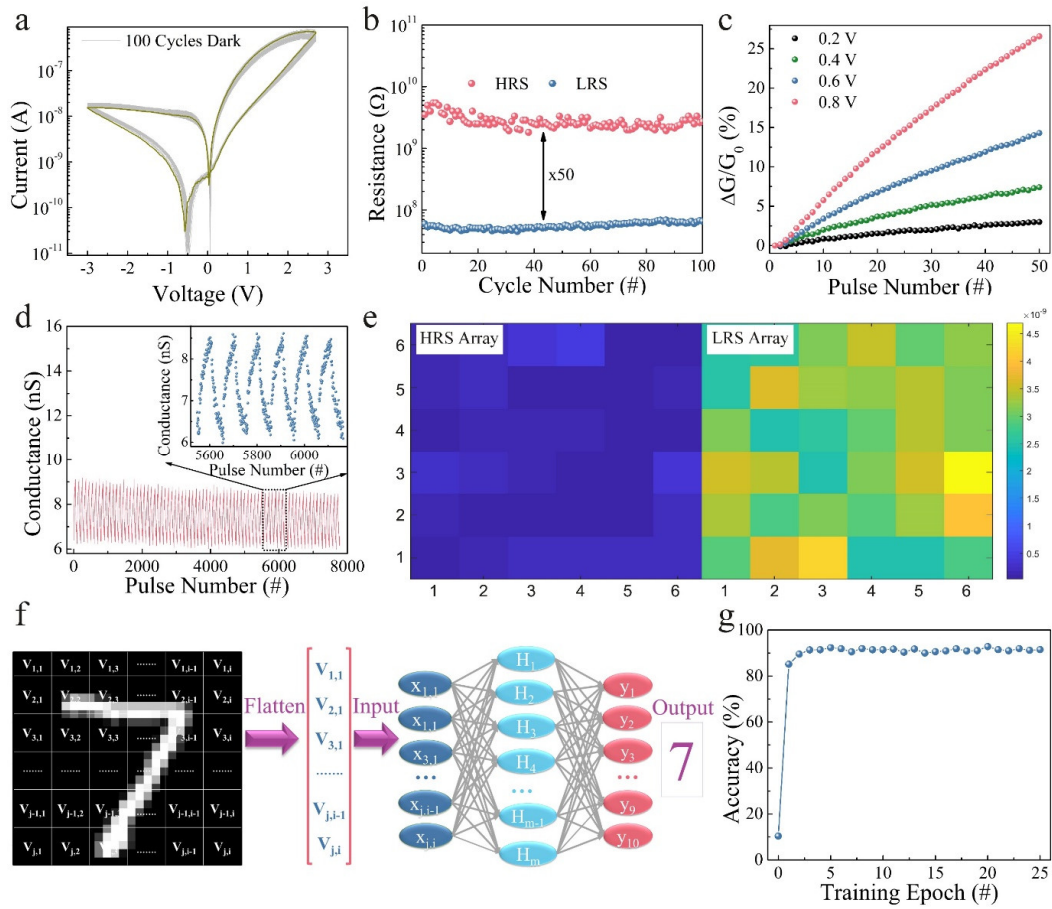


Figure 60. Electronic stimulations. (a) The I-V curves of electrical resistive switching for 100 cycles. (b) The distribution of HRS and LRS over 100 operation cycles. (c) Potential performances depending on the input electronic pulse amplitudes. (d) Potential/depression performances under positive/negative electronic pulses. The pulse duration was 100 ms, and the duty cycle was 50 %. G_0 represents the initial conductance of the device. ΔG represents the change of the conductance after the electronic pulses were applied to the device. (e) The statistical mapping of device-to-device variations in a 6 x 6 array. The colour bar represents the current value (unit: A) under different resistance states (f) Schematic diagram for handwritten recognition with neural networks. (g) The results of image recognition using neuromorphic computing based on the optoelectronic synapse.

Furthermore, potentiation/depression performances were observed (**Figure 60d**). The conductance increased continually as consecutive positive pulses were applied. In contrast, the continued decrease of conductance was observed when negative pulses were applied. This can mimic the synaptic potentiation and depression features in biological individuals. This characterization can be utilized for

neuromorphic computing. The statistics of the asymmetric nonlinearity (ANL) factor over cycle-to-cycle operations were analyzed as shown in **Figure 61a**. The ANL was calculated based on the following equation:⁴⁰²

$$ANL = \frac{G_P\left(\frac{N}{2}\right) - G_D\left(\frac{N}{2}\right)}{G_{max} - G_{min}} \quad \text{Eq. 66}$$

where G_P and G_D are the conductance under potentiation and depression operations, respectively. N is the number of pulses applied to the device for potentiation and depression operations. N was 50 in the test shown in this paper. The small ANL average factor of 0.6 and standard deviation of 0.2 were obtained in the optoelectronic device, which benefits the high computing accuracy of neuromorphic computing.⁵¹

The device-to-device variation is important for memory and computing accuracy.³⁷⁹ The statistical mapping of device-to-device variations in a 6 x 6 array (**Figure 60e**). Distinctive HRS and LRS were obtained in the integrated device array. The statistics of device-to-device variation were analyzed by fitting with the Gaussian Function (**Figure 61b**). The values of $\sigma/(\mu * r)$ HRS and LRS were 0.7 % and 3.4 % respectively. The results demonstrated small variations over the whole array, which is crucial for the computing accuracy based on the device.³⁹² The device can be integrated into a high-density array, such as a crossbar array or stacked three-dimensional (3D) array, for implementing matrix-vector multiplication (MVM) (**Figure 60f**). Weights in neural networks were stored locally as device conductance during computing processes. By utilizing Ohm's law and Kirchhoff's current law, the results of MVM considered a core computing task in deep learning algorithms can be obtained by measuring currents.³⁷⁹ This methodology can realize parallelism as the current can be sensed at once regardless of the array size (corresponding to the matrix size in deep learning), which is energy-efficient compared to that of traditional digital computing systems.³⁸⁹ A neuromorphic computing on handwritten recognition was implemented. A three-layer neural network consisting of the input layer (784 neurons), hidden layer (300 neurons), and output layer (10 neurons) was built up. The backpropagation algorithm was used to train the neural network. After merely three integrations, the recognition accuracy reached 90 % as shown in **Figure 60g**, demonstrating promising prospects for cognitive tasks.

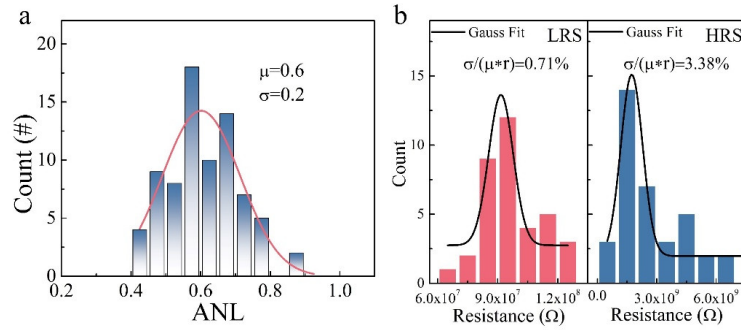


Figure 61. (a) The statistical analysis of ANL factor over cycle-to-cycle operations. (b) The statistical analysis of device-to-device variation. μ is expected value, σ is standard deviation, r is the ratio of HRS/LRS.

5.3.4 Mechanism of Optoelectronic Performances

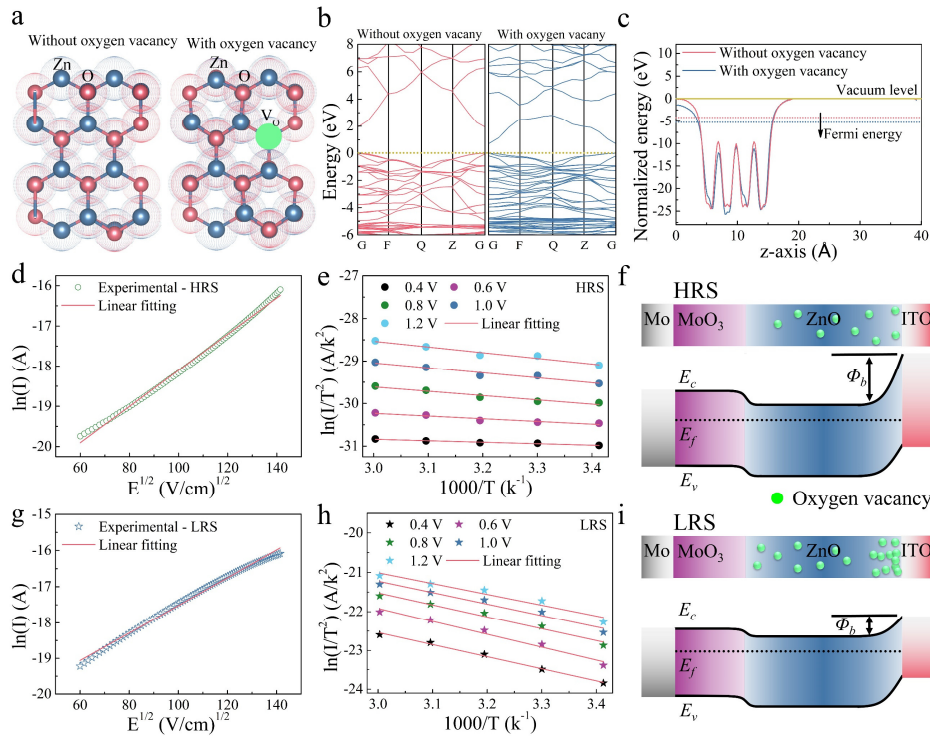


Figure 62. Resistive switching mechanism. (a) The ZnO with (right) and without (left) oxygen vacancies. (b) Band structures of the ZnO. (c) Electrostatic potential curves along the z -axis, the vacuum level was normalized to 0 eV. (d) The fitting of $\ln(I)$ vs. $E^{1/2}$ for the device at HRS. (e) The fitting of $\ln(I/T^2)$ vs. $1000/T$ for the device at HRS. (f) Schematic diagram of energy band of HRS. (g) The fitting of $\ln(I)$ vs. $E^{1/2}$ for the device at LRS. (h) The fitting of $\ln(I/T^2)$ vs. $1000/T$ for the device at LRS. (i) Schematic diagram of energy band of LRS.

Systematic investigations were implemented to study the working mechanism with density functional theory (DFT) calculations and experimental measurements. The DFT theory was employed to investigate the electric properties of the switching layer. The models of the pure ZnO (left) and ZnO with oxygen vacancies (right) were constructed for the calculation (**Figure 62a**). ZnO was a wurtzite structure. Oxygen vacancies were induced intentionally to investigate the changes in electronic characteristics. Band structures of the ZnO were calculated (**Figure 62b**). The corresponding density of states (DOS) curves are shown in **Figure 63**. After the oxygen vacancies were induced, the band gap narrowed from 1.91 eV to 0.77 eV, indicating that oxygen vacancies increased the conductivity.⁴⁴⁴ Notably, DFT calculations predict smaller band gap values compared to experimental measurement. This is due to the inaccurate evaluation of the repulsion effects between conduction levels and Zn 3d, resulting in the hybridization of the Zn 3d and O 2p levels.⁴⁴⁵ It still confirmed the trend of a narrower band gap and higher conductivity by inducing oxygen vacancies. Besides, the working function increased when oxygen vacancies were brought into ZnO (**Figure 62c**), which modulated the Schottky barrier height at the interfaces.⁴⁴⁶

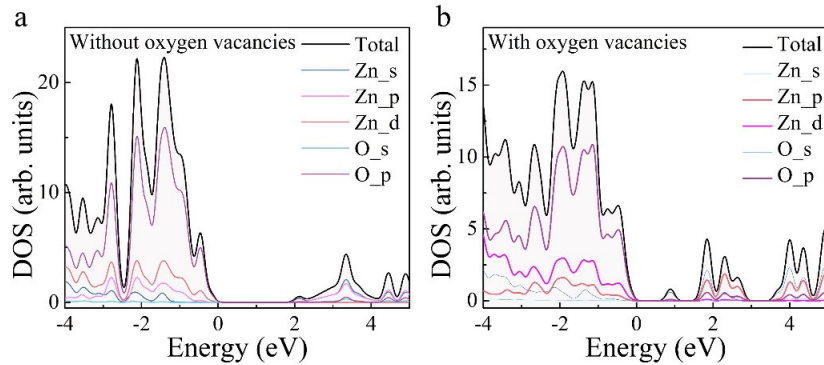


Figure 63. (a) The DOS curves of ZnO without (a) and with (b) oxygen vacancies.

The Schottky emission describes activated electrons overcoming the energy barrier. Modulating the barrier height can induce resistive switching.¹² The $\ln(I)$ of the device at HRS increased proportionally with the increase of $E^{1/2}$ (**Figure 62d**), demonstrating the Schottky emission mechanism. Furthermore, the plot of $\ln(I/T^2)$ vs. $1000/T$ for the device at HRS demonstrated a linear relationship (**Figure 62e**), which was consistent with the result in **Figure 62d**. A schematic diagram of the energy band for the device at HRS is depicted in **Figure 62f**. The working function Mo and MoO₃ were 4.6 eV and 4.9 eV

respectively.⁴⁴⁷ The interface of Mo/MoO₃ was likely to be an ohmic contact, indicating low contact resistance. The work function of ZnO was 3.8 eV. The working function of ITO can be as high as 5.2 eV.⁴⁴⁸ The Schottky barrier at the ZnO/ITO interface was higher. Because the working function difference at the ZnO/ITO interface was bigger than the MoO₃/ZnO counterpart.⁴⁴⁹ The asymmetric curve (**Figure 60a**) indicated higher current values under positive voltages. The overall energy barrier height was lowered under positive voltages. The Schottky barrier at the ZnO/ITO interface was more dominant. For the LRS, the Schottky emission fitting of $\ln(I)$ vs. $E^{1/2}$ is plotted (**Figure 62g**). The linear relationship indicated that the device followed the Schottky emission at the LRS. The temperature-dependent Schottky emission fitting also showed a linear relationship (**Figure 62h**). A schematic diagram of the energy band alignment at LRS is presented in **Figure 62i**. When positive voltages were applied, oxygen vacancies were generated at the ZnO/ITO interface, lowering the Schottky barrier height.¹² This will decrease the overall resistance of the device (LRS). Besides, generated oxygen vacancies decreased the resistance of bulk ZnO, which also benefited the smaller resistance of LRS.⁴⁴⁴ Therefore, the modulated Schottky emissions at the ITO/ZnO interface and the bulk resistance of ZnO governed the resistive switching. Additionally, a RESET operation was completed by applying negative voltages to remove oxygen vacancies and recover the original barrier height. Particularly, the barrier height and ZnO conductivity changed gradually by migrating oxygen vacancies.¹² The conductance of the device was modulated gradually, which was crucial for mimicking the plasticity of synapses.

5.3.5 Monolithic Neuromorphic Machine Vision System

Our optoelectronic synapse exhibited broadband spectrum sensitivity and electronic synaptic plasticity. Those features resemble the biological organs in the human visual system (**Figure 64a**). In human eyes, the retina shows a sensing ability to different colours owing to the functions of photoreceptors. The perceived signal is transformed into the visual cortex via neuron systems. The pre-processing operations are also done in the retina to improve the processing efficiency in the visual cortex. The core cognitive tasks are completed in the visual cortex. It relies on a complicated neural network with many neurons and synapses to implement memory and computing tasks, including pattern recognition. Similarly, a crossbar array of optoelectronic synapses (**Figure 64b**) can achieve pixel-by-pixel and broadband image sensing, corresponding to retinomorphic sensing. The integrated array can also play the role of kernel generator that can execute the convolution image processing. The processed

images are reconstructed based on the directly measured current. It can realize fast processing speed by avoiding redundant matrix calculations. Meanwhile, due to its compact bio-inspired structure, it was energy efficient due to the low-power consumption of the device under photonic operations. More importantly, the potentiation/depression function in the device is practicable for constructing artificial neural networks. This achieved VMM which was the most energy-consumption computing task for deep learning algorithms.³⁷⁹ Therefore, cognitive processing can be completed in the optoelectronic synapse array. This optoelectronic synapse can be used for front-end retinomorphic image sensing, convolutional processing, and back-end neuromorphic computing for cognitive tasks. It is very promising for constructing compact monolithic machine vision systems, which can improve image processing efficiency and decrease the fabrication costs of artificial vision systems.

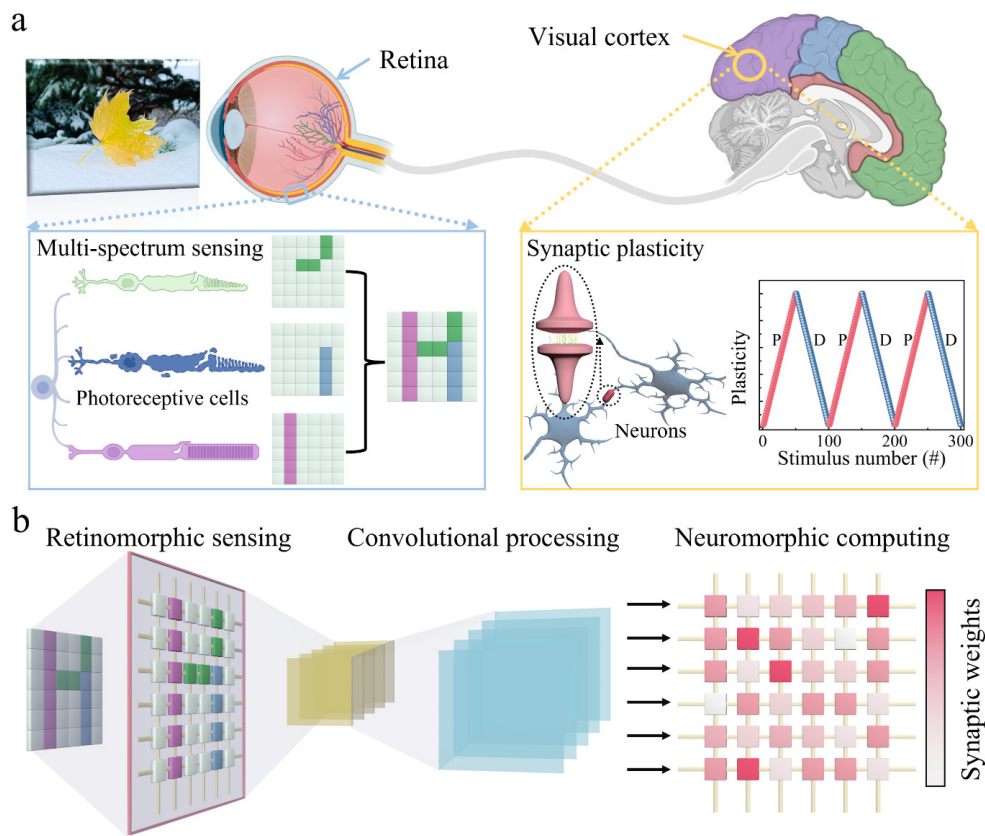


Figure 64. Monolithic neuromorphic machine vision system. (a) Schematic diagram of the retinomorphic sensing and processing in a human vision system. (b) Schematic diagram of the integrated optoelectronic synapse hardware for optical sensing, convolution processing, and neuromorphic computing.

5.4 Summary

In this work, an optoelectronic synapse has been fabricated to develop compact monolithic neuromorphic vision systems for information processing. The device was a two-terminal device based on metal oxide materials that are compatible with traditional CMOS processes, demonstrating easy scalability and high integration density with current semiconductor technology. The optoelectronic synapse was sensitive to a broadband spectrum (ultraviolet and visible light regions). It can mimic the biological plasticity of EPSC, PPF, SADP, and SNDP, which was used for image sensing, photonic computing, and optical communication. A very low energy consumption of 37 pJ was obtained under photonic operations. Based on the multi-spectrum sensitivity and near-constant current gains under photonic stimulations, a photonic-controlled kernel generator was developed for convolution processing. This realized the pre-processing of feature extraction with high-energy efficiency and fast processing speed, which can improve the subsequent cognitive processing efficiency. Meanwhile, stable resistive switching under electronic stimulations was observed. The resistive switching mechanism was due to the modulated barrier height and the conductivity of ZnO by controlling the migration of oxygen vacancies. The potentiation/depression was employed to implement neuromorphic computing. A recognition accuracy of over 90 % was obtained, indicating a practical application for cognitive tasks. For the first time, this broadband two-terminal optoelectronic synapse can be utilized for front-end retinomorphic image sensing, convolution processing, and back-end neuromorphic computing. This technology is promising for monolithic neuromorphic machine vision systems.

Chapter 6. Conclusion and Outlook

6.1 Conclusions

The thesis focuses on the memristive devices for advanced neuromorphic computing systems. Two-terminal memristive devices were fabricated based on chalcogenide and metal-oxide materials. Three major progresses are presented in three separate chapters. Firstly, a versatile memristive device (Ag/CISe/Mo) was demonstrated. The device showed non-volatile and volatile resistive switching simultaneously. It can be used for multiple roles of non-volatile memory, selectors, artificial neurons, and artificial synapses. Secondly, an intelligent matter (Ag/CIGSe/Mo) enabling reconfigurable temperature and humidity sensations was developed for sensory neuromorphic systems. Thirdly, an optoelectronic synapse (ITO/ZnO/MoO₃/Mo) enabling multi-spectrum sensitivity for monolithic machine vision systems was developed. The developed techniques in this thesis will benefit the development of advanced neuromorphic systems pushing forward AI technology. More detailed observations are shown below:

- (1) A versatile memristive (Ag/CISe/Mo) array covering multiple functions was developed. Non-volatile functionalities with a storage window of 4.0×10^5 and a retention time of 10,000s were obtained, indicating the application of nonvolatile memory. Besides, the Ag/CISe/Mo device showed diode-like volatile functionalities with a storage window of 7.0×10^4 and a rectification ratio of 4.0×10^4 . The high rectification ratio can be used as selectors to suppress sneaky currents in memristive arrays. The LIF neuron model based on the device has been studied, demonstrating potential as artificial neurons. Furthermore, the short-term synaptic PPF and long-term potentiation/depression performances were obtained in the same device. The image recognition simulation with the accuracy of $90 \pm 2\%$ was achieved, indicating the practicability of the artificial synapse for neuromorphic computing. A versatile memristor taking the multiple roles of non-volatile memory, selectors, artificial synapses, and artificial neurons will provide many advantages regarding circuit simplification, fabrication processes, and manufacturing costs. The devices with different top electrodes, operation temperatures, switching layer thicknesses, and conduction mechanisms were investigated to reveal the resistive switching mechanism. It has been confirmed that the volatile/non-volatile bifunctional resistive switching is attributed to the dynamics of Ag atoms. Moreover, this work presents a novel bottom-up approach to fabricate

crossbar arrays, where the CISE was grown locally by electrodeposition to form a patterned switching layer. This method can potentially decrease manufacturing costs and achieve high utilization efficiency of materials.

- (2) An intelligent matter enabling reconfigurable temperature and humidity sensations has been demonstrated for in-sensor computing. The delicate design was based on a memristive device with resistive switching capabilities to achieve reconfigurable sensory properties in a single device. External voltage triggered the formation/rupture of Ag MCF, introducing resistive switching. The device (Ag/CIGSe/Mo) can achieve reliable resistive switching behaviors. The existence and nonexistence of conductive filaments determined the metallic and semiconductive properties under different temperatures. Thus, opposite temperature coefficients of conductance were obtained at the LRS and HRS. Intelligent low-level sensory data processing was demonstrated. The intelligent matter with temperature sensations can work in the LRS mode, HRS mode, and HRS&LRS mode. Each mode has different sensation features and sensitivities. The reconfigurable sensation characteristics are promising for intelligent artificial skins for different working scenarios. Besides, water molecules influence the growth of conductive filaments, which affects the size of high-conductivity filaments and further modulates the value of the LRS. The device acted as sensory artificial synapses that can be utilized for high-level cognitive in-sensor computing. An ANN was constructed to implement the backpropagation algorithm for pattern recognition. Different recognition accuracies were obtained under different humidity levels, demonstrating sensory neuromorphic computing capabilities.
- (3) An optoelectronic synapse has been fabricated to develop compact monolithic neuromorphic vision systems for information processing. The device has a two-terminal structure based on metal oxide materials that are compatible with traditional CMOS processes, demonstrating easy scalability and high integration density with current semiconductor technology. The optoelectronic synapse was sensitive to a broadband spectrum (ultraviolet and visible light regions). It can mimic the biological plasticity of EPSC, PPF, SADP, and SNDP, which was used for image sensing, photonic computing, and optical communication. A low energy consumption of 37 pJ was obtained under photonic operations. Based on the multi-spectrum sensitivity and near-constant current gains under photonic stimulations, a photonic-controlled kernel generator

was developed for convolution processing. This technique realized the pre-processing of feature extraction with high-energy efficiency and fast processing speed. It improves the subsequent cognitive processing efficiency. Meanwhile, stable resistive switching under electronic stimulations was observed. The potentiation/depression can be employed to implement neuromorphic computing. For the first time, this broadband two-terminal optoelectronic synapse can be utilized for front-end retinomorphic image sensing, convolution processing, and back-end neuromorphic computing.

6.2 Outlook

As for future work, some extra efforts can be made regarding in-depth mechanism exploration, device performance improvement, large-scale array-level study, and novel systems design. A better understanding of resistive switching and high-performance devices are the foundation for memristive systems. Besides, array-level integrated devices and system-level investigation are required to realize hardware-based computing. The detailed future work is listed below:

- (1) In-depth understanding of cation-based and anion-based resistive switching is crucial for further improving the device's performance. It benefits the development of compact models. Especially, accurate SPICE models that are embeddable into the commercialized technology will accelerate the development of memristive systems. Some investigation by *in-situ* TEM to monitor the growth and shrinking of Ag filaments in the chalcogenides and migration of oxygen vacancies are be meaningful.⁴⁵⁰ Some other techniques, such as scanning probe microscopy and X-ray microscopy, may also provide essential information to supplement the picture of resistive switching mechanisms in both chalcogenides and metal oxides.
- (2) The performance of devices needs to be improved, especially for endurance and retention time. In this work, the endurance of thousands of cycles and retention time of ten thousand seconds were achieved, which is not practical for commercialized applications although it may be accountable for preliminary study.⁴⁵¹ Further optimizing the device structure, including the thin film thickness, the electrode material, and the device size, can be helpful to get more robust and reliable resistive switching properties.

- (3) More interesting properties based on the devices in this thesis can be explored. For example, the intelligent matter (Ag/CIGSe/Mo) shown in this thesis showed intelligent sensory functions to temperature and humidity. It also shows the potential of light sensitivity as Ag filaments interact with photons.⁹⁰ Besides, the oxide-based device may show humidity sensitivity except for light sensing.⁴⁵² Extra ability sensing can be added to current devices, which expands the applications of these devices.
- (4) Developing large-scale memristive arrays is essential for memristive-based computing systems. We have fabricated mini arrays (around 20-40 devices) in current research. This is for the preliminary investigations. More efforts are required to increase the integration density. To reach the goal, advanced lithography machines and thin film deposition techniques should be employed.⁴⁵³ Corresponding fabrication process needs to be explored before the array integration that exhibits high yield and good device-to-device variations.
- (5) Commercialized neuromorphic computers need system-level design and integration. After the success of fabricating high-density arrays. System design and integration implementing hardware computing will be considered.

Chapter 7. Research Contributions

7.1 Articles Published in Refereed Journals

- (1) **Tao Guo**, Bai Sun, Shubham Ranjan, Yixuan Jiao, Lan Wei, Y. Norman Zhou, and Yimin A. Wu. "From Memristive Materials to Neural Networks." ACS Applied Materials & Interfaces 12, no. 49 (2020): 54243-54265. **(PhD work in thesis, Chapter 2)**
- (2) **Tao Guo**, Kangqing Pan, Yixuan Jiao, Bai Sun, Cheng Du, Joel P. Mills, Zuolong Chen et al. "Versatile Memristor for Memory and Neuromorphic Computing." Nanoscale Horizons (2022). **(PhD work in thesis, Chapter 3)**
- (3) **Tao Guo**, Jiawei Ge, Yixuan Jiao, Youchao Teng, Bai Sun, Wen Huang, Hatameh Asgarimoghaddam et al. "Intelligent matter endows reconfigurable temperature and humidity sensations for in-sensor computing." Materials Horizons (2023). **(PhD work in thesis, Chapter 4)**
- (4) **Tao Guo**, Baizhou Zhang, Jiawei Ge, Bai Sun, Y. Norman Zhou, and Yimin A. Wu, Broadband optoelectronic synapse enables compact monolithic neuromorphic machine vision for information processing, Accepted by Advanced Functional Materials (adfm.202303879). **(PhD work in thesis, Chapter 5)**
- (5) **Tao Guo**, Jiawei Ge, Bai Sun, Kangqiang Pan, Zhao Pan, Lan Wei, Yong Yan, Y. Norman Zhou, and Yimin A. Wu. "Soft Biomaterials Based Flexible Artificial Synapse for Neuromorphic Computing." Advanced Electronic Materials (2022).
- (6) **Tao Guo**, K. Pan, B. Sun, L. Wei, Y. Yan, Y. N. Zhou, and Y. A. Wu. "Adjustable Leaky-Integrate-and-fire neurons based on memristor-coupled capacitors." Materials Today Advances 12 (2021): 100192.
- (7) **Tao Guo**, Bai Sun, Shubham Ranjan, Cheng Du, Bryce Joseph Kieffer, Joel Philip Mills, Yongcheng Tong, Lan Wei, Y. Norman Zhou, and Yimin A. Wu. "Electrocatalytic Hydrolysis Modulated Multistate Resistive Switching Behaviors in Memristors." physica status solidi (a).
- (8) Sun, Bai, Guangdong Zhou, **Tao Guo**, Y. Norman Zhou, and Yimin A. Wu. "Biomemristors as the next generation bioelectronics." Nano Energy (2020): 104938. (Co-first author)

- (9) Sun, B., S. Ranjan, G. Zhou, **Tao Guo**, Y. Xia, L. Wei, Y. N. Zhou, and Y. A. Wu. "Multistate resistive switching behaviors for neuromorphic computing in memristor." *Materials Today Advances* 9: 100125. (Co-first author)
- (10) Sun, Bai, **Tao Guo**, Guangdong Zhou, Jinggao Wu, Yuanzheng Chen, Y. Norman Zhou, and Yimin A. Wu. "A battery-like self-selecting biomemristor from earth-abundant natural biomaterials." *ACS Applied Biomaterials* 4, no. 2 (2021): 1976-1985. (Co-first author)
- (11) Sun, Bai, **Tao Guo**, Guangdong Zhou, Shubham Ranjan, Yixuan Jiao, Lan Wei, Y. Norman Zhou, and Yimin A. Wu. "Synaptic devices based neuromorphic computing applications in artificial intelligence." *Materials Today Physics* (2021): 100393. (Co-first author)
- (12) Sun, Bai, Shubham Ranjan, Guangdong Zhou, **Tao Guo**, Cheng Du, Lan Wei, Y. Norman Zhou, and Yimin A. Wu. "A True Random Number Generator Based on Ionic Liquid Modulated Memristors." *ACS Applied Electronic Materials* (2021)

7.2 Patent

- (1) Photonic-controlled crossbar for convolution operations. (Pending)

7.3 Awards Received

- (1) WIN Nanofellowship (Waterloo Institute of Nanotechnology), at University of Waterloo, August 2020 (Valued \$10,000 CAD). This prestigious scholarship is awarded to students with outstanding academic qualifications and research potential.
- (2) WIN Nanofellowship (Waterloo Institute of Nanotechnology), at University of Waterloo, August 2022 (Valued \$10,000 CAD). This prestigious scholarship is awarded to students with outstanding academic qualifications and research potential.

Letters of Copyright permission

Figure 1

This Agreement between the university of waterloo -- Tao Guo ("You") and Springer Nature ("Springer Nature") consists of your license details and the terms and conditions provided by Springer Nature and Copyright Clearance Center.


License Number	5530961256105	High-res required	no
License date	Apr 16, 2023	Will you be translating?	no
Licensed Content Publisher	Springer Nature	Circulation/distribution	100 - 199
Licensed Content Publication	Nature	Author of this Springer Nature content	no
Licensed Content Title	Brain-inspired computing needs a master plan	Title	Chalcogenide and metal-oxide memristive devices for advanced neuromorphic computing
Licensed Content Author	A. Mehonic et al	Institution name	the university of waterloo
Licensed Content Date	Apr 13, 2022	Expected presentation date	Aug 2023
Type of Use	Thesis/Dissertation	Portions	Figure 1a
Requestor type	academic/university or research institute		the university of waterloo Waterloo, ON N2V 2W5
Format	print and electronic	Requestor Location	ON, ON N2V 2W5 Canada Attn: the university of waterloo
Portion	figures/tables/illustrations	Total	0.00 USD
Number of figures/tables/illustrations	1		

Figure 2

This Agreement between the university of waterloo -- Tao Guo ("You") and Springer Nature ("Springer Nature") consists of your license details and the terms and conditions provided by Springer Nature and Copyright Clearance Center.

License Number	5530961382070
License date	Apr 16, 2023
Licensed Content Publisher Springer Nature	
Licensed Content Publication	Nature
Licensed Content Title	The missing memristor found
Licensed Content Author	Dmitri B. Strukov et al
Licensed Content Date	May 1, 2008
Type of Use	Thesis/Dissertation
Requestor type	academic/university or research institute
Format	print and electronic
Portion	figures/tables/illustrations
Number of figures/tables/illustrations	1
High-res required	no
Will you be translating?	no
Circulation/distribution	100 - 199
Author of this Springer Nature content	no
Title	Chalcogenide and metal-oxide memristive devices for advanced neuromorphic computing
Institution name	the university of waterloo
Expected presentation date	Aug 2023
Portions	Figure 1
Requestor Location	the university of waterloo Waterloo, ON N2V 2W5
Requestor Location	ON, ON N2V 2W5 Canada Attn: the university of waterloo
Total	0.00 USD

Figure 3 (a-b)



materials today
Research for sensing and diagnosis
Materials for tomorrow

Resistive switching in transition metal oxides
Author: Akihito Sawa
Publication: Materials Today
Publisher: Elsevier
Date: June 2008
Copyright © 2008 Elsevier Ltd.

Welcome to RightsLink

Elsevier has partnered with Copyright Clearance Center's RightsLink service to offer a variety of options for reusing this content.

Note: This article is available under the [Creative Commons CC-BY-NC-ND](#) license and permits non-commercial use of the work as published, without adaptation or alteration provided the work is fully attributed.

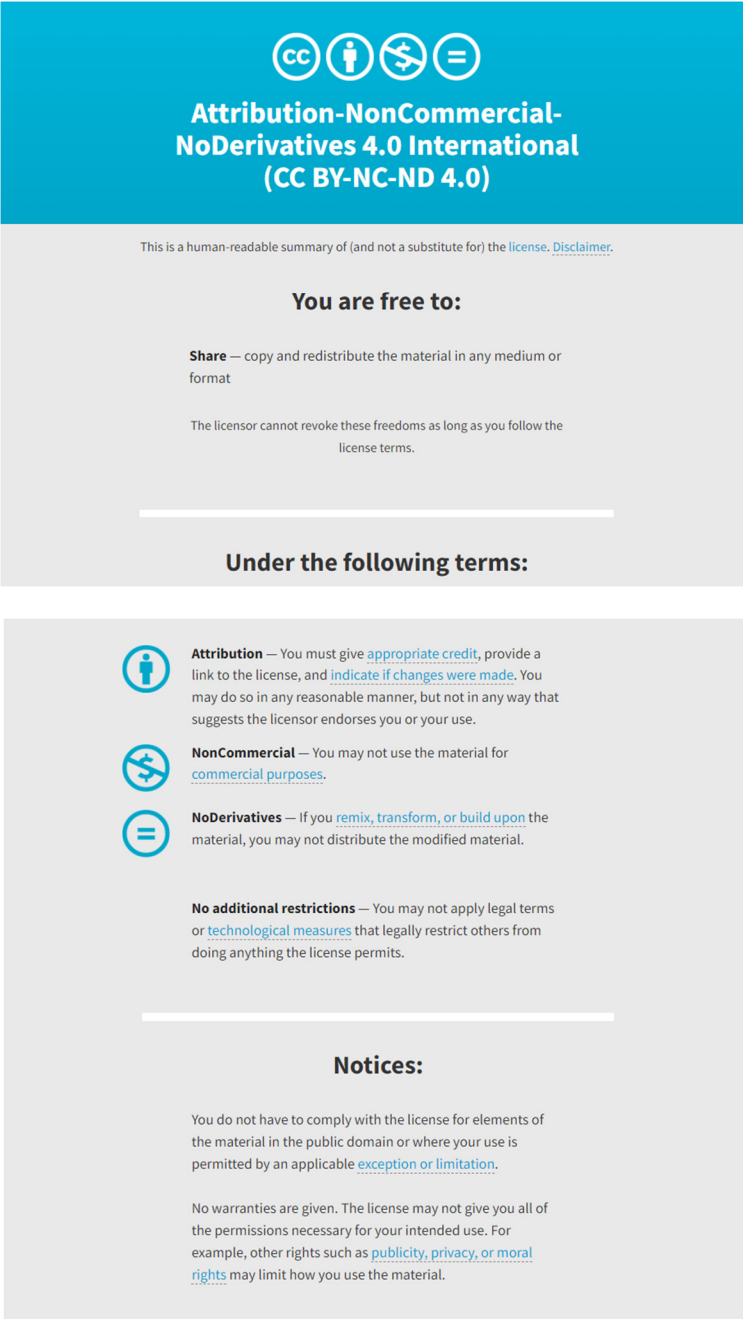
For commercial reuse, permission must be requested below.

Figure 3 (c-d)

This Agreement between the university of waterloo -- Tao Guo ("You") and John Wiley and Sons ("John Wiley and Sons") consists of your license details and the terms and conditions provided by John Wiley and Sons and Copyright Clearance Center.

License Number	5530961150817
License date	Apr 16, 2023
Licensed Content Publisher	John Wiley and Sons
Licensed Content Publication	Advanced Materials
Licensed Content Title	Redox-Based Resistive Switching Memories – Nanoionic Mechanisms, Prospects, and Challenges
Licensed Content Author	Kristof Sztot, Georgi Staikov, Regina Dittmann, et al
Licensed Content Date	Jul 6, 2009
Licensed Content Volume	21
Licensed Content Issue	25-26
Licensed Content Pages	32
Type of use	Dissertation/Thesis
Requestor type	University/Academic
Format	Print and electronic
Portion	Figure/table
Number of figures/tables	1
Will you be translating?	No
Title	Chalcogenide and metal-oxide memristive devices for advanced neuromorphic computing
Institution name	the university of waterloo
Expected presentation date	Aug 2023
Portions	Figure 2
Requestor Location	the university of waterloo Waterloo, ON N2V 2W5 ON, ON N2V 2W5 Canada Attn: the university of waterloo
Publisher Tax ID	EU826007151
Total	0.00 USD

Figure 4a



The image is a vertical rectangular graphic with a blue header and a light gray body. The header contains the Creative Commons icons (CC, person, crossed-out dollar sign, equals sign) and the text "Attribution-NonCommercial-NoDerivatives 4.0 International (CC BY-NC-ND 4.0)". Below the header, there is a disclaimer line, followed by a section titled "You are free to:" with a "Share" definition and a note that freedoms are not revocable. A horizontal line separates this from a section titled "Under the following terms:". This section lists four terms: Attribution (with person icon), NonCommercial (with crossed-out dollar sign icon), NoDerivatives (with equals sign icon), and No additional restrictions. A final horizontal line is followed by a "Notices:" section containing two paragraphs of text.

CC BY-NC-ND 4.0

Attribution-NonCommercial-NoDerivatives 4.0 International
(CC BY-NC-ND 4.0)

This is a human-readable summary of (and not a substitute for) the [license](#). [Disclaimer](#).

You are free to:

Share — copy and redistribute the material in any medium or format

The licensor cannot revoke these freedoms as long as you follow the license terms.

Under the following terms:

Attribution — You must give [appropriate credit](#), provide a link to the license, and [indicate if changes were made](#). You may do so in any reasonable manner, but not in any way that suggests the licensor endorses you or your use.

NonCommercial — You may not use the material for [commercial purposes](#).

NoDerivatives — If you [remix, transform, or build upon](#) the material, you may not distribute the modified material.


No additional restrictions — You may not apply legal terms or [technological measures](#) that legally restrict others from doing anything the license permits.

Notices:

You do not have to comply with the license for elements of the material in the public domain or where your use is permitted by an applicable [exception or limitation](#).

No warranties are given. The license may not give you all of the permissions necessary for your intended use. For example, other rights such as [publicity, privacy, or moral rights](#) may limit how you use the material.

Figure 4b



Back-End-of-Line SiC-Based Memristor for Resistive Memory and Artificial Synapse
Author: Ruomeng Huang, C. H. (Kees) de Groot, Liudi Jiang, et al
Publication: Advanced Electronic Materials
Publisher: John Wiley and Sons
Date: Jun 1, 2022

© 2022 The Authors. *Advanced Electronic Materials* published by Wiley-VCH GmbH

Open Access Article

This is an open access article distributed under the terms of the [Creative Commons CC BY](#) license, which permits unrestricted use, distribution, and reproduction in any medium, provided the original work is properly cited.

You are not required to obtain permission to reuse this article.

For an understanding of what is meant by the terms of the Creative Commons License, please refer to [Wiley's Open Access Terms and Conditions](#).


Permission is not required for this type of reuse.

Wiley offers a professional reprint service for high quality reproduction of articles from over 1400 scientific and medical journals. Wiley's reprint service offers:

- Peer reviewed research or reviews
- Tailored collections of articles
- A professional high quality finish
- Glossy journal style color covers
- Company or brand customisation
- Language translations
- Prompt turnaround times and delivery directly to your office, warehouse or congress.

Please contact our Reprints department for a quotation. Email corporatesaleseurope@wiley.com or corporatesalesusa@wiley.com or corporatesalesDE@wiley.com.

Figure 4c



Down-Scalable and Ultra-fast Memristors with Ultra-high Density Three-Dimensional Arrays of Perovskite Quantum Wires
Author: Swapnadeep Poddar, Yuting Zhang, Leilei Gu, et al
Publication: Nano Letters
Publisher: American Chemical Society
Date: Jun 1, 2021
Copyright © 2021, American Chemical Society

PERMISSION/LICENSE IS GRANTED FOR YOUR ORDER AT NO CHARGE

This type of permission/license, instead of the standard Terms and Conditions, is sent to you because no fee is being charged for your order. Please note the following:

- Permission is granted for your request in both print and electronic formats, and translations.
- If figures and/or tables were requested, they may be adapted or used in part.
- Please print this page for your records and send a copy of it to your publisher/graduate school.
- Appropriate credit for the requested material should be given as follows: "Reprinted (adapted) with permission from (COMPLETE REFERENCE CITATION). Copyright (YEAR) American Chemical Society." Insert appropriate information in place of the capitalized words.
- One-time permission is granted only for the use specified in your RightsLink request. No additional uses are granted (such as derivative works or other editions). For any uses, please submit a new request.

If credit is given to another source for the material you requested from RightsLink, permission must be obtained from that source.

[BACK](#) [CLOSE WINDOW](#)

Figure 4d

Rights and permissions

Open Access This article is distributed under the terms of the Creative Commons Attribution 2.0 International License (<https://creativecommons.org/licenses/by/2.0>), which permits unrestricted use, distribution, and reproduction in any medium, provided the original work is properly cited.

[Reprints and Permissions](#)

Figure 4e

Publisher's Note: MDPI stays neutral with regard to jurisdictional claims in published maps and institutional affiliations.



Copyright: © 2021 by the authors. Licensee MDPI, Basel, Switzerland. This article is an open access article distributed under the terms and conditions of the Creative Commons Attribution (CC BY) license (<https://creativecommons.org/licenses/by/4.0/>).

Figure 5a-b

SPRINGER NATURE

Surface diffusion-limited lifetime of silver and copper nanofilaments in resistive switching devices

Author: Wei Wang et al
Publication: Nature Communications
Publisher: Springer Nature
Date: Jan 8, 2019

Copyright © 2019, The Author(s)

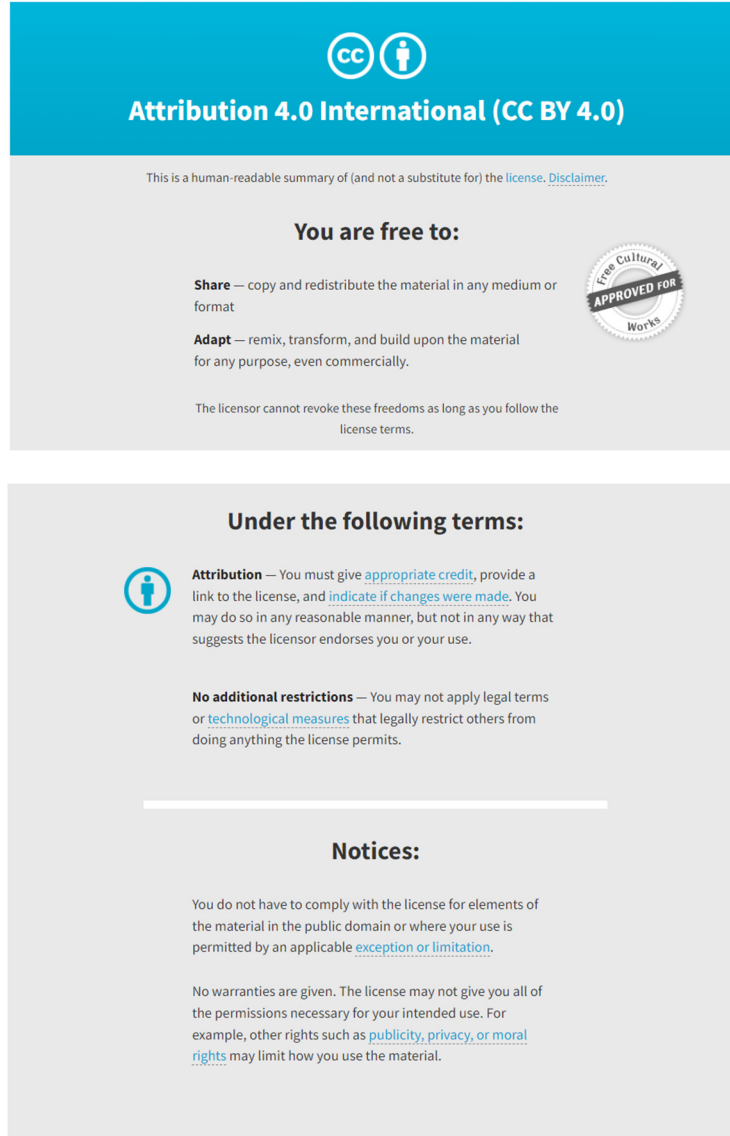
Creative Commons

This is an open access article distributed under the terms of the [Creative Commons CC BY](#) license, which permits unrestricted use, distribution, and reproduction in any medium, provided the original work is properly cited.

You are not required to obtain permission to reuse this article.
To request permission for a type of use not listed, please contact [Springer Nature](#)

© 2023 Copyright - All Rights Reserved | [Copyright Clearance Center, Inc.](#) | [Privacy statement](#) | [Data Security and Privacy](#) | [For California Residents](#) | [Terms and Conditions](#)
Comments? We would like to hear from you. E-mail us at customer-care@copyright.com

Figure 5c



The image shows a summary page for the Creative Commons Attribution 4.0 International License (CC BY 4.0). The page is divided into two main sections: "You are free to:" and "Under the following terms:". The "You are free to:" section lists the rights to share and adapt the material, with a "Free Cultural Works" seal. The "Under the following terms:" section details the attribution requirement and the prohibition of additional restrictions. A "Notices:" section at the bottom provides additional information about public domain elements, exceptions, and warranties.

CC BY


Attribution 4.0 International (CC BY 4.0)

This is a human-readable summary of (and not a substitute for) the license. [Disclaimer.](#)

You are free to:


Share — copy and redistribute the material in any medium or format

Adapt — remix, transform, and build upon the material for any purpose, even commercially.



The licensor cannot revoke these freedoms as long as you follow the license terms.

Under the following terms:

 **Attribution** — You must give [appropriate credit](#), provide a link to the license, and [indicate if changes were made](#). You may do so in any reasonable manner, but not in any way that suggests the licensor endorses you or your use.

No additional restrictions — You may not apply legal terms or [technological measures](#) that legally restrict others from doing anything the license permits.

Notices:

You do not have to comply with the license for elements of the material in the public domain or where your use is permitted by an applicable [exception or limitation](#).

No warranties are given. The license may not give you all of the permissions necessary for your intended use. For example, other rights such as [publicity, privacy, or moral rights](#) may limit how you use the material.

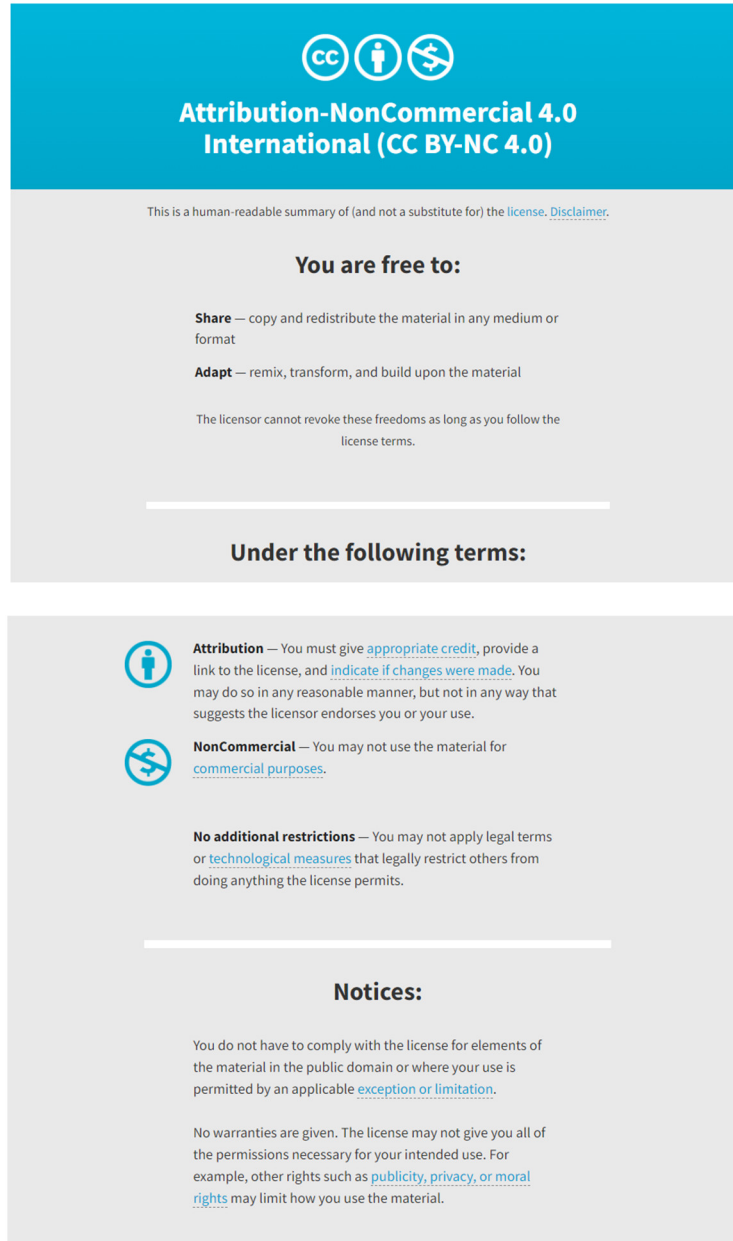
Figure 5d

Publisher’s Note: MDPI stays neutral with regard to jurisdictional claims in published maps and institutional affiliations.




Copyright: © 2022 by the authors. Licensee MDPI, Basel, Switzerland. This article is an open access article distributed under the terms and conditions of the Creative Commons Attribution (CC BY) license (<https://creativecommons.org/licenses/by/4.0/>).

Figure 5e



The image is a vertical graphic with a blue header and two grey sections. The header contains the CC BY-NC icons and the license title. The first grey section contains a disclaimer, a 'You are free to:' section with 'Share' and 'Adapt' definitions, and a note about license revocation. The second grey section contains 'Under the following terms:' followed by 'Attribution' and 'NonCommercial' definitions, a 'No additional restrictions' note, and a 'Notices:' section with two paragraphs of text.


Attribution-NonCommercial 4.0 International (CC BY-NC 4.0)

This is a human-readable summary of (and not a substitute for) the [license](#). [Disclaimer](#).


You are free to:


Share — copy and redistribute the material in any medium or format

Adapt — remix, transform, and build upon the material

The licensor cannot revoke these freedoms as long as you follow the license terms.

Under the following terms:

 **Attribution** — You must give [appropriate credit](#), provide a link to the license, and [indicate if changes were made](#). You may do so in any reasonable manner, but not in any way that suggests the licensor endorses you or your use.

 **NonCommercial** — You may not use the material for [commercial purposes](#).


No additional restrictions — You may not apply legal terms or [technological measures](#) that legally restrict others from doing anything the license permits.

Notices:

You do not have to comply with the license for elements of the material in the public domain or where your use is permitted by an applicable [exception or limitation](#).

No warranties are given. The license may not give you all of the permissions necessary for your intended use. For example, other rights such as [publicity, privacy, or moral rights](#) may limit how you use the material.

Figure 6a



High-Performance Flexible Polymer Memristor Based on Stable Filamentary Switching
Author: Xinshui Zhang, Cong Wu, Yinjie Lv, et al
Publication: Nano Letters
Publisher: American Chemical Society
Date: Sep 1, 2022
Copyright © 2022, American Chemical Society

PERMISSION/LICENSE IS GRANTED FOR YOUR ORDER AT NO CHARGE

This type of permission/license, instead of the standard Terms and Conditions, is sent to you because no fee is being charged for your order. Please note the following:

- Permission is granted for your request in both print and electronic formats, and translations.
- If figures and/or tables were requested, they may be adapted or used in part.
- Please print this page for your records and send a copy of it to your publisher/graduate school.
- Appropriate credit for the requested material should be given as follows: "Reprinted (adapted) with permission from {COMPLETE REFERENCE CITATION}. Copyright (YEAR) American Chemical Society." Insert appropriate information in place of the capitalized words.
- One-time permission is granted only for the use specified in your RightsLink request. No additional uses are granted (such as derivative works or other editions). For any uses, please submit a new request.

If credit is given to another source for the material you requested from RightsLink, permission must be obtained from that source.

[BACK](#) [CLOSE WINDOW](#)

Figure 6b

Rights and permissions

Open Access This article is distributed under the terms of the Creative Commons Attribution 2.0 International License (<https://creativecommons.org/licenses/by/2.0>), which permits unrestricted use, distribution, and reproduction in any medium, provided the original work is properly cited.

[Reprints and Permissions](#)

Figure 6c

This Agreement between the university of waterloo -- Tao Guo ("You") and Springer Nature ("Springer Nature") consists of your license details and the terms and conditions provided by Springer Nature and Copyright Clearance Center.

License Number	5530981356518
License date	Apr 16, 2023
Licensed Content Publisher	Springer Nature
Licensed Content Publication	Nature Electronics
Licensed Content Title	Wafer-scale integration of two-dimensional materials in high-density memristive crossbar arrays for artificial neural networks
Licensed Content Author	Shaochuan Chen et al
Licensed Content Date	Oct 19, 2020
Type of Use	Thesis/Dissertation
Requestor type	academic/university or research institute
Format	print and electronic
Portion	figures/tables/illustrations
Number of figures/tables/illustrations	1
High-res required	no
Will you be translating?	no
Circulation/distribution	100 - 199
Author of this Springer Nature content	no
Title	Chalcogenide and metal-oxide memristive devices for advanced neuromorphic computing
Institution name	the university of waterloo
Expected presentation date	Aug 2023
Portions	Figure 2e
Requestor Location	the university of waterloo Waterloo, ON N2V 2W5 ON, ON N2V 2W5 Canada Attn: the university of waterloo
Total	0.00 USD

Figure 6d

This Agreement between the university of waterloo -- Tao Guo ("You") and Springer Nature ("Springer Nature") consists of your license details and the terms and conditions provided by Springer Nature and Copyright Clearance Center.

License Number	5530981478473
License date	Apr 16, 2023
Licensed Content Publisher	Springer Nature
Licensed Content Publication	Nature
Licensed Content Title	Fully hardware-implemented memristor convolutional neural network
Licensed Content Author	Peng Yao et al
Licensed Content Date	Jan 29, 2020
Type of Use	Thesis/Dissertation
Requestor type	academic/university or research institute
Format	print and electronic
Portion	figures/tables/illustrations
Number of figures/tables/illustrations	1
High-res required	no
Will you be translating?	no
Circulation/distribution	100 - 199
Author of this Springer Nature content	no
Title	Chalcogenide and metal-oxide memristive devices for advanced neuromorphic computing
Institution name	the university of waterloo
Expected presentation date	Aug 2023
Portions	Figure 1c
Requestor Location	the university of waterloo Waterloo, ON N2V 2W5 ON, ON N2V 2W5 Canada Attn: the university of waterloo
Total	0.00 USD

Figure 6e

Dielectric Engineered Two-Dimensional Neuromorphic Transistors

Author: Du Xiang, Tao Liu, Xumeng Zhang, et al
Publication: Nano Letters
Publisher: American Chemical Society
Date: Apr 1, 2021

Copyright © 2021, American Chemical Society

PERMISSION/LICENSE IS GRANTED FOR YOUR ORDER AT NO CHARGE

This type of permission/license, instead of the standard Terms and Conditions, is sent to you because no fee is being charged for your order. Please note the following:

- Permission is granted for your request in both print and electronic formats, and translations.
- If figures and/or tables were requested, they may be adapted or used in part.
- Please print this page for your records and send a copy of it to your publisher/graduate school.
- Appropriate credit for the requested material should be given as follows: "Reprinted (adapted) with permission from {COMPLETE REFERENCE CITATION}. Copyright {YEAR} American Chemical Society." Insert appropriate information in place of the capitalized words.
- One-time permission is granted only for the use specified in your RightsLink request. No additional uses are granted (such as derivative works or other editions). For any uses, please submit a new request.

If credit is given to another source for the material you requested from RightsLink, permission must be obtained from that source.

[BACK](#) [CLOSE WINDOW](#)

Figure 6f

This Agreement between the university of waterloo -- Tao Guo ("You") and Springer Nature ("Springer Nature") consists of your license details and the terms and conditions provided by Springer Nature and Copyright Clearance Center.

License Number	5530990190419
License date	Apr 16, 2023
Licensed Content Publisher	Springer Nature
Licensed Content Publication	Nature Electronics
Licensed Content Title	Reinforcement learning with analogue memristor arrays
Licensed Content Author	Zhongrui Wang et al
Licensed Content Date	Mar 15, 2019
Type of Use	Thesis/Dissertation
Requestor type	academic/university or research institute
Format	print and electronic
Portion	figures/tables/illustrations
Number of figures/tables/illustrations	1
High-res required	no
Will you be translating?	no
Circulation/distribution	100 - 199
Author of this Springer Nature content	no
Title	Chalcogenide and metal-oxide memristive devices for advanced neuromorphic computing
Institution name	the university of waterloo
Expected presentation date	Aug 2023
Portions	Figure 1e
Requestor Location	the university of waterloo Waterloo, ON N2V 2W5 ON, ON N2V 2W5 Canada Attn: the university of waterloo
Total	0.00 USD
Terms and Conditions	

Figure 7a

SPRINGER NATURE

Evolution of the conductive filament system in HfO₂-based memristors observed by direct atomic-scale imaging

Author: Ying Zhang et al
Publication: Nature Communications
Publisher: Springer Nature
Date: Dec 13, 2021

Copyright © 2021, The Author(s)

Creative Commons

This is an open access article distributed under the terms of the [Creative Commons CC BY](#) license, which permits unrestricted use, distribution, and reproduction in any medium, provided the original work is properly cited.

You are not required to obtain permission to reuse this article.
To request permission for a type of use not listed, please contact [Springer Nature](#)

Figure 7b

Publisher's Note: MDPI stays neutral with regard to jurisdictional claims in published maps and institutional affiliations.



Copyright: © 2021 by the authors. Licensee MDPI, Basel, Switzerland. This article is an open access article distributed under the terms and conditions of the Creative Commons Attribution (CC BY) license (<https://creativecommons.org/licenses/by/4.0/>).

Figure 7c

SPRINGER NATURE

Voltage divider effect for the improvement of variability and endurance of TaOx memristor

Author: Kyung Min Kim et al
Publication: Scientific Reports
Publisher: Springer Nature
Date: Feb 2, 2016


Copyright © 2016, The Author(s)

Creative Commons

This is an open access article distributed under the terms of the [Creative Commons CC BY](#) license, which permits unrestricted use, distribution, and reproduction in any medium, provided the original work is properly cited.

You are not required to obtain permission to reuse this article.
To request permission for a type of use not listed, please contact [Springer Nature](#)

Figure 7d



Intrinsic Switching Behavior in HfO₂ RRAM by Fast Electrical Measurements on Novel 2R Test Structures

Conference Proceedings: 2012 4th IEEE International Memory Workshop
Author: A. Fantini
Publisher: IEEE
Date: May 2012
Copyright © 2012, IEEE

Thesis / Dissertation Reuse

The IEEE does not require individuals working on a thesis to obtain a formal reuse license, however, you may print out this statement to be used as a permission grant:

Requirements to be followed when using any portion (e.g., figure, graph, table, or textual material) of an IEEE copyrighted paper in a thesis:

- 1) In the case of textual material (e.g., using short quotes or referring to the work within these papers) users must give full credit to the original source (author, paper, publication) followed by the IEEE copyright line © 2011 IEEE.
- 2) In the case of illustrations or tabular material, we require that the copyright line © [Year of original publication] IEEE appear prominently with each reprinted figure and/or table.
- 3) If a substantial portion of the original paper is to be used, and if you are not the senior author, also obtain the senior author's approval.


Requirements to be followed when using an entire IEEE copyrighted paper in a thesis:

- 1) The following IEEE copyright/ credit notice should be placed prominently in the references: © [year of original publication] IEEE. Reprinted, with permission, from [author names, paper title, IEEE publication title, and month/year of publication]
- 2) Only the accepted version of an IEEE copyrighted paper can be used when posting the paper or your thesis on-line.
- 3) In placing the thesis on the author's university website, please display the following message in a prominent place on the website: In reference to IEEE copyrighted material which is used with permission in this thesis, the IEEE does not endorse any of [university/educational entity's name goes here]'s products or services. Internal or personal use of this material is permitted. If interested in reprinting/republishing IEEE copyrighted material for advertising or promotional purposes or for creating new collective works for resale or redistribution, please go to http://www.ieee.org/publications_standards/publications/rights/rights_link.html to learn how to obtain a License from RightsLink.

If applicable, University Microfilms and/or ProQuest Library, or the Archives of Canada may supply single copies of the dissertation.

[BACK](#) [CLOSE WINDOW](#)

Figure 9 and Figure 10

 Home Help Live Chat Tao Guo

From Memristive Materials to Neural Networks
Author: Tao Guo, Bai Sun, Shubham Ranjan, et al
Publication: Applied Materials
Publisher: American Chemical Society
Date: Dec 1, 2020
Copyright © 2020, American Chemical Society

PERMISSION/LICENSE IS GRANTED FOR YOUR ORDER AT NO CHARGE

This type of permission/license, instead of the standard Terms and Conditions, is sent to you because no fee is being charged for your order. Please note the following:

- Permission is granted for your request in both print and electronic formats, and translations.
- If figures and/or tables were requested, they may be adapted or used in part.
- Please print this page for your records and send a copy of it to your publisher/graduate school.
- Appropriate credit for the requested material should be given as follows: "Reprinted (adapted) with permission from (COMPLETE REFERENCE CITATION). Copyright (YEAR) American Chemical Society." Insert appropriate information in place of the capitalized words.
- One-time permission is granted only for the use specified in your RightsLink request. No additional uses are granted (such as derivative works or other editions). For any uses, please submit a new request.

If credit is given to another source for the material you requested from RightsLink, permission must be obtained from that source.

[BACK](#) [CLOSE WINDOW](#)

Figure 11a

This Agreement between the university of waterloo -- Tao Guo ("You") and Springer Nature ("Springer Nature") consists of your license details and the terms and conditions provided by Springer Nature and Copyright Clearance Center.

License Number	5530990734219
License date	Apr 16, 2023
Licensed Content Publisher	Springer Nature
Licensed Content Publication	Nature Communications
Licensed Content Title	Electrochemical dynamics of nanoscale metallic inclusions in dielectrics
Licensed Content Author	Yuchao Yang et al
Licensed Content Date	Jun 23, 2014
Type of Use	Thesis/Dissertation
Requestor type	academic/university or research institute
Format	print and electronic
Portion	figures/tables/illustrations
Number of figures/tables/illustrations	1
High-res required	no
Will you be translating?	no
Circulation/distribution	100 - 199
Author of this Springer Nature content	no
Title	Chalcogenide and metal-oxide memristive devices for advanced neuromorphic computing
Institution name	the university of waterloo
Expected presentation date	Aug 2023
Portions	Figure 4a
Requestor Location	the university of waterloo Waterloo, ON N2V 2W5 ON, ON N2V 2W5 Canada Attn: the university of waterloo
Total	0.00 USD

Figure 11b

This Agreement between the university of waterloo -- Tao Guo ("You") and Springer Nature ("Springer Nature") consists of your license details and the terms and conditions provided by Springer Nature and Copyright Clearance Center.

License Number	5530990834513
License date	Apr 16, 2023
Licensed Content Publisher	Springer Nature
Licensed Content Publication	Nature Communications
Licensed Content Title	Observation of conducting filament growth in nanoscale resistive memories
Licensed Content Author	Yuchao Yang et al
Licensed Content Date	Mar 13, 2012
Type of Use	Thesis/Dissertation
Requestor type	academic/university or research institute
Format	print and electronic
Portion	figures/tables/illustrations
Number of figures/tables/illustrations	1
High-res required	no
Will you be translating?	no
Circulation/distribution	100 - 199
Author of this Springer Nature content	no
Title	Chalcogenide and metal-oxide memristive devices for advanced neuromorphic computing
Institution name	the university of waterloo
Expected presentation date	Aug 2023
Portions	Figure 1
Requestor Location	the university of waterloo Waterloo, ON N2V 2W5 ON, ON N2V 2W5 Canada Attn: the university of waterloo
Total	0.00 USD

Figure 11c-d

This Agreement between the university of waterloo -- Tao Guo ("You") and Springer Nature ("Springer Nature") consists of your license details and the terms and conditions provided by Springer Nature and Copyright Clearance Center.

License Number	5530990938492
License date	Apr 16, 2023
Licensed Content Publisher	Springer Nature
Licensed Content Publication	Nature Communications
Licensed Content Title	In situ observation of filamentary conducting channels in an asymmetric Ta ₂ O ₅ -x/TaO ₂ -x bilayer structure
Licensed Content Author	Gyeong-Su Park et al
Licensed Content Date	Sep 6, 2013
Type of Use	Thesis/Dissertation
Requestor type	academic/university or research institute
Format	print and electronic
Portion	figures/tables/illustrations
Number of figures/tables/illustrations	1
High-res required	no
Will you be translating?	no
Circulation/distribution	100 - 199
Author of this Springer Nature content	no
Title	Chalcogenide and metal-oxide memristive devices for advanced neuromorphic computing
Institution name	the university of waterloo
Expected presentation date	Aug 2023
Portions	Figure 3
Requestor Location	the university of waterloo Waterloo, ON N2V 2W5 ON, ON N2V 2W5 Canada Attn: the university of waterloo
Total	0.00 USD

Figure 11e-g

SPRINGER NATURE

Evolution of the conductive filament system in HfO₂-based memristors observed by direct atomic-scale imaging

Author: Ying Zhang et al
Publication: Nature Communications
Publisher: Springer Nature
Date: Dec 13, 2021

Copyright © 2021, The Author(s)

Creative Commons

This is an open access article distributed under the terms of the [Creative Commons CC BY](#) license, which permits unrestricted use, distribution, and reproduction in any medium, provided the original work is properly cited.

You are not required to obtain permission to reuse this article.
To request permission for a type of use not listed, please contact [Springer Nature](#)

Figure 12a

This Agreement between the university of waterloo -- Tao Guo ("You") and John Wiley and Sons ("John Wiley and Sons") consists of your license details and the terms and conditions provided by John Wiley and Sons and Copyright Clearance Center.


License Number	5530991116112
License date	Apr 16, 2023
Licensed Content Publisher	John Wiley and Sons
Licensed Content Publication	Advanced Energy Materials
Licensed Content Title	Emerging Conductive Atomic Force Microscopy for Metal Halide Perovskite Materials and Solar Cells
Licensed Content Author	Yue Zhang, Zhuo Kang, Abdul Sattar, et al
Licensed Content Date	Feb 5, 2020
Licensed Content Volume	10
Licensed Content Issue	10
Licensed Content Pages	23
Type of use	Dissertation/Thesis
Requestor type	University/Academic
Format	Print and electronic
Portion	Figure/table
Number of figures/tables	1
Will you be translating?	No
Title	Chalcogenide and metal-oxide memristive devices for advanced neuromorphic computing
Institution name	the university of waterloo
Expected presentation date	Aug 2023
Portions	Figure 1
Requestor Location	the university of waterloo Waterloo, ON N2V 2W5 ON, ON N2V 2W5 Canada Attn: the university of waterloo
Publisher Tax ID	EU826007151

Figure 12b

This Agreement between the university of waterloo -- Tao Guo ("You") and AIP Publishing ("AIP Publishing") consists of your license details and the terms and conditions provided by AIP Publishing and Copyright Clearance Center.

License Number	5530991279778
License date	Apr 16, 2023
Licensed Content Publisher	AIP Publishing
Licensed Content Publication	Applied Physics Letters
Licensed Content Title	Direct observation of conducting filaments on resistive switching of NiO thin films
Licensed Content Author	J. Y. Son, Y.-H. Shin
Licensed Content Date	Jun 2, 2008
Licensed Content Volume	92
Licensed Content Issue	22
Type of Use	Thesis/Dissertation
Requestor type	University or Educational Institution
Format	Print and electronic
Portion	Photograph/Image
Number of Photographs/Images	1
Will you be translating?	No
Title	Chalcogenide and metal-oxide memristive devices for advanced neuromorphic computing
Institution name	the university of waterloo
Expected presentation date	Aug 2023
Portions	Figure 3
Requestor Location	the university of waterloo Waterloo, ON N2V 2W5 ON, ON N2V 2W5 Canada Attn: the university of waterloo
Total	0.00 USD

Figure 12c



Requesting permission to reuse content from an IEEE publication

Conductive-AFM tomography for 3D filament observation in resistive switching devices

Conference Proceedings: 2013 IEEE International Electron Devices Meeting

Author: U. Celano

Publisher: IEEE

Date: December 2013

Copyright © 2013, IEEE

Thesis / Dissertation Reuse

The IEEE does not require individuals working on a thesis to obtain a formal reuse license, however, you may print out this statement to be used as a permission grant:

Requirements to be followed when using any portion (e.g., figure, graph, table, or textual material) of an IEEE copyrighted paper in a thesis:

- 1) In the case of textual material (e.g., using short quotes or referring to the work within these papers) users must give full credit to the original source (author, paper, publication) followed by the IEEE copyright line © 2011 IEEE.
- 2) In the case of illustrations or tabular material, we require that the copyright line © [Year of original publication] IEEE appear prominently with each reprinted figure and/or table.
- 3) If a substantial portion of the original paper is to be used, and if you are not the senior author, also obtain the senior author's approval.

Requirements to be followed when using an entire IEEE copyrighted paper in a thesis:

- 1) The following IEEE copyright/ credit notice should be placed prominently in the references: © [year of original publication] IEEE. Reprinted, with permission, from [author names, paper title, IEEE publication title, and month/year of publication]
- 2) Only the accepted version of an IEEE copyrighted paper can be used when posting the paper or your thesis on-line.
- 3) In placing the thesis on the author's university website, please display the following message in a prominent place on the website: In reference to IEEE copyrighted material which is used with permission in this thesis, the IEEE does not endorse any of [university/educational entity's name goes here]'s products or services. Internal or personal use of this material is permitted. If interested in reprinting/republishing IEEE copyrighted material for advertising or promotional purposes or for creating new collective works for resale or redistribution, please go to http://www.ieee.org/publications_standards/publications/rights/rights_link.html to learn how to obtain a License from RightsLink.

If applicable, University Microfilms and/or ProQuest Library, or the Archives of Canada may supply single copies of the dissertation.

[BACK](#) [CLOSE WINDOW](#)

Figure 12d-e

Resistive Switching Mechanisms on TaOx and SrRuO3 Thin-Film Surfaces Probed by Scanning Tunneling Microscopy

Author: Marco Moors, Kiran Kumar Adepalli, Qiyang Lu, et al
Publication: ACS Nano
Publisher: American Chemical Society
Date: Jan 1, 2016

Copyright © 2016, American Chemical Society

PERMISSION/LICENSE IS GRANTED FOR YOUR ORDER AT NO CHARGE

This type of permission/license, instead of the standard Terms and Conditions, is sent to you because no fee is being charged for your order. Please note the following:

- Permission is granted for your request in both print and electronic formats, and translations.
- If figures and/or tables were requested, they may be adapted or used in part.
- Please print this page for your records and send a copy of it to your publisher/graduate school.
- Appropriate credit for the requested material should be given as follows: "Reprinted (adapted) with permission from {COMPLETE REFERENCE CITATION}. Copyright {YEAR} American Chemical Society." Insert appropriate information in place of the capitalized words.
- One-time permission is granted only for the use specified in your RightsLink request. No additional uses are granted (such as derivative works or other editions). For any uses, please submit a new request.

If credit is given to another source for the material you requested from RightsLink, permission must be obtained from that source.

[BACK](#) [CLOSE WINDOW](#)

Figure 13a-b

Conduction Channel Formation and Dissolution Due to Oxygen Thermophoresis/Diffusion in Hafnium Oxide Memristors

Author: Suhas Kumar, Ziwen Wang, Xiaopeng Huang, et al
Publication: ACS Nano
Publisher: American Chemical Society
Date: Dec 1, 2016

Copyright © 2016, American Chemical Society

PERMISSION/LICENSE IS GRANTED FOR YOUR ORDER AT NO CHARGE

This type of permission/license, instead of the standard Terms and Conditions, is sent to you because no fee is being charged for your order. Please note the following:

- Permission is granted for your request in both print and electronic formats, and translations.
- If figures and/or tables were requested, they may be adapted or used in part.
- Please print this page for your records and send a copy of it to your publisher/graduate school.
- Appropriate credit for the requested material should be given as follows: "Reprinted (adapted) with permission from (COMPLETE REFERENCE CITATION). Copyright (YEAR) American Chemical Society." Insert appropriate information in place of the capitalized words.
- One-time permission is granted only for the use specified in your RightsLink request. No additional uses are granted (such as derivative works or other editions). For any uses, please submit a new request.

If credit is given to another source for the material you requested from RightsLink, permission must be obtained from that source.

[BACK](#) [CLOSE WINDOW](#)

Figure 13c-d

This Agreement between the university of waterloo -- Tao Guo ("You") and John Wiley and Sons ("John Wiley and Sons") consists of your license details and the terms and conditions provided by John Wiley and Sons and Copyright Clearance Center.

License Number	5531000571450
License date	Apr 16, 2023
Licensed Content Publisher	John Wiley and Sons
Licensed Content Publication	Advanced Materials
Licensed Content Title	Controlled Formation of Conduction Channels in Memristive Devices Observed by X-ray Multimodal Imaging
Licensed Content Author	Dillon D. Fong, Hua Zhou, Badri Narayanan, et al
Licensed Content Date	Aug 3, 2022
Licensed Content Volume	34
Licensed Content Issue	35
Licensed Content Pages	9
Type of use	Dissertation/Thesis
Requestor type	University/Academic
Format	Print and electronic
Portion	Figure/table
Number of figures/tables	2
Will you be translating?	No
Title	Chalcogenide and metal-oxide memristive devices for advanced neuromorphic computing
Institution name	the university of waterloo
Expected presentation date	Aug 2023
Portions	Figure 1 and Figure 2
Requestor Location	the university of waterloo Waterloo, ON N2V 2W5 ON, ON N2V 2W5 Canada Attn: the university of waterloo
Publisher Tax ID	EU826007151
Total	0.00 USD

Figure 14a

This Agreement between the university of waterloo -- Tao Guo ("You") and AIP Publishing ("AIP Publishing") consists of your license details and the terms and conditions provided by AIP Publishing and Copyright Clearance Center.

License Number	5531000823921
License date	Apr 16, 2023
Licensed Content Publisher	AIP Publishing
Licensed Content Publication	Journal of Applied Physics
Licensed Content Title	Multilevel resistive switching in Ti/Cu _x O/Pt memory devices
Licensed Content Author	Sheng-Yu Wang, Chin-Wen Huang, Dai-Ying Lee, et al
Licensed Content Date	Dec 1, 2010
Licensed Content Volume	108
Licensed Content Issue	11
Type of Use	Thesis/Dissertation
Requestor type	University or Educational Institution
Format	Print and electronic
Portion	Figure/Table
Number of figures/tables	1
Will you be translating?	No
Title	Chalcogenide and metal-oxide memristive devices for advanced neuromorphic computing
Institution name	the university of waterloo
Expected presentation date	Aug 2023
Portions	Figure 3
Requestor Location	the university of waterloo Waterloo, ON N2V 2W5
	ON, ON N2V 2W5 Canada Attn: the university of waterloo
Total	0.00 USD

Figure 14b-c

This Agreement between the university of waterloo -- Tao Guo ("You") and AIP Publishing ("AIP Publishing") consists of your license details and the terms and conditions provided by AIP Publishing and Copyright Clearance Center.

License Number 5531000925835

License date Apr 16, 2023

Licensed Content
Publisher AIP Publishing

Licensed Content
Publication Applied Physics Letters

Licensed Content
Title Study of conduction and switching mechanisms in Al/AlOx/WOx/W resistive switching memory for multilevel applications

Licensed Content
Author Ye Zhang, Huaqiang Wu, Yue Bai, et al

Licensed Content
Date Jun 10, 2013

Licensed Content
Volume 102

Licensed Content
Issue 23

Type of Use Thesis/Dissertation

Requestor type University or Educational Institution

Format Print and electronic

Portion Figure/Table

Number of
figures/tables 1

Will you be
translating? No

Title Chalcogenide and metal-oxide memristive devices for advanced neuromorphic computing

Institution name the university of waterloo

Expected
presentation date Aug 2023

Portions Figure 5

Requestor
Location the university of waterloo
Waterloo, ON N2V 2W5
ON, ON N2V 2W5
Canada
Attn: the university of waterloo

Total 0.00 USD

Figure 14d-e

This Agreement between the university of waterloo -- Tao Guo ("You") and AIP Publishing ("AIP Publishing") consists of your license details and the terms and conditions provided by AIP Publishing and Copyright Clearance Center.

License Number	5531001029036
License date	Apr 16, 2023
Licensed Content Publisher	AIP Publishing
Licensed Content Publication	Applied Physics Letters
Licensed Content Title	On the resistive switching mechanisms of Cu/ZrO ₂ :Cu/Pt
Licensed Content Author	Weihua Guan, Ming Liu, Shibing Long, et al
Licensed Content Date	Dec 1, 2008
Licensed Content Volume	93
Licensed Content Issue	22
Type of Use	Thesis/Dissertation
Requestor type	University or Educational Institution
Format	Print and electronic
Portion	Figure/Table
Number of figures/tables	1
Will you be translating?	No
Title	Chalcogenide and metal-oxide memristive devices for advanced neuromorphic computing
Institution name	the university of waterloo
Expected presentation date	Aug 2023
Portions	Figure 3
Requestor Location	the university of waterloo Waterloo, ON N2V 2W5
	ON, ON N2V 2W5 Canada Attn: the university of waterloo
Total	0.00 USD

Figure 14f-g

Generic Relevance of Counter Charges for Cation-Based Nanoscale Resistive Switching Memories

Author: Stefan Tappertzhofen, Iliia Valov, Tohru Tsuruoka, et al
Publication: ACS Nano
Publisher: American Chemical Society
Date: Jul 1, 2013

Copyright © 2013, American Chemical Society

PERMISSION/LICENSE IS GRANTED FOR YOUR ORDER AT NO CHARGE

This type of permission/license, instead of the standard Terms and Conditions, is sent to you because no fee is being charged for your order. Please note the following:

- Permission is granted for your request in both print and electronic formats, and translations.
- If figures and/or tables were requested, they may be adapted or used in part.
- Please print this page for your records and send a copy of it to your publisher/graduate school.
- Appropriate credit for the requested material should be given as follows: "Reprinted (adapted) with permission from {COMPLETE REFERENCE CITATION}. Copyright {YEAR} American Chemical Society." Insert appropriate information in place of the capitalized words.
- One-time permission is granted only for the use specified in your RightsLink request. No additional uses are granted (such as derivative works or other editions). For any uses, please submit a new request.

If credit is given to another source for the material you requested from RightsLink, permission must be obtained from that source.

[BACK](#) [CLOSE WINDOW](#)

Figure 15b-e

SPRINGER NATURE	<p>Understanding memristive switching via in situ characterization and device modeling</p> <p>Author: Wen Sun et al Publication: Nature Communications Publisher: Springer Nature Date: Aug 1, 2019</p> <p><i>Copyright © 2019, The Author(s)</i></p>
<p>Creative Commons</p> <p>This is an open access article distributed under the terms of the Creative Commons CC BY license, which permits unrestricted use, distribution, and reproduction in any medium, provided the original work is properly cited.</p> <p>You are not required to obtain permission to reuse this article.</p> <p>To request permission for a type of use not listed, please contact Springer Nature</p>	

Figure 17a

This Agreement between the university of waterloo -- Tao Guo ("You") and Springer Nature ("Springer Nature") consists of your license details and the terms and conditions provided by Springer Nature and Copyright Clearance Center.

License Number	5531001377588
License date	Apr 16, 2023
Licensed Content Publisher	Springer Nature
Licensed Content Publication	Nature Electronics
Licensed Content Title	Neuro-inspired computing chips
Licensed Content Author	Wenqiang Zhang et al
Licensed Content Date	Jul 21, 2020
Type of Use	Thesis/Dissertation
Requestor type	academic/university or research institute
Format	print and electronic
Portion	figures/tables/illustrations
Number of figures/tables/illustrations	1
High-res required	no
Will you be translating?	no
Circulation/distribution	100 - 199
Author of this Springer Nature content	no
Title	Chalcogenide and metal-oxide memristive devices for advanced neuromorphic computing
Institution name	the university of waterloo
Expected presentation date	Aug 2023
Portions	Figure 1
Requestor Location	the university of waterloo Waterloo, ON N2V 2W5 ON, ON N2V 2W5 Canada Attn: the university of waterloo
Total	0.00 USD

Figure 17b-c

This Agreement between the university of waterloo -- Tao Guo ("You") and Springer Nature ("Springer Nature") consists of your license details and the terms and conditions provided by Springer Nature and Copyright Clearance Center.

License Number	5531001473117
License date	Apr 16, 2023
Licensed Content Publisher	Springer Nature
Licensed Content Publication	Nature Reviews, Physics
Licensed Content Title	Physics for neuromorphic computing
Licensed Content Author	Danijela Marković et al
Licensed Content Date	Jul 28, 2020
Type of Use	Thesis/Dissertation
Requestor type	non-commercial (non-profit)
Format	print and electronic
Portion	figures/tables/illustrations
Number of figures/tables/illustrations	1
Will you be translating?	no
Circulation/distribution	100 - 199
Author of this Springer Nature content	no
Title	Chalcogenide and metal-oxide memristive devices for advanced neuromorphic computing
Institution name	the university of waterloo
Expected presentation date	Aug 2023
Portions	Figure 1
Requestor Location	the university of waterloo Waterloo, ON N2V 2W5 ON, ON N2V 2W5 Canada Attn: the university of waterloo
Total	0.00 USD

Figure 17d-e

This Agreement between the university of waterloo -- Tao Guo ("You") and Springer Nature ("Springer Nature") consists of your license details and the terms and conditions provided by Springer Nature and Copyright Clearance Center.

License Number	5531010107543
License date	Apr 16, 2023
Licensed Content Publisher	Springer Nature
Licensed Content Publication	Nature Electronics
Licensed Content Title	Near-sensor and in-sensor computing
Licensed Content Author	Feichi Zhou et al
Licensed Content Date	Nov 17, 2020
Type of Use	Thesis/Dissertation
Requestor type	academic/university or research institute
Format	print and electronic
Portion	figures/tables/illustrations
Number of figures/tables/illustrations	1
High-res required	no
Will you be translating?	no
Circulation/distribution	100 - 199
Author of this Springer Nature content	no
Title	Chalcogenide and metal-oxide memristive devices for advanced neuromorphic computing
Institution name	the university of waterloo
Expected presentation date	Aug 2023
Portions	Figure 3
Requestor Location	the university of waterloo Waterloo, ON N2V 2W5 ON, ON N2V 2W5 Canada Attn: the university of waterloo
Total	0.00 USD

Figure 19a

This Agreement between the university of waterloo -- Tao Guo ("You") and Springer Nature ("Springer Nature") consists of your license details and the terms and conditions provided by Springer Nature and Copyright Clearance Center.

License Number	5531010250444
License date	Apr 16, 2023
Licensed Content Publisher	Springer Nature
Licensed Content Publication	Nature
Licensed Content Title	Training and operation of an integrated neuromorphic network based on metal-oxide memristors
Licensed Content Author	M. Prezioso et al
Licensed Content Date	May 7, 2015
Type of Use	Thesis/Dissertation
Requestor type	academic/university or research institute
Format	print and electronic
Portion	figures/tables/illustrations
Number of figures/tables/illustrations	1
High-res required	no
Will you be translating?	no
Circulation/distribution	100 - 199
Author of this Springer Nature content	no
Title	Chalcogenide and metal-oxide memristive devices for advanced neuromorphic computing
Institution name	the university of waterloo
Expected presentation date	Aug 2023
Portions	Figure 1
Requestor Location	the university of waterloo Waterloo, ON N2V 2W5 ON, ON N2V 2W5 Canada Attn: the university of waterloo
Total	0.00 USD

Figure 19b

This Agreement between the university of waterloo -- Tao Guo ("You") and Springer Nature ("Springer Nature") consists of your license details and the terms and conditions provided by Springer Nature and Copyright Clearance Center.

License Number	5531010352307
License date	Apr 16, 2023
Licensed Content Publisher	Springer Nature
Licensed Content Publication	Nature
Licensed Content Title	Fully hardware-implemented memristor convolutional neural network
Licensed Content Author	Peng Yao et al
Licensed Content Date	Jan 29, 2020
Type of Use	Thesis/Dissertation
Requestor type	academic/university or research institute
Format	print and electronic
Portion	figures/tables/illustrations
Number of figures/tables/illustrations	1
High-res required	no
Will you be translating?	no
Circulation/distribution	100 - 199
Author of this Springer Nature content	no
Title	Chalcogenide and metal-oxide memristive devices for advanced neuromorphic computing
Institution name	the university of waterloo
Expected presentation date	Aug 2023
Portions	Figure 1
Requestor Location	the university of waterloo Waterloo, ON N2V 2W5 ON, ON N2V 2W5 Canada Attn: the university of waterloo
Total	0.00 USD

Figure 19c-d

This Agreement between the university of waterloo -- Tao Guo ("You") and Springer Nature ("Springer Nature") consists of your license details and the terms and conditions provided by Springer Nature and Copyright Clearance Center.

License Number	5531010432864
License date	Apr 16, 2023
Licensed Content Publisher	Springer Nature
Licensed Content Publication	Nature Electronics
Licensed Content Title	Lego-like reconfigurable AI chips
Licensed Content Author	Shi-Jun Liang et al
Licensed Content Date	Jun 16, 2022
Type of Use	Thesis/Dissertation
Requestor type	academic/university or research institute
Format	print and electronic
Portion	figures/tables/illustrations
Number of figures/tables/illustrations	1
High-res required	no
Will you be translating?	no
Circulation/distribution	100 - 199
Author of this Springer Nature content	no
Title	Chalcogenide and metal-oxide memristive devices for advanced neuromorphic computing
Institution name	the university of waterloo
Expected presentation date	Aug 2023
Portions	Figure 1
Requestor Location	the university of waterloo Waterloo, ON N2V 2W5 ON, ON N2V 2W5 Canada Attn: the university of waterloo
Total	0.00 USD

Figure 20a

This Agreement between the university of waterloo -- Tao Guo ("You") and Springer Nature ("Springer Nature") consists of your license details and the terms and conditions provided by Springer Nature and Copyright Clearance Center.

License Number	5531010554418
License date	Apr 16, 2023
Licensed Content Publisher	Springer Nature
Licensed Content Publication	Nature
Licensed Content Title	Ultrafast machine vision with 2D material neural network image sensors
Licensed Content Author	Lukas Mennel et al
Licensed Content Date	Mar 4, 2020
Type of Use	Thesis/Dissertation
Requestor type	academic/university or research institute
Format	print and electronic
Portion	figures/tables/illustrations
Number of figures/tables/illustrations	1
High-res required	no
Will you be translating?	no
Circulation/distribution	100 - 199
Author of this Springer Nature content	no
Title	Chalcogenide and metal-oxide memristive devices for advanced neuromorphic computing
Institution name	the university of waterloo
Expected presentation date	Aug 2023
Portions	Figure 1
Requestor Location	the university of waterloo Waterloo, ON N2V 2W5 ON, ON N2V 2W5 Canada Attn: the university of waterloo
Total	0.00 USD

Figure 20b-c

This Agreement between the university of waterloo -- Tao Guo ("You") and John Wiley and Sons ("John Wiley and Sons") consists of your license details and the terms and conditions provided by John Wiley and Sons and Copyright Clearance Center.

License Number	5531010677048
License date	Apr 16, 2023
Licensed Content Publisher	John Wiley and Sons
Licensed Content Publication	Advanced Functional Materials
Licensed Content Title	MXene-ZnO Memristor for Multimodal In-Sensor Computing
Licensed Content Author	Su-Ting Han, Qiufan Liao, Chenliang Su, et al
Licensed Content Date	Feb 19, 2021
Licensed Content Volume	31
Licensed Content Issue	21
Licensed Content Pages	10
Type of use	Dissertation/Thesis
Requestor type	University/Academic
Format	Print and electronic
Portion	Figure/table
Number of figures/tables	1
Will you be translating?	No
Title	Chalcogenide and metal-oxide memristive devices for advanced neuromorphic computing
Institution name	the university of waterloo
Expected presentation date	Aug 2023
Portions	Figure 7
Requestor Location	the university of waterloo Waterloo, ON N2V 2W5 ON, ON N2V 2W5 Canada Attn: the university of waterloo
Publisher Tax ID	EU826007151
Total	0.00 USD

Figure 20d

This Agreement between the university of waterloo -- Tao Guo ("You") and John Wiley and Sons ("John Wiley and Sons") consists of your license details and the terms and conditions provided by John Wiley and Sons and Copyright Clearance Center.

License Number	5531010788745
License date	Apr 16, 2023
Licensed Content Publisher	John Wiley and Sons
Licensed Content Publication	Advanced Functional Materials
Licensed Content Title	Broadband Visual Adaption and Image Recognition in a Monolithic Neuromorphic Machine Vision System
Licensed Content Author	Zhenxing Wang, Jun He, Ruiqing Cheng, et al
Licensed Content Date	Dec 5, 2022
Licensed Content Volume	33
Licensed Content Issue	5
Licensed Content Pages	9
Type of use	Dissertation/Thesis
Requestor type	University/Academic
Format	Print and electronic
Portion	Figure/table
Number of figures/tables	1
Will you be translating?	No
Title	Chalcogenide and metal-oxide memristive devices for advanced neuromorphic computing
Institution name	the university of waterloo
Expected presentation date	Aug 2023
Portions	Figure 1
Requestor Location	the university of waterloo Waterloo, ON N2V 2W5
	ON, ON N2V 2W5 Canada Attn: the university of waterloo
Publisher Tax ID	EU826007151
Total	0.00 USD

References

1. Mehonic, A. Brain-inspired computing needs a master plan. *6*.
2. Yang, R., Huang, H.-M. & Guo, X. Memristive Synapses and Neurons for Bioinspired Computing. *Advanced Electronic Materials* **5**, 1900287 (2019).
3. Zhou, F. Near-sensor and in-sensor computing. **3**, 8 (2020).
4. Strukov, D. B., Snider, G. S., Stewart, D. R. & Williams, R. S. The missing memristor found. *Nature* **453**, 80–83 (2008).
5. Wang, T. *et al.* Reconfigurable neuromorphic memristor network for ultralow-power smart textile electronics. *Nat Commun* **13**, 7432 (2022).
6. Choi, B. J. *et al.* High-Speed and Low-Energy Nitride Memristors. *Advanced Functional Materials* **26**, 5290–5296 (2016).
7. Pi, S. *et al.* Memristor crossbar arrays with 6-nm half-pitch and 2-nm critical dimension. *Nature Nanotech* **14**, 35–39 (2019).
8. Kaspar, C., Ravoo, B. J., van der Wiel, W. G., Wegner, S. V. & Pernice, W. H. P. The rise of intelligent matter. *Nature* **594**, 345–355 (2021).
9. Sun, W. *et al.* Understanding memristive switching via in situ characterization and device modeling. *Nat Commun* **10**, 3453 (2019).
10. Yeon, H. *et al.* Alloying conducting channels for reliable neuromorphic computing. *Nat. Nanotechnol.* **15**, 574–579 (2020).
11. Wang, R. *et al.* Recent Advances of Volatile Memristors: Devices, Mechanisms, and Applications. *Advanced Intelligent Systems* **2**, 2000055 (2020).

12. Dittmann, R., Menzel, S. & Waser, R. Nanoionic memristive phenomena in metal oxides: the valence change mechanism. *Advances in Physics* 1–195 (2022)
doi:10.1080/00018732.2022.2084006.
13. Carlos, E., Branquinho, R., Martins, R., Kiazadeh, A. & Fortunato, E. Recent Progress in Solution-Based Metal Oxide Resistive Switching Devices. *Advanced Materials* **33**, 2004328 (2021).
14. Menzel, L. *et al.* Ultrafast machine vision with 2D material neural network image sensors. *Nature* **579**, 62–66 (2020).
15. Guo, T. *et al.* Versatile memristor for memory and neuromorphic computing. *Nanoscale Horiz.* 10.1039/D1NH00481F (2022) doi:10.1039/D1NH00481F.
16. Guo, T. *et al.* Intelligent matter endows reconfigurable temperature and humidity sensations for in-sensor computing. *Mater. Horiz.* 10.1039/D2MH01491B (2023)
doi:10.1039/D2MH01491B.
17. Lanza, M. *et al.* Memristive technologies for data storage, computation, encryption, and radio-frequency communication. *Science* **376**, eabj9979 (2022).
18. Chua, L. O. & Kang, S. M. Memristive devices and systems. *Proceedings of the IEEE* **64**, 209–223 (1976).
19. Prodromakis, T., Toumazou, C. & Chua, L. Two centuries of memristors. *Nature Mater* **11**, 478–481 (2012).
20. Dearnaley, G., Stoneham, A. M. & Morgan, D. V. Electrical phenomena in amorphous oxide films. *Rep. Prog. Phys.* **33**, 1129–1191 (1970).
21. Hickmott, T. W. Low-Frequency Negative Resistance in Thin Anodic Oxide Films. *Journal of Applied Physics* **33**, 2669–2682 (1962).

22. Chua, L. Memristor-The missing circuit element. *IEEE Transactions on Circuit Theory* **18**, 507–519 (1971).
23. Sawa, A. Resistive switching in transition metal oxides. *Materials Today* **11**, 28–36 (2008).
24. Borghetti, J. *et al.* ‘Memristive’ switches enable ‘stateful’ logic operations via material implication. *Nature* **464**, 873–876 (2010).
25. Zhu, X. *et al.* Observation of Conductance Quantization in Oxide-Based Resistive Switching Memory. *Advanced Materials* **24**, 3941–3946 (2012).
26. Jo, S. H. *et al.* Nanoscale Memristor Device as Synapse in Neuromorphic Systems. *Nano Lett.* **10**, 1297–1301 (2010).
27. Waser, R., Dittmann, R., Staikov, G. & Szot, K. Redox-Based Resistive Switching Memories - Nanoionic Mechanisms, Prospects, and Challenges. *Adv. Mater.* **21**, 2632–2663 (2009).
28. Waser, R. & Aono, M. Nanoionics-based resistive switching memories. *Nature Mater* **6**, 833–840 (2007).
29. Lanza, M. *et al.* Recommended Methods to Study Resistive Switching Devices. *Adv. Electron. Mater.* **5**, 1800143 (2019).
30. Chen, S. *et al.* Wafer-scale integration of two-dimensional materials in high-density memristive crossbar arrays for artificial neural networks. *Nat Electron* **3**, 638–645 (2020).
31. Poddar, S. *et al.* Down-Scalable and Ultra-fast Memristors with Ultra-high Density Three-Dimensional Arrays of Perovskite Quantum Wires. *Nano Lett.* **21**, 5036–5044 (2021).
32. Kapur, O. *et al.* Back-End-of-Line SiC-Based Memristor for Resistive Memory and Artificial Synapse. *Advanced Electronic Materials* **8**, 2200312 (2022).
33. Prakash, A., Jana, D., Samanta, S. & Maikap, S. Self-compliance-improved resistive switching using Ir/TaOx/W cross-point memory. *Nanoscale Res Lett* **8**, 527 (2013).

34. Min, S.-Y. & Cho, W.-J. Memristive Switching Characteristics in Biomaterial Chitosan-Based Solid Polymer Electrolyte for Artificial Synapse. *International Journal of Molecular Sciences* **22**, 773 (2021).
35. Wang, W. *et al.* Surface diffusion-limited lifetime of silver and copper nanofilaments in resistive switching devices. *Nat Commun* **10**, 81 (2019).
36. Ren, Y. *et al.* Flexible Pyrene/Phenanthro[9,10-d]imidazole-Based Memristive Devices for Mimicking Synaptic Plasticity. *Advanced Intelligent Systems* **1**, 1900008 (2019).
37. Ho, T.-L. *et al.* Multi-Level Resistive Switching in SnSe/SrTiO₃ Heterostructure Based Memristor Device. *Nanomaterials* **12**, 2128 (2022).
38. Zhang, Y. *et al.* Three-dimensional perovskite nanowire array-based ultrafast resistive RAM with ultralong data retention. *Science Advances* **7**, eabg3788 (2021).
39. Palumbo, F. *et al.* A Review on Dielectric Breakdown in Thin Dielectrics: Silicon Dioxide, High-k, and Layered Dielectrics. *Advanced Functional Materials* **30**, 1900657 (2020).
40. Li, Y. *et al.* Anomalous resistive switching in memristors based on two-dimensional palladium diselenide using heterophase grain boundaries. *Nat Electron* **4**, 348–356 (2021).
41. Gao, B. *et al.* Modeling of Retention Failure Behavior in Bipolar Oxide-Based Resistive Switching Memory. *IEEE Electron Device Letters* **32**, 276–278 (2011).
42. Wang, H., Zhu, B., Ma, X., Hao, Y. & Chen, X. Physically Transient Resistive Switching Memory Based on Silk Protein. *Small* **12**, 2715–2719 (2016).
43. Xu, J. *et al.* Biodegradable Natural Pectin-Based Flexible Multilevel Resistive Switching Memory for Transient Electronics. *Small* **15**, 1803970 (2019).
44. Kim, S. *et al.* Effect of Scaling WO_x -Based RRAMs on Their Resistive Switching Characteristics. *IEEE Electron Device Letters* **32**, 671–673 (2011).

45. Wang, Z. *et al.* Ultrafast Accelerated Retention Test Methodology for RRAM Using Micro Thermal Stage. *IEEE Electron Device Letters* **38**, 863–866 (2017).
46. Wang, L.-G. *et al.* Excellent resistive switching properties of atomic layer-deposited Al₂O₃/HfO₂/Al₂O₃ trilayer structures for non-volatile memory applications. *Nanoscale Res Lett* **10**, 135 (2015).
47. Wang, Z. *et al.* Memristors with diffusive dynamics as synaptic emulators for neuromorphic computing. *Nature Mater* **16**, 101–108 (2017).
48. Midya, R. *et al.* Anatomy of Ag/Hafnia-Based Selectors with 10^{10} Nonlinearity. *Adv. Mater.* **29**, 1604457 (2017).
49. Jiang, H. *et al.* A novel true random number generator based on a stochastic diffusive memristor. *Nat Commun* **8**, 882 (2017).
50. Zhang, X. *et al.* An artificial spiking afferent nerve based on Mott memristors for neurorobotics. *Nat Commun* **11**, 51 (2020).
51. Ielmini, D. & Wong, H.-S. P. In-memory computing with resistive switching devices. *Nat Electron* **1**, 333–343 (2018).
52. Zhou, G. *et al.* Negative Photoconductance Effect: An Extension Function of the TiO_x-Based Memristor. *Advanced Science* **8**, 2003765 (2021).
53. Rahaman, S. Z. *et al.* Excellent resistive memory characteristics and switching mechanism using a Ti nanolayer at the Cu/TaO_x interface. *Nanoscale Res Lett* **7**, 345 (2012).
54. Yao, P. *et al.* Fully hardware-implemented memristor convolutional neural network. *Nature* **577**, 641–646 (2020).
55. Xiang, D., Liu, T., Zhang, X., Zhou, P. & Chen, W. Dielectric Engineered Two-Dimensional Neuromorphic Transistors. *Nano Letters* **9**.

56. Wang, Z. *et al.* Reinforcement learning with analogue memristor arrays. *Nat Electron* **2**, 115–124 (2019).
57. Gao, S., Yi, X., Shang, J., Liu, G. & Li, R.-W. Organic and hybrid resistive switching materials and devices. *Chemical Society Reviews* **48**, 1531–1565 (2019).
58. Sun, B., Zhou, G., Guo, T., Zhou, Y. N. & Wu, Y. A. Biomemristors as the next generation bioelectronics. *Nano Energy* **75**, 104938 (2020).
59. Rajan, K. *et al.* Spin-coated silver nanocomposite resistive switching devices. *Microelectronic Engineering* **168**, 27–31 (2017).
60. Younis, A., Chu, D., Lin, X., Lee, J. & Li, S. Bipolar resistive switching in p-type Co₃O₄ nanosheets prepared by electrochemical deposition. *Nanoscale Res Lett* **8**, 36 (2013).
61. Lanza, M., Molas, G. & Naveh, I. The gap between academia and industry in resistive switching research. *Nat Electron* 1–4 (2023) doi:10.1038/s41928-023-00954-8.
62. Zhang, X., Wu, C., Lv, Y., Zhang, Y. & Liu, W. High-Performance Flexible Polymer Memristor Based on Stable Filamentary Switching. *Nano Lett.* **22**, 7246–7253 (2022).
63. Zhang, Y. *et al.* Evolution of the conductive filament system in HfO₂-based memristors observed by direct atomic-scale imaging. *Nat Commun* **12**, 7232 (2021).
64. Patil, H. *et al.* Stable and Multilevel Data Storage Resistive Switching of Organic Bulk Heterojunction. *Nanomaterials* **11**, 359 (2021).
65. Kim, K. M. *et al.* Voltage divider effect for the improvement of variability and endurance of TaOx memristor. *Sci Rep* **6**, 20085 (2016).
66. Fantini, A. *et al.* Intrinsic Switching Behavior in HfO₂ RRAM by Fast Electrical Measurements on Novel 2R Test Structures. in *2012 4th IEEE International Memory Workshop* 1–4 (2012). doi:10.1109/IMW.2012.6213646.

67. Burr, G. W. *et al.* Phase change memory technology. *Journal of Vacuum Science & Technology B* **28**, 223–262 (2010).
68. Wang, Z. J. & Bai, Y. Resistive Switching Behavior in Ferroelectric Heterostructures. *Small* **15**, 1805088 (2019).
69. Chanthbouala, A. *et al.* Vertical-current-induced domain-wall motion in MgO-based magnetic tunnel junctions with low current densities. *Nature Phys* **7**, 626–630 (2011).
70. Chen, S. & Valov, I. Design of Materials Configuration for Optimizing Redox-Based Resistive Switching Memories. *Advanced Materials* **34**, 2105022 (2022).
71. Di, J. *et al.* Recent advances in resistive random access memory based on lead halide perovskite. *InfoMat* **3**, 293–315 (2021).
72. Hardtdegen, A. *et al.* Improved Switching Stability and the Effect of an Internal Series Resistor in HfO₂/TiO_x Bilayer ReRAM Cells. *IEEE Transactions on Electron Devices* **65**, 3229–3236 (2018).
73. Marchewka, A. *et al.* Nanoionic Resistive Switching Memories: On the Physical Nature of the Dynamic Reset Process. *Advanced Electronic Materials* **2**, 1500233 (2016).
74. Kwon, D.-H. *et al.* Atomic structure of conducting nanofilaments in TiO₂ resistive switching memory. *Nature Nanotech* **5**, 148–153 (2010).
75. Xie, H. *et al.* Nitrogen-induced improvement of resistive switching uniformity in a HfO₂-based RRAM device. *Semicond. Sci. Technol.* **27**, 125008 (2012).
76. Kim, S. *et al.* Neuronal dynamics in HfO_x/AlO_y-based homeothermic synaptic memristors with low-power and homogeneous resistive switching. *Nanoscale* **11**, 237–245 (2019).
77. Bagdzevicius, S. *et al.* Superposition of interface and volume type resistive switching in perovskite nanoionic devices. *Journal of Materials Chemistry C* **7**, 7580–7592 (2019).

78. Yang, J. J. *et al.* Memristive switching mechanism for metal/oxide/metal nanodevices. *Nature Nanotech* **3**, 429–433 (2008).
79. Muenstermann, R., Menke, T., Dittmann, R. & Waser, R. Coexistence of Filamentary and Homogeneous Resistive Switching in Fe-Doped SrTiO₃ Thin-Film Memristive Devices. *Advanced Materials* **22**, 4819–4822 (2010).
80. Lee, J. & Lu, W. D. On-Demand Reconfiguration of Nanomaterials: When Electronics Meets Ionics. *Advanced Materials* **30**, 1702770 (2018).
81. Yang, Y. & Lu, W. Nanoscale resistive switching devices: mechanisms and modeling. *Nanoscale* **5**, 10076 (2013).
82. Valov, I. Redox-Based Resistive Switching Memories (ReRAMs): Electrochemical Systems at the Atomic Scale. *ChemElectroChem* **1**, 26–36 (2014).
83. Tsuruoka, T. *et al.* Redox Reactions at Cu,Ag/Ta₂O₅ Interfaces and the Effects of Ta₂O₅ Film Density on the Forming Process in Atomic Switch Structures. *Advanced Functional Materials* **25**, 6374–6381 (2015).
84. Jang, J., Pan, F., Braam, K. & Subramanian, V. Resistance Switching Characteristics of Solid Electrolyte Chalcogenide Ag₂Se Nanoparticles for Flexible Nonvolatile Memory Applications. *Advanced Materials* **24**, 3573–3576 (2012).
85. Ali, A. *et al.* Thickness-dependent monochalcogenide GeSe-based CBRAM for memory and artificial electronic synapses. *Nano Res.* **15**, 2263–2277 (2022).
86. Park, S. P. *et al.* Analysis of the Bipolar Resistive Switching Behavior of a Biocompatible Glucose Film for Resistive Random Access Memory. *Advanced Materials* **30**, 1800722 (2018).
87. Yang, Y. *et al.* Observation of conducting filament growth in nanoscale resistive memories. *Nat Commun* **3**, 732 (2012).

88. Yang, Y. *et al.* Electrochemical dynamics of nanoscale metallic inclusions in dielectrics. *Nat Commun* **5**, 4232 (2014).
89. Chang, C.-F. *et al.* Direct Observation of Dual-Filament Switching Behaviors in Ta₂O₅-Based Memristors. *Small* **13**, 1603116 (2017).
90. Wang, Y. *et al.* Memristor-based biomimetic compound eye for real-time collision detection. *Nat Commun* **12**, 5979 (2021).
91. Liu, Z. *et al.* High Temperature CsPbBr₃I_{3-x} Memristors Based on Hybrid Electrical and Optical Resistive Switching Effects. *ACS Appl. Mater. Interfaces* **13**, 58885–58897 (2021).
92. Milano, G. *et al.* Water-Mediated Ionic Migration in Memristive Nanowires with a Tunable Resistive Switching Mechanism. *ACS Appl. Mater. Interfaces* **12**, 48773–48780 (2020).
93. Wedig, A. *et al.* Nanoscale cation motion in TaO_x, HfO_x and TiO_x memristive systems. *Nature Nanotech* **11**, 67–74 (2016).
94. Sousa, V. Chalcogenide materials and their application to Non-Volatile Memories. *Microelectronic Engineering* **88**, 807–813 (2011).
95. Panca, A. *et al.* Flexible Oxide Thin Film Transistors, Memristors, and Their Integration. *Advanced Functional Materials* **n/a**, 2213762.
96. Santini, C. A. *et al.* Oxygenated amorphous carbon for resistive memory applications. *Nat Commun* **6**, 8600 (2015).
97. Li, Y. *et al.* Recent advances in organic-based materials for resistive memory applications. *InfoMat* **2**, 995–1033 (2020).
98. Chung, I. & Kanatzidis, M. G. Metal Chalcogenides: A Rich Source of Nonlinear Optical Materials. *Chem. Mater.* **26**, 849–869 (2014).

99. Xu, Z., Bando, Y., Wang, W., Bai, X. & Golberg, D. Real-Time In Situ HRTEM-Resolved Resistance Switching of Ag₂S Nanoscale Ionic Conductor. *ACS Nano* **4**, 2515–2522 (2010).
100. Schindler, C., Meier, M., Waser, R. & Kozicki, M. N. Resistive switching in Ag-Ge-Se with extremely low write currents. in *2007 Non-Volatile Memory Technology Symposium* 82–85 (2007). doi:10.1109/NVMT.2007.4389953.
101. Zhuge, F. *et al.* Mechanism for resistive switching in chalcogenide-based electrochemical metallization memory cells. *AIP Advances* **5**, 057125 (2015).
102. Hirose, Y. & Hirose, H. Polarity-dependent memory switching and behavior of Ag dendrite in Ag-photodoped amorphous As₂S₃ films. *Journal of Applied Physics* **47**, 2767–2772 (1976).
103. Kozicki, M. N. & Mitkova, M. Mass transport in chalcogenide electrolyte films – materials and applications. *Journal of Non-Crystalline Solids* **352**, 567–577 (2006).
104. Fujii, T., Arita, M., Takahashi, Y. & Fujiwara, I. *In situ* transmission electron microscopy analysis of conductive filament during solid electrolyte resistance switching. *Appl. Phys. Lett.* **98**, 212104 (2011).
105. Lee, T. S. *et al.* The forming-free bipolar resistive switching characteristics of Ag₂Se thin film. *J. Phys. D: Appl. Phys.* **50**, 205103 (2017).
106. Ciocchini, N. *et al.* Bipolar switching in chalcogenide phase change memory. *Sci Rep* **6**, 29162 (2016).
107. Rehman, S., Kim, K., Hur, J.-H. & Kim, D. Phase transformation induced resistive switching behavior in Al/Cu₂Se/Pt. *J. Phys. D: Appl. Phys.* **50**, 135301 (2017).
108. Gubicza, A., Csontos, M., Halbritter, A. & Mihály, G. Resistive switching in metallic Ag₂S memristors due to a local overheating induced phase transition. *Nanoscale* **7**, 11248–11254 (2015).

109. Gupta, A., Sakthivel, T. & Seal, S. Recent development in 2D materials beyond graphene. *Progress in Materials Science* **73**, 44–126 (2015).
110. Liu, Y. *et al.* Approaching the Schottky–Mott limit in van der Waals metal–semiconductor junctions. *Nature* **557**, 696–700 (2018).
111. Li, H. *et al.* High-performance sub-10-nm monolayer black phosphorene tunneling transistors. *Nano Res.* **11**, 2658–2668 (2018).
112. Sangwan, V. K. & Hersam, M. C. Neuromorphic nanoelectronic materials. *Nat. Nanotechnol.* **15**, 517–528 (2020).
113. Duerloo, K.-A. N., Li, Y. & Reed, E. J. Structural phase transitions in two-dimensional Mo- and W-dichalcogenide monolayers. *Nat Commun* **5**, 4214 (2014).
114. Zhang, F. *et al.* Electric-field induced structural transition in vertical MoTe₂- and Mo_{1-x}W_xTe₂-based resistive memories. *Nature Mater* **18**, 55–61 (2019).
115. Zhu, X., Li, D., Liang, X. & Lu, W. D. Ionic modulation and ionic coupling effects in MoS₂ devices for neuromorphic computing. *Nature Mater* **18**, 141–148 (2019).
116. Wang, A., Dong, J., Li, Y., Cao, K. & Jie, W. Zn vacancy complex-determined filamentary resistive switching characteristics in Au/ZnSe/ITO chalcogenide-based memory cells. *AIP Advances* **9**, 095058 (2019).
117. Wang, Z.-P. *et al.* Type-I Core–Shell ZnSe/ZnS Quantum Dot-Based Resistive Switching for Implementing Algorithm. *Nano Lett.* **20**, 5562–5569 (2020).
118. Zhang, L. *et al.* Localized resistive switching in a ZnS–Ag/ZnS double-layer memory. *J. Phys. D: Appl. Phys.* **47**, 455101 (2014).
119. Sun, X. *et al.* Single-Crystal Graphene-Directed van der Waals Epitaxial Resistive Switching. *ACS Appl. Mater. Interfaces* **10**, 6730–6736 (2018).

120. Zhang, X., Qiao, H., Nian, X., Huang, Y. & Pang, X. Resistive switching memory behaviours of MoSe₂ nano-islands array. *J Mater Sci: Mater Electron* **27**, 7609–7613 (2016).
121. Jian, J. *et al.* Low-Operating-Voltage Resistive Switching Memory Based on the Interlayer-Spacing Regulation of MoSe₂. *Advanced Electronic Materials* **8**, 2100905 (2022).
122. Zhao, X. *et al.* Reversible alternation between bipolar and unipolar resistive switching in Ag/MoS₂/Au structure for multilevel flexible memory. *Journal of Materials Chemistry C* **6**, 7195–7200 (2018).
123. He, H.-K. *et al.* Ultrafast and stable phase transition realized in MoTe₂-based memristive devices. *Mater. Horiz.* **9**, 1036–1044 (2022).
124. Kozicki, M. N., Park, M. & Mitkova, M. Nanoscale memory elements based on solid-state electrolytes. *IEEE Transactions on Nanotechnology* **4**, 331–338 (2005).
125. Čajko, K. O., Sekulić, D. L. & Lukić-Petrović, S. R. Dielectric and bipolar resistive switching properties of Ag doped As–S–Se chalcogenide for non-volatile memory applications. *Materials Chemistry and Physics* **296**, 127301 (2023).
126. Mazumder, A. *et al.* Nonvolatile Resistive Switching in Layered InSe via Electrochemical Cation Diffusion. *Advanced Electronic Materials* **8**, 2100999 (2022).
127. Goux, L. *et al.* Influence of the Cu-Te composition and microstructure on the resistive switching of Cu-Te/Al₂O₃/Si cells. *Applied Physics Letters* **99**, 053502 (2011).
128. Woo, H., Vishwanath, S. K. & Jeon, S. Excellent Resistive Switching Performance of Cu–Se-Based Atomic Switch Using Lanthanide Metal Nanolayer at the Cu–Se/Al₂O₃ Interface. *ACS Appl. Mater. Interfaces* **10**, 8124–8131 (2018).
129. Guo, T. *et al.* Overwhelming coexistence of negative differential resistance effect and RRAM. *Phys. Chem. Chem. Phys.* **20**, 20635–20640 (2018).

130. Dong, X.-F. *et al.* Coexistence of Bipolar Resistive Switching and the Negative Differential Resistance Effect from a Kesterite Memristor. *J. Phys. Chem. C* **125**, 923–930 (2021).
131. Wu, Z. *et al.* Bipolar Resistive Switching in the Ag/Sb₂Te₃/Pt Heterojunction. *ACS Appl. Electron. Mater.* **3**, 2766–2773 (2021).
132. Yang, Y. *et al.* A new opportunity for the emerging tellurium semiconductor: making resistive switching devices. *Nat Commun* **12**, 6081 (2021).
133. Khan, A. I. *et al.* Ultralow-switching current density multilevel phase-change memory on a flexible substrate. *Science* **373**, 1243–1247 (2021).
134. Jaafar, A. H. *et al.* Electrodeposition of GeSbTe-Based Resistive Switching Memory in Crossbar Arrays. *J. Phys. Chem. C* **125**, 26247–26255 (2021).
135. Loke, D. *et al.* Breaking the Speed Limits of Phase-Change Memory. *Science* **336**, 1566–1569 (2012).
136. Lee, W. *et al.* Effect of $\text{Ge}_2\text{Sb}_2\text{Te}_5$ Thermal Barrier on Reset Operations in Filament-Type Resistive Memory. *IEEE Electron Device Letters* **32**, 1573–1575 (2011).
137. Yoo, S., Eom, T., Gwon, T. & Seong Hwang, C. Bipolar resistive switching behavior of an amorphous $\text{Ge}_2\text{Sb}_2\text{Te}_5$ thin films with a Te layer. *Nanoscale* **7**, 6340–6347 (2015).
138. Rebora, C. *et al.* Conductive-bridge memory cells based on a nanoporous electrodeposited GeSbTe alloy. *Nanotechnology* **30**, 025202 (2018).
139. Zhang, Z. *et al.* Electrochemical metallization cell with solid phase tunable $\text{Ge}_2\text{Sb}_2\text{Te}_5$ electrolyte. *Sci Rep* **8**, 12101 (2018).
140. Kim, S. *et al.* Excellent resistive switching in nitrogen-doped $\text{Ge}_2\text{Sb}_2\text{Te}_5$ devices for field-programmable gate array configurations. *Applied Physics Letters* **99**, 192110 (2011).

141. Huang, Y.-H., Chen, H.-A., Wu, H.-H. & Hsieh, T.-E. Forming-free, bi-directional polarity conductive-bridge memory devices with Ge₂Sb₂Te₅ solid-state electrolyte and Ag active electrode. *Journal of Applied Physics* **117**, 014505 (2015).
142. Kim, W. *et al.* Electroforming-Free Bipolar Resistive Switching in GeSe Thin Films with a Ti-Containing Electrode. *ACS Appl. Mater. Interfaces* **11**, 38910–38920 (2019).
143. Zhao, X. *et al.* Breaking the Current-Retention Dilemma in Cation-Based Resistive Switching Devices Utilizing Graphene with Controlled Defects. *Advanced Materials* **30**, 1705193 (2018).
144. Cho, D.-Y., Luebben, M., Wiefels, S., Lee, K.-S. & Valov, I. Interfacial Metal–Oxide Interactions in Resistive Switching Memories. *ACS Appl. Mater. Interfaces* **9**, 19287–19295 (2017).
145. Xiao, N. *et al.* Resistive Random Access Memory Cells with a Bilayer TiO₂/SiO_x Insulating Stack for Simultaneous Filamentary and Distributed Resistive Switching. *Advanced Functional Materials* **27**, 1700384 (2017).
146. Chang, W.-Y. *et al.* Unipolar resistive switching characteristics of ZnO thin films for nonvolatile memory applications. *Appl. Phys. Lett.* **92**, 022110 (2008).
147. Son, J. Y. & Shin, Y.-H. Direct observation of conducting filaments on resistive switching of NiO thin films. *Appl. Phys. Lett.* **92**, 222106 (2008).
148. Lin, K.-L. *et al.* Electrode dependence of filament formation in HfO₂ resistive-switching memory. *Journal of Applied Physics* **109**, 084104 (2011).
149. Yang, W.-Y., Kim, W.-G. & Rhee, S.-W. Radio frequency sputter deposition of single phase cuprous oxide using Cu₂O as a target material and its resistive switching properties. *Thin Solid Films* **517**, 967–971 (2008).

150. Jana, D., Samanta, S., Maikap, S. & Cheng, H.-M. Evolution of complementary resistive switching characteristics using IrOx/GdOx/Al₂O₃/TiN structure. *Appl. Phys. Lett.* **108**, 011605 (2016).
151. Liao, Z. L. *et al.* Categorization of resistive switching of metal-Pr_{0.7}Ca_{0.3}MnO₃-metal devices. *Appl. Phys. Lett.* **94**, 253503 (2009).
152. Park, G.-S. *et al.* In situ observation of filamentary conducting channels in an asymmetric Ta₂O_{5-x}/TaO_{2-x} bilayer structure. *Nat Commun* **4**, 2382 (2013).
153. Yan, X. *et al.* Memristor with Ag-Cluster-Doped TiO₂ Films as Artificial Synapse for Neuroinspired Computing. *Advanced Functional Materials* **28**, 1705320 (2018).
154. Fujii, T. *et al.* Hysteretic current–voltage characteristics and resistance switching at an epitaxial oxide Schottky junction SrRuO₃/SrTi_{0.99}Nb_{0.01}O₃. *Appl. Phys. Lett.* **86**, 012107 (2005).
155. Sawa, A., Fujii, T., Kawasaki, M. & Tokura, Y. Hysteretic current–voltage characteristics and resistance switching at a rectifying Ti/Pr_{0.7}Ca_{0.3}MnO₃ interface. *Appl. Phys. Lett.* **85**, 4073–4075 (2004).
156. Peng, H. Y. *et al.* Electrode dependence of resistive switching in Mn-doped ZnO: Filamentary versus interfacial mechanisms. *Appl. Phys. Lett.* **96**, 192113 (2010).
157. Yoon, J. H. *et al.* A Low-Current and Analog Memristor with Ru as Mobile Species. *Advanced Materials* **32**, 1904599 (2020).
158. Lee, M.-J. *et al.* A fast, high-endurance and scalable non-volatile memory device made from asymmetric Ta₂O_{5-x}/TaO_{2-x} bilayer structures. *Nature Mater* **10**, 625–630 (2011).
159. Biju, K. P. *et al.* Highly asymmetric bipolar resistive switching in solution-processed Pt/TiO₂/W devices for cross-point application. *Current Applied Physics* **11**, S102–S106 (2011).

160. Ismail, M., Hashmi, A., Rana, A. M. & Kim, S. Eradicating negative-Set behavior of TiO₂-based devices by inserting an oxygen vacancy rich zirconium oxide layer for data storage applications. *Nanotechnology* **31**, 325201 (2020).
161. Yan, Y. *et al.* Area-Type Electronic Bipolar Switching Al/TiO_{1.7}/TiO₂/Al Memory with Linear Potentiation and Depression Characteristics. *ACS Appl. Mater. Interfaces* **13**, 39561–39572 (2021).
162. Xue, D. *et al.* Flexible resistive switching device based on the TiO₂ nanorod arrays for non-volatile memory application. *Journal of Alloys and Compounds* **822**, 153552 (2020).
163. Zhao, J., Zhang, M., Wan, S., Yang, Z. & Hwang, C. S. Highly Flexible Resistive Switching Memory Based on the Electronic Switching Mechanism in the Al/TiO₂/Al/Polyimide Structure. *ACS Appl. Mater. Interfaces* **10**, 1828–1835 (2018).
164. Kim, S., Jeong, H. Y., Kim, S. K., Choi, S.-Y. & Lee, K. J. Flexible Memristive Memory Array on Plastic Substrates. *Nano Lett.* **11**, 5438–5442 (2011).
165. Wan, F. *et al.* Truly Electroforming-Free Memristor Based on TiO₂-CoO Phase-Separated Oxides with Extremely High Uniformity and Low Power Consumption. *Advanced Functional Materials* **30**, 2007101 (2020).
166. Zhang, R. *et al.* Role of Oxygen Vacancies at the TiO₂/HfO₂ Interface in Flexible Oxide-Based Resistive Switching Memory. *Advanced Electronic Materials* **5**, 1800833 (2019).
167. Ismail, M., Chand, U., Mahata, C., Nebhen, J. & Kim, S. Demonstration of synaptic and resistive switching characteristics in W/TiO₂/HfO₂/TaN memristor crossbar array for bioinspired neuromorphic computing. *Journal of Materials Science & Technology* **96**, 94–102 (2022).

168. Xu, D., Xiong, Y., Tang, M. & Zeng, B. Coexistence of the bipolar and unipolar resistive switching behaviors in vanadium doped ZnO films. *Journal of Alloys and Compounds* **584**, 269–272 (2014).
169. Li, S.-S. & Su, Y.-K. Conductive filaments controlled ferromagnetism in Co-doped ZnO resistive switching memory device. *Jpn. J. Appl. Phys.* **58**, SBBI01 (2019).
170. Zhao, X. *et al.* Li-Doping Effect on Characteristics of ZnO Thin Films Resistive Random Access Memory. *Micromachines* **11**, 889 (2020).
171. Li, S.-S. & Su, Y.-K. Improvement of the performance in Cr-doped ZnO memory devices via control of oxygen defects. *RSC Advances* **9**, 2941–2947 (2019).
172. Wang, Y., Cao, M., Bian, J., Li, Q. & Su, J. Flexible ZnO Nanosheet-Based Artificial Synapses Prepared by Low-Temperature Process for High Recognition Accuracy Neuromorphic Computing. *Advanced Functional Materials* **n/a**, 2209907.
173. Li, X. *et al.* Atomic Layer Deposition of Ga₂O₃/ZnO Composite Films for High-Performance Forming-Free Resistive Switching Memory. *ACS Appl. Mater. Interfaces* **12**, 30538–30547 (2020).
174. Kim, D., Shin, J. & Kim, S. Resistive Switching Characteristics of ZnO-Based RRAM on Silicon Substrate. *Metals* **11**, 1572 (2021).
175. Shang, J. *et al.* Highly flexible resistive switching memory based on amorphous-nanocrystalline hafnium oxide films. *Nanoscale* **9**, 7037–7046 (2017).
176. Chen, P.-H., Su, Y.-T. & Chang, F.-C. Stabilizing Resistive Switching Characteristics by Inserting Indium-Tin-Oxide Layer as Oxygen Ion Reservoir in HfO₂-Based Resistive Random Access Memory. *IEEE Transactions on Electron Devices* **66**, 1276–1280 (2019).

177. Li, Z. *et al.* Coexistence of Digital and Analog Resistive Switching With Low Operation Voltage in Oxygen-Gradient HfO_x Memristors. *IEEE Electron Device Letters* **40**, 1068–1071 (2019).
178. Liang, H.-N. *et al.* Resistive Switching Characteristics of HfO_x-Based Memristor by Inserting GeTe Layer. *IEEE Transactions on Electron Devices* **70**, 83–87 (2023).
179. Wang, M., Guo, K. & Cheng, H. Stretchable HfO₂-Based Resistive Switching Memory Using the Wavy Structured Design. *IEEE Electron Device Letters* **41**, 1118–1121 (2020).
180. Ji, Y. *et al.* Flexible Nanoporous WO_{3-x} Nonvolatile Memory Device. *ACS Nano* **10**, 7598–7603 (2016).
181. Koroleva, A. A. *et al.* Impact of the Atomic Layer-Deposited Ru Electrode Surface Morphology on Resistive Switching Properties of TaO_x-Based Memory Structures. *ACS Appl. Mater. Interfaces* **12**, 55331–55341 (2020).
182. Sun, Y. M. *et al.* Modulating metallic conductive filaments via bilayer oxides in resistive switching memory. *Appl. Phys. Lett.* **114**, 193502 (2019).
183. Chen, Y. *et al.* Electroforming-Free, Flexible, and Reliable Resistive Random-Access Memory Based on an Ultrathin TaO_x Film. *ACS Appl. Mater. Interfaces* **12**, 10681–10688 (2020).
184. Choi, H.-H. *et al.* Facilitation of the thermochemical mechanism in NiO-based resistive switching memories via tip-enhanced electric fields. *Journal of Industrial and Engineering Chemistry* **94**, 233–239 (2021).
185. Jiang, X. (江雪) *et al.* Effect of deposition temperature on ultra-low voltage resistive switching behavior of Fe-doped SrTiO₃ films. *Applied Physics Letters* **116**, 102101 (2020).

186. Ahn, M. *et al.* Memristors Based on (Zr, Hf, Nb, Ta, Mo, W) High-Entropy Oxides. *Advanced Electronic Materials* **7**, 2001258 (2021).
187. Wang, C. *et al.* HfO_x/AlO_y Superlattice-Like Memristive Synapse. *Advanced Science* **9**, 2201446 (2022).
188. Yang, Y. & Huang, R. Probing memristive switching in nanoionic devices. *Nat Electron* **1**, 274–287 (2018).
189. Sood, A. *et al.* Universal phase dynamics in VO₂ switches revealed by ultrafast operando diffraction. *Science* **373**, 352–355 (2021).
190. Bian, K. *et al.* Scanning probe microscopy. *Nat Rev Methods Primers* **1**, 1–29 (2021).
191. Lanza, M. A Review on Resistive Switching in High-k Dielectrics: A Nanoscale Point of View Using Conductive Atomic Force Microscope. *Materials* **7**, 2155–2182 (2014).
192. Dubost, V. *et al.* Resistive Switching at the Nanoscale in the Mott Insulator Compound GaTa₄Se₈. *Nano Lett.* **13**, 3648–3653 (2013).
193. Si, H. *et al.* Emerging Conductive Atomic Force Microscopy for Metal Halide Perovskite Materials and Solar Cells. *Advanced Energy Materials* **10**, 1903922 (2020).
194. Pan, C. *et al.* Coexistence of Grain-Boundaries-Assisted Bipolar and Threshold Resistive Switching in Multilayer Hexagonal Boron Nitride. *Advanced Functional Materials* **27**, 1604811 (2017).
195. Celano, U. *et al.* Conductive-AFM tomography for 3D filament observation in resistive switching devices. in *2013 IEEE International Electron Devices Meeting* 21.6.1-21.6.4 (2013). doi:10.1109/IEDM.2013.6724679.
196. Moors, M. *et al.* Resistive Switching Mechanisms on TaO_x and SrRuO₃ Thin-Film Surfaces Probed by Scanning Tunneling Microscopy. *ACS Nano* **10**, 1481–1492 (2016).

197. Lanza, M., Celano, U. & Miao, F. Nanoscale Characterization of Resistive Switching Using Advanced Conductive Atomic Force Microscopy–Based Setups. 25.
198. Celano, U. *et al.* Imaging the Three-Dimensional Conductive Channel in Filamentary-Based Oxide Resistive Switching Memory. *Nano Lett.* **15**, 7970–7975 (2015).
199. Shi, Y. *et al.* (Invited) Elucidating the Origin of Resistive Switching in Ultrathin Hafnium Oxides through High Spatial Resolution Tools. *ECS Trans.* **64**, 19 (2014).
200. Kumar, S. *et al.* Conduction Channel Formation and Dissolution Due to Oxygen Thermophoresis/Diffusion in Hafnium Oxide Memristors. *ACS Nano* **10**, 11205–11210 (2016).
201. Liu, H. *et al.* Controlled Formation of Conduction Channels in Memristive Devices Observed by X-ray Multimodal Imaging. *Advanced Materials* **34**, 2203209 (2022).
202. Chao, W., Harteneck, B. D., Liddle, J. A., Anderson, E. H. & Attwood, D. T. Soft X-ray microscopy at a spatial resolution better than 15 nm. *Nature* **435**, 1210–1213 (2005).
203. Kilcoyne, A. L. D. *et al.* Interferometer-controlled scanning transmission X-ray microscopes at the Advanced Light Source. *J Synchrotron Rad* **10**, 125–136 (2003).
204. Liu, H. *et al.* Quantitative Observation of Threshold Defect Behavior in Memristive Devices with Operando X-ray Microscopy. *ACS Nano* **12**, 4938–4945 (2018).
205. Lim, E. & Ismail, R. Conduction Mechanism of Valence Change Resistive Switching Memory: A Survey. *Electronics* **4**, 586–613 (2015).
206. Chen, A. *et al.* Non-volatile resistive switching for advanced memory applications. in *IEEE International Electron Devices Meeting, 2005. IEDM Technical Digest.* 746–749 (2005).
doi:10.1109/IEDM.2005.1609461.

207. Kim, H.-D., An, H.-M., Lee, E. B. & Kim, T. G. Stable Bipolar Resistive Switching Characteristics and Resistive Switching Mechanisms Observed in Aluminum Nitride-based ReRAM Devices. *IEEE Transactions on Electron Devices* **58**, 3566–3573 (2011).
208. Wang, S.-Y., Lee, D.-Y., Huang, T.-Y., Wu, J.-W. & Tseng, T.-Y. Controllable oxygen vacancies to enhance resistive switching performance in a ZrO₂-based RRAM with embedded Mo layer. *Nanotechnology* **21**, 495201 (2010).
209. Croitoru, N., Lazarescu, M., Popescu, C., Telnic, M. & Vescan, L. Ohmic and non-ohmic conduction in some amorphous semiconductors. *Journal of Non-Crystalline Solids* **8–10**, 781–786 (1972).
210. Kim, S., Jeong, H. Y., Choi, S.-Y. & Choi, Y.-K. Comprehensive modeling of resistive switching in the Al/TiO_x/TiO₂/Al heterostructure based on space-charge-limited conduction. *Appl. Phys. Lett.* **97**, 033508 (2010).
211. Wang, S.-Y., Huang, C.-W., Lee, D.-Y., Tseng, T.-Y. & Chang, T.-C. Multilevel resistive switching in Ti/Cu_xO/Pt memory devices. *Journal of Applied Physics* **108**, 114110 (2010).
212. Chakrabarti, S., Samanta, S., Maikap, S., Rahaman, S. Z. & Cheng, H.-M. Temperature-Dependent Non-linear Resistive Switching Characteristics and Mechanism Using a New W/WO₃/WO_x/W Structure. *Nanoscale Res Lett* **11**, 389 (2016).
213. Gao, X. *et al.* Effect of top electrode materials on bipolar resistive switching behavior of gallium oxide films. *Appl. Phys. Lett.* **97**, 193501 (2010).
214. Choi, B. J. *et al.* Trilayer Tunnel Selectors for Memristor Memory Cells. *Advanced Materials* **28**, 356–362 (2016).

215. Tsai, T.-L., Lin, Y.-H. & Tseng, T.-Y. Resistive Switching Characteristics of WO₃/ZrO₂ Structure With Forming-Free, Self-Compliance, and Submicroampere Current Operation. *IEEE Electron Device Letters* **36**, 675–677 (2015).
216. Zhang, Y. *et al.* Study of conduction and switching mechanisms in Al/AIO_x/WO_x/W resistive switching memory for multilevel applications. *Appl. Phys. Lett.* **102**, 233502 (2013).
217. Jo, M. *et al.* Novel cross-point resistive switching memory with self-formed schottky barrier. in *2010 Symposium on VLSI Technology* 53–54 (2010). doi:10.1109/VLSIT.2010.5556121.
218. Guan, W., Liu, M., Long, S., Liu, Q. & Wang, W. On the resistive switching mechanisms of Cu/ZrO₂:Cu/Pt. *Appl. Phys. Lett.* **93**, 223506 (2008).
219. Tappertzhofen, S. *et al.* Generic Relevance of Counter Charges for Cation-Based Nanoscale Resistive Switching Memories. *ACS Nano* **7**, 6396–6402 (2013).
220. Guo, T. *et al.* Effect of crystalline state on conductive filaments forming process in resistive switching memory devices. *Materials Today Communications* **20**, 100540 (2019).
221. Yi, M. *et al.* Temperature dependence of resistive switching behaviors in resistive random access memory based on graphene oxide film. *Nanotechnology* **25**, 185202 (2014).
222. Q. Wang, Z. *et al.* Performance improvement of resistive switching memory achieved by enhancing local-electric-field near electromigrated Ag-nanoclusters. *Nanoscale* **5**, 4490–4494 (2013).
223. Tsunoda, K. *et al.* Bipolar resistive switching in polycrystalline TiO₂ films. *Appl. Phys. Lett.* **90**, 113501 (2007).
224. Tsuruoka, T. *et al.* Effects of Moisture on the Switching Characteristics of Oxide-Based, Gapless-Type Atomic Switches. *Advanced Functional Materials* **22**, 70–77 (2012).

225. Lübben, M. *et al.* Graphene-Modified Interface Controls Transition from VCM to ECM Switching Modes in Ta/TaOx Based Memristive Devices. *Advanced Materials* **27**, 6202–6207 (2015).
226. Gul, F. Carrier transport mechanism and bipolar resistive switching behavior of a nano-scale thin film TiO₂ memristor. *Ceramics International* **44**, 11417–11423 (2018).
227. Chen, S.-W. & Wu, J.-M. Unipolar resistive switching behavior of BiFeO₃ thin films prepared by chemical solution deposition. *Thin Solid Films* **519**, 499–504 (2010).
228. Yu, S., Guan, X. & Wong, H.-S. P. On the stochastic nature of resistive switching in metal oxide RRAM: Physical modeling, monte carlo simulation, and experimental characterization. in *2011 International Electron Devices Meeting* 17.3.1-17.3.4 (2011).
doi:10.1109/IEDM.2011.6131572.
229. Chaurasiya, R. *et al.* First-principles simulation of neutral and charged oxygen vacancies in m-ZrO₂: an origin of filamentary type resistive switching. *Nanotechnology* **33**, 345203 (2022).
230. Linn, E., Siemon, A., Waser, R. & Menzel, S. Applicability of Well-Established Memristive Models for Simulations of Resistive Switching Devices. *IEEE Transactions on Circuits and Systems I: Regular Papers* **61**, 2402–2410 (2014).
231. Huang, P. *et al.* A Physics-Based Compact Model of Metal-Oxide-Based RRAM DC and AC Operations. *IEEE Transactions on Electron Devices* **60**, 4090–4097 (2013).
232. Du, Y. *et al.* Symmetrical Negative Differential Resistance Behavior of a Resistive Switching Device. *ACS Nano* **6**, 2517–2523 (2012).
233. Zhang, H. *et al.* Ionic doping effect in ZrO₂ resistive switching memory. *Appl. Phys. Lett.* **96**, 123502 (2010).

234. Clima, S. *et al.* Intrinsic Tailing of Resistive States Distributions in Amorphous HfO_x and TaO_x Based Resistive Random Access Memories. *IEEE Electron Device Letters* **36**, 769–771 (2015).
235. Traoré, B. *et al.* HfO₂-Based RRAM: Electrode Effects, Ti/HfO₂ Interface, Charge Injection, and Oxygen (O) Defects Diffusion Through Experiment and Ab Initio Calculations. *IEEE Transactions on Electron Devices* **63**, 360–368 (2016).
236. He, Y. *et al.* Molecular Dynamics Study of the Switching Mechanism of Carbon-Based Resistive Memory. *IEEE Transactions on Electron Devices* **57**, 3434–3441 (2010).
237. Maldonado, D. *et al.* Variability estimation in resistive switching devices, a numerical and kinetic Monte Carlo perspective. *Microelectronic Engineering* **257**, 111736 (2022).
238. Broglia, G., Ori, G., Larcher, L. & Montorsi, M. Molecular dynamics simulation of amorphous HfO₂ for resistive RAM applications. *Modelling Simul. Mater. Sci. Eng.* **22**, 065006 (2014).
239. Yu, S., Yin Chen, Y., Guan, X., Philip Wong, H.-S. & Kittl, J. A. A Monte Carlo study of the low resistance state retention of HfO_x based resistive switching memory. *Appl. Phys. Lett.* **100**, 043507 (2012).
240. Wojtyniak, M. *et al.* Electro-degradation and resistive switching of Fe-doped SrTiO₃ single crystal. *Journal of Applied Physics* **113**, 083713 (2013).
241. Menzel, S., Kaupmann, P. & Waser, R. Understanding filamentary growth in electrochemical metallization memory cells using kinetic Monte Carlo simulations. *Nanoscale* **7**, 12673–12681 (2015).
242. Kaniselvan, M., Luisier, M. & Mladenović, M. An Atomistic Model of Field-Induced Resistive Switching in Valence Change Memory. *ACS Nano* (2023) doi:10.1021/acsnano.2c12575.

243. Bocquet, M. *et al.* Compact Modeling Solutions for Oxide-Based Resistive Switching Memories (OxRAM). *Journal of Low Power Electronics and Applications* **4**, 1–14 (2014).
244. Zidan, M. A. Memristor Circuits and Systems. 163.
245. Zhu, J., Zhang, T., Yang, Y. & Huang, R. A comprehensive review on emerging artificial neuromorphic devices. *Applied Physics Reviews* **7**, 011312 (2020).
246. Fleck, K. *et al.* Uniting Gradual and Abrupt set Processes in Resistive Switching Oxides. *Phys. Rev. Applied* **6**, 064015 (2016).
247. Lee, H. J. *et al.* Effect of oxygen flow rate on long-term and short-term Schottky barrier modulations in Pd/IGZO/SiO₂/p⁺-Si memristors. *Materials Science in Semiconductor Processing* **153**, 107183 (2023).
248. Chang, T. *et al.* Synaptic behaviors and modeling of a metal oxide memristive device. *Appl. Phys. A* **102**, 857–863 (2011).
249. Siemon, A. *et al.* Simulation of TaOx-based complementary resistive switches by a physics-based memristive model. in *2014 IEEE International Symposium on Circuits and Systems (ISCAS)* 1420–1423 (2014). doi:10.1109/ISCAS.2014.6865411.
250. Guo, T. *et al.* Adjustable Leaky-Integrate-and-fire neurons based on memristor-coupled capacitors. *Materials Today Advances* **12**, 100192 (2021).
251. Bocquet, M. *et al.* Robust Compact Model for Bipolar Oxide-Based Resistive Switching Memories. *IEEE Transactions on Electron Devices* **61**, 674–681 (2014).
252. Kim, S., Kim, H.-D. & Choi, S.-J. Compact Two-State-Variable Second-Order Memristor Model. *Small* **12**, 3320–3326 (2016).
253. Pan, C. *et al.* Model for multi-filamentary conduction in graphene/hexagonal-boron-nitride/graphene based resistive switching devices. *2D Mater.* **4**, 025099 (2017).

254. Linn, E., Menzel, S., Ferch, S. & Waser, R. Compact modeling of CRS devices based on ECM cells for memory, logic and neuromorphic applications. *Nanotechnology* **24**, 384008 (2013).
255. Hassan, A. M., Fahmy, H. A. H. & Rafat, N. H. Enhanced Model of Conductive Filament-Based Memristor via Including Trapezoidal Electron Tunneling Barrier Effect. *IEEE Transactions on Nanotechnology* **15**, 484–491 (2016).
256. Zhang, W. *et al.* Neuro-inspired computing chips. *Nat Electron* **3**, 371–382 (2020).
257. Marković, D., Mizrahi, A., Querlioz, D. & Grollier, J. Physics for neuromorphic computing. *Nat Rev Phys* **2**, 499–510 (2020).
258. Haensch, W. *et al.* Compute in-Memory with Non-Volatile Elements for Neural Networks: A Review from a Co-Design Perspective. *Advanced Materials* **n/a**, 2204944.
259. Schuman, C. D. *et al.* Opportunities for neuromorphic computing algorithms and applications. *Nat Comput Sci* **2**, 10–19 (2022).
260. Sze, V., Chen, Y.-H., Yang, T.-J. & Emer, J. S. Efficient Processing of Deep Neural Networks: A Tutorial and Survey. *Proceedings of the IEEE* **105**, 2295–2329 (2017).
261. Wan, W. *et al.* A compute-in-memory chip based on resistive random-access memory. *Nature* **608**, 504–512 (2022).
262. Capra, M. *et al.* Hardware and Software Optimizations for Accelerating Deep Neural Networks: Survey of Current Trends, Challenges, and the Road Ahead. *IEEE Access* **8**, 225134–225180 (2020).
263. Chai, Y. In-sensor computing for machine vision. *Nature* **579**, 32–33 (2020).
264. Moin, A. *et al.* A wearable biosensing system with in-sensor adaptive machine learning for hand gesture recognition. *Nat Electron* **4**, 54–63 (2021).

265. Zhang, Z. *et al.* In-sensor reservoir computing system for latent fingerprint recognition with deep ultraviolet photo-synapses and memristor array. *Nat Commun* **13**, 6590 (2022).
266. Lee, S., Peng, R., Wu, C. & Li, M. Programmable black phosphorus image sensor for broadband optoelectronic edge computing. *Nat Commun* **13**, 1485 (2022).
267. Kim, Y. *et al.* A bioinspired flexible organic artificial afferent nerve. *Science* **360**, 998–1003 (2018).
268. Fu, T. *et al.* Bioinspired bio-voltage memristors. *Nat Commun* **11**, 1861 (2020).
269. Kumar, S., Wang, X., Strachan, J. P., Yang, Y. & Lu, W. D. Dynamical memristors for higher-complexity neuromorphic computing. *Nat Rev Mater* **7**, 575–591 (2022).
270. Wang, Y. *et al.* Band-tailored van der Waals heterostructure for multilevel memory and artificial synapse. *InfoMat* **3**, 917–928 (2021).
271. Wang, W. *et al.* Learning of spatiotemporal patterns in a spiking neural network with resistive switching synapses. *Science Advances* **4**, eaat4752 (2018).
272. Liu, K. *et al.* An optoelectronic synapse based on α -In₂Se₃ with controllable temporal dynamics for multimode and multiscale reservoir computing. *Nat Electron* **5**, 761–773 (2022).
273. Cai, F. *et al.* Power-efficient combinatorial optimization using intrinsic noise in memristor Hopfield neural networks. *Nat Electron* **3**, 409–418 (2020).
274. Wang, Y. *et al.* MXene-ZnO Memristor for Multimodal In-Sensor Computing. *Adv. Funct. Mater.* 2100144 (2021) doi:10.1002/adfm.202100144.
275. Li, C. *et al.* A Camel Nose-Inspired Highly Durable Neuromorphic Humidity Sensor with Water Source Locating Capability. *ACS Nano* **16**, 1511–1522 (2022).
276. Wang, M. *et al.* Artificial Skin Perception. *Advanced Materials* **33**, 2003014 (2021).

277. Kwon, S. M. *et al.* Environment-Adaptable Artificial Visual Perception Behaviors Using a Light-Adjustable Optoelectronic Neuromorphic Device Array. *Advanced Materials* **31**, 1906433 (2019).
278. Liu, Y. *et al.* Self-powered high-sensitivity sensory memory actuated by triboelectric sensory receptor for real-time neuromorphic computing. *Nano Energy* **75**, 104930 (2020).
279. Lee, Y. R., Trung, T. Q., Hwang, B.-U. & Lee, N.-E. A flexible artificial intrinsic-synaptic tactile sensory organ. *Nat Commun* **11**, 2753 (2020).
280. Cui, B. *et al.* Ferroelectric photosensor network: an advanced hardware solution to real-time machine vision. *Nat Commun* **13**, 1707 (2022).
281. Qiumei, Z., Dan, T. & Fenghua, W. Improved Convolutional Neural Network Based on Fast Exponentially Linear Unit Activation Function. *IEEE Access* **7**, 151359–151367 (2019).
282. Häusser, M. The Hodgkin-Huxley theory of the action potential. *Nat Neurosci* **3**, 1165–1165 (2000).
283. Jiang, H. *et al.* Cyclical sensing integrate-and-fire circuit for memristor array based neuromorphic computing. in *2016 IEEE International Symposium on Circuits and Systems (ISCAS)* 930–933 (2016). doi:10.1109/ISCAS.2016.7527394.
284. Yang, J.-Q. *et al.* Leaky integrate-and-fire neurons based on perovskite memristor for spiking neural networks. *Nano Energy* **74**, 104828 (2020).
285. Huang, H.-M. *et al.* Quasi-Hodgkin–Huxley Neurons with Leaky Integrate-and-Fire Functions Physically Realized with Memristive Devices. *Advanced Materials* **31**, 1803849 (2019).
286. Kim, M. S. *et al.* Bio-Inspired Artificial Vision and Neuromorphic Image Processing Devices. *Advanced Materials Technologies* **7**, 2100144 (2022).

287. Prezioso, M. *et al.* Training and operation of an integrated neuromorphic network based on metal-oxide memristors. *Nature* **521**, 61–64 (2015).
288. Yao, P. *et al.* Face classification using electronic synapses. *Nat Commun* **8**, 15199 (2017).
289. Sheridan, P. M. *et al.* Sparse coding with memristor networks. *Nature Nanotech* **12**, 784–789 (2017).
290. Serb, A. *et al.* Unsupervised learning in probabilistic neural networks with multi-state metal-oxide memristive synapses. *Nat Commun* **7**, 12611 (2016).
291. LeCun, Y., Bengio, Y. & Hinton, G. Deep learning. *Nature* **521**, 436–444 (2015).
292. Choi, C. *et al.* Reconfigurable heterogeneous integration using stackable chips with embedded artificial intelligence. *Nat Electron* **5**, 386–393 (2022).
293. Liang, S.-J. & Miao, F. Lego-like reconfigurable AI chips. *Nat Electron* **5**, 327–328 (2022).
294. Sun, F., Lu, Q., Feng, S. & Zhang, T. Flexible Artificial Sensory Systems Based on Neuromorphic Devices. *ACS Nano* **15**, 3875–3899 (2021).
295. Yu, J. *et al.* Bioinspired interactive neuromorphic devices. *Materials Today* **60**, 158–182 (2022).
296. Wan, C. *et al.* An Artificial Sensory Neuron with Tactile Perceptual Learning. *Advanced Materials* **30**, 1801291 (2018).
297. Yun, S.-Y. *et al.* Self-aware artificial auditory neuron with a triboelectric sensor for spike-based neuromorphic hardware. *Nano Energy* **109**, 108322 (2023).
298. Zhang, Y. *et al.* Self-Powered Bidirectional Photoresponse in High-Detectivity WSe₂ Phototransistor with Asymmetrical van der Waals Stacking for Retinal Neurons Emulation. *ACS Nano* **16**, 20937–20945 (2022).

299. Zhu, Q.-B. *et al.* A flexible ultrasensitive optoelectronic sensor array for neuromorphic vision systems. *Nat Commun* **12**, 1798 (2021).
300. Jang, H. *et al.* In-sensor optoelectronic computing using electrostatically doped silicon. *Nat Electron* **5**, 519–525 (2022).
301. Cai, Y. *et al.* Broadband Visual Adaption and Image Recognition in a Monolithic Neuromorphic Machine Vision System. *Advanced Functional Materials* **n/a**, 2212917.
302. Xia, Q. *et al.* Two- and Three-Terminal Resistive Switches: Nanometer-Scale Memristors and Memistors. *Advanced Functional Materials* **21**, 2660–2665 (2011).
303. Lu, W. & Lieber, C. M. Nanoelectronics from the bottom up. *Nature Mater* **6**, 841–850 (2007).
304. Huang, W. *et al.* Memristive Artificial Synapses for Neuromorphic Computing. *Nano-Micro Lett.* **13**, 85 (2021).
305. Lv, Z. *et al.* Semiconductor Quantum Dots for Memories and Neuromorphic Computing Systems. *Chem. Rev.* **120**, 3941–4006 (2020).
306. Lv, Z. *et al.* Phototunable Biomemory Based on Light-Mediated Charge Trap. *Advanced Science* **5**, 1800714 (2018).
307. Lv, Z., Zhou, Y., Han, S.-T. & Roy, V. A. L. From biomaterial-based data storage to bio-inspired artificial synapse. *Materials Today* **21**, 537–552 (2018).
308. Midya, R. *et al.* Reservoir Computing Using Diffusive Memristors. *Advanced Intelligent Systems* **1**, 1900084 (2019).
309. Yu, M. J. *et al.* Three Musketeers: demonstration of multilevel memory, selector, and synaptic behaviors from an Ag-GeTe based chalcogenide material. *Journal of Materials Research and Technology* **15**, 1984–1995 (2021).

310. Liu, T., Verma, M., Kang, Y. & Orlowski, M. Volatile resistive switching in Cu/TaO_x/δ-Cu/Pt devices. *Appl. Phys. Lett.* **101**, 073510 (2012).
311. Shi, Y. *et al.* Coexistence of volatile and non-volatile resistive switching in 2D h-BN based electronic synapses. in *2017 IEEE International Electron Devices Meeting (IEDM)* 5.4.1-5.4.4 (IEEE, 2017). doi:10.1109/IEDM.2017.8268333.
312. Abbas, H. *et al.* The coexistence of threshold and memory switching characteristics of ALD HfO₂ memristor synaptic arrays for energy-efficient neuromorphic computing. *Nanoscale* **12**, 14120–14134 (2020).
313. Li, Y. *et al.* Coexistence of diode-like volatile and multilevel nonvolatile resistive switching in a ZrO₂/TiO₂ stack structure. *Nanotechnology* **26**, 391001 (2015).
314. Abbas, H. *et al.* Reversible transition of volatile to non-volatile resistive switching and compliance current-dependent multistate switching in IGZO/MnO RRAM devices. *Applied Physics Letters* **6** (2019).
315. Du, G., Li, H., Mao, Q. & Ji, Z. Controllable volatile to nonvolatile resistive switching conversion and conductive filaments engineering in Cu/ZrO₂/Pt devices. *J. Phys. D: Appl. Phys.* **49**, 445105 (2016).
316. Simanjuntak, F. M., Chandrasekaran, S., Pattanayak, B., Lin, C.-C. & Tseng, T.-Y. Peroxide induced volatile and non-volatile switching behavior in ZnO-based electrochemical metallization memory cell. *Nanotechnology* **28**, 38LT02 (2017).
317. Yoon, S. J. *et al.* Compliance current and temperature effects on non-volatile memory switching and volatile switching dynamics in a Cu/SiO_x/p⁺⁺-Si device. *Appl. Phys. Lett.* **115**, 212102 (2019).

318. He, N. *et al.* Reversible Transition of Volatile and Nonvolatile Switching in Ag–In–Zn–S Quantum Dot-Based Memristors with Low Power Consumption for Synaptic Applications. *ACS Appl. Nano Mater.* acsanm.0c03180 (2021) doi:10.1021/acsanm.0c03180.
319. Michelakaki, I., Bousoulas, P., Stathopoulos, S., Boukos, N. & Tsoukalas, D. Coexistence of bipolar and threshold resistive switching in TiO₂ based structure with embedded hafnium nanoparticles. *J. Phys. D: Appl. Phys.* **50**, 045103 (2017).
320. Munjal, S. & Khare, N. Compliance current controlled volatile and nonvolatile memory in Ag/CoFe₂O₄/Pt resistive switching device. *Nanotechnology* **32**, 185204 (2021).
321. Lian, X. *et al.* Electrical Properties and Biological Synaptic Simulation of Ag/MXene/SiO₂/Pt RRAM Devices. *Electronics* **9**, 2098 (2020).
322. Cho, H. & Kim, S. Emulation of Biological Synapse Characteristics from Cu/AlN/TiN Conductive Bridge Random Access Memory. *Nanomaterials* **10**, 1709 (2020).
323. Kamble, G. U. *et al.* Highly-stable memristive devices with synaptic characteristics based on hydrothermally synthesized MnO₂ active layers. *Journal of Alloys and Compounds* **872**, 159653 (2021).
324. Dongale, T. D., Khot, A. C., Takaloo, A. V., Son, K. R. & Kim, T. G. Multilevel resistive switching and synaptic plasticity of nanoparticulated cobaltite oxide memristive device. *Journal of Materials Science & Technology* **78**, 81–91 (2021).
325. Khot, A. C., Dongale, T. D., Park, J. H., Kesavan, A. V. & Kim, T. G. Ti₃C₂-Based MXene Oxide Nanosheets for Resistive Memory and Synaptic Learning Applications. *ACS Appl. Mater. Interfaces* **13**, 5216–5227 (2021).

326. Patil, A. A., Wagh, S. V., Dongale, T. D. & Kim, D. Electrospun 1D f-MWCNTs-TiO₂ composite nanofibers for resistive memory and synaptic learning applications. *Materials Letters* **280**, 128587 (2020).
327. Dongale, T. D., Khot, A. C., Takaloo, A. V. & Kim, T. G. Facile synthesis of nickel cobaltite quasi-hexagonal nanosheets for multilevel resistive switching and synaptic learning applications. *NPG Asia Mater* **13**, 1–12 (2021).
328. Wang, Z. *et al.* Threshold Switching of Ag or Cu in Dielectrics: Materials, Mechanism, and Applications. *Adv. Funct. Mater.* **28**, 1704862 (2018).
329. Kim, K.-H. *et al.* A Functional Hybrid Memristor Crossbar-Array/CMOS System for Data Storage and Neuromorphic Applications. *Nano Lett.* **12**, 389–395 (2012).
330. Soltz, D., Dagan, G. & Cahen, D. IONIC MOBILITY AND ELECTRONIC JUNCTION MOVEMENT IN CuInSe₂. 6.
331. Chernyak, L., Gartsman, K., Cahen, D. & Stafsudd, O. M. Electronic effects of ion mobility in semiconductors: Semionic behaviour of CuInSe₂. *Journal of Physics and Chemistry of Solids* **56**, 1165–1191 (1995).
332. Bhattacharya, R. N., Oh, M.-K. & Kim, Y. CIGS-based solar cells prepared from electrodeposited precursor films. *Solar Energy Materials and Solar Cells* **98**, 198–202 (2012).
333. Bhattacharya, R. N. Electrodeposited Two-Layer Cu–In–Ga–Se/In–Se Thin Films. *J. Electrochem. Soc.* **157**, D406 (2010).
334. Contreras-Ruiz, M. A., Mendez-Blas, A. & Calixto, Ma. E. Band gap tuning of Cu(In,Ga)Se₂ thin films by electrodeposition and their subsequent selenization using a rapid thermal annealing system. *J Solid State Electrochem* (2020) doi:10.1007/s10008-020-04832-7.

335. Londhe, P. U., Rohom, A. B., Fernandes, R., Kothari, D. C. & Chaure, N. B. Development of Superstrate CuInGaSe₂ Thin Film Solar Cells with Low-Cost Electrochemical Route from Nonaqueous Bath. *ACS Sustainable Chem. Eng.* **6**, 4987–4995 (2018).
336. Lara-Lara, B. & Fernández, A. M. CIGS thin film growing by electrodeposition technique using mechanical perturbation at the working electrode. *J Mater Sci: Mater Electron* **27**, 5099–5106 (2016).
337. Schwarzacher, W. Electrodeposition: A Technology for the Future. *Electrochem. Soc. Interface* **15**, 32–33 (2006).
338. Hubert, C. *et al.* The Zn(S,O,OH)/ZnMgO buffer in thin film Cu(In,Ga)(S,Se)₂-based solar cells part I: Fast chemical bath deposition of Zn(S,O,OH) buffer layers for industrial application on Co-evaporated Cu(In,Ga)Se₂ and electrodeposited CuIn(S,Se)₂ solar cells. *Progress in Photovoltaics: Research and Applications* **17**, 470–478 (2009).
339. Chen, Y. *et al.* Plating Uniformity of Bottom-up Copper Pillars and Patterns for IC Substrates with Additive-assisted Electrodeposition. *Electrochimica Acta* **120**, 293–301 (2014).
340. van de Burgt, Y. *et al.* A non-volatile organic electrochemical device as a low-voltage artificial synapse for neuromorphic computing. *NATURE MATERIALS* **27** (2017).
341. Fuller, E. J. *et al.* Li-Ion Synaptic Transistor for Low Power Analog Computing. *Advanced Materials* **29**, 1604310 (2017).
342. UCI Machine Learning Repository. <https://archive.ics.uci.edu/ml/index.php>.
343. Aida, Y. *et al.* Cu-rich CuInSe₂ solar cells with a Cu-poor surface. *Progress in Photovoltaics: Research and Applications* **23**, 754–764 (2015).
344. Rincón, C. & Ramírez, F. J. Lattice vibrations of CuInSe₂ and CuGaSe₂ by Raman microspectrometry. *Journal of Applied Physics* **72**, 4321–4324 (1992).

345. Lauth, J. *et al.* Virtually Bare Nanocrystal Surfaces: Significantly Enhanced Electrical Transport in CuInSe₂ and CuIn_{1-x}Ga_xSe₂ Thin Films upon Ligand Exchange with Thermally Degradable 1-Ethyl-5-Thiotetrazole. *Advanced Functional Materials* **24**, 1081–1088 (2014).
346. Zhao, Y. *et al.* High Efficiency CIGS Solar Cells by Bulk Defect Passivation through Ag Substituting Strategy. *ACS Appl. Mater. Interfaces* **12**, 12717–12726 (2020).
347. Jorcin, J.-B., Orazem, M. E., Pèbère, N. & Tribollet, B. CPE analysis by local electrochemical impedance spectroscopy. *Electrochimica Acta* **51**, 1473–1479 (2006).
348. Irvine, J. T. S., Sinclair, D. C. & West, A. R. Electroceramics: Characterization by Impedance Spectroscopy. *Advanced Materials* **2**, 132–138 (1990).
349. Bouferra, R., Marín, G., Amhil, S., Wasim, S. M. & Essaleh, L. Low temperature electrical impedance spectroscopy characterization of n type CuInSe₂ semiconductor compound. *Physica B: Condensed Matter* **565**, 14–17 (2019).
350. Patil, S. K., Koledintseva, M. Y., Schwartz, R. W. & Huebner, W. Prediction of effective permittivity of diphasic dielectrics using an equivalent capacitance model. *J. Appl. Phys.* **104**, 074108 (2008).
351. Li, P. W., Anderson, R. A. & Plovnick, R. H. Dielectric constant of CuInSe₂ by capacitance measurements. *Journal of Physics and Chemistry of Solids* **40**, 333–334 (1979).
352. Chang, T., Jo, S.-H. & Lu, W. Short-Term Memory to Long-Term Memory Transition in a Nanoscale Memristor. *ACS Nano* **5**, 7669–7676 (2011).
353. Liu, D., Cheng, H., Wang, G., Zhu, X. & Wang, N. Diode-like volatile resistive switching properties in amorphous Sr-doped LaMnO₃ thin films under lower current compliance. *Journal of Applied Physics* **114**, 154906 (2013).

354. Lv, Z. *et al.* Mimicking Neuroplasticity in a Hybrid Biopolymer Transistor by Dual Modes Modulation. *Advanced Functional Materials* **29**, 1902374 (2019).
355. Sun, H. *et al.* Direct Observation of Conversion Between Threshold Switching and Memory Switching Induced by Conductive Filament Morphology. *Advanced Functional Materials* **24**, 5679–5686 (2014).
356. Schlößer, D. C. *et al.* Kinetics of island diffusion on Cu(111) and Ag(111) studied with variable-temperature STM. *Surface Science* **465**, 19–39 (2000).
357. Laidler, K. J. The development of the Arrhenius equation. *J. Chem. Educ.* **61**, 494 (1984).
358. Jensen, F. Activation energies and the arrhenius equation. *Quality and Reliability Engineering International* **1**, 13–17 (1985).
359. Chauhan, S. M., Chaki, S. H., Deshpande, M. P., Malek, T. J. & Tailor, J. P. Thermal Decomposition Study on CuInSe₂ Single Crystals. *Int J Thermophys* **39**, 18 (2017).
360. Ma, Y. *et al.* Evolution of the conductive filament with cycling in TaOx-based resistive switching devices. *Journal of Applied Physics* **128**, 194501 (2020).
361. Wang, Z. *et al.* Capacitive neural network with neuro-transistors. *Nat Commun* **9**, 3208 (2018).
362. Du, C. *et al.* Reservoir computing using dynamic memristors for temporal information processing. *Nat Commun* **8**, 2204 (2017).
363. Huang, W. *et al.* Zero-power optoelectronic synaptic devices. *Nano Energy* **73**, 104790 (2020).
364. Valov, I. *et al.* Nanobatteries in redox-based resistive switches require extension of memristor theory. *Nat Commun* **4**, 1771 (2013).

365. Lv, Z. Self-assembling crystalline peptide microrod for neuromorphic function implementation. 19.
366. Jo, S. H., Kim, K.-H. & Lu, W. Programmable Resistance Switching in Nanoscale Two-Terminal Devices. *Nano Lett.* **9**, 496–500 (2009).
367. Legg, S. & Hutter, M. Universal Intelligence: A Definition of Machine Intelligence. *Minds & Machines* **17**, 391–444 (2007).
368. Zhang, H.-T. *et al.* Reconfigurable perovskite nickelate electronics for artificial intelligence. 8 (2022).
369. Wan, C. *et al.* Artificial Sensory Memory. *Adv. Mater.* **32**, 1902434 (2020).
370. Ahmed, T. *et al.* Fully Light-Controlled Memory and Neuromorphic Computation in Layered Black Phosphorus. *Adv. Mater.* 13 (2020).
371. Li, G. *et al.* Photo-induced non-volatile VO₂ phase transition for neuromorphic ultraviolet sensors. *Nat Commun* **13**, 1729 (2022).
372. Meng, J. *et al.* Integrated In-Sensor Computing Optoelectronic Device for Environment-Adaptable Artificial Retina Perception Application. *Nano Lett.* acs.nanolett.1c03240 (2021) doi:10.1021/acs.nanolett.1c03240.
373. Liao, F. *et al.* Bioinspired in-sensor visual adaptation for accurate perception. *Nat Electron* (2022) doi:10.1038/s41928-022-00713-1.
374. Li, T. *et al.* 2D oriented covalent organic frameworks for alcohol-sensory synapses. *Mater. Horiz.* **8**, 2041–2049 (2021).
375. Li, E. *et al.* Synaptic Transistor Capable of Accelerated Learning Induced by Temperature-Facilitated Modulation of Synaptic Plasticity. *ACS Appl. Mater. Interfaces* **11**, 46008–46016 (2019).

376. Liu, L. *et al.* Stretchable Neuromorphic Transistor That Combines Multisensing and Information Processing for Epidermal Gesture Recognition. *ACS Nano* acsnano.1c08482 (2022) doi:10.1021/acsnano.1c08482.
377. Wang, Z. *et al.* Resistive switching materials for information processing. *Nat Rev Mater* **5**, 173–195 (2020).
378. Oh, C., Jo, M. & Son, J. All-Solid-State Synaptic Transistors with High-Temperature Stability Using Proton Pump Gating of Strongly Correlated Materials. *ACS Appl. Mater. Interfaces* **11**, 15733–15740 (2019).
379. Xia, Q. & Yang, J. J. Memristive crossbar arrays for brain-inspired computing. *Nat. Mater.* **18**, 309–323 (2019).
380. DeVoe, D. L. Thermal issues in MEMS and microscale systems. *IEEE Transactions on Components and Packaging Technologies* **25**, 576–583 (2002).
381. Figeys, D. & Pinto, D. Lab-on-a-Chip: A Revolution in Biological and Medical Sciences. *Anal. Chem.* **72**, 330 A–335 A (2000).
382. Yang, F., Yang, N., Huo, X. & Xu, S. Thermal sensing in fluid at the micro-nano-scales. *Biomicrofluidics* **12**, 041501 (2018).
383. Andersson, H. & van den Berg, A. Microfluidic devices for cellomics: a review. *Sensors and Actuators B: Chemical* **92**, 315–325 (2003).
384. Rein, J. *et al.* Unlocking the Potential of High-Throughput Experimentation for Electrochemistry with a Standardized Microscale Reactor. *ACS Cent. Sci.* **7**, 1347–1355 (2021).
385. Seeger, K. *Semiconductor Physics*. (Springer Science & Business Media, 2013).
386. Latha, M. *et al.* Solution based synthesis of Cu(In,Ga)Se₂ microcrystals and thin films. *RSC Adv.* **9**, 35197–35208 (2019).

387. Yan, Y. *et al.* Cu(In,Ga)Se₂ thin films annealed with SnSe₂ for solar cell absorber fabricated by magnetron sputtering. *Solar Energy* **155**, 601–607 (2017).
388. Guo, T. *et al.* From Memristive Materials to Neural Networks. *ACS Appl. Mater. Interfaces* **12**, 54243–54265 (2020).
389. Sebastian, A., Le Gallo, M., Khaddam-Aljameh, R. & Eleftheriou, E. Memory devices and applications for in-memory computing. *Nat. Nanotechnol.* **15**, 529–544 (2020).
390. Figurov, A., Pozzo-Miller, L. D., Olafsson, P., Wang, T. & Lu, B. Regulation of synaptic responses to high-frequency stimulation and LTP by neurotrophins in the hippocampus. *Nature* **381**, 706–709 (1996).
391. Huh, W., Lee, D. & Lee, C.-H. Memristors Based on 2D Materials as an Artificial Synapse for Neuromorphic Electronics. *Advanced Materials* **32**, 2002092 (2020).
392. Sun, B. *et al.* Synaptic devices based neuromorphic computing applications in artificial intelligence. *Materials Today Physics* 100393 (2021) doi:10.1016/j.mtphys.2021.100393.
393. Zhang, H., Arens, E., Huizenga, C. & Han, T. Thermal sensation and comfort models for non-uniform and transient environments: Part I: Local sensation of individual body parts. *Building and Environment* **45**, 380–388 (2010).
394. Nguyen, T.-N. & Shin, D. Statistical Memristor-Based Temperature Sensors without Analog-to-Digital Conversion. in *2018 IEEE 7th Non-Volatile Memory Systems and Applications Symposium (NVMSA)* 99–104 (2018). doi:10.1109/NVMSA.2018.00024.
395. Milano, G. *et al.* Structure-Dependent Influence of Moisture on Resistive Switching Behavior of ZnO Thin Films. *Advanced Materials Interfaces* **8**, 2100915 (2021).
396. Mufti, N. *et al.* Review of CIGS-based solar cells manufacturing by structural engineering. *Solar Energy* **207**, 1146–1157 (2020).

397. Yang, Y. C., Pan, F., Liu, Q., Liu, M. & Zeng, F. Fully Room-Temperature-Fabricated Nonvolatile Resistive Memory for Ultrafast and High-Density Memory Application. *Nano Lett.* **9**, 1636–1643 (2009).
398. Yang, C.-S. *et al.* Moisture effects on the electrochemical reaction and resistance switching at Ag/molybdenum oxide interfaces. *Physical Chemistry Chemical Physics* **18**, 12466–12475 (2016).
399. Theelen, M. Stability of Cu(In,Ga)Se₂ solar cells: A literature review. *Solar Energy* **42** (2016).
400. Carlton, K. Teaching about heat and temperature. *Phys. Educ.* **35**, 101–105 (2000).
401. Kim, S., Lim, M., Kim, Y., Kim, H.-D. & Choi, S.-J. Impact of Synaptic Device Variations on Pattern Recognition Accuracy in a Hardware Neural Network. *Sci Rep* **8**, 2638 (2018).
402. Chang, C. *et al.* Mitigating Asymmetric Nonlinear Weight Update Effects in Hardware Neural Network Based on Analog Resistive Synapse. *IEEE Journal on Emerging and Selected Topics in Circuits and Systems* **8**, 116–124 (2018).
403. Vetter, J. S., DeBenedictis, E. P. & Conte, T. M. Architectures for the Post-Moore Era.
404. Wang, R. *et al.* Bio-Inspired In-Sensor Compression and Computing Based on Phototransistors. *Small* **18**, 2201111 (2022).
405. Artal, P. Image Formation in the Living Human Eye. *Annual Review of Vision Science* **1**, 1–17 (2015).
406. Wässle, H. Parallel processing in the mammalian retina. *Nat Rev Neurosci* **5**, 747–757 (2004).
407. Liao, F. *et al.* Bioinspired in-sensor visual adaptation for accurate perception. *Nat Electron* (2022) doi:10.1038/s41928-022-00713-1.

408. Wang, C.-Y. *et al.* Gate-tunable van der Waals heterostructure for reconfigurable neural network vision sensor. *Sci. Adv.* **6**, eaba6173 (2020).
409. Li, Y., Wang, J., Yang, Q. & Shen, G. Flexible Artificial Optoelectronic Synapse based on Lead-Free Metal Halide Nanocrystals for Neuromorphic Computing and Color Recognition. *Advanced Science* **n/a**, 2202123.
410. Yang, C. *et al.* Photoelectric Memristor-Based Machine Vision for Artificial Intelligence Applications. *ACS Materials Lett.* 504–526 (2023) doi:10.1021/acsmaterialslett.2c00911.
411. Pi, L. *et al.* Broadband convolutional processing using band-alignment-tunable heterostructures. *Nat Electron* **5**, 248–254 (2022).
412. Gong, J. *et al.* Methylammonium halide-doped perovskite artificial synapse for light-assisted environmental perception and learning. *Materials Today Physics* **21**, 100540 (2021).
413. Li, G. *et al.* Photo-induced non-volatile VO₂ phase transition for neuromorphic ultraviolet sensors. *Nat Commun* **13**, 1729 (2022).
414. Liu, Q. *et al.* All-in-one metal-oxide heterojunction artificial synapses for visual sensory and neuromorphic computing systems. *Nano Energy* **97**, 107171 (2022).
415. Luo, Z.-D. *et al.* Artificial Optoelectronic Synapses Based on Ferroelectric Field-Effect Enabled 2D Transition Metal Dichalcogenide Memristive Transistors. *ACS Nano* **14**, 746–754 (2020).
416. Zhang, Z. *et al.* All-in-one two-dimensional retinomorphic hardware device for motion detection and recognition. *Nat. Nanotechnol.* (2021) doi:10.1038/s41565-021-01003-1.
417. Zhou, F. *et al.* Optoelectronic resistive random access memory for neuromorphic vision sensors. *Nat. Nanotechnol.* **14**, 776–782 (2019).

418. Kumar, M., Lim, J. & Seo, H. Highly transparent reconfigurable non-volatile multilevel optoelectronic memory for integrated self-powered brain-inspired perception. *Nano Energy* **89**, 106471 (2021).
419. Shan, X. *et al.* Plasmonic Optoelectronic Memristor Enabling Fully Light-Modulated Synaptic Plasticity for Neuromorphic Vision. *Advanced Science* **n/a**, 2104632.
420. Cai, Y. *et al.* Broadband Visual Adaption and Image Recognition in a Monolithic Neuromorphic Machine Vision System. *Adv Funct Materials* 2212917 (2022)
doi:10.1002/adfm.202212917.
421. Du, J. *et al.* A robust neuromorphic vision sensor with optical control of ferroelectric switching. *Nano Energy* **89**, 106439 (2021).
422. Hong, X. *et al.* Two-Dimensional Perovskite-Gated AlGa_N/Ga_N High-Electron-Mobility-Transistor for Neuromorphic Vision Sensor. *Advanced Science* **n/a**, 2202019.
423. Sun, Y. *et al.* Mesoscopic sliding ferroelectricity enabled photovoltaic random access memory for material-level artificial vision system. *Nat Commun* **13**, 5391 (2022).
424. Tsai, D.-S. *et al.* Ultra-High-Responsivity Broadband Detection of Si Metal–Semiconductor–Metal Schottky Photodetectors Improved by ZnO Nanorod Arrays. *ACS Nano* **5**, 7748–7753 (2011).
425. You, D. *et al.* Photovoltaic-pyroelectric effect coupled broadband photodetector in self-powered ZnO/ZnTe core/shell nanorod arrays. *Nano Energy* **62**, 310–318 (2019).
426. Dang, Y. *et al.* Solution processed hybrid Graphene-MoO₃ hole transport layers for improved performance of organic solar cells. *Organic Electronics* **67**, 95–100 (2019).

427. Simanjuntak, F. M. *et al.* Enhancing the memory window of AZO/ZnO/ITO transparent resistive switching devices by modulating the oxygen vacancy concentration of the top electrode. *J Mater Sci* **50**, 6961–6969 (2015).
428. Makuła, P., Pacia, M. & Macyk, W. How To Correctly Determine the Band Gap Energy of Modified Semiconductor Photocatalysts Based on UV–Vis Spectra. *J. Phys. Chem. Lett.* **9**, 6814–6817 (2018).
429. Liu, H. *et al.* Fast and Enhanced Broadband Photoresponse of a ZnO Nanowire Array/Reduced Graphene Oxide Film Hybrid Photodetector from the Visible to the Near-Infrared Range. *ACS Appl. Mater. Interfaces* **7**, 6645–6651 (2015).
430. Das, J. *et al.* Micro-Raman and XPS studies of pure ZnO ceramics. *Physica B: Condensed Matter* **405**, 2492–2497 (2010).
431. Ko Park, S.-H. & Lee, Y. E. Controlling preferred orientation of ZnO thin films by atomic layer deposition. *Journal of Materials Science* **39**, 2195–2197 (2004).
432. Jadkar, V. *et al.* Synthesis of orthorhombic-molybdenum trioxide (α -MoO₃) thin films by hot wire-CVD and investigations of its humidity sensing properties. *J Mater Sci: Mater Electron* **28**, 15790–15796 (2017).
433. Xi, Y. *et al.* In-memory Learning with Analog Resistive Switching Memory: A Review and Perspective. *Proceedings of the IEEE* **109**, 14–42 (2021).
434. Guo, T. *et al.* Soft Biomaterials Based Flexible Artificial Synapse for Neuromorphic Computing. *Advanced Electronic Materials* **n/a**, 2200449.
435. Hou, Y.-X. *et al.* Large-Scale and Flexible Optical Synapses for Neuromorphic Computing and Integrated Visible Information Sensing Memory Processing. *ACS Nano* **15**, 1497–1508 (2021).

436. Khan, S. *et al.* Superconducting optoelectronic single-photon synapses. *Nat Electron* (2022) doi:10.1038/s41928-022-00840-9.
437. Albawi, S., Mohammed, T. A. & Al-Zawi, S. Understanding of a convolutional neural network. in *2017 International Conference on Engineering and Technology (ICET)* 1–6 (2017). doi:10.1109/ICEngTechnol.2017.8308186.
438. Li, S. *et al.* Wafer-Scale 2D Hafnium Diselenide Based Memristor Crossbar Array for Energy-Efficient Neural Network Hardware. *Advanced Materials* **34**, 2103376 (2022).
439. Yang, T.-J., Chen, Y.-H., Emer, J. & Sze, V. A method to estimate the energy consumption of deep neural networks. in *2017 51st Asilomar Conference on Signals, Systems, and Computers* 1916–1920 (IEEE, 2017). doi:10.1109/ACSSC.2017.8335698.
440. Li, D., Chen, X., Becchi, M. & Zong, Z. Evaluating the Energy Efficiency of Deep Convolutional Neural Networks on CPUs and GPUs. in *2016 IEEE International Conferences on Big Data and Cloud Computing (BDCloud), Social Computing and Networking (SocialCom), Sustainable Computing and Communications (SustainCom) (BDCloud-SocialCom-SustainCom)* 477–484 (IEEE, 2016). doi:10.1109/BDCloud-SocialCom-SustainCom.2016.76.
441. Ni, L., Liu, Z., Yu, H. & Joshi, R. V. An Energy-Efficient Digital ReRAM-Crossbar-Based CNN With Bitwise Parallelism. *IEEE Journal on Exploratory Solid-State Computational Devices and Circuits* **3**, 37–46 (2017).
442. Amer, G. M. H. & Abushaala, A. M. Edge detection methods. in *2015 2nd World Symposium on Web Applications and Networking (WSWAN)* 1–7 (2015). doi:10.1109/WSWAN.2015.7210349.
443. Tian, J. *et al.* Memristive Fast-Canny Operation for Edge Detection. *IEEE Transactions on Electron Devices* **69**, 6043–6048 (2022).

444. Qi, J. *et al.* Resistive Switching in Single Epitaxial ZnO Nanoislands. *ACS Nano* **6**, 1051–1058 (2012).
445. Gallegos, M. V. *et al.* Effect of Mn in ZnO using DFT calculations: Magnetic and electronic changes. *Journal of Alloys and Compounds* **795**, 254–260 (2019).
446. Hur, J. H., Lee, M.-J., Lee, C. B., Kim, Y.-B. & Kim, C.-J. Modeling for bipolar resistive memory switching in transition-metal oxides. *Phys. Rev. B* **82**, 155321 (2010).
447. Lu, Q. *et al.* Molybdenum metal gate MOS technology for post-SiO₂/gate dielectrics. in *International Electron Devices Meeting 2000. Technical Digest. IEDM (Cat. No.00CH37138)* 641–644 (2000). doi:10.1109/IEDM.2000.904401.
448. Rittich, J., Jung, S., Siekmann, J. & Wuttig, M. Indium-Tin-Oxide (ITO) Work Function Tailoring by Covalently Bound Carboxylic Acid Self-Assembled Monolayers. *physica status solidi (b)* **255**, 1800075 (2018).
449. Fu, Y. *et al.* Enhancing LiAlOX synaptic performance by reducing the Schottky barrier height for deep neural network applications. **9** (2020).
450. Jeong, D. S. *et al.* Emerging memories: resistive switching mechanisms and current status. *Rep. Prog. Phys.* **75**, 076502 (2012).
451. Lanza, M. *et al.* Standards for the Characterization of Endurance in Resistive Switching Devices. *ACS Nano* acsnano.1c06980 (2021) doi:10.1021/acsnano.1c06980.
452. Zhou, G. *et al.* Coexistence of Negative Differential Resistance and Resistive Switching Memory at Room Temperature in TiO_x Modulated by Moisture. *Advanced Electronic Materials* **4**, 1700567 (2018).
453. Adam, G. C., Khiat, A. & Prodromakis, T. Challenges hindering memristive neuromorphic hardware from going mainstream. *Nat Commun* **9**, 5267 (2018).